Vietnam Ministry of Science and Technology

P-ISSN 2525-2461 • E-ISSN 2615-9937

Vietnam Journal of Science, Technology and Engineering

JUNE 2023 • VOLUME 65 NUMBER 2

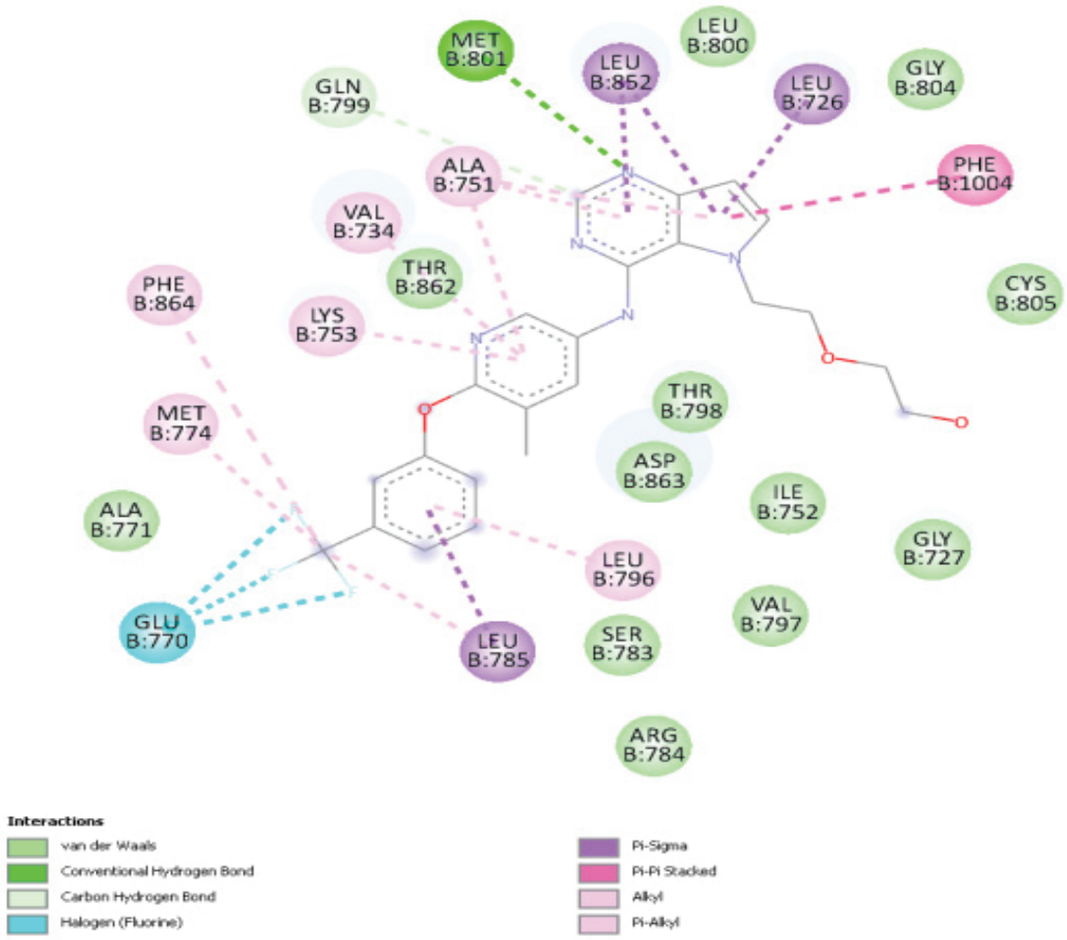

Screening *in silico* the human epidermal growth factor receptor-2 inhibitory effect of isoflavones by molecular docking method for their potential use in breast cancer

VIETNAM JOURNAL OF SCIENCE, TECHNOLOGY AND ENGINEERING * JUNE 2023 * VOLUME 65 NUMBER 2

vietnamscience.vn or vietnamscience.vjst.vn

Vietnam Journal of Science, Technology and Engineering (VJSTE) **is a quarterly double-blind peer-reviewed academic journal. VJSTE publishes research articles and review articles in all areas of science, technology and engineering with the focus on the physical sciences, life sciences and environmental sciences including the following topics:**

- **Physical Sciences**
- **Agriculture**
- **Medicine**
- **Pharmacology**
- **Biology**
- **Biotechnology**
- **Biomedical Applications**
- **Ecology**
- **Climatology**
- **Environmental Science.**

CLASSIFICATION SCHEME

1. **Mathematics and Computer Science**
   - **1.1. Mathematics**
   - **1.2. Computer Science**
   - **1.3. Computational Science**
2. **Physical Sciences**
   - **2.1. Physics**
   - **2.2. Chemistry**
   - **2.3. Engineering**
3. **Life Sciences**
   - **3.1. Agriculture**
   - **3.2. Medicine**
   - **3.3. Pharmacology**
   - **3.4. Biology**
   - **3.5. Biotechnology**
   - **3.6. Biomedical Applications**
4. **Earth Sciences**
   - **4.1. Geography**
   - **4.2. Geology**
   - **4.3. Geophysics**
   - **4.4. Oceanography**
5. **Environmental Sciences**
   - **5.1. Ecology**
   - **5.2. Climatology**
   - **5.3. Environmental Science**

CONTENTS

JUNE 2023 • VOLUME 65 NUMBER 2

27

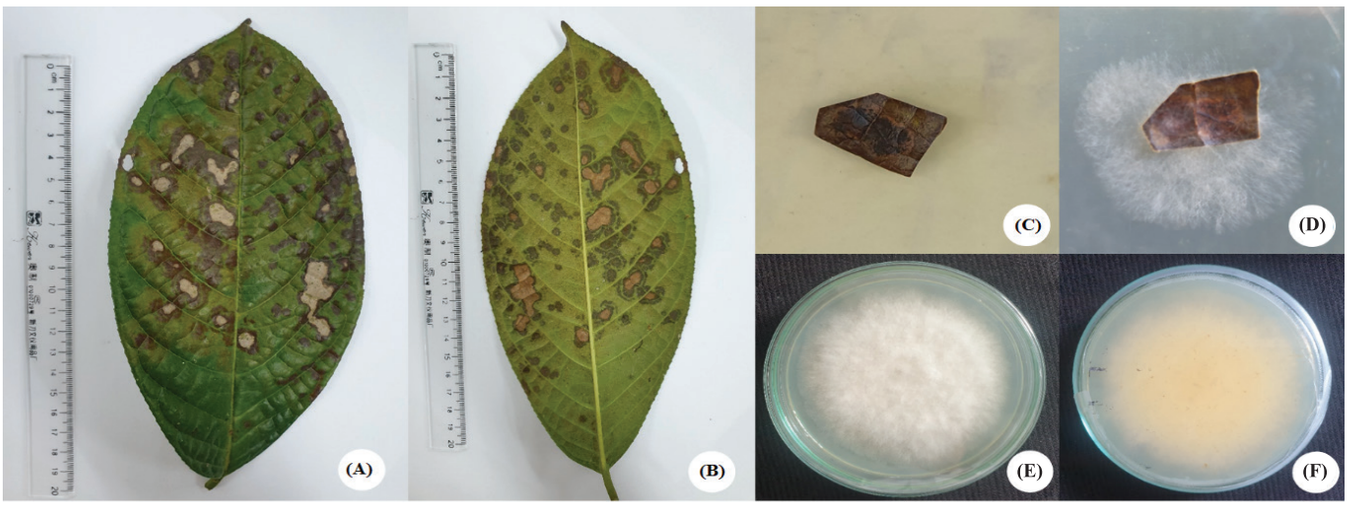

PHYSICAL SCIENCES

LIFE SCIENCES

CONTENTS

JUNE 2023 • VOLUME 65 NUMBER 2

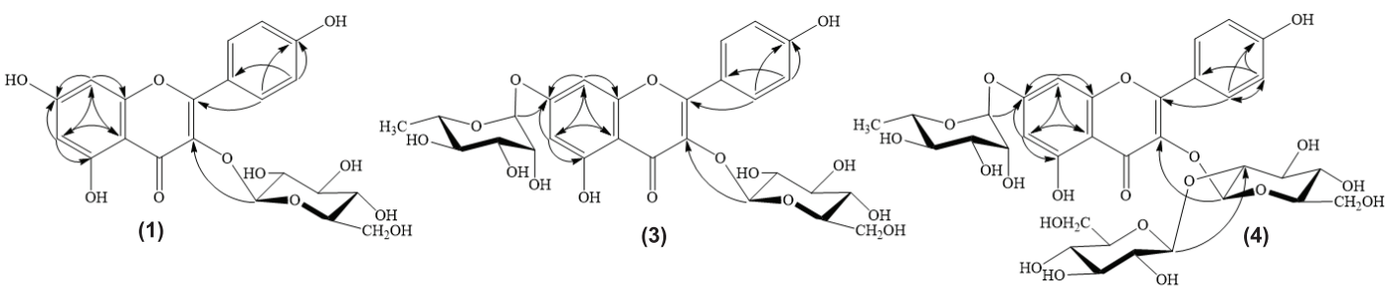

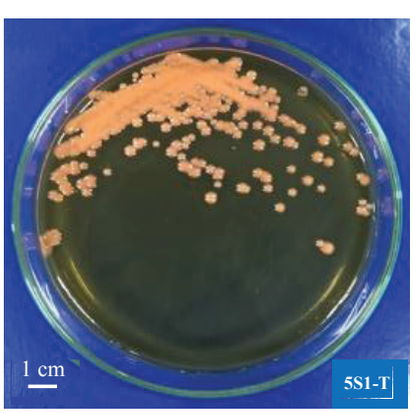

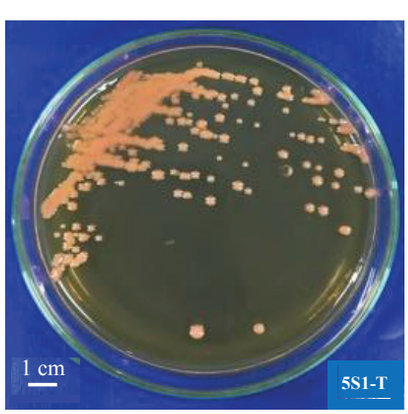

DOI: 10.31276/VJSTE.65(2).03-09

Density functional theory studies on molecular structure, vibrational spectra, AIM, HOMO-LUMO, electronic properties, and NBO analysis of benzoic acid monomer and dimer

Tan Trung Truong[1*], Phuong Dong Nguyen[2], Thi Ngan Nguyen[1], Thi Thu Thuy Le[1], Ngoc Huong Nguyen[1]

[1]Dong Nai Technology University, 5 Nguyen Khuyen Street, Trang Dai Ward, Bien Hoa City, Dong Nai Province, Vietnam
[2]Department of Chemistry, Soongsil University, 369 Sangdo-ro, Dongjak-gu, Seoul, Korea

Received 14 January 2022; revised 15 March 2022; accepted 29 March 2022

Abstract:
In this study, the group of authors investigated the molecular structure, vibrational frequencies, and atom-in-molecule (AIM) analysis of the benzoic acid monomer and dimer. Geometry optimization and vibrational frequency calculations for the monomer and dimer were carried out at the density functional theory (DFT) level with the 6-311++G(2d,p) basis set. UV-Vis spectroscopy and electronic properties (for example, excitation energies, and oscillator strengths) were calculated by time-dependent DFT (TD-DFT) in different solvents. The calculated absorption values mainly represented excitation from HOMO-1 (H-1) → LUMO and HOMO → LUMO+2 (L+2). The structure-activity relationship was interpreted by its molecular electrostatic potential (MEP) surface, which is very useful to the research of molecular structures and their physiochemical-property relationships. The highest occupied molecular orbital (HOMO)-lowest unoccupied molecular orbital (LUMO) energy was fully analysed. The HOMO-LUMO energy gap and other related molecular properties were also calculated. In addition, natural bond orbital (NBO) analysis was carefully carried out to investigate the various intra-intermolecular interactions in the molecular system.

Keywords: **atom-in-molecule, benzoic acid, highest occupied molecular orbital-lowest unoccupied molecular orbital analysis, molecular electrostatic potential, natural bond orbital.**

Classification numbers: **2.1, 2.2**

1. Introduction

Benzoic acid is chemically known as benzene carboxylic acid. Its molecular formula is C_6H_5COOH. This colourless crystalline solid is the simplest aromatic carboxylic acid, which has been known for a long time as the source of a large number of synthesis processes of organic compounds. Indeed, many organic compounds have been synthesized from benzoic acid in many industries and its use in the production of glycol benzoates as plasticizers in adhesive formulations is increasing [1]. Besides, salts and esters of benzoic acid are used as preservatives in foods, drugs, and personal products. In the treatment of fungal skin disease and other diseases such as tines, ringworm, and athlete's foot, benzoic acid is the vital component of benzoin resins and ointments [2].

Hydrogen bonded (A−H···B) molecules have been considered as major points of interest due to their very important role in many fields like chemistry, physics, and biology [3]. Crystal structures of benzoic acids have been determined from neutron diffraction over temperatures between 20-175 K [4]. Molecules can form cyclic hydrogen bond dimers between the carboxylic acid group. In recent years, infrared spectra of the OH stretch region of benzoic acid dimers has been studied by G.M. Florio, et al. (2001) [5] using the double resonance method of fluorescence-dip IR spectroscopy in a supersonic jet. The authors have also computed theoretical IR spectra of the benzoic acid dimer [5, 6]. The infrared spectrum of hydrogen-bonded benzoic acid has been recorded previously [7] and more recently by M. Boczar, et al. (2004) [8]. The geometric structures of the benzoic acid molecule have been investigated by A. Kumer, et al. (2019) [9]. The optimized structural parameters and HOMO, LUMO of the benzoic acid molecule are provided from theoretical calculations using HyperChem 8.0.10 software, but the effect of hydrogen bonding, charge transfer, and NBO analysis has not yet been discussed.

To the best of our knowledge, an extensive investigation of the structural, vibrational, and electronic properties of the monomer and dimer of benzoic acid have not been reported yet in the literature. Hence, we focused our investigation on the monomer and dimer of benzoic acid in the gas phase as we are interested in the dominant contribution to intermolecular interaction between two monomers. The

*Corresponding author: Email: truongtantrung@dntu.edu.vn

detail of vibrational infrared and UV-Vis spectra of benzoic acid molecules were analysed by computational results. Besides, the energy values of HOMO and LUMO molecular orbitals with their corresponding HOMO-LUMO energy gap are studied. In addition, the stabilization resonance energy $E^{(2)}$ was calculated by NBO analysis. Finally, the structure-chemical reactivity relationship and the MEP surface of the title compound were undertaken for the first time.

2. Computational methods

The molecular structure of the title compound was fully optimized at the DFT level using the hybrid functional B3LYP (Becke's three-parameter exchange functional [10] combined with the Lee-Yang-Parr correlation functional [11]) with the 6-311++G(2d,p) basis set [12]. Topological parameters such as electron density (ρ(r)), Laplacian of electron density (∇^2(ρ®), electron kinetic energy density (G(r)), and electron potential energy density (V(r)) at bond critical points (BCP) of intermolecular interactions were identified using AIM 2000 [13] software based on Bader's atom in molecules theory. NBO calculations were performed using GenNBO 5.G [14] as implemented in the Gaussian 09 package at the DFT/B3LYP/6-311++G(2d,p) level. Besides, the MEP [15] of benzoic acid was investigated using theoretical calculations. All calculations were carried out using the GAUSSIAN 09 program [16]. The GaussView program [17] was considered to obtain visual animations and also for the verification of the normal modes assignment.

3. Results and discussion

3.1. Molecular geometry

The optimized geometrical structure of the title compound dimer was performed in the gas phase by DFT at the B3LYP/6-311++G(2d,p) basis set and is presented in Fig. 1. The selected geometric parameters are tabulated in Table 1.

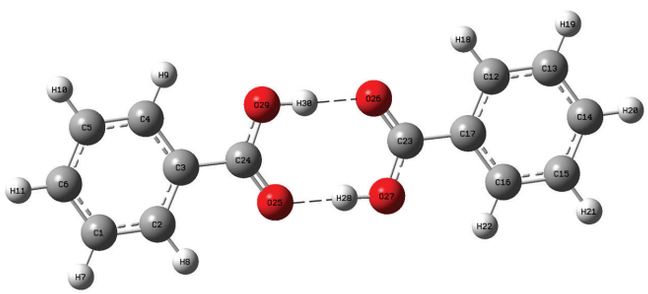

Fig. 1. The optimized geometric structure of benzoic acid dimer by B3LYP/6-311++G(2d,p).

The molecular structure of the benzoic acid dimer is formed by two benzoic acid monomers. The intermolecular hydrogen bond distances are shown in Table 1. The strong intermolecular interaction O27–H28···O25 is formed with a bond distance of 1.637 Å. At the B3LYP/6-311++G** and B3LYP/cc-pVTZ levels, the lengths of O–H···O were 1.663 Å and 1.635 Å, respectively [8], while the distance between O26(27)···O29(25) is about 2.641 Å. The difference between the calculated value in this work and in the literature [8] is around 0.022 Å. As can be seen in Table 1, most of the bond lengths and bond angles estimated at the B3LYP/6-311++G(2d,p) level agree with experimental values.

Table 1. Selected parameters of an optimized geometric of benzoic acid dimer by B3LYP/6-311++G(2d,p).

Parameters	B3LYP/6-311++G(2d,p)	Experimental
Bond lengths (Å)		
C24–O29	1.319	1.29[b]
C24–O25	1.230	1.24[b]
C24–C3	1.485	1.48[b]
C1–C2	1.388	1.42[b]
C2–C3	1.397	1.39[b]
C3–C4	1.397	1.39[b]
C4–C5	1.389	1.41[b]
C5–C6	1.392	1.36[b]
C1–H7	1.083	0.96[b]
C2–H8	1.082	0.79[b]
C4–H9	1.081	0.79[b]
C5–H10	1.083	0.96[b]
C6–H11	1.084	0.91[b]
Bond angles (°)		
O25–C24–O29	123.319	122[b]
C3–C24–O29	114.663	118[b]
C3–C24–O25	122.018	122[b]
Intermolecular H-bond lengths (Å) and angles (°)		
C23–O26–H30	124.88	
CH23–O27–H28	110.41	
O26(27)···O29(25)	2.641	2.64[a]; 2.629[b]
O27–H28···O25	1.637	1.64[b]

[a]: Ref. [18]; [b]: Ref. [19].

In addition, the thermodynamic properties (i.e., zero-point vibrational energy, electronic energy, entropy, enthalpy, and free energy) of a benzoic acid molecule in the gas phase and in a solvent phase (water, methanol, and ethanol) are presented in Table 2. It can be clearly observed from Table 2 that the effects of the solvent phase can be seen in the thermodynamic properties and electronic energy (E) of the solvents, which decrease in the order of gas > water > methanol > ethanol. This shows that molecules of benzoic acid become stabilized in less polar solvents.

Table 2. Calculated thermodynamic properties for benzoic acid with DFT/B3LYP/6-311G++(2d,p).

Phase	ZPVE[a]	E[b]	S[c]	H[d]	F[e]
Gas	72.2014	-264151.7618	84.6390	77.2835	52.0486
Water	71.8701	-264157.6992	85.2760	76.9811	51.5567
Methanol	71.9366	-264159.9909	85.1460	77.0382	51.6520
Ethanol	71.9535	-264160.3021	85.1610	77.0507	51.6602

[a]: Zero-point vibrational energy (ZPVE) (kcal/mol); [b]: Electronic energy (E) (kcal/mol); [c]: Entropy (S) (cal/mol-K); [d]: Enthalpy (H) (kcal/mol); [e]: Free energy (F) (kcal/mol).

3.2. UV-Vis and electronic properties

The solvents' effect on UV-Vis spectra and electronic properties were calculated with DFT based on the CAM-B3LYP [20] using different levels of theory. Theoretical optical absorption spectrum for the gas phase and solvents such as water, methanol (MeOH), and ethanol (EtOH) of benzoic acid in the wavelength region of 150-300 nm is displayed in Fig. 2. The calculated absorption wavelength, excitation energies, and oscillator strengths of benzoic acid were gathered in Table 3.

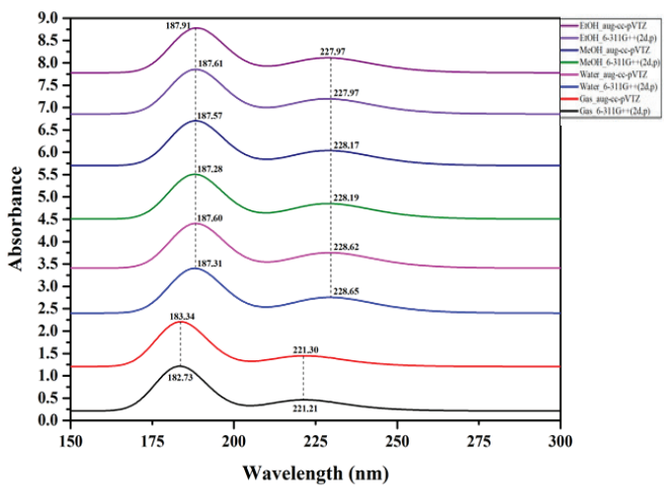

Fig. 2. UV-Vis absorption spectra of benzoic acid in gas phase and in various solvents at different levels of theory.

As it can be seen in Fig. 2 and Table 3, the calculated absorption value for benzoic acid in gas phase have been found to be 183 nm (excited state 5) and 221 nm (excited state 3). This peak mainly represents excitation from HOMO-1 (H-1) → LUMO (73%) and HOMO → LUMO+2 (L+2) (75%). In water, the ~188-nm peak (excited state 5) and ~229-nm peak (excited state 3) for benzoic acid were predicted by DFT. Its major contributions were (H-1) → LUMO (90%) and HOMO → (L+2) (89%). The ~188-nm peak (6.52-6.54 eV) and ~228-nm peak (5.43-5.44 eV) were predicted in MeOH and EtOH solvents by DFT/CAM-B3LYP with 6-311G++(2d,p) and aug-cc-pVTZ basis sets, respectively. The major contributions were (H-1) → LUMO (90%) and HOMO → (L+2) (88%) for MeOH solvent and (H-1) → LUMO (89%) and HOMO → (L+2) (88%) for EtOH solvent.

Table 3. The calculated absorption wavelength λ (nm), excitation energy E (eV), and oscillator strength (f) of benzoic acid in gas phase and various solvents (water, MeOH, EtOH).

Solvent	State	TD-DFT/CAM-B3LYP/6-311G++(2d,p)				TD-DFT/CAM-B3LYP/aug-cc-pVTZ			
		λ (nm)	*E (eV)*	*Osc. Strength*	*MO contribution*	*λ (nm)*	*E (eV)*	*Osc. Strength*	*MO contribution*
Gas	1	242.43	5.11	0.0202		242.29	5.12	0.0196	
	2	237.67	5.22	0.0000		238.70	5.19	0.0000	
	3	221.21	5.60	0.2136	From H-1 to LUMO (73%), from HOMO to LUMO (14%), from HOMO to L+2 (10%)	221.30	5.60	0.2105	From H-1 to LUMO (72%), from HOMO to LUMO (15%), from HOMO to L+3 (10%)
	4	185.26	6.69	0.2683		185.59	6.68	0.2653	
	5	182.73	6.79	0.6232	From H-1 to LUMO (10%), from HOMO to L+2 (75%), from H-1 to L+2 (8%), from H-1 to L+10 (2%)	183.34	6.76	0.0008	From HOMO to L+1 (80%), from H-1 to L+1 (3%), from HOMO to L+2 (4%), HOMO to L+5 (3%), HOMO to L+15 (4%)
	6	182.42	6.80	0.0007		182.99	6.78	0.6311	
	7	180.16	6.88	0.0068		181.13	6.84	0.0063	
	8	171.08	7.25	0.0000		172.20	7.20	0.0000	
Water	1	247.14	5.02	0.0373		246.99	5.02	0.0365	
	2	230.54	5.38	0.0000		231.11	5.36	0.0000	
	3	228.65	5.42	0.3252	From H-1 to LUMO (90%), from HOMO to L+2 (6%)	228.62	5.42	0.3218	From H-1 to LUMO (90%), from HOMO to L+2 (6%)
	4	189.63	6.54	0.3266		189.95	6.53	0.3254	
	5	187.31	6.62	0.6418	From HOMO to L+2 (89%), from H-1 to LUMO (5%), from H-1 to L+9 (2%)	187.60	6.61	0.6546	From HOMO to L+2 (88%), from H-1 to LUMO (6%)
	6	180.77	6.86	0.0000		182.52	6.79	0.0000	
	7	177.99	6.97	0.0053		179.82	6.90	0.0049	
	8	175.83	7.05	0.0000		176.74	7.02	0.0000	
MeOH	1	246.76	5.02	0.0367		246.61	5.03	0.0359	
	2	230.31	5.38	0.0000		230.88	5.37	0.0000	
	3	228.19	5.43	0.3207	From H-1 to LUMO (90%), from HOMO to L+2 (6%)	228.17	5.43	0.3172	From H-1 to LUMO (89%), from HOMO to L+2 (7%)
	4	189.55	6.54	0.3303		189.86	6.53	0.3290	
	5	187.28	6.62	0.6451	From HOMO to L+2 (88%), from H-1 to LUMO (6%), from H-1 to L+9 (2%)	187.57	6.61	0.6578	From HOMO to L+2 (88%), from H-1 to LUMO (6%)
	6	180.90	6.85	0.0001		182.62	6.79	0.0001	
	7	178.14	6.96	0.0053		179.95	6.89	0.0049	
	8	175.52	7.06	0.0000		176.43	7.03	0.0000	
EtOH	1	246.45	5.03	0.0373		246.31	5.03	0.0365	
	2	231.44	5.36	0.0000		232.03	5.34	0.0000	
	3	227.97	5.44	0.3234	From H-1 to LUMO (89%), from HOMO to LUMO (2%), from HOMO to L+2 (6%)	227.97	5.44	0.3202	From H-1 to LUMO (89%), from HOMO to LUMO (2%), from HOMO to L+3 (7%)
	4	189.82	6.53	0.3426		190.13	6.52	0.3414	
	5	187.61	6.61	0.6539	From HOMO to L+2 (88%), from H-1 to LUMO (6%), from H-1 to L+10 (2%)	187.91	6.60	0.6669	From HOMO to L+3 (87%), from H-1 to LUMO (6%)
	6	181.24	6.84	0.0001		182.96	6.78	0.0001	
	7	178.58	6.94	0.0051		180.39	6.87	0.0048	
	8	175.23	7.08	0.0000		176.16	7.04	0.0000	

H and L represents the molecular orbital of the HOMO (H) and LUMO (L), respectively.

3.3. AIM analysis

Topological geometry of a benzoic acid dimer using AIM software is shown in Fig. 3. Topological parameters for the title compound dimer are given in Table 4.

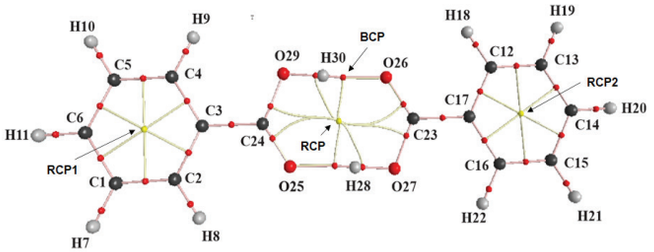

Fig. 3. Topological geometry of BCP (small red spheres) and RCP (small yellow spheres) for a benzoic acid dimer calculated with B3LYP/6-311++G(2d,p).

From Table 4, the electron density (ρ(rc)) and Laplacian ($\nabla^2\rho(rc)$) at the BCP of H···O contacts are 0.051 and 0.126 a.u., respectively. They all fit within the criteria for formation of hydrogen bonds (HBs) [21]. The O–H···O interactions are partly covalent in nature as indicated by $\nabla^2\rho(rc)>0$ (0.126 a.u), $H(rc)\leq 0$ (-0.007), and $G/|V(rc)|\leq 1$ (-0.846 a.u). The strength of the hydrogen bond interaction increases with increasing local electron density at BCP of HBs through the hydrogen bond energies (E_{HB}). In this work, E_{HB} was calculated to be -59.6 kJ.mol^{-1}. The calculated value of E_{HB} affirmed that the HBs found in the title compound belong to strong hydrogen bonding [3, 22].

Table 4. AIM analysis for a cyclic dimer of benzoic acid using B3LYP/6-311++G(2d,p).

Parameter	O–H	O–H···O	RCP1[a]	RCP2[b]	RCP[c]
ρ(rc)	0.321	0.051	0.023	0.023	0.009
$\Delta^2\rho(rc)$	-2.377	0.126	0.159	0.159	0.035
λ_1	-1.647	-0.093	-0.018	-0.018	-0.008
λ_2	-1.629	-0.092	0.088	0.088	0.014
λ_3	0.899	0.310	0.089	0.089	0.029
G(rc)	0.067	0.038	0.034	0.034	0.008
V(rc)	-0.728	-0.045	-0.028	-0.028	-0.007
G/|V(rc)|	-0.092	-0.846	-1.217	-1.217	-1.174
H(rc)	-0.661	-0.007	0.006	0.006	0.001

[a, b, c]: labelled in Fig. 3.

3.4. Vibrational analysis

The title compound consists of 15 atoms and therefore exhibits 39 normal modes of vibrations. The monomer structure has C_1 point group symmetry. The vibrational analysis of benzoic acid is performed on the basis of the characteristic vibrations of C–H, O–H, C=O, –COOH, and phenyl ring modes. The calculated and experimental IR spectra of the title molecule are given in Fig. 4. The vibrational analysis of the title compound was performed on the basis of the characteristic vibrations of the most important excited states in the molecule. The vibrational assignments for different functional groups are discussed below.

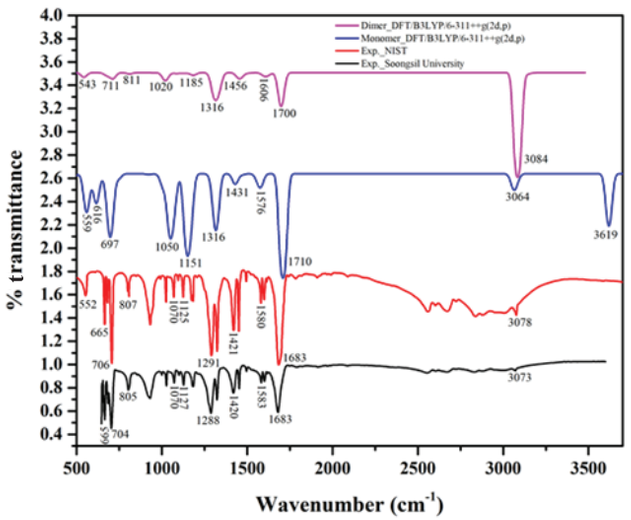

Fig. 4. Experimental and calculated FT-IR spectra of benzoic acid monomer and dimer.

Carboxylic acids group vibrations: Carbonyl and hydroxyl groups are best characterized by carboxylic acid groups. When a non-hydrogen bond is observed in the region 3700-3500 cm^{-1}, the existence of a hydrogen bond formation lowers the O–H stretching frequency in the 3500-3200 cm^{-1} region. In our theoretical calculations of a

Table 5. Experimental and calculated vibrational frequencies and assignments based on potential energy distribution (PED) calculation of the benzoic acid monomer and dimer with B3LYP/6-311++G(2d,p).

No.	Frequencies (cm^{-1})			[b]Assignments based on PED calculations
	Exp.[a]	*Cal_monomer*	*Cal_dimer*	
1	552	559	543	$\delta(H_{15}\text{-}O_{14}\text{-}C_{12}\text{-}C_3)$
2	665	616	-	$\beta(O_{13}\text{-}C_{12}\text{-}O_{14}) + \beta(C_1\text{-}C_6\text{-}C_5)$
3	706	697	711	$\delta(H_7\text{-}C_1\text{-}C_6\text{-}C_5) + \delta(H_{10}\text{-}C_5\text{-}C_6\text{-}C_1) + \delta(C_3\text{-}C_2\text{-}C_6\text{-}C_1) + \gamma(O_{13}\text{-}C_3\text{-}O_{14}\text{-}C_{12})$
4	1070	1050	1020	$\nu(C_2\text{-}C_1) + \nu(O_{14}\text{-}C_{12}) + \beta(H_9\text{-}C_4\text{-}C_5)$
5	1125	1151	1185	$\beta(H_{15}\text{-}O_{14}\text{-}C_{12}) + \beta(H_9\text{-}C_4\text{-}C_5)$
6	1291	1316	1316	$\nu(O_{14}\text{-}C_{12}) + \nu(C_{12}\text{-}C_3) + \beta(H_{15}\text{-}O_{14}\text{-}C_{12}) + \beta(O_{13}\text{-}C_{12}\text{-}O_{14})$
7	1421	1431	1456	$\beta(H_7\text{-}C_1\text{-}C_2) + \beta(H_{10}\text{-}C_5\text{-}C_6) + \beta(H_{11}\text{-}C_6\text{-}C_1)$
8	1580	1576	1606	$\nu(C_2\text{-}C_1) + \nu(C_4\text{-}C_5)$
9	1683	1710	1700	$\nu(O_{13}\text{-}C_{12})$
10	-	3064	-	$\nu(C_1\text{-}H_7) + \nu(C_5\text{-}H_{10}) + \nu(C_6\text{-}H_{11})$
11	3078	3619	3084	$\nu(O_{14}\text{-}H_{15})$

[a]: Frequencies_Exp.: https://webbook.nist.gov/cgi/cbook.cgi?ID=C65850&Type=IR-SPEC&Index=4; [b]: Abbreviations: ν, β, δ, and γ denote stretching, in-plane bending and torsion modes, respectively. The assignments of the vibrational frequencies were performed by PED analysis by using VEDA4 program [23].

benzoic acid monomer, the IR band at 3619 cm^{-1} is assigned to O–H stretching modes as observed in Table 5. The values of these modes show agreement with experimental values. While in the dimer, these modes are seen at 3084 cm^{-1} because the O–H stretching wave number is shifted due to resonance in the dimer. These results agree with data from literature [24]. The in-plane O–H bend and out-of-plane O–H bend vibrations occur at 1350±50 cm^{-1} and 650±50 cm^{-1}, respectively. Accordingly, an O–H out-of-plane bend can be observed in FT-IR at 559 and 543 cm^{-1} (monomer and dimer, respectively). Besides, the C=O stretching of carboxylic acids located in the region 1760-1690 cm^{-1} [25]. The biggest C=O stretching vibration in the carboxylic acid group of a benzoic acid monomer is calculated at 1710 cm^{-1}. In dimer form, these stretching modes are assigned at 1700 cm^{-1} as in Table 5.

Carbon-hydrogen vibrations: For all aromatic and heteroaromatic organic compounds, 2C–H stretching vibrations are observed in the region 3250-2950 cm^{-1} whereas the region 3250-3100 cm^{-1} contains the asymmetric stretching mode and 3100-2950 cm^{-1} contains the symmetric stretching mode of vibrations [26]. C–H bending vibrations are observed in the 1300-1000 cm^{-1} region while the out-of-plane bending vibrations occur in the 1000-675 cm^{-1} [24]. From Table 5, the C–H stretching modes of the title compound are observed in FT-IR at 3064 cm^{-1}. The calculated C–H out-of-plane bending is assigned to the bands at 697 cm^{-1}. These results are also seen in the literature [8, 27].

Carbon-carbon ring vibrations: C–C stretching vibrations usually occur within the range of 1625-1430 cm^{-1} in the ring [28]. For example, C–C stretching was observed at 1586, 1547, 1420, and 1306 cm^{-1} [29] and also at the frequencies 1369, 1551, 1584, and 1612 cm^{-1} [30]. In this study, the C–C modes for the benzoic acid monomer and dimer were observed at 1576 and 1606 cm^{-1}, respectively, and assigned by PED.

3.5. NBO analysis

NBO analysis for the benzoic acid dimer were performed using B3LYP/6-311++G(2d,p). The energy difference between donor and acceptor i and j NBO orbitals in a.u., F(i,j), which is the Fock matrix element, and $E^{(2)}$, the energy of hyper-conjugative interactions (kcal.mol^{-1}), are gathered in Table 6.

Table 6. Second order perturbation theory of the Fock matrix of a benzoic acid dimer by NBO analysis.

Interaction (donor → acceptor)[a]		E(i)–E(j)	F(i,j)	$E^{(2)b}$
LP(2) O25	σ*C24–O29	3.17	0.308	36.12
LP(2) O29	σ*C24–O25	3.55	0.178	10.77
LP(2) O26	σ*C23–O27	4.13	1.109	59.30
LP(1) O25	σ*C3–C24	7.76	9.919	87.78
LP(2) O26	σ*C17–C23	4.13	1.109	59.30
LP(2) O25	σ*O27–H28	4.37	0.169	7.91
LP(1) O26	σ*O29–H30	1.88	0.232	35.36

[a]: See Fig. 1 for atom numbering; [b]: kcal.mol^{-1} is the unit of $E^{(2)}$.

The O–H···O bond in the title compound dimer is confirmed by lone-pair orbital in the electron donation to the σ* antibonding orbital for LP(O) → σ*(O–H) interactions. The orbital interaction in lone-pairs of oxygen atoms LP(O25) → σ*(O27–H28), LP(O26) → σ*(O29–H30) had $E^{(2)}$ values of 7.91 and 35.36 kcal.mol^{-1} respectively. These $E^{(2)}$ values show the formation of intermolecular HBs. The existence of interactions in the dimer of benzoic acid is also confirmed by AIM analysis as shown in Fig 3. Similarly, the $E^{(2)}$ value was 87.78 kcal.mol^{-1} for the interaction (O25) → σ*(C3–C24), which is a huge value. This results in intramolecular charge transfer causing stabilization of the molecular system.

3.6. Frontier molecular orbitals and MEP

The energies of the two most important molecular orbitals in a molecule are both used to describe various chemical properties, for example, the HOMO and LUMO and the value of energy separation between the HOMO and LUMO ($\Delta E_{HOMO-LUMO}$). Several chemical parameters, such as ionization potential (I), electron affinity (A), electronic chemical potentials (μ), global hardness (η), electrophilicity (ω), electronegativity (χ), and chemical softness (S) can be evaluated from the HOMO, LUMO energy [31-33]. The calculated results are shown in Fig. 5A. The calculated values of HOMO and LUMO energy are -7.460 and -1.791 eV, respectively. The $\Delta E_{HOMO-LUMO}$ energy gap is estimated to be 5.669 eV, which clarifies the interactions of charge transfer occurring in benzoic acid. The HOMO-LUMO gap is related to chemical reactivity or kinetic stability, and since both have negative values, they decide the chemical stability of the molecule.

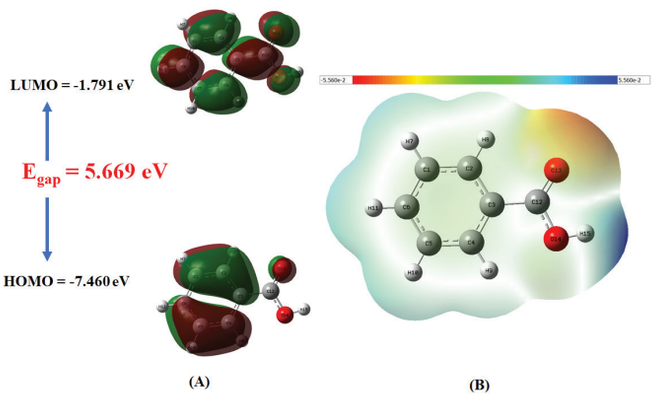

Fig. 5. (A) The frontier molecular orbitals; (B) MEP map for benzoic acid calculated by DFT at the B3LYP/6-311++G(2d,p) level.

The MEP is a plot of electrostatic potential mapped onto a constant electron density surface. The surfaces of the molecule having different electrostatic potentials are represented by various colours. The surface is coloured according to the local electrostatic potential (e.g., red/negative, green/near zero, and blue/positive). The values of the electrostatic potential decrease in the order blue > green > yellow > orange > red [34]. From the MEP shown in Fig. 5B, it is evident that the negative (red colour) charge covers the carbonyl oxygen atom O25(26) and the positive region (blue colour) covers the carboxylic acid hydrogen atom H28(30)–O25(26). This confirms the existence of an intermolecular O27(29)–H28(30)···O25(26) interaction.

4. Conclusions

In the present theoretical study, structural, vibrational, and electronic investigations with AIM, FT-IR, MEP, HOMO-LUMO, and NBO analysis of the monomer and dimer of benzoic acid have been carried with the B3LYP/6-311++G(2d,p) basis set. The geometrical parameters of bond lengths and angles have been calculated and compared with their experimental values. The solvent effect on the electronic absorption spectra of benzoic acid was analysed in the gas phase as well as in various solvents by using UV-Vis spectroscopy and DFT calculations. The HOMO-LUMO energy gap was calculated to be 5.669 eV. The low HOMO-LUMO band gap indicated that benzoic acid is more reactive and has less kinetic stability. The hydrogen bond interaction was studied by AIM analysis. The strength of the interaction was evaluated using NBO analysis through the energy of the hyperconjugative interaction $E^{(2)}$ value. The energy value of the LP(1) O26 → σ^*O29–H30 interaction was 35.36 kcal.mol^{-1} indicating the existence of hydrogen bond interactions in the dimer. The electrostatic potential map was also discussed.

CRediT author statement

Tan Trung Truong: Method, Data analysis, Writing, Edited and Revised; Phuong Dong Nguyen: Method, Data analysis, Writing; Thi Ngan Nguyen: Method, Data analysis, Writing; Thi Thu Thuy Le: Method, Data analysis, Writing; Ngoc Huong Nguyen: Method, Data analysis, Writing.

ACKNOWLEDGEMENTS

We are thankful to Professor Renjith Thomas, Changanassery 686101, Kerala INDIA and also thankful to Ph.D. Phan Dang Cam Tu, Laboratory of Computational Chemistry and Modelling, Quy Nhon University for all kind of supporting the Gaussian 09 program.

COMPETING INTERESTS

The authors declare that there is no conflict of interest regarding the publication of this article.

REFERENCES

[1] W.D. McBride, C. Greene, L. Foreman, et al. (2015), "The profit potential of certified organic field crop production", *USDA, Economic Research Service*, Economic Research Report no. ER-188, 52pp.

[2] N. Akhtar, A. Verma, K. Pathak (2015), "Topical delivery of drugs for the effective treatment of fungal infections of skin", *Current Pharmaceutical Design*, **21(20)**, pp.2892-2913, DOI: 10.2174/1381612821666150428150456.

[3] G.R. Desiraju, T. Steiner (2001), *The Weak Hydrogen Bond: In Structural Chemistry And Biology*, Oxford University Press, DOI: 10.1093/acprof:oso/9780198509707.001.0001.

[4] C.C. Wilson, N. Shankland, A.J. Florence (1996), "A single-crystal neutron diffraction study of the temperature dependence of hydrogen-atom disorder in benzoic acid dimers", *Journal of The Chemical Society, Faraday Transactions*, **92(24)**, pp.5051-5057, DOI: 10.1039/FT9969205051.

[5] G.M. Florio, E.L. Sibert, T.S. Zwier (2001), "Fluorescence-dip IR spectra of jet-cooled benzoic acid dimer in its ground and first excited singlet states", *Faraday Discussions*, **118**, pp.315-330, DOI: 10.1039/B009594J.

[6] G.M. Florio, T.S. Zwier, E.M. Myshakin, et al. (2003), "Theoretical modelling of the OH stretch infrared spectrum of carboxylic acid dimers based on first-principles anharmonic couplings", *The Journal of Chemical Physics*, **118(4)**, pp.1735-1746, DOI: 10.1063/1.1530573.

[7] H.T. Flakus, M. Chełmecki (2002), "Infrared spectra of the hydrogen bond in benzoic acid crystals: Temperature and polarization effects", *Spectrochimica Acta Part A: Molecular and Biomolecular Spectroscopy*, **58(1)**, pp.179-196, DOI: 10.1016/S1386-1425(01)00525-X.

[8] M. Boczar, K. Szczeponek, M.J. Wójcik, et al. (2004), "Theoretical modeling of infrared spectra of benzoic acid and its deuterated derivative", *Journal of Molecular Structure*, **700(1-3)**, pp.39-48, DOI: 10.1016/j.molstruc.2004.03.024.

[9] A. Kumer, N. Sarker, S. Paul (2019), "The theoretical investigation of HOMO, LUMO, thermophysical properties and QSAR study of some aromatic carboxylic acids using HyperChem programming", *International Journal of Chemistry and Technology*, **3(1)**, pp.26-37, DOI: 10.32571/ijct.478179.

[10] A.D. Becke (1988), "Density-functional exchange-energy approximation with correct asymptotic behavior", *Physical Review A*, **38(6)**, DOI: 10.1103/PhysRevA.38.3098.

[11] C. Lee, W. Yang, R.G. Parr (1988), "Development of the Colle-Salvetti correlation-energy formula into a functional of the electron density", *Physical Review B*, **37(2)**, DOI: 10.1103/PhysRevB.37.785.

[12] R.A. Kendall, T.H Dunning, R.J. Harrison (1992), "Electron affinities of the first-row atoms revisited. Systematic basis sets and wave functions", *The Journal of Chemical Physics*, **96(9)**, pp.6796-6806, DOI: 10.1063/1.462569.

[13] F.B. König, J. Schönbohm (2000), *AIM 2000 1.0*, University of Applied Sciences: Bielefeld, Germany.

[14] E. Glendening, J.K. Badenhoop, A.E. Reed, et al. (2001), *Gen NBO 5.G*, Theoretical Chemistry Institute: University of Wisconsin.

[15] P. Politzer, P.R. Laurence, K. Jayasuriya (1985), "Molecular electrostatic potentials: An effective tool for the elucidation of biochemical phenomena", *Environmental Health Perspectives*, **61**, pp.191-202, DOI: 10.1289/ehp.8561191.

[16] M.J. Frisch, G.W. Trucks, H.B. Schlegel, et al. (2009), *Gaussian 09*, https://gaussian.com/g09citation/, accessed 20 October 2021.

[17] R. Dennington, T. Keith, J. Millam (2009), *GaussView*, Version 5, https://www.scirp.org/(S(vtj3fa45qm1ean45vvffcz55))/reference/ReferencesPapers.aspx?ReferenceID=1958990, accessed 20 October 2021.

[18] G.A. Sim, J.M. Robertson, T.H. Goodwin (1955), "The crystal and molecular structure of benzoic acid", *Acta Crystallographica*, **8(3)**, pp.157-164, DOI: 10.1107/S0365110X55000601.

[19] C.C. Wilson, N. Shankland, A.J. Florence (1996), "Direct determination of the temperature dependence of proton transfer in the benzoic acid dimer by single crystal neutron diffraction", *Chemical Physics Letters*, **253(1-2)**, pp.103-107, DOI: 10.1016/0009-2614(96)00217-5.

[20] T. Yanai, D.P. Tew, N.C. Handy (2004), "A new hybrid exchange-correlation functional using the Coulomb-attenuating method (CAM-B3LYP)", *Chemical Physics Letters*, **393(1-3)**, pp.51-57, DOI: 10.1016/j.cplett.2004.06.011.

[21] U. Koch, P.L. Popelier (1995), "Characterization of CHO hydrogen bonds on the basis of the charge density", *The Journal of Physical Chemistry*, **99(24)**, pp.9747-9754, DOI:10.1021/J100024A016.

[22] G.A. Jeffrey (1997), *An Introduction to Hydrogen Bonding*, Oxford University Press, 320pp, DOI: 10.1021/ja9756331.

[23] M.H. Jamroz (2004), "Vibrational energy distribution analysis VEDA 4", *Warsaw Business Journal*, https://www.scienceopen.com/document?vid=c3aca357-33d7-4fa8-8fb3-6711575c8e32, accessed 20 October 2021.

[24] N. Issaoui, H. Ghalla, S. Muthu, et al. (2015), "Molecular structure, vibrational spectra, AIM, HOMO-LUMO, NBO, UV, first order hyperpolarizability, analysis of 3-thiophenecarboxylic acid monomer and dimer by Hartree-Fock and density functional theory", *Spectrochimica Acta Part A: Molecular and Biomolecular Spectroscopy*, **136**, pp.1227-1242, DOI: 10.1016/j.saa.2014.10.008.

[25] M.K. Matysek, A. Matwijczuk, M. Florek, et al. (2018), "Application of FTIR spectroscopy for analysis of the quality of honey", *BIO Web of Conferences*, **10**, DOI: 10.1051/bioconf/20181002008.

[26] R.M. Silverstein, G.C. Bassler (1962), "Spectrometric identification of organic compounds", *Journal of Chemical Education*, **39(11)**, DOI: 10.1021/ed039p546.

[27] S.G. Stepanian, I.D. Reva, E.D. Radchenko, et al. (1996), "Infrared spectra of benzoic acid monomers and dimers in argon matrix", *Vibrational Spectroscopy*, **11(2)**, pp.123-133, DOI: 10.1016/0924-2031(95)00068-2.

[28] E.B. Sas, M. Kurt, M. Can, et al. (2016), "Spectroscopic studies on 9H-carbazole-9-(4-phenyl) boronic acid pinacol ester by DFT method", *Journal of Molecular Structure*, **1118**, pp.124-138, DOI: 10.1016/j.molstruc.2016.03.064.

[29] V. Dixit, R.A. Yadav (2015), "Experimental IR and Raman spectroscopy and DFT methods based material characterization and data analysis of 2-Nitrophenol", *Biochemistry and Pharmacology*, **4**, DOI: 10.4173/2167-0501.1000183.

[30] E.G. Lewars (2003), *Computational Chemistry*, Springer Dordrecht, DOI: 10.1007/978-90-481-3862-3.

[31] K. Fukui (1982), "Role of frontier orbitals in chemical reactions", *Science*, **218(4574)**, pp.747-754, DOI: 10.1126/science.218.4574.747.

[32] E.A.M. Gad, E.M.S. Azzam, S.A.H. Hussien (2018), "Theoretical approach for the performance of 4-mercapto-1- alkylpyridin-1-ium bromide as corrosion inhibitors using DFT", *Egyptian Journal of Petroleum*, **27(4)**, pp. 695-69, DOI: 10.1016/j.ejpe.2017.10.005.

[33] M. Miar, A. Shiroudi, K. Pourshamsian, et al. (2020), "Theoretical investigations on the HOMO-LUMO gap and global reactivity descriptor studies, natural bond orbital, and nucleus-independent chemical shifts analyses of 3-phenylbenzo [d] thiazole-2 (3 H)-imine and its para-substituted derivatives: Solvent and substituent effects", *Journal of Chemical Research*, **45(1-2)**, pp.147-158 DOI: 10.1177/1747519820932091.

[34] I. Warad, O. Ali, A.A. Ali, et al. (2020), "Synthesis and spectral Identification of three Schiff bases with a 2-(piperazin-1-yl)-N-(thiophen-2-yl methylene) ethanamine moiety acting as novel pancreatic lipase inhibitors: Thermal, DFT, antioxidant, antibacterial, and molecular docking investigations", *Molecules*, **25(9)**, DOI: 10.3390/molecules25092253.

DOI: 10.31276/VJSTE.65(2).10-14

Effects of gold and platinum on the activity of catalysts for the complete oxidation reaction of hydrocarbons and carbon monoxide

Cuong Huynh Le Huy*

Faculty of Chemical Engineering, Ho Chi Minh City University of Food Industry (HUFI), 140 Le Trong Tan Street, Tay Thanh Ward, Tan Phu District, Ho Chi Minh City, Vietnam

Received 14 March 2023; revised 27 March 2023; accepted 3 April 2023

Abstract:

This study presents synthesis results of catalysts made of perovskite-like oxide $La_{2-x}Sr_xCuO_4$ (x=0.0, 0.5, 1.0) using the citrate method and crystallisation at 800°C. The structure of the catalysts was characterised by X-ray diffraction (XRD). The perovskite-like oxide catalyst activity was enhanced with gold (Au) and platinum (Pt). Au was mounted on the perovskite-like oxide catalysts by the sol-gel method. The activity of the perovskite-like oxide $La_{2-x}Sr_xCuO_4$ (x=0.0, 0.5, 1.0) and the perovskite catalyst $LaMnO_3$/$LaCuO_3$ was evaluated by complete oxidation of volatile hydrocarbons (HCs) in a mixture of toluene and methyl ethyl ketone (MEK) and carbon monoxide (CO) in a microflow analysis system combined with gas chromatography. The results showed that the light-off temperature (the 50% conversion temperature of the catalysts) of the Pt, Au/perovskite catalyst samples decreased significantly. The light-off temperature of the Au/$LaSrCuO_4$ Au nanoparticle catalysts in the complete CO oxidation reaction reached a temperature of 150°C, lower than the Pt/$LaSrCuO_4$ catalyst (170°C), allowing replacement of previous Pt catalysts with Au nanoparticle catalysts. The $LaSrCuO_4$ catalyst had better oxidising activities than the La_2CuO_4 catalyst, indicating that the addition of strontium (Sr) has increased the catalyst activity, and demonstrates the potential for application in catalytic converters in motorcycles.

Keywords: **catalytic converter, gold catalyst, $La_{2-x}Sr_xCuO_4$, perovskite-like oxide, platinum catalyst.**

Classification numbers: **2.2, 2.3**

1. Introduction

Emissions emitted from industrial activities, motorcycle, and automobile engines affect the environment. Using a catalyst to completely oxidise the exhaust gases is a highly effective method. Inexpensive catalysts based on metal oxides are often used such as copper oxide, cobalt oxide, manganese oxide, chromium oxide, and nickel oxide. However, oxidation temperatures to achieve high conversion is quite high [1]. Metal-based catalysts such as Pt, Rh, and Pd are highly active, but expensive, and tend to be inactive in gas streams containing chlorine and sulfur compounds. This type of catalyst is now widely used in catalytic converters [1, 2].

Perovskite catalysts with the general formula ABO_3 have been studied. Perovskite catalysts can displace precious metals in the complete oxidation of HCs [2-6]. Elements A and B in ABO_3 are replaced by metals with different oxidation states and change the activity of the catalyst. For example, in the catalytic material $La_{1-x}Sr_xMnO_3$, the authors partially replaced the La^{3+} ion with the Sr^{3+} ion, which increased defects in the structure and changed the catalytic properties [2, 3, 7].

Au metal has been used as a catalyst since 1906, but it was not until the 1980s that Au was intensively studied by M. Haruta (2004) [8]. Au catalysts are highly effective in the field of environmental chemistry and exhaust gas treatment. Au catalysts are used very effectively for the oxidation reaction of not only CO but also many other compounds. Au catalysts can be carried on metal oxides such as Fe_2O_3, MgO, ZrO_2, Al_2O_3, ZnO, and TiO_2, and they have very strong activity and can be used for low-temperature CO oxidation reactions [8-10].

In one study [11], the authors made coatings with a perovskite Al-$La_{0.8}Sr_{0.2}CoO_3$ (LSCO) catalyst coating on a ceramic carrier. The results showed a significant reduction in HCs and CO when the LSCO coating was applied.

Pd catalysts on the perovskite $LaAlO_3$ have been studied to reduce NO at low temperatures. The catalyst Pd/$La_{0.9}Ba_{0.1}AlO_{3-\delta}$ has significantly higher activity than other Pd catalysts at temperatures lower than 300°C [12].

In another study [13], the author replaced 0.05 moles of La with Pd, which enhanced the activity of the $LaMnO_3$ catalyst during CO oxidation. The catalysts $La_{0.9}Pd_{0.1}MnO_3$ and $La_{0.85}Pd_{0.15}MnO_3$ exhibited extremely high activity.

The results of another study [14] demonstrated the synthesis of perovskite oxide $LaCuO_3$ and $LaCu_{0.53}Ni_{0.47}O_3$, prepared by the sol-gel citrate method, with 5% NiO/$LaCuO_3$ was prepared by impregnation. Products were obtained after heat treatment in

*Email: cuonghlh@hufi.edu.vn

air at 800°C. The most successful results were achieved using the 5% NiO/$LaCuO_3$ precursor, where the amount of treated methane (CH_4) increased by 16.5% compared to $LaCu_{0.53}Ni_{0.47}O_3$.

In the present work, the authors study the effects of Au and Pt catalysts on the perovskite-like oxide $La_{2-x}Sr_xCuO_4$ (x=0.0, 0.5, 1.0) in a complete oxidation reaction of HCs and CO.

2. Experimental section and methods

2.1. Synthesis of the perovskite-like oxide $La_{2-x}Sr_xCuO_4$ (x=0.0, 0.5, 1.0), perovskite $LaMnO_3$ and $LaCuO_3$

A mixture consisting of 4.33 g $La(NO_3)_3.6H_2O$, m (g) $Sr(NO_3)_2$, and n (g) $Cu(NO_3)_2$, such that the molar ratio of La:Sr:Cu=(2-x):x:1 (x=0.0, 0.5, 1.0), was evenly dissolved in 20 ml H_2O, then added to another solution containing 3.82 g citric acid, 2.23 g ethylene glycol, and 20 ml H_2O. The mixture was stirred continuously at a temperature of 60°C until a highly viscous mixture (gel) was obtained. The gel was placed into a thermostat tank and dried at a temperature of 80°C over a period of 12 hours. This process produced the amorphous citrate precursors. The resulting porous solid was calcined at 800°C in an oxygen stream for 5 hours. The resulting black solid was the perovskite-like oxide $La_{2-x}Sr_xCuO_4$.

The synthesis of the perovskite $LaMnO_3$ and perovskite $LaCuO_3$ was similar to $La_{2-x}Sr_xCuO_4$, in which $Sr(NO_3)_2$ was replaced by $Mn(NO_3)_2$ and $Cu(NO_3)_2$ with the molar ratio of La:Mn=1:1 (La:Cu=1:1).

2.2. Preparation of perovskite-like oxide with Au and Pt catalysts

Preparation of platin/perovskite-like oxide catalyst: The calculated $PtCl_4$ solution was added to a 250 ml beaker and water was added at a rate of 10 ml/g catalyst. The perovskite-like oxide material was ground very finely, and a mixture was created. The mixture was stirred for approximately 5 hours at 70°C. Then, it was placed in a beaker in a thermostat tank at 80°C for 12 hours. The catalyst was filtered to remove all the Cl^- ions. The catalyst was placed in the drying cabinet for 2 hours at 100°C to drain all the water. The catalyst was then calcined for 5 hours at 500°C to obtain the Pt/perovskite-like oxide catalyst.

Preparation of Au/perovskite-like oxide catalysts:

Chemicals: Au chloride solution $HAuCl_4.3H_2O$ with 5.07 mM Au (Japan); $NaBH_4$ (Merck); sol stabiliser: polyvinyl alcohol (PVA) $(C_2H_4O)_x$ (China).

The Au sol was stabilised by PVA. The required amount of $HAuCl_4.3H_2O$ solution was placed into a 250 ml beaker. PVA solution was added and stirred at a rate of 1000 rpm at 60°C for 1 hour. Then, 0.1 M $NaBH_4$ solution was added dropwise while maintaining a stirring rate of 1000 rpm at 60°C for 2 hours. The pre-determined amount of perovskite was added to the mixture, and stirring was continued for 5 hours at 60°C. The mixture was filtered with distilled water and the resulting solids were dried at 140°C for 2 hours. The solids were calcined at 500°C for 5 hours to obtain the Au/perovskite-like oxide catalyst.

Research has shown that even small minor quantities of Au nanocatalysts can significantly enhance the low-temperature oxidation of CO and other compounds [8-10]. The Au sols are stabilised in PVA in proportions given by Table 1.

Table 1. Preparation of Au sols on the perovskite-like oxide.

No.	Sol			Carrier
	[PVA] (µg/ml)	*[Au] (µg/ml)*	*PVA/Au (wt/wt)*	
1	64	100	64/100	Perovskite-like oxide $La_{2-x}Sr_xCuO_4$
2	100	100	100/100	

2.3. Characteristics and activity of the catalysts

The structural characteristics of the catalyst were evaluated by XRD (Siemens, Germany). The scanning angle was varied from 0°<2θ<70° at a scanning speed of 1°/min and using Cu Kα radiation at a wavelength of 1.5406 Å.

The dispersion of the Au/perovskites was determined by field emission-scanning electron microscopy (FE-SEM) imaging on a Hitachi S-4800.

The activity of the catalysts was determined through the complete oxidation reactions of HCs such as toluene, MEK, and CO. The process was conducted by gas chromatography on a trace-flow system.

Toluene and MEK analysis conditions: The gas chromatography machine used was a Varian aerograph series 2800 with a flame ionization detector (FID). The separation column was di-n-decyl phthalate 15% Chromosorb 60-80 mesh. The N_2 carrier gas was set to 20 KPa. The H_2 flow rate was 2.7 l/hour, and the air flow rate was 13.8 l/hour. The column temperature was 83°C.

CO analysis conditions: The gas chromatography machine was a chromatron GCHF 18.3 with a thermal conductivity detector (TCD). The separation column was ZV95 zeolite, and the column temperature was room temperature.

Determine conversion degree: The conversion of HC to CO was determined by calculating the area of the input peaks and output peaks according to the following formula:

$$\theta = \left(1 - \frac{S_O}{S_I}\right) \times 100\%$$

where: θ is the conversion degree (%); S_1 is the maximum area of the starting material (unreacted); S_0 is the area of peak of the material remaining after the reaction.

3. Results and discussion

3.1. Structural characteristics of perovskite-like oxide

The perovskite-like oxide catalysts $La_{2-x}Sr_xCuO_4$ (x=0.0, 0.5, 1.0) were crystallized at 800°C. The XRD analysis results of the catalysts are presented in Fig. 1.

Lanthanum oxide crystals are diffracted at 2θ=26.2, 30.1, 39.9, 47.2, 47.2, 52.4, and 57.5°. Copper oxide crystals are diffracted at 2θ=35.55, 35.57, 38.41, and 38.73°. The strontium oxide crystals are diffracted at 2θ=26.46, 30.02, 32.36, 38.25, 44.14, 48.26, and 50.21°. Sr was added to the structure (x=0.5 and x=1.0), the XRD

spectra appeared to show diffraction characteristics of Sr oxide crystals. The XRD spectrum for $LaSrCuO_4$ (x=1.0) in Fig. 1 also showed that the clearest diffractions.

The XRD of perovskite samples $LaMnO_3$ and $LaCuO_3$ crystallized at 800°C similar to the results in studies [2, 14].

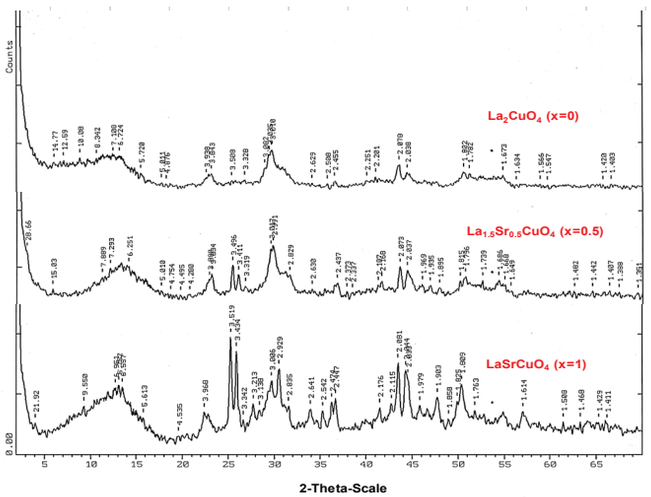

Fig. 1. XRD spectra of the perovskite-like oxide $La_{2-x}Sr_xCuO_4$ (x=0.0, 0.5, 1.0) at 800°C.

3.2. Activity of perovskite-like oxide catalysts in the complete oxidation of the mixture toluene and MEK

The activity of perovskite-like oxide $LaSrCuO_4$ and perovskite $LaMnO_3$/$LaCuO_3$ catalysts were evaluated in the complete oxidation reaction of the mixture toluene and MEK. The results are presented in Fig. 2 and Table 2.

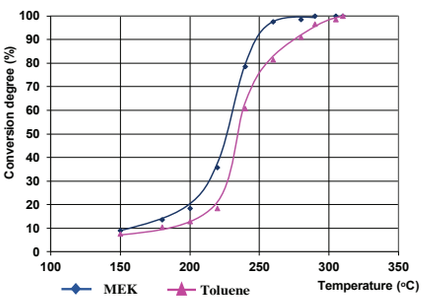

Fig. 2. The conversion degree of the toluene and MEK mixture on the $LaSrCuO_4$ catalyst at 800°C.

Table 2. The light-off temperature of perovskite catalysts in the complete oxidation of the toluene and MEK mixture.

Catalysts	The light-off temperature (°C)	
	Toluene	*MEK*
$LaMnO_3$	230	190
$LaCuO_3$	235	205
$LaSrCuO_4$	235	220

The results from Fig. 2 show that the light-off temperature of MEK on $LaSrCuO_4$ is lower than that of toluene (temperatures at 220°C and 235°C).

The results of Table 2 show that the perovskite catalysts $LaMnO_3$/$LaCuO_3$ and the perovskite-like oxide $LaSrCuO_4$ catalyst are fully applicable to the treatment of motorcycle exhaust gases. These catalysts are capable of completely oxidising VOCs such as toluene and MEK present in motorcycle exhaust gases, and the catalyst can work at lower temperatures if toluene and MEK are present. The light-off temperature ranges from 230-260°C, which is suitable for the highest working temperature of motorcycle exhaust gases.

The results from Table 2, the perovskite catalyst $LaMnO_3$ has the light-off temperature of MEK is lower than that of toluene. This is also consistent with the theory. Because MEK has an intramolecular oxygen element, its oxidation capacity occurs more easily than that of toluene. Besides, the presence of MEK makes toluene more susceptible to oxidation in the absence of MEK. The light-off temperature of toluene in the presence of MEK was 230°C compared to 245°C without MEK [5, 6].

The light-off temperature of the catalyst is the temperature at which the catalyst converts 50% of the substance to be processed. This can be considered as the priming temperature, which is the lowest temperature at which the catalyst begins to have the activity required for industrial application. This temperature partly reflects the true value of the catalyst [1, 2].

According to a study [2], thermal decomposition of toluene in perovskite catalysts releases energy (39,500 to 74,000 kJ), whereas MEK gives off a much higher energy (137,000 to 230,000 kJ). MEK emits a large amount of heat, which speeds up the reaction process, resulting in MEK being better oxidised. Thus, the conversion degree is higher than that of toluene, the jump interval is shorter, and the light-off temperature is lower.

According to a previous study, Pt carried in large specific surface carriers such as Al_2O_3 is considered a traditional catalyst for the deep oxidation of HCs [2]. With perovskite catalysts, they also have strong oxidizing activity. However, when carrying out Pt impregnation on perovskite, the activity of the catalysts increases further, and the light-off temperature decreases significantly.

The catalytic mechanism is explained as follows: The perovskite catalysts are applied in the catalytic converter to treat the exhaust gases of motorcycles. The catalytic converter converts toxic substances into CO_2 and H_2O [2-6, 11-14]. The activity of the catalytic converter is shown in Fig. 3.

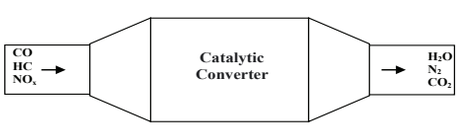

Fig. 3. The activity of a catalytic converter.

The catalytic converter has three simultaneous functions:

Reduction of nitrogen oxides (NO_x) into nitrogen and oxygen elements:

$NOx \rightarrow Nx + Ox$

Oxidation of CO to carbon dioxide:

$CO + O_2 \rightarrow CO_2$

Oxidation of HCs into carbon dioxide and water:

$C_xH_{4x} + 2xO_2 \rightarrow xCO_2 + 2xH_2O$

Reactions require high activation energies for the reaction to begin and the reaction lasts a long time if there are no catalysts. In the presence of catalysts, the activation energy for the reaction and reaction time are significantly reduced.

These reactions are varied, HCs include not only toluene and MEK but also many compounds contained in gasoline or diesel.

The oxidation mechanism of the catalyst is as follows: In the catalytic process, there is oxidation and reduction. For oxidation, oxygen is needed, and for reduction, CO is needed. Toxic substances such as CO, HCs, NO_x, and the components involved in the reaction such as O_2 and CO must exist in a specific proportion to ensure the best conversion degree is achieved.

For a chemical reaction to occur, the catalyst requires a minimum temperature, called the light-off temperature. For the conversion to reach 50%, the temperature of the catalysts must immediately reach 250-280°C. Therefore, the catalytic converter is located directly above the exhaust pipe. The old catalytic converters have a high light-off temperature. The best temperature range is between 400-800°C [2-6, 11-14].

The catalytic converter of the motorcycles must have a light-off temperature as low as possible to meet the above requirements.

3.3. Activity of Au and Pt on perovskite-like oxide catalyst $La_{2-x}Sr_xCuO_4$ in the CO oxidation reaction

The perovskite-like oxide catalysts $La_{2-x}Sr_xCuO_4$ (x=0.0, 0.5, 1.0) prepared with x=1.0 had the best crystallinity at 800°C. Therefore, that $LaSrCuO_4$ sample was chosen as the carrier for the preparation of the $Au/LaSrCuO_4$ catalyst.

The FE-SEM image of the catalyst sample 1% Au/$LaSrCuO_4$/100 PVA/100 Au is shown in Fig. 4.

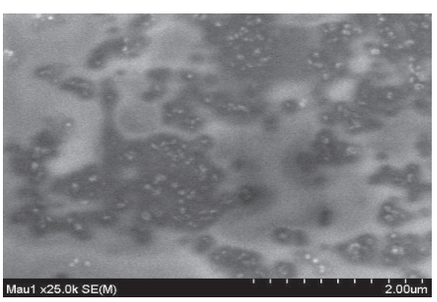

Fig. 4. FE-SEM image of 1% Au/$LaSrCuO_4$/100 PVA/100 Au catalyst.

Figure 4 shows Au particles dispersed in the catalyst, with an average particle size estimate of 34.64 nm.

The FE-SEM image of the 1% Au/$LaSrCuO_4$/64 PVA/100 Au catalyst sample is shown in Fig. 5.

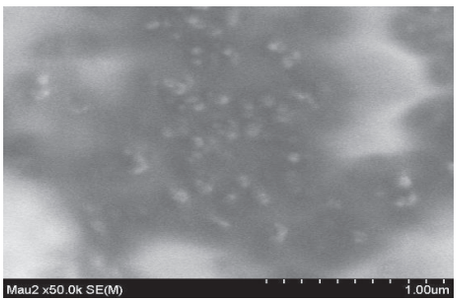

Fig. 5. FE-SEM image of a catalyst 1% Au/$LaSrCuO_4$/64 PVA/100 Au.

The FE-SEM image from Fig. 5 shows the dispersion of the Au nanoparticles in the 1% Au/$LaSrCuO_4$/64 PVA/100 Au sample with an average particle size of 36.12 nm.

FE-SEM images showed Au nanoparticles formed on the sample. When the ratio was reduced from 100 PVA/100 Au to 64 PVA/100 Au, the Au nanoparticle size increased. This is also consistent with the study of F. Forta, et al. (2000) [9].

The catalytic activity in the CO oxidation reaction was carried out on perovskite-like oxide catalysts $La_{2-x}Sr_xCuO_4$ (x=0.0, 0.5, 1.0) with 1% Pt and 1% Au. The results are shown in Figs. 6, 7 and Table 3.

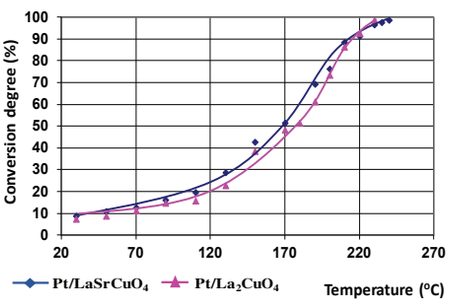

Fig. 6. The CO conversion on 1% Pt/La_2CuO_4 800°C and 1% Pt/$LaSrCuO_4$ 800°C catalysts.

The results from Fig. 6, the light-off temperature of the Pt/$LaSrCuO_4$ and Pt/La_2CuO_4 samples was 170 and 180°C. The Pt/$LaSrCuO_4$ catalyst had a lower light-off temperature due to the addition of the Sr element into the structure. Thus, the Pt/$LaSrCuO_4$ catalyst is suitable for industrial production, especially for very high heat and mechanical resistance applications.

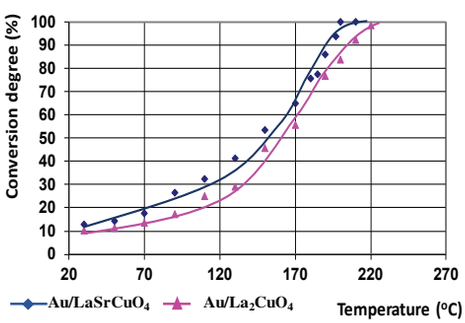

Fig. 7. The CO conversion on 1% Au/La_2CuO_4 800°C and 1% Au/$LaSrCuO_4$ 800°C (100 PVA/100 Au) catalysts.

The results from Fig. 7, the light-off temperatures of the $Au/LaSrCuO_4$ and Au/La_2CuO_4 catalysts were 150 and 160°C. Au catalysts are particularly effective for CO complete oxidation reactions. The results are similar to that of toluene oxidation [5], where $Au/LaSrCuO_4$ catalyst outperformed the Au/La_2CuO_4 catalyst.

Table 3. The light-off temperature of the catalysts in the CO complete oxidation reaction.

Catalysts	Light-off temperature (°C)
$Pt/LaSrCuO_4$	170
Pt/La_2CuO_4	180
$Au/LaSrCuO_4$	150
Au/La_2CuO_4	160
$0.64\ Au/LaSrCuO_4$	160
$0.64\ Au/La_2CuO_4$	170

The CO conversion results from Tables 2 and 3 show that the light-off temperature is lower than that of the toluene and MEK mixture. The light-off temperature of the $Au/LaSrCuO_4$ catalyst was the lowest at 150°C.

The results show that $Au/LaSrCuO_4$ 800°C is a catalyst with good activity. The light-off temperature of $Au/LaSrCuO_4$ for a complete oxidation reaction of CO was 150°C, while the light-off temperature of $Pt/LaSrCuO_4$ was 170°C. The working temperature of the $Au/LaSrCuO_4$ catalyst is very favourable for applications in the treatment of motorcycle exhaust gases.

The results from Tables 2 and 3, the light-off temperatures of all catalysts did not exceed 270°C, which is the highest temperature that a motorcycle engine can reach during work [2-6, 11-14]. Therefore, it can be confirmed that all catalysts in this study are capable of treating motorcycle exhaust gases, of which the perovskite-like oxide $Au/LaSrCuO_4$ catalyst was the most active.

Perovskites can be dual-acting catalysts that have many prospects for practical application, for example, they can simultaneously process HCs and CO. This shows that CO and HCs do not have the opposite chemical effect when the two substances are present in the system at the same time. The CO conversion temperature is lower than that of toluene, therefore, if a product of toluene oxidation has CO, then this gas will also be completely converted to CO_2. In addition, CO is an easily oxidised gas; therefore, under the conditions of the toluene oxidation reaction, if there is unconverted CO gas, the content in exhaust gases will be small.

4. Conclusions

The synthesis of perovskite-like oxide catalysts $La_{2-x}Sr_xCuO_4$ (x=0.0, 0.5, 1.0) by the citrate method and crystallization at 800°C produced good catalytic activity for the complete oxidation of the mixture of toluene and MEK, in which the $LaSrCuO_4$ catalyst (x=1.0) was the best performing. The light-off temperature of the $Au/LaSrCuO_4$ Au nanoparticle catalyst in the complete oxidation reaction of CO reached 150°C, lower than that of the $Pt/LaSrCuO_4$ catalyst (170°C). This would allow the replacement of previous Pt catalysts with a better performing, Au nanoparticle catalyst. Additionally, the $LaSrCuO_4$ catalyst (x=1.0) had better oxidising activity than the La_2CuO_4 catalyst (x=0.0), showing that a partial replacement of La^{3+} ions with Sr^{3+} ions increased catalyst activity. Thus, there is potential for application of these catalysts in the catalytic converter of motorcycles.

ACKNOWLEDGEMENTS

This work was supported by Ho Chi Minh City University of Food Industry (HUFI).

COMPETING INTERESTS

The author declares that there is no conflict of interest regarding the publication of this article.

REFERENCES

[1] S.N. Viet, P.N. Huu (2002), "Synthesis, characterisation, and catalytic properties of perovskite $LaCoO_3$ synthesised by citrate method", *Journal of Chemistry and Applications*, **4**, pp.20-26.

[2] S. Irusta, M.P. Pina, M. Menéndez, et al. (1998), "Catalytic combustion of volatile organic compounds over La-Based Perovskites", *Journal of Catalysis*, **179(2)**, pp.400-412, DOI: 10.1006/jcat.1998.2244.

[3] R. Burch, P.J.F. Harris, C. Pipe (2001), "Preparation and characterization of supported $La0.8Sr0.2MnO_3$+x", *Applied Catalysis A*, **210(1-2)**, pp.63-73, DOI: 10.1016/S0926-860X(00)00790-0.

[4] V. Choudhary, S. Banerjee, B.S. Uphade (2000), "Activation by hydrothermal treatment of low surface area ABO_3-type perovskite oxide catalysts", *Applied Catalysis A: General*, **197**, pp.183-186, DOI: 10.1016/S0926-860X(99)00485-8.

[5] C.H.L. Huy, T.D. Minh (2019), "Study of perovskite- like La_2-xSrxCuO_4 (x=0.0, 0.5, 1.0) catalysts for toluene total oxidation reaction", *Vietnam Journal of Natural Resources and Environment*, **10(312)**, pp.19-22.

[6] C.H.L. Huy (2007), *Study on Gold, Platin Catalysts Based on Perovskite Used for Oxidation Reaction of CO and HC*, Master of Engineering Thesis, Ho Chi Minh City University of Technology.

[7] H.M. Zang, Y. Teraoka, N. Yamazoe (1988), "Preparation of supported La Sr MnO by the citrate process", *Applied Catalysis*, **41**, pp.137-141, DOI: 10.1016/S0166-9834(00)80388-7.

[8] M. Haruta (2004), "Nanoparticulate gold catalysts for low temperature CO oxidation", *Journal of New Materials for Electrochemical Systems*, **7(3)**, pp.163-172, DOI: 10.1002/chin.200448226.

[9] F. Porta, L. Prati, M. Rossi, et al. (2000), "Metal sols a useful tool for heterogeneous gold catalyst preparation: Reinvestigation of liquid phase oxidation", *Catalysis Today*, **61(1-4)**, pp.165-172, DOI: 10.1016/S0920-5861(00)00370-9.

[10] I.P. Silverwood (2002), *Synthesis and Characterization of Au/Fe_2O_3 Catalysts*, Master of Science Thesis, University of Edinburgh.

[11] X. Wu, M. Fischer, A. Nolte, et al. (2022), "Perovskite catalyst for in-cylinde coating to reduce raw pollutant emissions of internal combustion engines", *ACS Omega*, **7(6)**, pp.5340-5349, DOI: 10.1021/acsomega.1c06530.

[12] T. Higo, K. Ueno, Y. Omori, et al. (2019), "Perovskite lattice oxygen contributes to low-temperature catalysis for exhaust gas cleaning", *RSC Advances*, **9(39)**, pp.22721-22728, DOI: 10.1039/C9RA03050F.

[13] B. Kucharczyk (2015), "Catalytic oxidation of carbon monoxide on Pd-containing $LaMnO_3$ perovskites", *Catalysis Letters*, **145**, pp.1237-1245, DOI: 10.1007/s10562-015-1518-3.

[14] F. Touahra, A. Rabahi, R. Chebout, et al. (2016), "Enhanced catalytic behaviour of surface dispersed nickel on $LaCuO_3$ perovskite in the production of syngas: An expedient approach to carbon resistance during CO_2 reforming of methane", *International Journal of Hydrogen Energy*, **41**, pp.2477-2486, DOI:10.1016/j.ijhydene.2015.12.062.

DOI: 10.31276/VJSTE.65(2).15-19

Preparation of TiO_2 pigment from ilmenite ore concentrate by molten alkaline process

Thi Thao Nguyen[1], Ky Nam Pham[2], Thi Hinh Dinh[3], Vu Diem Ngoc Tran[1*], Aman Ullah[4]

[1]*Hanoi University of Science and Technology, 1 Dai Co Viet Street, Bach Khoa Ward, Hai Ba Trung District, Hanoi, Vietnam*

[2]*Center for Structures and Materials, Viettel Aerospace Institute - Viettel Group, D26 Cau Giay New Urban Area, Yen Hoa Ward, Cau Giay District, Hanoi, Vietnam*

[3]*Faculty of Material Science and Engineering, Phenikaa University, Yen Nghia Ward, Ha Dong District, Hanoi, Vietnam*

[4]*Department of Physics, University of Science and Technology Bannu, Bannu Township, 28100, Khyber Pakhtunkhwa, Pakistan*

Received 12 August 2021; revised 19 October 2021; accepted 5 November 2021

Abstract:

TiO_2 pigment production from an ilmenite concentrate via a molten alkaline process was investigated. The ilmenite concentrate (54.19% TiO_2) was first roasted in the molten NaOH system at various temperatures ranging from 600 to 800°C while the mass ratio of NaOH/ilmenite was varied within the range of 0.8-1.2 for 1 hour. The achieved roasted efficiency was up to 93.93% at a temperature of 700°C and NaOH/ilmenite ratio of 1:1. The roasted product was first leached in water and then in a solution of HCl 20% at 50°C for 2 hours. The $TiOCl_2$ solution was hydrolysed at 95°C for 2 hours. Precipitation of the hydrolysis process was then calcinated at 800°C. The final obtained product contained up to 96.37% of TiO_2. Ilmenite can be used as a raw material in a molten alkaline process. It is obvious that not only high purities of TiO_2 could be achieved, but also the reduction of waste materials, raw materials, energy, and time.

Keywords: **ilmenite, NaOH, roasting, rutile, TiO_2.**

Classification numbers: **2.2, 2.3**

1. Introduction

Titanium dioxide pigment (TiO_2) has high chemical and thermal stability, is non-toxic, has corrosion resistance, and a high optical refractive index. Therefore, this pigment has been widely used in a variety of areas including paint, paper, plastic, and cosmetics, among others, due to its remarkable qualities [1].

There are more than 100 different minerals containing more than 1% TiO_2. Among them, ilmenite and rutile are the minerals of choice in industry. Ilmenite accounts for more than 90% of the Ti metallurgy industry uses [2]. The ilmenite $FeTiO_3$ is one of the primary raw materials for titanium-containing material and iron production. Vietnam has large titanium ore deposits with approximately 650 million tons of heavy minerals located mostly along the middle coast of Vietnam spreading from Thanh Hoa province to Ba Ria - Vung Tau province [3]. Recently, the Vietnamese titanium industry processed high grade ore and titanium slag with around 80% TiO_2 content. Despite this, TiO_2 pigment has not yet been processed in Vietnam [4, 5].

There are two commercial processes for recovering TiO_2 including the sulfate process and chloride process [1, 2]. In the past decade, a new process called the "molten alkaline process" was investigated for the synthesis of TiO_2 pigment [6-15]. Titanium slags were used as raw materials containing ~80% TiO_2. Recently, some metallurgists used ilmenite ore ($FeTiO_3$) to replace titanium slag in molten alkaline processes [14, 15].

The exploratory research of TiO_2 pigment production using ilmenite as raw materials through the molten alkaline process has been proposed as a new method for obtaining high quality TiO_2 and also to reducing the amount of waste, save raw materials, energy, and time.

In this study, TiO_2 pigment was prepared from Ha Tinh ilmenite ore concentrate (IOC) via the molten alkaline process.

2. Experimental procedure

Ha Tinh IOC was used as a raw material; its chemical composition was analysed by X-ray Fluorescence (XRF-Viet Space 5008P) as shown in Table 1 which contains 54.19% TiO_2. The X-ray diffraction (XRD- Bruker D8-Advance) analysis of the ilmenite concentrate (Fig. 1) indicates that the main titanium components are $FeTiO_3$, TiO_2, $Fe_2Ti_3O_9$, and Fe_2O_3.

Table 1. Chemical compositions of Ha Tinh IOC.

Component	Content (wt. %)
TiO_2	54.19
FeO	34.16
SiO_2	4.01
Al_2O_3	4.28
MnO	2.82
Nb_2O_3	0.17
ZrO_2	0.32
Other	0.05

*Corresponding author: Email: ngoc.tranvudiem@hust.edu.vn

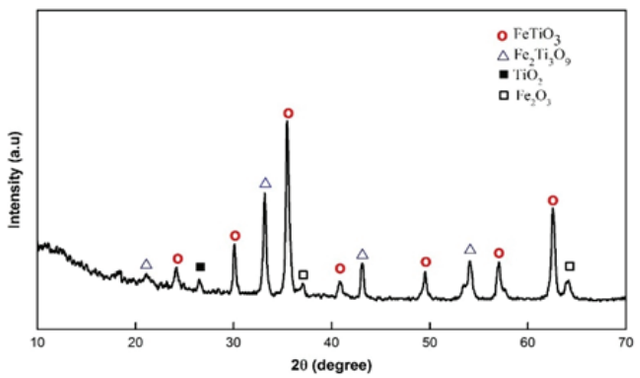

Fig. 1. X-ray diffraction pattern of Ha Tinh IOC.

TiO_2 was produced from IOC by the alkaline molten salt process. IOC mixed with NaOH were roasted in nickel crucibles inside a muffle furnace. The alkaline roast was then leached in water to remove both the excess NaOH as well as soluble impurities such as silicate and aluminate. After the first leaching, the water-leached sample was subsequently subjected to hydrochloric acid leaching. The solution was then subjected to hydrolysis, and precipitation was calcinated as shown in Fig. 2.

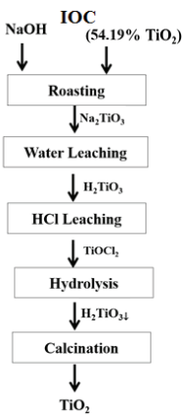

Fig. 2. The experimental procedure.

The selection of roasting temperature depends on raw materials, thus, the roasting temperature was studied at 600-800°C, which is higher than that for titanium slag or upgrading ilmenite at about 500°C based on previous research [9, 10]. The IOC (54.19% TiO_2) was first roasted in the molten NaOH system at various temperatures ranging from 600 to 800°C with the NaOH/IOC mass ratio varied within 0.8-1.2 for 1 hour. The roasted product was then leached in water and later in HCl 20% at 50°C for 2 hours. The $TiOCl_2$ solution was hydrolysed at 95°C for 2 hours. The precipitation resulting from the hydrolysis process was then calcinated at 800°C.

3. Results and discussion

The IOC was roasted in the NaOH molten system to prepare Na_2TiO_3. The main goal of the alkaline roasting process is to destroy the very strong and compact crystal structures of pure Ti minerals (rutile, anatase, or synthetic rutile) as these minerals are extremely resistant to direct acid leaching in comparison with ilmenite, which contains much higher amounts of iron oxides that facilitate its acid digestion [16]. TiO_2 is converted to Na_2TiO_3 through the alkaline roasting process for separation of Ti from Fe and other impurities that formed like $NaFeO_2$, Na_2AlO_2, Na_2SiO_3, etc [2]. The roasting reactions occurred by the following chemical reactions:

$$4FeTiO_3 + 12NaOH + O_2 = 4Na_2TiO_3 + 4NaFeO_2 + 6H_2O \quad (1)$$

$$TiO_2 + 2NaOH = Na_2TiO_3 + H_2O \quad (2)$$

$$Fe_2O_3 + 2NaOH = NaFeO_2 + H_2O \quad (3)$$

$$SiO_2 + 2NaOH = Na_2SiO_3 + H_2O \quad (4)$$

$$Al_2O_3 + 2NaOH = 2NaAlO_2 + H_2O \quad (5)$$

$$MnO + 2NaOH + O_2 = Na_3MnO_4 + H_2O \quad (6)$$

$$ZrO_2 + 2NaOH = Na_2ZrO_3 + H_2O \quad (7)$$

$$Nb_2O_3 + 2NaOH + O_2 = 2NaNbO_3 + H_2O \quad (8)$$

This study focuses on determining the effect of roasting temperature and mass ratio of NaOH/IOC on the efficiency of the roasting process. The roasting temperature was varied from 600 to 800°C with a 50°C increment along with using a NaOH/IOC mass ratio of 1/1 for 60 min. The results are shown in Table 2 and Fig. 3. The efficiency of decomposed TiO_2 increases from 81.59 to 93.93% when increasing of temperature from 600 to 700°C because of the molten NaOH system. After that, the efficiency slightly decreased at a higher temperature of 800°C (93.58%).

Table 2. Effect of temperature on efficiency of TiO_2 roasting.

Temperature (°C)	Roasting efficiency of TiO_2 (%)
600	81.59
650	84.81
700	93.93
750	93.93
800	93.58

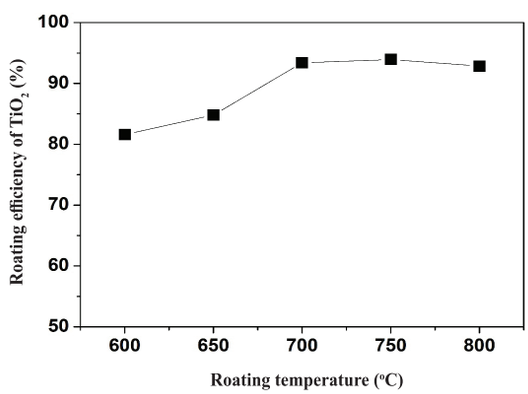

Fig. 3. Effect of roasting temperature on roasting efficiency of TiO_2 (%).

In previous research, the effect of roasting temperature at 500-550°C for 1-1.5 hours and TiO_2/NaOH ratio of ~ 1-1.2 for titanium slag raw materials were observed [5-11]. For IOC, the reactions between NaOH and ore were negligible at a temperature of 600°C, but these reactions strongly occurred when the temperature reached 700-800°C. The optimum roasting temperature was found to be 700°C, and it agrees well with the results of other works [12, 14].

To study the effect of NaOH/IOC mass ratios, the NaOH/IOC ratios were varied within the range of 0.8, 0.9, 1, 1.1; and 1.2. The results are summarized in Table 3 and collectively plotted in Fig. 4. The obtained results show that when the ratios changed from 0.8 to 1.0, the roasting efficiency of TiO_2 increased from 83.73 to 93.93% while the efficiency remained constant at higher ratios of 1.1 and 1.2. The results can be explained by the fact that the molten NaOH system acts as a high temperature ionized solvent above 350°C, in which titanium dioxide and other titanium compounds have high solubility.

On other hand, NaOH melting provides O^{2-}, and it combines with the oxygen in the air to oxidize titanium oxide (Ti_2O_3) to form Na_2TiO_3. Therefore, increasing NaOH content significantly increased the O^{2-} content in solution, thus increasing roasting speed [8].

Table 3. Effect of NaOH/IOC mass ratio on roasting efficiency of TiO_2.

NaOH/IOC mass ratio	Roasting efficiency of TiO_2 (%)
0.8	83.73
0.9	88.02
1.0	93.93
1.1	93.93
1.2	93.93

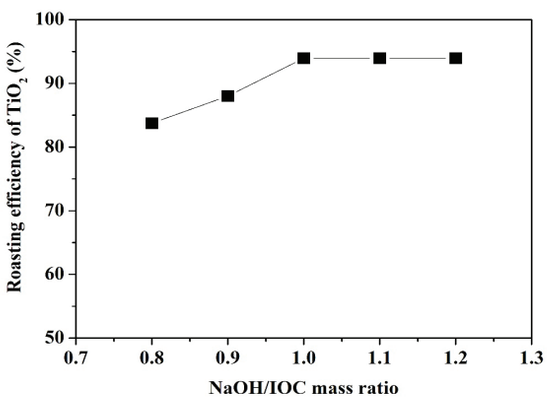

Fig. 4. Effect of NaOH/IOC mass ratio to roasting efficiency of TiO_2.

The product of roasting was analysed by XRD as shown in Fig. 5. This figure shows that the titanium exists in the form of sodium titanium oxide (Na_2TiO_3).

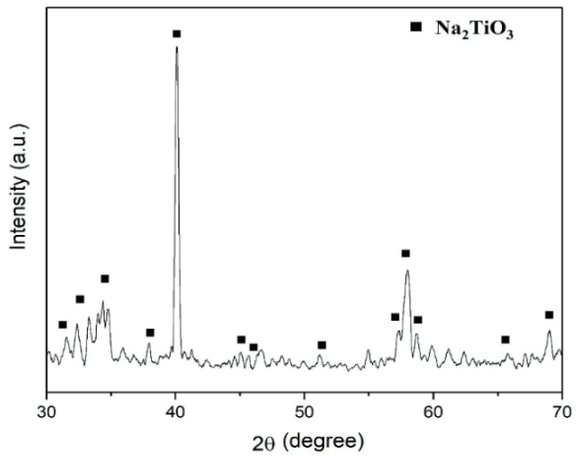

Fig. 5. X-ray diffraction pattern of IOC roasting production.

The Na_2TiO_3 was leached in water to form a solid of H_2TiO_3 at 60°C for 10 min as shown in reaction 9:

$$Na_2TiO_3 + 2H_2O = H_2TiO_3 + 2NaOH \quad (9)$$

In this process, Mn, Al, and Si form a water solute that can be removed in a water solution [12]. The obtained solid was continuously leached in a hydrochloric acid solution to form a solution as shown in the following reaction:

$$H_2TiO_3 + 2HCl = TiOCl_2 + 2H_2O \quad (10)$$

This process transfers titanium from a solid into a solution. However, iron and other impurities were also dissolved. The leaching parameter was studied as a function of HCl concentration (15-20%), a temperature range of 20-80°C, and leaching times from 30 to 150 min. The effect of HCl acid concentration on the efficiency of H_2TiO_3 is shown in Table 4 and Fig. 6.

The efficiency of the leaching process increased from 80.51 to 93.93% along with increasing HCl concentration from 15 to 20%. During the leaching process, the 15% HCl concentration can be hydrolysed into H_2TiO_3 to reduce the titanium content of the solution. At higher HCl concentrations, impurities can be dissolved in the solution that were probably caused by hydrolysis processes [15]. Based on the results, an HCl concentration of 20% was used for the hydrolysis process.

Table 4. Effect of HCl concentration on leaching efficiency of TiO_2.

HCl concentration (%)	Leaching efficiency of TiO_2 (%)
15.0	80.51
17.5	91.25
20.0	93.93
22.5	89.10
25.0	83.20

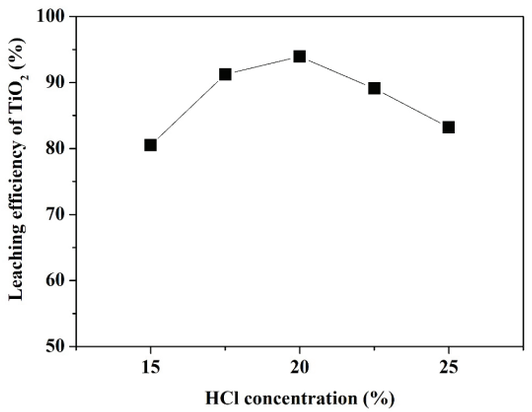

Fig. 6. Effect of HCl concentration on leaching efficiency of TiO_2.

Leaching temperature was studied as a function of 20, 40, 60 and 80°C with 20% HCl for 60 min, and the results are presented in Table 5 and Fig. 7.

Table 5. Effect of leaching temperature on leaching efficiency of TiO_2.

Leaching temperature (°C)	Leaching efficiency of TiO_2 (%)
20	84.81
40	88.03
60	93.93
80	89.10

Figure 7 shows that the highest TiO_2 content in solution reaches 93.93% at a temperature to 60°C. At the temperature above 60°C, the leaching efficiency of TiO_3 decreased because of H_2TiO_3 hydrolysis. Thus, a leaching temperature of 60°C was selected for the next study.

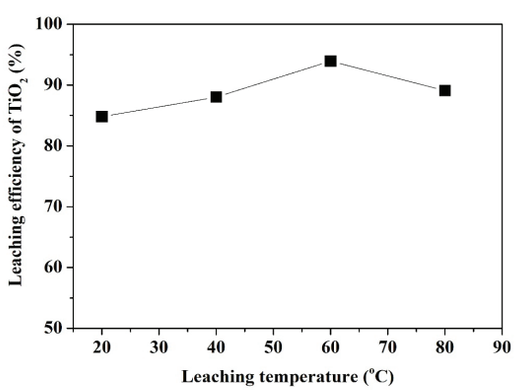

Fig. 7. Effect of leaching temperature on leaching efficiency of TiO_2.

The effect of leaching time on TiO_2 leaching efficiency was investigated as a function of 30, 60, 120, 150 and 180 min while the parameters of 20% HCl and 60°C were kept constant. The results obtained are shown in Table 6 and Fig. 8. The leaching efficiency of TiO_2 increased as the leaching time increased from 30 to 60 min, and this value remained constant at higher leaching times.

Table 6. Effect of leaching time on leaching efficiency of TiO_2.

Leaching time (min)	Leaching efficiency of TiO_2 (%)
30	88.56
60	93.93
90	93.39
120	93.93

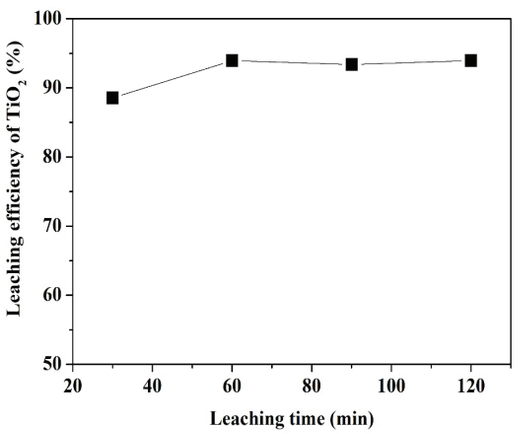

Fig. 8. Effect of leaching time on leaching efficiency of TiO_2.

The dissolved Ti can react with water molecules to form insoluble hydrate solutions through hydrolysis and precipitation of a hydrous titanium oxide compound. The product of low temperature hydrolysis (20-80°C) is $Ti(OH)_4$ or $TiO_2.2H_2O$, however, that of higher temperatures (80-110°C) is $TiO(OH)_2$ or $TiO_2.H_2O$ [12].

The $TiOCl_2$ solution was hydrolysed at 95°C for 2 hours according to reaction (11):

$$TiOCl_2 + 2H_2O \rightarrow TiO(OH)_2 + 2HCl \quad (11)$$

The exact mechanism of the thermal hydrolysis of Ti solution is unclear, however, some have thought it to be the transfer of H^+ ions from the hydration shell of Ti ions into the solution with subsequent coordination with OH^- and colloidal aggregation [8, 12]. This hydrated compound is then calcinated to form a crystalline product. The type of TiO_2 crystal depends on the acid used during the leaching process. The hydrolysis of chloride solutions yielded rutile upon calcination [12].

To obtain TiO_2, the precipitation product of $TiO(OH)_2$ was calcinated at 800°C for 2 hours. The reactions can be represented by the following reaction (12):

$$TiO(OH)_2 \xrightarrow{t^o} TiO_2 + H_2O \quad (12)$$

The chemical compound and phase content of the final product of TiO_2 was analysed by XRF and XRD, respectively, as shown in Fig. 6 and Table 4. The final TiO_2 product was a rutile crystal structure with a TiO_2 content of 96.37 wt. % (Table 7, Fig. 9).

Table 7. Chemical composition of TiO_2 product.

Component	Content (wt. %)
TiO_2	96.37
FeO	1.02
SiO_2	1.33
Al_2O_3	0.22
ZrO_2	0.70
Nb_2O_3	0.35
Other	0.01

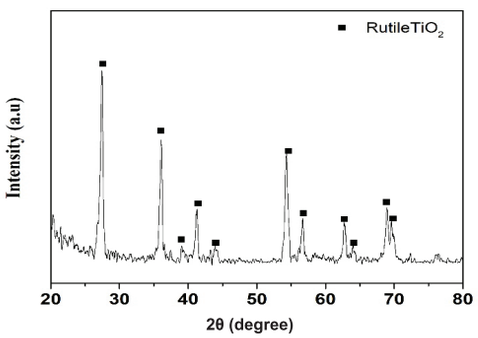

Fig. 9. X-ray diffraction pattern of the TiO_2 product.

The molten alkaline process has been introduced to produce pure TiO_2 from various titanium sources [12, 13]. A comparison of our results with the results of other research is shown in Table 8. In the table, the 98.39% TiO_2 was synthesized by the same process using raw materials of upgrading ilmenite (82% TiO_2) [13]. S. Sanchez-Segado, et al. (2015) [15] observed a similar quality to our product (95% TiO_2) from Bomar IOC.

Table 8. Comparative study of TiO_2 production.

Raw materials	Production of TiO_2 (%)	Ref.
Ha Tinh IOC (54.19% TiO_2)	96.37	This study
Upgrading ilmenite 82% TiO_2	98.39	[13]
Bomar IOC 61% TiO_2	95	[15]

4. Conclusions

This study was conducted to obtain a final TiO_2 concentration of 96.37 wt. % from a Ha Tinh IOC (54.19% TiO_2) by a molten alkaline process with roasting conditions of 700°C and a NaOH/ilmenite ratio of 1:1. The roasted product was first leached in water at 60°C for 10 min and then in a solution of HCl 20% at 50°C for 2 hours. The $TiOCl_2$ solution was hydrolysed at 95°C for 2 hours and then calcinated at 800°C to obtain a product containing up to 96.37% of TiO_2. This result demonstrates that the molten alkaline process can be applied to the synthesis TiO_2 from the IOC of Vietnam. The molten alkaline process was used in the fabrication of TiO_2 pigment by various raw materials from low grade TiO_2 (ilmenites) to high grade TiO_2 (slag, upgrading ilmenite). This process not only yielded high grade TiO_2, but also used ilmenite ores in a direction in which the impurities, materials, time, and energy were reduced.

CRediT author statement

Thi Thao Nguyen: Conceptilization, Methodology, Formal analysis, Writing; Ky Nam Pham: Data analyst; Thi Hinh Dinh: Data analyst; Vu Diem Ngoc Tran: Formal analysis, Review, Editing; Aman Ullah: Review, Data analyst.

ACKNOWLEDGEMENTS

This research is funded by Hanoi University of Science and Technology (HUST) under grant number T2020-PC-028.

COMPETING INTERESTS

The authors declare that there is no conflict of interest regarding the publication of this article.

REFERENCES

[1] W. Zhang, Z. Zhu, C.Y. Cheng (2011), "A literature review of titanium metallurgical processes", *Hydrometallurgy*, **108(3-4)**, pp.177-188, DOI: 10.1016/j.hydromet.2011.04.005.

[2] S. Sin, S.H. Joo, D. Lee, et al. (2020), "Leaching behavior of titanium from Na_2TiO_3", *Mater. Trans.*, **61**, pp.150-155, DOI: 10.2320/matertrans.MT-M2019198.

[3] B. Nam, H. Giao (2016), "Status of development orientations for mining titanium placer in Vietnam", *Journal of Mining Science and Technology*, **1**, pp.40-50, DOI: 10.17073/2500-0632-2016-1-40-50.

[5] T.N. Than, N.B. Duong, T.T. Nguyen, et al. (2016), *Manufacturing Processes for The Production of Titanium Dioxide Pigment*, Metallurgical Engineering & Advanced Materials Technology, pp.172-177.

[6] M. Gázquez, J. Pedro, R. Vaca, et al. (2014), "A review of the production cycle of titanium dioxide pigment", *Materials Sciences and Applications*, **5**, pp.441-445, DOI: 10.4236/msa.2014.57048.

[7] Y. Zhang, T. Qi, Y. Zhang (2009), "A novel preparation of titanium dioxide from titanium slag", *Hydrometallurgy*, **96(1-2)**, pp.52-56, DOI: 10.1016/j.hydromet.2008.08.002.

[8] S. Middlemas, Z.Z. Fang, P. Fan (2013), "A new method for production of titanium dioxide pigment", *Hydrometallurgy*, **131**, pp.107-113, DOI: 10.1016/j.hydromet.2012.11.002.

[9] Y. Han, T. Sun, J. Li, et al. (2012), "Preparation of titanium dioxide from titania-rich slag by molten NaOH method", *Int. J. Miner. Metall. Mater.*, **19**, pp.205-211, DOI: 10.1007/s12613-012-0539-9.

[10] S. Zaki (2017), "Alkali roasting of titania slag for preparation of high grade-TiO_2", *Inorg. Chem. Ind. J.*, **12(1)**, pp.1-9.

[11] S.C. Middlemas (2014), *Energy-Conscious Production of Titania and Titanium Powders from Slag*, University of Utah, 212pp.

[12] A. Manhique, W. Focke, C. Madivate (2011), "Titania recovery from low-grade titaniferrous", *Hydrometallurgy*, **109(3)**, pp.230-236, DOI: 10.1016/j.hydromet.2011.07.008.

[13] T. Ngoc, N. Thao (2019), "New process to improve of TiO_2 content from upgrading ilmenite using molten NaOH", *Journal of Metal Science and Technology*, **84**, pp.38-42.

[14] S. Parirenyatwa, L. Castejon, S.S. Segado, et al. (2016), "Comparative study of alkali roasting and leaching of chromite ores and titaniferous minerals", *Hydrometallurgy*, **165**, pp.213-226, DOI: 10.1016/j.hydromet.2015.08.002.

[15] S.S. Segado, A. Lahiri, A. Jha (2015), "Alkali roasting of bomar ilmenite: Rare earths recovery and physico-chemical changes", *Open Chem.*, **13**, pp.270-278, DOI: 10.1515/chem-2015-0033.

[16] M. Ismael, O.M. Husaini, M.F. Shakat (2020), "New method to prepare high purity anatase TiO_2 through alkaline roasting and acid leaching from non-conventional minerals resource", *Hydrometallurgy*, **195**, DOI: 10.1016/j.hydromet.2020.105399.

 DOI: 10.31276/VJSTE.65(2).20-25

Study on the modification of fly ash as a coagulant

Ngoc Tu Nguyen*, Quang Huy Trinh, Thi Thu Ha Nguyen, Van Duc Tran, Thi Thuy Hang Ho

Faculty of Natural Resources and Environment, Vietnam National University of Agriculture, Trau Quy Town, Gia Lam District, Hanoi, Vietnam

Received 12 January 2022; revised 16 February 2022; accepted 22 February 2022

Abstract:

This study was carried out to produce a complex coagulant containing aluminum and iron salt from coal fly ash by H_2SO_4 acid. An application of this extracted solution as a coagulant was also investigated by the jar-test process. Fly ash collected at the Electrostatic precipitation (ESP) system in Mong Duong thermal power plant are mainly round and fine particles with diameters ranging from 0.2-8 µm, containing aluminum and iron of 15 and 6% respectively. At a room temperature of 25°C, with 1 M H_2SO_4 acid solution and the retention time of 20 minutes, the maximum contents of around 60.16 mg.l^{-1} of Fe and 4.37 mg.l^{-1} of Al were the most favorable to convert aluminum and iron from mineral forms to sulfate salt-based forms. The produced complex coagulants from fly ash of the Mong Duong power plant are proved to be effective for total suspended solids (TSS) removal from wastewater where the highest efficiency achieved 83.6% at the coagulant solution ratio of 5% (w/w) with a concentration of TSS in the initial wastewater was 60 g.l^{-1}. The positive results from this study open a meaningful approach toward a huge of fly ash produced from thermal power plants as well as other coal-burn-related activities in Vietnam.

Keywords: **coagulant, coagulation, fly ash, modification, wastewater treatment.**

Classification numbers: **2.2, 5.3**

1. Introduction

Fly ash is a byproduct generated from burning coal in thermal power plants. In Vietnam, with consumption of nearly 100 million tons of coal per year for running thermal power plants in recent years, it is estimated that the average amount of created fly ash collected from the ESP filter system will be increased from 30 million tons in 2025 to 38 million tons in 2030 [1]. The main response to this solid waste is only being disposed of in ash ponds surrounding the plants [2]. Some environmental problems related to this unsafe restoration are soil, water and air pollution as well as soil malfunction.

With a huge amount created every year over the world, fly ash has been widely utilized as an amendment for highway road bases [3, 4], construction products such as cement or brick [5, 6] as well as stabilizing clay-based building materials [7, 8]. In the field of environmental treatment, the promising use of fly ash for wastewater treatment was classified based on either physical method (absorption, filtration) or chemical method (photocatalysis and Fenton process) [9]. In terms of the physical method, utilization to synthesize zeolite materials for water treatment absorption was widely applied [10-12]. Ceramic filtration made from fly ash is an inexpensive micro-porous inorganic membrane [13, 14]. For chemical applications, fly ash with a high surface area for the deposition and growth of metal oxide nanoparticles (Fe, Ag, ZnO and TiO_2) led to utilizing of this by-product for photocatalytic support [15, 16]. Fly ash contains different metals Fe, Al, Mn, Cu, Ni and/or its oxides was investigated as a supporter of Fenton processes [17, 18].

Using ores as raw materials for manufacturing commercial coagulants is largely applied in recent years. The main composition of popular coagulants is ferric sulfate - $Fe_2(SO_4)_3$ and aluminum sulfate $Al_2(SO_4)_3$. These coagulants are widely used for both wastewater and drinking water treatment. The coagulation process is the major physicochemical treatment method for the reduction of suspended solids and turbidity. Iron coagulant in the ferric form behaves similarly to aluminum sulfate and forms ferric hydroxide floc in the presence of bicarbonate alkalinity. Fly ash is rich in iron and aluminum oxides. Converting these oxides to sulfate forms is the scientific basis of recycling fly ash as a coagulant material.

Aluminum and iron salts were created by soaking fly ash in H_2SO_4 acid. The extracted solution is then to be used

*Corresponding author: Email: nguyenngoctu@vnua.edu.vn

as a mixed coagulation agent. Jar-test process has shown the efficiency in removal of TSS from wastewater. This successful result is considered as a suitable solution to open a new approach to reducing huge fly ash in Vietnam, suggesting further work on fly ash.

2. Methodology

2.1. Research materials

Fly ash was collected from Mong Duong 2 thermal power plant in Cam Pha city, Quang Ninh province, Vietnam. The fly ash was captured by an ESP filter system. The density of fly ash was 2.24 $g.cm^{-3}$ and 2.1% moisture.

2.2. Research methods

2.2.1. Fly ash analysis

The morphological and chemical compositions of the fly ash material were examined by scanning electron microscopy (SEM) coupled with - energy-dispersive X-ray spectrometry (EDS) (FESEM S-4800, Hitachi). SEM analysis was conducted with 500x and 2000x magnifications. EDS analysis was at 1.060 keV.

Fig. 1. Fly ash collected from the ESP system at Mong Duong 2 thermal power plant.

2.2.2. Aluminum and iron extraction experiment

The oxides of aluminum and iron in fly ash were decomposed by using sulfuric acid at different concentrations at 0.5, 1, 2, 3 and 4 M (Table 1). Each 20 gram of dried fly ash was mixed with 45 ml of sulfuric acid at concentrations ranging from 0.5, 1, 2, 3, and 4 M, the retention time of the experiments remained at 20 minutes. All of the experiments were carried out at room temperature (22-25°C). All experiments were performed in triplicate.

Table 1. Experimental conditions.

Acid Cont. (M) / Temp. (°C)	0	0,5	1	2	3	4
25	Control	TM1	TM2	TM3	TM4	TM5

2.2.3. Chemical analysis

The content of Al^{3+} and Fe^{3+} ions in the extracted solution were measured by AAS (AAS 300 - Perkin Elmer).

2.2.4. Jar-test

The jar-test method was used to determine the efficiency of the complex coagulant (Fig. 2). The modified solution with different ratios of 1, 3 and 5% was added to 300 ml of artificial wastewater with the TSS concentration of 500 $mg.l^{-1}$. The solution was stirred at approximately 100 rpm for 1 minute then reduced the stirring speed to 35 rpm for 20 minutes. The containers were allowed to settle for 20 minutes.

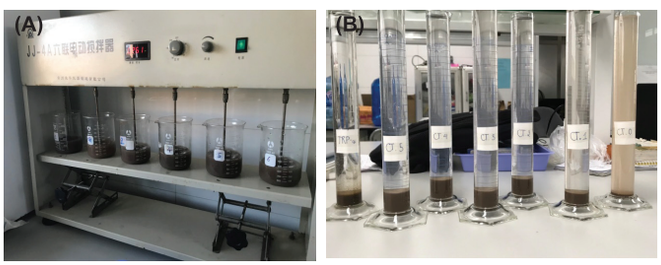

Fig. 2. The jar-test experiment (A) and the coagulation process (B).

2.2.5. Data processing

T-test was used to clarify the significant difference at $p<0.05$. All of the analytical data were processed and indicated by SignmaPlot 14 software.

3. Results and discussion

3.1. Physio-chemical properties of fly ash

3.1.1. Size distribution of fly ash

The resultant combustion product from coal-fired thermal plants includes bottom ash and fly ash. While the bottom ash was easily collected from the furnace because of its heavyweight and large dimension, the fly ash with a very fine particle and low weight was only captured from the ESP filter system.

The ESP fly ash at Mong Duong 2 thermal power plant has a round and very fine particle ranging from 0.2-8 µm. Fig. 3 shows that these fine particles are aggregated into micron and sub-micron sizes. This result is compatible with other research. L.V. Thien, et al. (2019) [19] showed that the fly ash from some coal power plants such as Pha Lai, Ha Khanh and Ninh Binh was primarily silt-size particles (0.2-5 µm) and that number of fly ash diameter of the Soma thermal power plant was from 4.5-7.5 µm according to the work of A. Bicer (2018) [20].

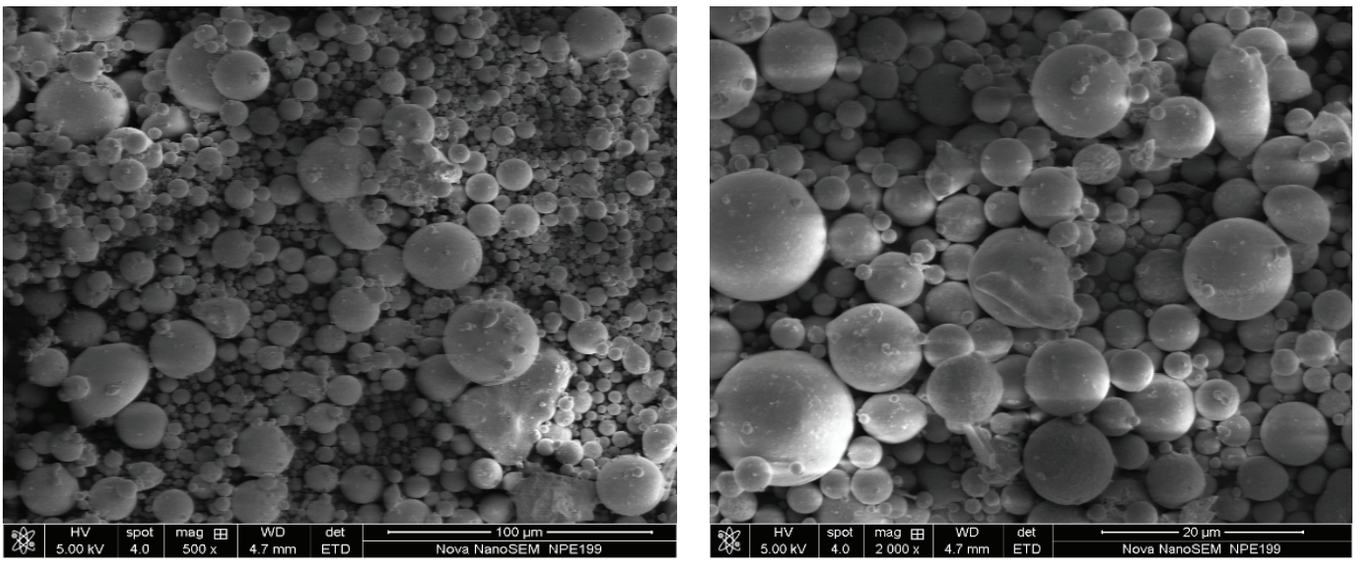

Fig. 3. Scanning electron micrograph of the fly ash (Mong Duong).

3.1.2. Chemical composition of the fly ash

Iron and aluminum sulfate salts play an important role in the coagulation process for waste and wastewater treatment.

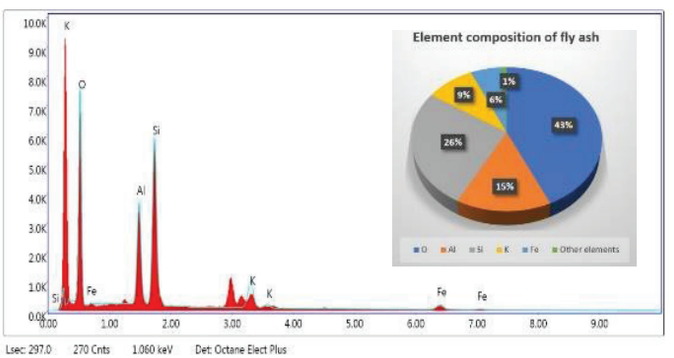

Fig. 4. Chemical composition of fly ash by EDX technique.

Figure 4 shows that the fly ash is mainly composed of oxygen (43%), Si (26%), Al (15%), K (9%), Fe (6%) and others (1%). According to L.V. Thien, et al. (2019) [19], the composition of elements detected in fly ash was the highest percentages of Si, Al and Fe, and significant percentages of Mg, K and Ca. These aluminum and iron in fly ash may play an important role in producing coagulation agents based on aluminum and iron sulfate salt content [21].

3.2. Aluminum and iron extraction

Aluminum and iron sulfate play an important role in the coagulation process. That means, in this research, converting aluminum oxide and iron oxide to sulfate salt forms will determine the efficiency of the coagulation process. The impact of H_2SO_4 acid concentration on the conversion efficiencies of Al and Fe was shown in Fig. 5.

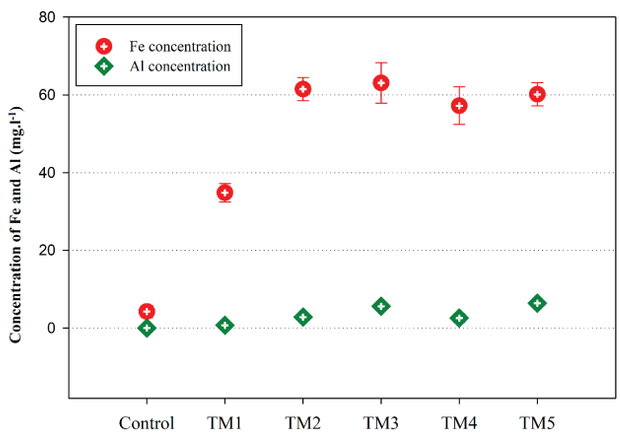

Fig. 5. The converting efficiencies of Al and Fe.

Figure 5 shows that the leaching processes of both Al and Fe increase with an increase in acid concentration. While the leached concentration of Fe rose sharply when the H_2SO_4 concentration from 0.5 to 1 M was then kept stable at a higher acid concentration from 1 to 4 M. The concentration of extracted Al tended to remain stable between 0.75 M to 6.43 M when the acid concentration changed from 0.5 to 4 M. Fig. 5 also showed that the leaching capacity of Fe from fly ash was always higher than that of Al, getting the maximum value around 60.16 $mg.l^{-1}$ Fe, compared to 4.37 $mg.l^{-1}$ Al. In other words, the higher the H_2SO_4 concentration, the higher the concentration of aluminum and iron obtained. In our study, the maximum conversion efficiency of Fe was realized with 1 M H_2SO_4 acid solution at room temperature (22-25°C), with a retention time of 20 minutes.

The difference in leaching between Fe and Al in this study may be explained by the reason that aluminum is an

amphoteric metal oxide so self-organized porous anodic oxide films are produced when reactive metals such as aluminum and titanium are electrochemically oxidized in baths that dissolve the oxide [22]. M. Fan, et al. (2005) [23] reported the conversion efficiencies of 84.8% for iron and only 55.1% for aluminum at 120°C and after 4 hours of reaction time. The phases of iron oxides in raw fly ash are mainly of hematite, magnetite and/or maghemite which could be easily dissolved in acid solution than aluminum oxides [24].

3.3. Application of the complex coagulant solution

The modified complex coagulant solution of aluminum and iron sulfate was applied to remove TSS in water by the jar-test process. The volume ratio of extracted solution applied in this study was 1, 3, and 5% (w/w). The coagulation efficiency was determined by the amount of collected TSS ($mg.l^{-1}$, Fig. 6) and by the transmittance (T%, Fig. 7).

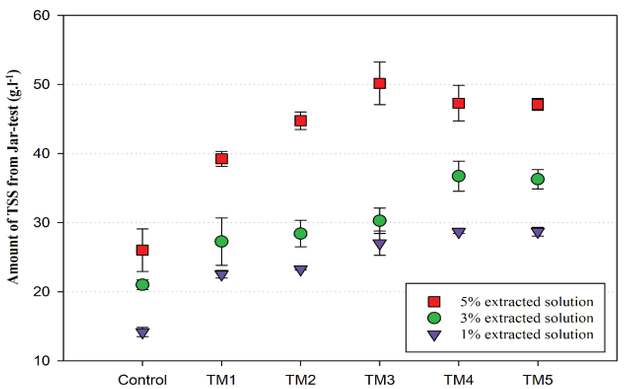

Fig. 6. The efficiency of TSS removal by the complex coagulant.

The most common tendency is that the treatment efficiency increases gradually with the amount of added coagulant solution. With the treatment adding 5% extracted solution, the amount of settled TSS was twice as high as the control sample, achieving 50.16 $g.l^{-1}$ compared to only 26.0 $g.l^{-1}$ of the control. In the lower extracted solution, 3% and 1%, TSS removal efficiency is significantly lower than that in the 5% solution. With a concentration of TSS in the initial wastewater is 60 $g.l^{-1}$, it was achieved the highest TSS removal efficiency of 83.6% at the coagulant solution ratio of 5% (w/w). L. Forminte, et al. (2020) [25] synthesized new material from fly ash with sulfuric acid and used this complex material in the coagulation process. It obtained a TSS removal efficiency of 84% at the coagulant dosage of 60 $mg.l^{-1}$. According to H. Saleem (2013) [26], using ferrous and aluminum sulfate from fly ash as a coagulant condensed about 75% of turbidity, 73% of color, and 93% of TSS.

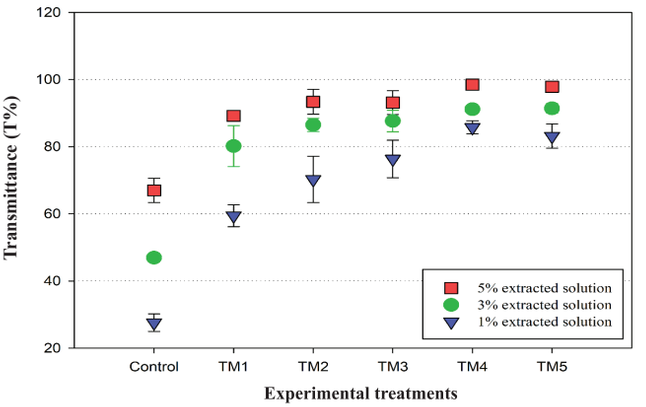

Fig. 7. The efficiency of transmittance by the complex coagulant.

Similar to TSS removal efficiency, the transmittance of water after treatment has also the same result (Fig. 7). In all of the experimental formulas, the highest TSS removal capacity, as well as the transmittance efficiency, were always achieved at TM3 (treated with H_2SO_4 2 M) and TM4 (treated with H_2SO_4 3 M). These TM3 and TM4 treatments were also the best conversion ratio of aluminum and iron into the solution which was mentioned above.

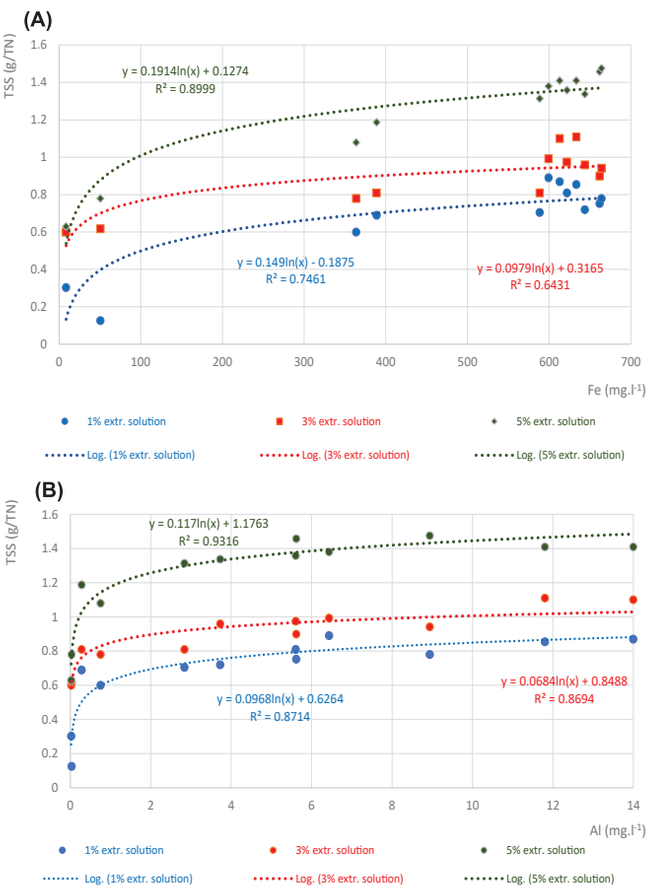

Fig. 8. Correlation between coagulation efficiency and Fe (A), Al (B) contents.

To determine the factors affecting the coagulation efficiency, the significant correlation (t-test) between Fe and Al concentrations (via the volume of complex coagulant solution) with the amount of settled solid was collected after the coagulation processes. The results in Fig. 8 show that the correlations coefficient (R^2) between the settled solid amount and the leached Fe content were 0.746, 0.643 and 0.899 at 1, 3, and 5% dosage of the complex coagulant solution, respectively. These correlation coefficients for aluminum were 0.871, 0.869 and 0.932, respectively. All correlations are significant at the p=0.001 significance level with n=11 samples. From the Fig. 8, it can be seen that the effect of aluminum sulfate on the TSS removal efficiency was remarkably higher than that of iron sulfate. With the same amount of TSS removed, the change in the concentration of aluminum sulfate was always lower than the concentration of iron sulfate. Moreover, the correlation factors that showed the relationship between the amount of coagulant and removed TSS, the of aluminum sulfate was also higher compared to the iron factors. According to X. Huang, et al. (2016) [27], the floc properties in the coagulation process were affected by the initial solution pH and flocs created by aluminum sulfate coagulant were the largest in size among those of the coagulants of iron and titanium sulfates at a pH of 5.

4. Conclusions

Fly ash collected at the ESP system in Mong Duong thermal power plant are mainly round and fine particles with diameters ranging from 0.2-8 µm. With containing aluminum and iron of 15% and 6% respectively, this fly ash was considered a resource of Al and Fe to produce a potential complex coagulant solution.

The produced complex coagulant from fly ash of Mong Duong thermal power plant containing both aluminum and iron ions are proved to be effective for TSS removal in the wastewater. At a room temperature of 25°C, with 1 M H_2SO_4 acid solution and a retention time of 20 minutes, the maximum contents of around 60.16 $mg.l^{-1}$ of Fe and 4.37 $mg.l^{-1}$ of Al were the most favorable to convert aluminum and iron from mineral forms to sulfate salt-based forms. In this study, the H_2SO_4 acid concentration is the factor that has the greatest influence on converting iron into a sulfate salt-based form. Meanwhile, aluminum is less affected because of its amphoteric metal.

The application of this extracted coagulant solution to remove TSS in wastewater has shown its potential results when the highest efficiency achieved 83.6% at the coagulant solution ratio of 5% (w/w) with the concentration of TSS in the initial wastewater was 60 $g.l^{-1}$. Positive results from this study open a meaningful approach toward a huge of fly ash produced from thermal power as well as other coal-burn-related activities in Vietnam.

CRediT author statement

Ngoc Tu Nguyen: Conceptualization, Methodology, Supervision, Writing original draft; Quang Huy Trinh: Validation, Taxonomic identification, Review and Editing; Thi Thu Ha Nguyen: Data curation, Validation; Van Duc Tran: Supporting data analysis, Sample analysis; Thi Thuy Hang Ho: Supervise and comment on editing the manuscript for completeness.

ACKNOWLEDGEMENTS

This research is funded by Vietnam National University of Agriculture (Grant number: T2021-13-21VB).

COMPETING INTERESTS

The authors declare that there is no conflict of interest regarding the publication of this article.

REFERENCES

[1] The Prime Minister (2011), *Decision No. 1208/QD-TTg Approving The National Master Plan for Power Development in The 2011-2020 Period, With Considerations to 2030* (in Vietnamese).

[2] Vietnam Electricity Corporation (2018), *Report on The Fly Ash Disposal from Coal Fired Powed Plants* (in Vietnamese).

[3] N.M. Jackson, S. Schultz, P. Sander, et al. (2009), "Beneficial use of CFB ash in pavement construction applications", *Fuel*, **88(7)**, pp.1210-1215, DOI: 10.1016/j.fuel.2008.04.031.

[4] C.S. Shon, Y.S. Jung, D. Saylak (2013), "Evaluation of synthetic aggregates using off-ASTM specification ashes as road base course materials", *Construction and Building Materials*, **38**, pp.508-514, DOI: 10.1016/j.conbuildmat.2012.08.014.

[5] C. Chen, Q. Li, L.F. Shen, et al. (2011), "Potential for manufacturing unfired-bricks using circulating fluidized bed combustion fly ash", *Asian Journal of Chemistry*, **23(8)**, pp.3449-3453.

[6] T. Wu, M. Chi, R. Huang (2014), "Characteristics of CFBC fly ash and properties of cement-based composites with CFBC fly ash and coal-fired fly ash", *Construction and Building Materials*, **66**, pp.172-180, DOI: 10.1016/j.conbuildmat.2014.05.057.

[7] W.N. Wczelik, A. Lagosz, B. Kowalski, et al. (2014), "Calorimetry in testing waste materials from the brown coal combustion", *Journal of Thermal Analysis and Calorimetry*, **118(1)**, pp.123-131, DOI: 10.1007/s10973-014-3963-4.

[8] Ohenoja, P.A. Tanskanen, O. Peltosaari, et al. (2016), "Effect of particle size distribution on the self-hardening property of biomass-peat fly ash from a bubbling fluidized bed combustion", *Fuel Processing Technology*, **148**, pp.60-66, DOI: 10.1016/j.fuproc.2016.02.023.

[9] F. Mushtaq, M. Zahid, I.A. Bhatti, et al. (2019), "Possible applications of coal fly ash in wastewater treatment", *Journal of Environmental Management*, **240**, pp.27-46, DOI: 10.1016/j.jenvman.2019.03.054.

[10] C.W. Purnomo, C. Salim, H. Hinode (2012), "Synthesis of pure Na-X and Na-A zeolite from bagasse fly ash", *Microporous and Mesoporous Materials*, **162**, pp.6-13, DOI: 10.1016/j.micromeso.2012.06.007.

[11] W. Franus, M. Wdowin, M. Franus (2014), "Synthesis and characterization of zeolites prepared from industrial fly ash", *Environmental Monitoring and Assessment*, **186(9)**, pp.5721-5729, DOI: 10.1007/s10661-014-3815-5.

[12] N. Koshy, D. Singh (2016), "Fly ash zeolites for water treatment applications", *Journal of Environmental Chemical Engineering*, **4(2)**, pp.1460-1472, DOI: 10.1016/j.jece.2016.02.002.

[13] Y. Dong, J. Zhou, B. Lin, et al. (2009), "Reaction-sintered porous mineral-based mullite ceramic membrane supports made from recycled materials", *Journal of Hazardous Materials*, **172(1)**, pp.180-186, DOI: 10.1016/j.jhazmat.2009.06.148.

[14] J. Cao, X. Dong, L. Li, et al. (2014), "Recycling of waste fly ash for production of porous mullite ceramic membrane supports with increased porosity", *Journal of The European Ceramic Society*, **34(13)**, pp.3181-3194, DOI: 10.1016/j.jeurceramsoc.2014.04.011.

[15] P.A.K. Reddy, P.V.L. Reddy, E. Kwon, et al. (2016), "Recent advances in photocatalytic treatment of pollutants in aqueous media", *Environment International*, **91**, pp.94-103, DOI: 10.1016/j.envint.2016.02.012.

[16] Z. Zhao, Y. Lei, W. Liu, et al. (2017), "Fly ash cenospheres as multifunctional supports of g-C_3N_4/N-TiO_2 with enhanced visible-light photocatalytic activity and adsorption", *Advanced Powder Technology*, **28(12)**, pp.3233-3240, DOI: 10.1016/j.apt.2017.09.035.

[17] A. Zhang, N. Wang, J. Zhou, et al. (2012), "Heterogeneous Fenton-like catalytic removal of p-nitrophenol in water using acid-activated fly ash", *Journal of Hazardous Materials*, **201**, pp.68-73, DOI: 10.1016/j.jhazmat.2011.11.033.

[18] H. Narayani, R. Augustine, S. Sumi, et al. (2017), "Removal of basic and industrial azo reactive dyes from aqueous solutions via Fenton-like reactions using catalytic non-magnetic Pd-flyash and magnetic Pd-FeO-flyash composite particles", *Separation and Purification Technology*, **172**, pp.338-349, DOI: 10.1016/j.seppur.2016.08.027.

[19] L.V. Thien, N.T.T. Chau, L.T.T. Hong, et al. (2019), "Properties of fly ashes from thermal power stations in relation to use as soil amendments", *Sains Malaysiana*, **48(4)**, pp.745-755, DOI: 10.17576/jsm-2019-4804-06.

[20] A. Bicer (2018), "Effect of fly ash particle size on thermal and mechanical properties of fly ash-cememt composites", *Thermal Science and Engineering Progress*, **8**, pp.78-82, DOI: 10.1016/j.tsep.2018.07.014.

[21] L. Yan, Y. Wang, H. Ma, et al. (2012), "Feasibility of fly ash-based composite coagulant for coal washing wastewater treatment", *Journal of Hazardous Materials*, **203-204**, pp.221-228, DOI: 10.1016/j.jhazmat.2011.12.004.

[22] O.O. Capraz, P. Shrotriya, P. Skeldon, et al. (2015), "Role of oxide stress in the initial growth of self-organized porous aluminum oxide", *Electrochimica Acta*, **167**, pp.404-411, DOI: 10.1016/J.ELECTACTA.2015.03.017.

[23] M. Fan, R.C. Brown, T.D. Wheelock, et al. (2005), "Production of a complex coagulant from fly ash", *Chemical Engineering Journal*, **106(3)**, pp.269-277, DOI: 10.1016/j.cej.2004.12.044.

[24] A. Shemi, R.N. Mpana, S. Ndlovu, et al. (2012), "Alternative techniques for extracting alumina from coal fly ash", *Minerals Engineering*, **34**, pp.30-37, DOI: 10.1016/j.mineng.2012.04.007.

[25] L. Forminte, G. Ciobanu, G. Buema, et al. (2020), "New materials synthesized by sulfuric acid attack over power plant fly ash", *Rev. Chim.*, **71**, pp.48-58, DOI: 10.37358/RC.20.7.8224.

[26] H. Saleem (2013), "Exploitation of low cost coal fly ash adsorbent with coagulants for the treatment of industrial complex nature dyes wastewater", *International Journal of Scientific and Engineering Research*, **4(9)**, pp.109-119.

[27] X. Huang, B. Gao, S. Zhao, et al. (2016), "Application of titanium sulfate in a coagulation-ultrafiltration process: A comparison with aluminum sulfate and ferric sulfate", *RSC Advances,* **6(55)**, pp.49469-49477, DOI: 10.1039/C6RA05075A.

DOI: 10.31276/VJSTE.65(2).26-29

Characterisation of *Colletotrichum siamense* TD1 causing anthracnose leaf spots of *Camellia tamdaoensis* Ninh et Hakoda at the Tam Dao National Park

Hong Viet La[1*], Duc Hoang Le[2], Thao Thanh Thi Duong[3], Bang Phi Cao[4], Ha Duc Chu[5]

[1]*The Institute for Science and Application, Hanoi Pedagogical University 2, Nguyen Van Linh Street, Xuan Hoa Ward, Phuc Yen City, Vinh Phuc Province, Vietnam*
[2]*Institute of Biotechnology, Vietnam Academy of Science and Technology, 18 Hoang Quoc Viet Street, Nghia Do Ward, Cau Giay District, Hanoi, Vietnam*
[3]*Hanoi Metropolitan University, 98 Duong Quang Ham Street, Quan Hoa Ward, Cau Giay District, Hanoi, Vietnam*
[4]*Faculty of Natural Sciences, Hung Vuong University, Nong Trang Ward, Viet Tri City, Phu Tho Province, Vietnam*
[5]*Faculty of Agricultural Technology, University of Engineering and Technology, Vietnam National University - Hanoi, 144 Xuan Thuy Street, Cau Giay District, Hanoi, Vietnam*

Received 29 December 2021; revised 17 February 2022; accepted 1 March 2022

Abstract:

***Camellia* L. is a precious medicinal plant with 16 different species and high economic value. In Tam Dao National Park, Vinh Phuc, *Camellia* L. is rich in ingredients. Anthracnose is a severe disease caused by fungi on the leaves of *Camellia* L., however, research of the fungus causing anthracnose on leaves of *Camellia* L. in Vietnam remains limited. In this study, anthracnose-infected leaves of *Camellia tamdaoensis* Ninh et Hakoda in Tam Dao National Park were collected, and the causative agent was isolated. Eleven fungal strains that cause anthracnose were obtained through gene sequence identification of the internal transcribed spacer (*ITS)* region. One fungal strain was selected to isolate DNA and determine the gene sequence of the *ITS* region. Based on this *ITS* sequence, the causative agent on leaves of *C. tamdaoensis* Ninh et Hakoda was *Colletotrichum siamense* TD1. The *ITS* sequence was determined to be 522 bp in length, 52.30% of guanine-cytosine (GC) content, and was registered on GenBank with accession number OK560718. Pathogenicity tests were conducted to fulfil Koch's postulates. This is the first report of anthracnose leaf spots of *C. tamdaoensis* Ninh et Hakoda caused by *C. siamense* TD1 in Vietnam. The results of anthracnose fungi provide helpful information for disease management and are necessary for future studies on selecting disease-resistant varieties of *Camellia* L.**

Keywords: **anthracnose, *Camellia tamdaoensis* Ninh et Hakoda, *Colletotrichum siamense*, golden camellia, Tam Dao National Park.**

Classification numbers: **3.1, 3.4**

1. Introduction

Golden camellia belongs to the *Camellia* L. genus, *Theaceae* family. They are shrubs and small-sized trees that are naturally distributed in Vietnam. Its benefits are well-known in traditional medicine for improving human health. In Tam Dao, a large number of *Camellia* species were discovered in the National Park and natural zone [1]. Especially, *C. tamdaoensis* Ninh et Hakoda is one of the many unique plants scattered in the forest of this mountain. In recent years, anthracnose has become one of the most severe fungal diseases globally and severe anthracnose symptoms can be seen on the leaves of the *Camellia* genus. The first observed symptom appears as random chlorotic spots on leaves after which they coalesce and form large spots. The visual spots become dark brown or black depending on damage level [2]. In the past, morphological characters and host ranges were mainly used to classify the *Colletotrichum* species [3]. They were conidial, conidiophore, and acervuli morphology or sensitive to benomyl [4, 5]. However, it is challenging to identify taxonomies based on the morphological differences of *Colletotrichum* species because their morphological characteristics were strongly affected by both laboratory and natural conditions. Currently, molecular tools give biologists many advantages to rapidly recognise *Colletotrichum* species at the genus level [3]. The nuclear *ITS* regions have been used to separate *Colletotrichum* species [4]. In this study, we aimed to collect a leaf with a disease related to anthracnose of *C. tamdaoensis* Ninh et Hakoda and describe the symptoms of this disease. Then, the fungal pathogen was isolated on a specific medium and molecular identification was performed based on sequencing the *ITS* sequence. Consequently, *C. tamdaoensis* Ninh et Hakoda was reinfected with the fungus to test pathogenicity ability.

2. Materials and methods

2.1. Collection of the disease leaf and describe the symptoms

C. tamdaoensis Ninh et Hakoda plant with anthracnose leaf spots were obtained from the Tam Dao National Park, Tam Dao district, Vinh Phuc province in May 2021. The symptoms of anthracnose disease were observed with an increase from small brown spots to black necrotic spots appearing on the leaf and stem. Diseased leaves of *C. tamdaoensis* Ninh et Hakoda were taken from these infected plants, packed in a

*Corresponding author: Email: laviethong@hpu2.edu.vn

cooler box, and transported to the laboratory of The Institute for Science and Application, Hanoi Pedagogical University 2.

2.2. Fungal isolation

Disease spots on leaves of *C. tamdaoensis* Ninh et Hakoda with typical symptoms of anthracnose were cut off and washed with 75% (v/v) ethanol for 30 s, with 5% (v/v) sodium hypochlorite for 1 min, which was followed by rinsing with sterilised water three times, and finally laid to dry on sterile filter paper [6, 7]. The explants were placed onto Petri plates containing Potato dextrose agar (PDA) medium and incubated at 25°C. Isolates were subcultured aseptically to fresh PDA.

2.3. Extraction of fungal DNA and PCR amplification for ITS and sequencing

The total DNA from fungal isolates was extracted by cetyltrimethylammonium bromide (CTAB) method where mycelia served as explants [8]. Amplification of the *ITS* region was performed using the primers *ITS1* and *ITS4* [9]. Primers were synthesised by Phusa Co., Ltd. (Can Tho, Vietnam). Amplification was performed in a PCR Thermal Cycler (TP600, Takara). The PCR products were purified and sequenced at the National Key Laboratory of Gene Technology, Institute of Biotechnology, Vietnam Academy of Science and Technology.

2.4. Molecular analysis

The sequence of *ITS Colletotrichum* isolate in this study was aligned using Bioedit software (version 7.2.5) and submitted to GenBank under accession number OK560718. To study it in more detail, nine *ITS* sequences of *Colletotrichum* species were retrieved from NCBI and used to compare the GC content and length, and to construct the phylogenetic tree using Molecular evolutionary genetics analysis (MEGA) (ver 7.0) with the maximum likelihood method with 1,000 bootstrap replicates. The species-level of the isolate was identified based on phylogenetic approaches [10].

2.5. Pathogenicity test

Colletotrichum sp. was tested on detached leaves of *C. tamdaoensis* Ninh et Hakoda under artificial conditions. *Colletotrichum* sp. was incubated on PDA plates for 7 days at 25°C. Sterile distilled water was adjusted to the conidial suspension to $2.0x10^6$ conidia/ml. Fresh young leaves without disease were used for inoculation. The leaves were washed with running water, were sterilised with 75% (v/v) ethanol, and finally rinsed in sterile water. Afterward, detached healthy leaves were placed on a plastic box with moist tissue papers. A sterilised needle was used to make wounds on the surface of the fine leaf. Each wound was inoculated with a 100 µl conidial suspension, and sterile distilled water served as the control.

The enamel basins were sealed by plastic film and incubated in a growth chamber at 25°C. Virulence was assessed by measuring lesion length at 8 days post inoculation (dpi) in two perpendicular directions on each leaf.

3. Results

3.1. Symptoms of leaf camellia species disease and isolation

Typical anthracnose symptoms in *C. tamdaoensis* Ninh et Hakoda were clearly expressed on leaves whose necrosis spots were dark brown or black. The results showed that the symptoms occurred on two sides of the diseased leaves (Figs. 1A, B). Firstly, the disease spots usually appear small and brown. Then, these brown spots spread and the color changes. These symptoms on the disease leaf of *C. tamdaoensis hakodae* in this study were the same as the previously described study on *Camellia chrysantha* (Hu) [2].

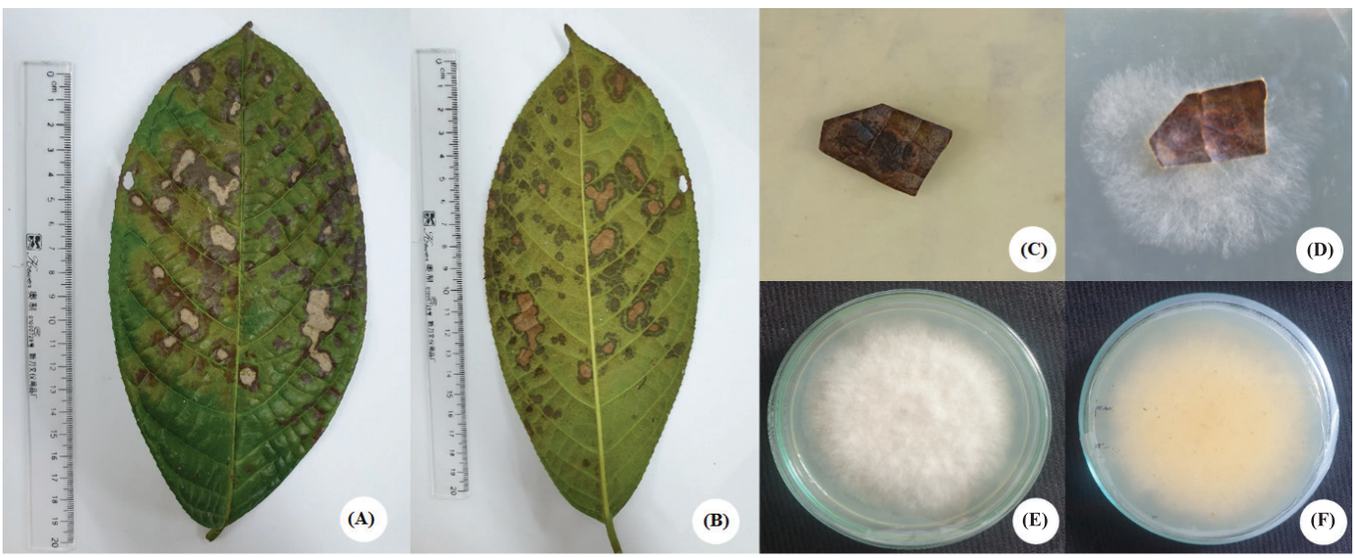

Fig. 1. Symptoms on diseased leaves and fungal isolation from *C. tamdaoensis* Ninh et Hakoda. (A, B) Upper and lower of disease leaf; **(C)** Leaf section put on PDA medium; **(D)** Mycelia growth; **(E, F)** Upper and lower of fungal isolate implied anthracnose after 7 days culture.

Eighteen leaf sections were surface-sterilised, put on PDA media, and inoculated at 25°C in the incubator. After 7 days of culture, we obtained 11 fungal-like isolates. They had the same morphology of mycelium with white color (Figs. 1C, D, E, F). One of them was selected to study further. According to previous publications, anthracnose is caused by many different fungal agents such as *C. siamense* causing disease on *C. sinensis* [11] and *C. fructicola* causing disease on *Citrus sinensis* [12]. However, in *C. chrysantha*, anthracnose was caused by *C. siamense* and *C. fructicola* [2]. The initial classification agent that caused anthracnose in this study belonged to *Collectotricum* sp.

3.2. Molecular characteristics of ITS from fungal agent caused to Anthracnose

The length and GC content of ITS: This study used *ITS* sequences of ten species/strains of *Colletotrichum* from GenBank to analyse the length and GC content. The results, given in Table 1, showed that the lengths of *ITS* fragments range from 522 bp of *Colletotrichum* sp. species to 603 bp of the *Colletotrichum siamense* strain Cg131. The GC content also increased from 51.41 to 52.34%. In *Colletotrichum* sp., the GC content was 52.30%, which was similar to the analysed *ITS* sequences. The high GC levels usually indicate gene stability.

Table 1. Molecular comparison of *ITS* sequences from the isolated fungal agent that caused anthracnose in *C. tamdaoensis* Ninh et Hakoda.

Order	Species/strains	GenBank accession	Length (bp)	GC content (%)
1	*Colletotrichum siamense* TD1	OK560718	522	52.30
2	*Colletotrichum siamense* strain rb12	MT434638.1	593	51.43
3	*Colletotrichum siamense* strain rb10	MT434636.1	593	51.43
4	*Colletotrichum siamense* strain Hainan21	MG830366.1	563	52.22
5	*Colletotrichum siamense* strain Cg131	KU642474.1	603	51.41
6	*Colletotrichum siamense* isolate GQHZJ20	MN296085.1	564	51.95
7	*Colletotrichum siamense* isolate GQHZJ19	MN296084.1	556	52.34
8	*Colletotrichum queenslandicum* isolate RHCOL1	KT372377.1	599	51.92
9	*Colletotrichum eremochloae* strain CBS 129661	MH865527.1	541	53.97
10	*Colletotrichum endophyticum clone EIPP*	MK330020.1	593	51.43
11	*Colletotrichum boninense* isolate PL9	MK685133.1	586	51.88

This evidence demonstrated that the anthracnose causing-fungal agent may belong to the *Collectotricum* genus.

Genetical relationship of Colletotrichum based on ITS RNA ribosomal: In *Camellia oleifera* in China, the most common cause of anthracnose disease in fruit consists of 5 strains including *C. fructicola*, *C. camelliae*, *C. aenigma*, *C. siamense*, *and C. gloeosporioides* while in leaves is *C. fructicola* [13].

In this study, no anthracnose symptoms were observed on *C. tamdaoensis* Ninh et Hakoda leaves while 11 strains were isolated from symptomatic leaves, which had similar mycelium morphology. The *ITS* sequence of the fungal agent in this study was amplified by PCR using ITS 1 and ITS 4 primers. This product was sequenced and used to build a phylogenetic tree using MEGA 7 software. The results demonstrated that the isolate belonged to *Colletotrichum siamense* with 96-99% homology to other *Colletotrichum siamense* species (Fig. 2). To our knowledge, there has been no publication describing *Colletotrichum siamense* on golden tea *C. tamdaoensis* Ninh et Hakoda at the Tam Dao National Park.

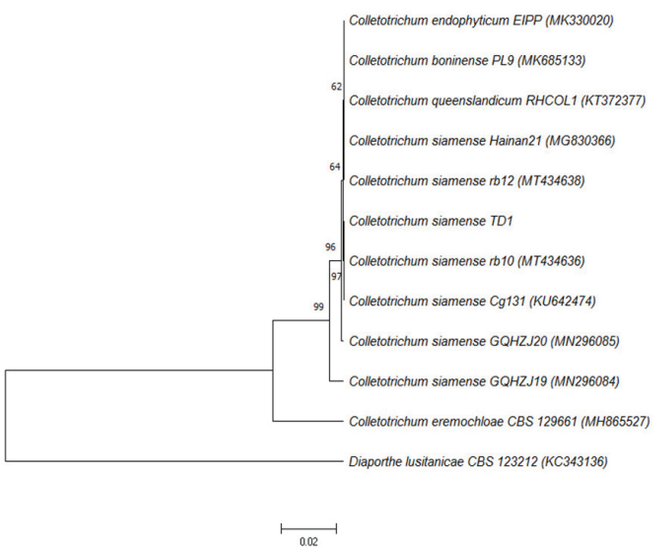

Fig. 2. Phylogenetic tree using the DNA ribosomal ITS of Colletrichum isolated from Camellia hakodae disease symptom leaf in Tam Dao, Vinh Phuc. C. hakodae isolate was labeled with the red rectangle. Expressed value at the phylogenetic tree was a bootstrap of 1000 replications. 0.02 bar was nucleotide substitution rate units. Diaporthe lusitanicae was used as the outgroup.

3.3. Virulence test

Colletotrichum sp. was grown and infected back to the detached leaf of *C. tamdaoensis* Ninh et Hakoda. Similar symptoms to those observed in the field developed on all infected leaves (Fig. 3). The controls showed no symptoms.

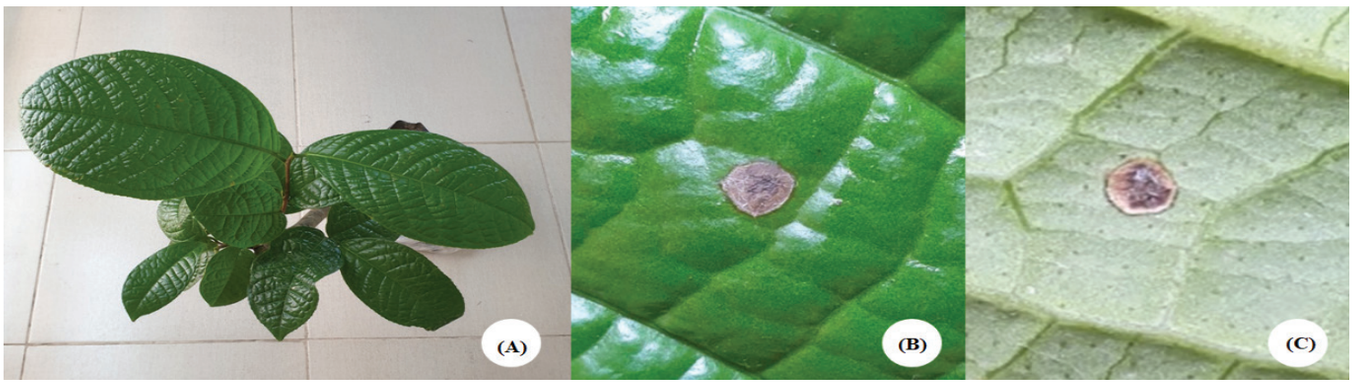

Fig. 3. Pathogenicity test back on the healthy leaf of *C. tamdaoensis* Ninh et Hakoda. (A) Whole plant, **(B, C)** Lesions caused by *Colletotrichum siamense* TD1, on upper and lower sides, respectively.

This result demonstrated that the isolate from *C. tamdaoensis* Ninh et Hakoda disease caused anthracnose.

4. Conclusions

A fungal strain causing anthracnose disease has been isolated from *C. tamdaoensis* Ninh et Hakoda collected the Tam Dao National Park. Diseased leaves showed typical anthracnose symptoms such as necrotic spots, which were initially brown, then spreading and turning black. The *ITS* sequence fragment of the pathogen was determined to have a length of 522 bp and GC content of 52.30%. By genetic relationship analysis based on the *ITS* sequence, *Colletotrichum siamense* TD1 was identified as the causative agent. The pathogenicity of *Colletotrichum siamense* TD1 was tested on leaves by artificial inoculation. The necrotic spot symptoms appeared after 7 days, which was similar to those collected in the wild.

CRediT author statement

Hong Viet La: Conceptualisation, Methodology, Reviewing and Editing; Duc Hoang Le: Doing experiments; Data analysis; Thao Thanh Thi Duong: Doing experiments, Data curation; Bang Phi Cao: Writing - Original draft preparation; Ha Duc Chu: Data analysis, Investigation.

COMPETING INTERESTS

The authors declare that there is no conflict of interest regarding the publication of this article.

REFERENCES

[1] N. Tran (2007), "Diversity of wild Camellia species of Tam Dao National Park", *Journal of Science, Natural Science and Technology*, **23**, pp.152-154.

[2] J. Zhao, T. Liu, D.P. Zhang, et al. (2021), "First report of anthracnose caused by *Colletotrichum siamense* and *C. fructicola* of *Camellia chrysantha* in China", *Plant Disease*, **105(7)**, DOI: 10.1094/PDIS-11-20-2324-PDN.

[3] K.D. Hyde, L. Cai, P.F. Cannon, et al. (2009), "*Colletotrichum* - Names in current use", *Fungal Diversity*, **39(7)**, pp.147-182.

[4] S. Freeman, D. Minz, E. Jurkevitch, et al. (2000), "Molecular analyses of *Colletotrichum* species from almond and other fruits", *Phytopathology*, **90(6)**, pp.608-614, DOI: 10.1094/PHYTO.2000.90.6.608.

[5] M. Valero, S.G. Martínez, M. Giner, et al. (2010), "Benomyl sensitivity assays and species-specific PCR reactions highlight association of two *Colletotrichum gloeosporioides* types and *C. acutatum* with rumple disease on Primofiori lemons", *European Journal of Plant Pathology*, **127**, pp.399-405, DOI: 10.1007/s10658-010-9606-0.

[6] Australian Centre for International Agricultural Research (2008), *Diagnostic Manual for Plant Diseases in Vietnam.*

[7] P. Win (2018), "Diversity of tea endophytic fungi: Cultivar and tissue preferences", *Applied Ecology and Environmental Research*, **16(1)**, pp.677-695, DOI: 10.15666/aeer/1601_677695.

[8] J. Sambrook, D.W. Russell (2001), *Molecular Cloning: A Laboratory Manual* (Third Edition), Cold Spring Harbor Laboratory Press, 999pp.

[9] T.J. White, T. Bruns, S. Lee, et al. (1990), "Amplification and direct sequencing of fungal ribosomal RNA genes for phylogenetics", *PCR Protocols*, **31**, pp.315-322, DOI: 10.1016/B978-0-12-372180-8.50042-1.

[10] M. Fu, P.W. Crous, Q. Bai, et al. (2019), "*Colletotrichum* species associated with anthracnose of *Pyrus* spp. in China", *Persoonia*, **42**, pp.1-35, DOI: 10.3767/persoonia.2019.42.01.

[11] N.N. Shi, Y.X. Du, H.C. Ruan, et al. (2018), "First report of *Colletotrichum fructicola* causing anthracnose on *Camellia sinensis* in Guangdong province, China", *Plant Disease*, **102(1)**, DOI: 10.1094/PDIS-05-17-0705-PDN.

[12] W.L. Hu, Y.Z. Ma, J.Z. Chen (2019), "First report of *Citrus sinensis* anthracnose caused by *Colletotrichum fructicola* in China", *Plant Disease*, **103(5)**, DOI: 10.1094/PDIS-08-18-1466-PDN.

[13] Y. Wang, J.Y. Chen, X. Xu, et al. (2020), "Identification and characterization of *Colletotrichum* species associated with anthracnose disease of *Camellia oleifera* in China", *Plant Dis.*, **104(2)**, pp.474-482, DOI: 10.1094/PDIS-11-18-1955-RE.

DOI: 10.31276/VJSTE.65(2).30-36

Effects of culture conditions on isolated microspore culture of melon (*Cucumis melo* L.)

Minh Ly Nguyen*, Ton Nu Bao Tien Huyen

The University of Danang - University of Science and Education, 459 Ton Duc Thang Street, Lien Chieu District, Da Nang City, Vietnam

Received 1 June 2022; revised 15 August 2022; accepted 26 August 2022

Abstract:

Isolated microspore culture is a useful tool to produce pure, fully homozygous parental lines in a short time. This study evaluated factors including the microspore developmental stage, cell culture density, and heat treatment influencing callus formation from melon microspores (*Cucumis melo* L.). The results showed that the obtained number of calli induced was highest (11.00±1.02) when cultivating flower buds with sizes 7.0-7.9 mm that contained microspores at middle-to-late uninucleate stages. The optimal microspore density for culture is 4×10^4 cells. The cultured medium was NLN, containing 130 g/l of sucrose at pH 5.8. Heat treatment at 40°C for 48 hours was best suited for callus induction of all flower bud sizes. The survival rate of microspores after 7 days of culture was lower than before inoculation and was only 75.6%. The development of the microspores and the arising of calli and embryos have been observed and evaluated for morphological cell characteristics. However, in this study, no mature embryo formation or seedling regeneration was observed.

Keywords: **anthers, callus, *Cucumis melo* L., cytology, flower buds, microspore developmental stage.**

Classification numbers: **3.1, 3.4**

1. Introduction

In vitro doubled haploid (DH) plants produced via androgenesis or gynogenesis are useful tools for both basic studies and applied research (e.g., genetic research or crop breeding) [1, 2]. Androgenesis methods are more attractive and have greater potential than gynogenesis ones. Indeed, the number of male haploid cells (microspores/pollens) is much greater than that of female haploid cells (ovules) produced by the same flower. Besides, female haploid cells exist in ovules that are covered by nucellar and tegument tissue layers and these ovules are located inside the ovary while male haploid cells are only included within the anther wall. Therefore, ovary culture requires much more time and advanced technical skills.

The method of androgenic DH plant production based on *in vitro* microspore embryogenesis includes anther culture and isolated microspore culture. Anther culture is widely used to produce DHs, however, there are some limitations involved in anther walls. Anther wall layers have a protective role and provide nutrition for microspores, but they may secrete inhibitors or toxic molecules in the case of injured tissues [3]. Moreover, embryos or calli can develop not only from microspores but also from anther walls when cultured *in vitro* [1, 4, 5]. Isolated microspore culture is an alternative technique used in plant-breeding programs. Over the past few years, studies related to isolated microspore culture have focused on *Brassica* and cereal species [1]. *In vitro* plants can be regenerated directly from microspores, embryos, or indirectly through the arising of calli formed from microspores.

Melon (*Cucumis melo* L.) has economic importance as a fruit crop [6] with more than 1 million ha involved in worldwide production in 2018 (Food and Agriculture Organization Corporate Statistical Database). Currently, most of the widespread melon varieties are hybrids, but up until now the technique of a DH line production in microspore cultures of this crop has not yet been performed. The amount of research related to this technique in melons as well as other species of the cucumber family (cucumbers, watermelons, squash) is still very limited [7]. The first DH melon plant was created in 1987 through the pollination technique of irradiated pollen grains [8]. T. Suprunova, et al. (2008) [9] obtained callus from cultured cucumber microspores.

The success of the above methods depends on many factors such as genotype, developmental stage of

*Corresponding author: Email: nmly@ued.udn.vn

microspores, nutrient medium component, the addition of growth regulators, the cell density, heat shock treatment, microspore isolation technique, and other culture conditions [1, 10]. Several studies on crucible plants evaluated the effect of the developmental stage of cultured microspores on embryonic formation, namely, that microspores from the late nucleate to the early binucleate stage were suitable for culture [11-13]. Meanwhile, the development of microspores is associated with the length of flower buds, flower leaves, or their proportions [9, 14]. Other studies focused on assessing the effects of high temperatures on the culture process [15, 16].

In a previous study, we determined the correlation between morphological characteristics, specifically the size of buds and anthers, with the development stages of melon microspore (*Cucumis melo* L.) [17]. Buds 6.0-8.9 mm in length contained mid-to-late vacuolated microspores. The present study aims to investigate microspore embryogenesis under different culture conditions. A few factors include the effects of microspore developmental stages, cell density, and stress treatment on the frequency of microspore embryogenesis in melons.

2. Materials and methods

2.1. Materials

The melon called F_1 hybrid Kim Hong Ngoc produced by Chia Tai Seed Company in Thailand was used for this study. Flower buds of all lengths ranging from 6.0 to 8.9 mm at 1 mm intervals were collected at 5:30-6:30 am and stored for 24 hours at 4°C in the dark. At least 10 buds were collected for each of the intervals.

2.2. Method

Assessing the viability and developmental stage of the microspores before culture: The analysis of the viability and developmental stage of the microspores was performed as described previously [17]. Briefly, the microspores were incubated with 2% acetocarmine for 30 min and observed under the Zeiss Axio Lab1 optical microscope (Suzhou Co., Ltd). The survival rate of the microspores was assessed by three different observation fields with 100 cells (a) per field. The percentage of living cells was calculated by:

$$\text{Percentage of living cells (\%)} = \frac{\text{live cells}}{\text{a}} \text{ x } 100.$$

Staining with 4, 6-diamidino-2-phenylindole (DAPI) fluorescent dye was used to identify the cell developmental stage. After staining, cells were observed through a Zeiss Axio Lab1 fluorescent microscope (Suzhou Co., Ltd).

Isolated microspore culture procedure: The protocol of isolated microscope culture was performed as described previously [18]. Briefly, the collected healthy flower buds were classified into three different size groups before cold pre-treatment. The bud surfaces were sterilized in 2.5% NaClO for 10 min and were rinsed in cold sterile distilled water three times for 1, 4, and 10 min, respectively. The buds were transferred to a mortar with 2 ml of sterile NLN liquid medium (pH 5.8) with 13% sucrose (NLN-13) that was slightly squeezed to free the microspores. After that, the suspensions were filtered in a centrifuge tube through two layers of nested sterile filters and the volume of each tube (10 ml) was adjusted before centrifugation at 4°C at 800 rpm for 5 min before resuspension (repeated twice). After the final washing, the pellet was suspended in 1 ml cold MS liquid medium (pH 5.8) with 13% sucrose (MS-13) and 20 µl of suspension was used to count cell density by a Fuchs-Rosenthal counting chamber and photographed under the Zeiss Axio Lab1 microscope (Suzhou Co., Ltd) at 10X magnification. The Fuchs-Rosenthal chamber has 16 squares, each with an area of 1.0×1.0 mm^2, and the depth of the counting chamber is 0.2 mm. Microspores were counted in 5 sub-cells, then multiplied by 16,000 to give a sub-microspore density of over 1 ml. The plating density for culture was adjusted by MS-13, and 3 ml microspore suspension was poured into sterile plastic Petri dishes (50×12 mm) wrapped with Parafilm membranes. The cultured plates were incubated in the dark at different temperatures for heat shock and then at 25°C continuously.

Effect of flower bud sizes and cell densities on the induction of embryogenesis from microspores: In the previous study, a correlation of bud and anther morphology with developmental stages of microspores in melon (*Cucumis melo* L.) was conducted [17]. In fact, 56.8% of microspores from 6.0-8.9 mm long buds were in the late uninucleate stage. In this study, three different groups of bud sizes i.e., 6.0-6.9, 7.0-7.9, and 8.0-8.9 mm were tested and different microspore densities were also tested: 4×10^4, 6×10^4, 8×10^4, and 16×10^4 cells/ml. Both factors were combined as a treatment. The cultured plates in this experiment were incubated at 37°C for 48 hours and then transferred to 25°C. All samples were kept under dark conditions.

Effect of temperature on the induction of embryogenesis from microspores: The appropriate density of microspores from the previous experiment was used in this experiment. Four different temperatures (33, 35, 37, and 40°C) over three periods (24, 48, and 72 hours) in three flower bud sizes (6.0-6.9 mm, 7.0-7.9 mm, and 8.0-8.9 mm) were studied.

After heat shock treatment, the culture samples were kept at 25°C in dark conditions, periodically tested, and evaluated for callus arising by direct observation under a stereoscopic microscope.

Histological observation: For observation of early development in culture, during the first 7 days, 50-100 µl of sample from a dish was collected, stained with 2% Acetocarmine, and observed under a Zeiss Axio Lab1 fluorescent microscope (Suzhou Co., Ltd). The survival rate of the cultured microspores was determined at two different times (T_1: at the time of culture; T_2: after one week of culture).

Periodic observations were carried out under a Zeiss Stemi 2000-C stereomicroscope (Suzhou Co., Ltd) to document each alteration during sporogenesis at intervals of 2 days until embryos or calli formed.

Experimental design and statistical analysis: Each experiment was conducted using a completely randomised design with three replications and 5 Petri dishes per replicate. The number of calli or embryos per dish was recorded over 30 days. The data was processed using IBM SPSS Statistic 23 (IBM Corporation, USA) with average M and standard error (±SEM) with a confidence interval of 95% ($t_{0.05}$×SEM) as outputs. Statistically significant differences were determined by the student's t-test value.

3. Results and discussion

3.1. Viability of microspores

For microspore culture, it is necessary to evaluate the number of cells for culture. For melons, the total number of microspores per flower bud is about 180,000 to 510,000 cells with an average number of 336,204±118,695 cells/bud. The highest number of cells was found in the 7.0-7.9 mm-long buds, followed by 6.0-6.9-mm buds and the 8.0-8.9-mm ones (Table 1). The number of cells tended to decrease as the length of the flower bud increased. The petals at bud sizes of 8.0-8.9 mm grew outside sepal and thus were affected by environmental factors such as light intensity or insect activity. This trend has also been recorded in *Raphanus sativus* L. cvs. Taebaek and Chungwoon (Monsanto Co., Seoul, Korea). Indeed, M-sized (4.0±0.5 mm) flower buds had the highest number of microspores, followed by the S- and L-sized flower buds (2.0±0.5 and 6.0±0.5 mm, respectively) [5]. In rapeseed (*Brassica napus* L.), a flower bud could contain more than 100,000 microspores, and about 50-70% of that number can be easily separated and served for the culture process [18].

Cell viability is one of the important factors in embryo or callus production. The viability rate of microspores after cold pre-treatment (T_1) in all three groups reached about 80%. In particular, the highest was recorded at 6.0-6.9 mm (Table 1). According to the study of D. Yi, et al. (2019) [19], cold pre-treatment under dark conditions at 4°C for 24 hours gave a 20% tree regeneration efficiency. This incurred rate was higher than at 4°C for 12 hours and 4°C for 48 hours (14.17 and 9.17%).

Table 1. Survival rate of microspores of different sizes after cold pre-treatment (T_1).

No.	Flower bud size (mm)	Number of microspores (cells/bud)	Viability rate (%)
1	6.0-6.9	436,500±105,831	88.78±3.30[a]
2	7.0-7.9	442,500±28,722	86.80±1.47[a]
3	8.0-8.9	251,500±86,094	79.06±3.18[a]

Note: Different letters on the same column indicate a statistically significant discrepancy in the sample average with p<0.05.

Microspores were assessed for their ability at three different times (T_0: before cold pre-treatment; T_1: at the time of culturing; T_2: after a week of culture). Table 2 shows that the survival rate of microspores reached over 80% at the culture time. The proportion of cells living before culture reaches 86.5% and decreases slightly after cold pre-processing. After a 7-days culture period, the survival rate of cells is about 75.6%.

Table 2. Survival rate of microspores at different times.

No.	Time	Proportion of living cells
1	T_0	86.50±2,45[a]
2	T_1	83.45±2,09[a]
3	T_2	75.64±1,99[b]

Note: Different letters on the same column indicate a statistically significant discrepancy in the sample average with p<0.05.

The results in this study were higher than in the study of tomatoes [20]. At the time of separation from the anarchy, the viability of microspores reached nearly 90%; however, after six days, this rate dropped to about 50%. This difference may be due to differences in genotype and culture conditions.

3.2. Anatomical observations of the microspore developmental stages and embryo or callus formation

Morphological changes in the microspores and the formation of the embryo or callus during cultivation have been monitored and periodically observed under fluorescent and stereoscopic microscopes. At the time of culture, most microspores were at the middle-to-late uninucleate stages (Fig. 1A1-A2). After 5 days of culture, microspores began to break out of the microspore wall and divide to form a

primordium (Fig. 1A3-A8 and Fig. 2A1, arrow marks) and form disorganized cell structures (astrocyte figure, Fig. 2A1). After germination, that germ continued to divide (Fig. 1) and bind together (Fig. 2A2). Similar observations have been reported for beetroot trees. The spores after division have different tendencies, for example, some stop growing after a few divisions, some form callus-like structures, and only a few form embryos [21].

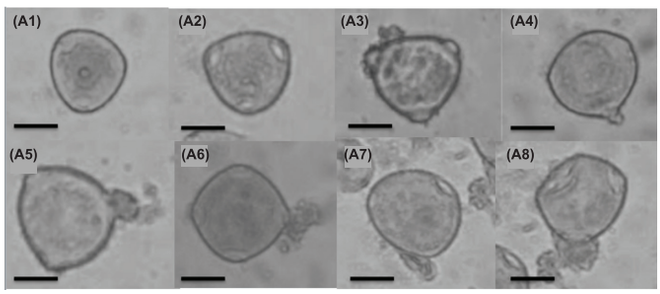

Fig. 1. The development of microspores during culture. (A1) Middle uninucleate stage; **(A2)** Late uninucleate stages; **(A3-A8)** Forming a primordium from microspores. Ratio bar = 20 µm.

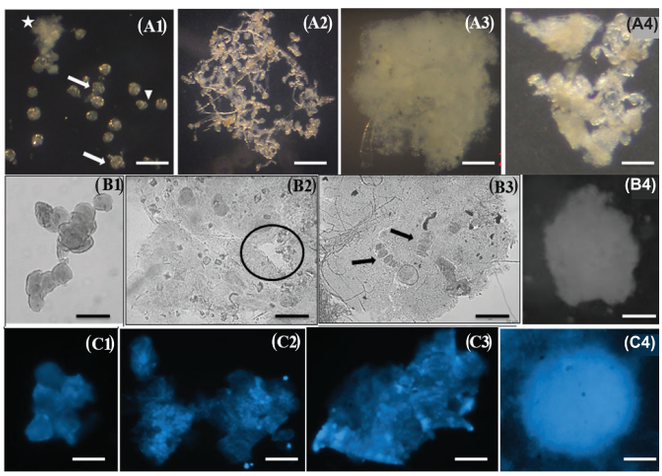

Fig. 2. Callus growth of melon microspores *in vitro*. (A1-A4) Callus formation process (ratio bar = 0.1 mm); **(B1-B4)** Histological observation of callus (scale bar = 50 µm); **(C1-C4)** Histological observation of callus. Scale bar = 50 µm.

Different forms of cell induction involved in embryonic or callus formation were all observed in a cultured environment. After stress treatment, cell observations showed that some cells continue to grow in a gamenial pathway, becoming mature pollen (triangular symbol, Fig. 2A1). In addition, a certain number of microspores did not show any morphological change from the initial implantation and some cells died or stopped growing. This is similarly indicated in the other studies [21, 22].

After 15 days, callus-like structures began to appear in two different forms. Fig. 2A3 shows the form of block callus, which is tightly bound, white, and amorphic. Meanwhile, Fig. 2A4 represents the cluster callus structure, which is discrete, yellowish-white, and amorphic. Histological observations show that inside the cluster callus is the presence of cells that are continuing to divide (arrow mark Fig. 2B3) and form a space between parts in a discrete callus (circled, Fig. 2B2).

After eight weeks, arising calli and the continuation of the growth phase is no different from the original and embryo-like structures can be observed on the surface of some discrete calli (Fig. 2). Embryonic structures at the late spherical and heart-shaped stages were given in which a protective layer was distinguished. However, under these conditions, further development of these structures into mature embryos or germinated seedlings were not observed.

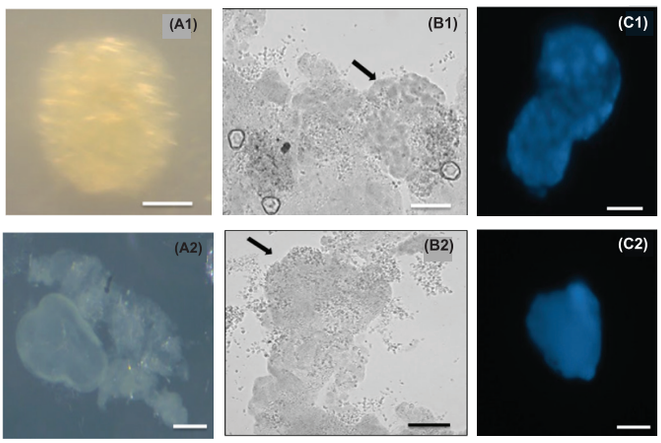

Fig. 3. The development of embryos in the culture environment of melon microspores. (A1) Spherical embryo; **(A2)** Heart-shaped embryo, scale bar = 0.2 mm; **(B1)** Spherical workpiece (arrow mark); **(B2)** Heart-shaped embryo (arrow mark), scale bar = 100 µm; **(C1)** Spherical embryo; **(C2)** Heart-shaped embryo (even arrow), scale bar = 50 µm.

3.3. Influences of microspore density and flower bud size on callus induction

Microspore density and bud size significantly affected the success of isolated microspore cultures [4]. In this study, a significant number of calli were observed at 4×10^4 cells/ml in three size groups (Table 3). In particular, the highest number of calli was recorded in flower buds of 7.0-7.9 mm (11.00±1.02 callus/petri dish).

In studies of *Brassica napus* L., the culture density for embryonic growth was 4×10^4 (cells/ml) in flower buds of 3.3 to 3.4 mm [23] while other studies showed that the highest embryo induction was given in 2.5-3.0 mm buds containing middle nucleate microspores in the range of 7×10^4 to 10×10^4 (cell/ml) [24]. In the study on *Brassica oleracea* cabbage, the cell density of 15×10^4 (cells/ml) in flower buds was 4.5 to 4.6 mm long for the highest embryonic arising rate of 15.2±2.17 [25].

Table 3. Interactive effect of microspore density and flower bud size on callus induction.

No.	Cell density (cell/ml)	Number of calluses at different flower bud sizes (callus/petri dish)		
		6.0-6.9	*7.0-7.9*	*8.0-8.9*
1	4×10^4	4.33 ± 1.06^{a}	11.00 ± 1.02^{a}	1.33 ± 0.51^{a}
2	6×10^4	2.58 ± 0.89^{f}	5.00 ± 1.13^{b}	0.67 ± 0.26^{a}
3	8×10^4	0.5 ± 0.29^{b}	2.92 ± 1.05^{b}	0.5 ± 0.23^{a}
4	16×10^4	0.83 ± 0.41^{b}	4.08 ± 0.89^{b}	0.33 ± 0.14^{a}

Note: Different letters on the same column indicate a statistically significant discrepancy in the sample average with $p<0.05$.

The establishment of optimal culture density is the initial step toward an efficient protocol. In previous studies, a lower density than the optimal value affected embryo production [25]. In addition, high density increases the single effect between cells that release nicotinamide and purine metabolising agents, which have a strong effect on the early stages of embryogenesis. However, when plating density is higher than the optimal concentration, autoxidation or inhibitory compounds can affect the reduction of embryos or calli [26, 27] and increase abnormal morphology [28].

Effect of heat shock and flower bud size on callus induction: Heat shock is an important factor in isolated microspore culture. Without heat stress, microspores form pollen through gametogenesis. The appropriate temperature will stimulate and transfer from the gametophytic to the sporophytic pathway [2].

Temperature stress during culture depends on the ecological type of the mother plant. For example, cucumbers from cold regions like Jinglv No. 4 cucumbers in the northern region of China have a good responses to cold pre-treatment while varieties from more temperate regions such as Erzaozi in southern China have a better responses to high-temperature conditions. For melons, the optimum development temperature is between 18 and 28°C and can withstand up to 40°C for several hours per day [26]. In this study, high-temperature experiments over three different periods were conducted and the results are shown in Table 4.

Table 4. The interaction effect of flower bud heat shock and size on callus induction.

No.	Temperature and time	Number of calli of different flower buds per a petri dish		
		6.0-6.9	*7.0-7.9*	*8.0-8.9*
1	33°C in 24 h	0.6 ± 0.16^{a}	3.3 ± 0.47^{a}	3.5 ± 0.72^{ab}
2	33°C in 48 h	1.8 ± 0.33^{abc}	7.0 ± 0.67^{abc}	3.8 ± 0.49^{abc}
3	33°C in 72 h	1.3 ± 0.42^{ab}	4.1 ± 0.46^{f}	2.2 ± 0.36^{ab}
4	35°C in 24 h	1.3 ± 0.34^{ab}	4.1 ± 0.72^{f}	1.6 ± 0.45^{a}
5	35°C in 48 h	2.9 ± 0.28^{abc}	7.7 ± 0.75^{bc}	4.0 ± 0.42^{abc}
6	35°C in 72 h	4.3 ± 0.40^{cd}	6.5 ± 0.64^{abc}	4.7 ± 0.50^{bc}
7	37°C in 24 h	3.3 ± 0.50^{bc}	5.2 ± 0.42^{ab}	3.5 ± 0.4^{ab}
8	37°C in 48 h	7.0 ± 0.86^{e}	9.4 ± 0.85^{c}	6.1 ± 0.66^{cd}
9	37°C in 72 h	3.3 ± 0.42^{bc}	6.4 ± 0.54^{abc}	4.2 ± 0.36^{bc}
10	40°C in 24 h	6.5 ± 0.86^{de}	8.1 ± 1.13^{bc}	6.2 ± 0.73^{cd}
11	40°C in 48 h	8.5 ± 0.95^{e}	17.9 ± 1.89^{d}	8.9 ± 0.53^{e}
12	40°C in 72 h	7.1 ± 0.48^{e}	9.3 ± 0.79^{c}	7.6 ± 0.60^{de}

Note: Different letters on the same column indicate a statistically significant discrepancy in the sample average with $p<0.05$.

In general, the temperature has a significant effect on callus induction. In this study, at lower stress temperatures for short times (i.e., 33°C for 24 hours), the lowest number of calli was generated (0.6±0.16). In contrast, heat shock treatment at 40°C for 48 hours was the most suitable treatment for callus production in all flower bud sizes. Specifically, 17.9±1.89 calli/petri dish were formed in buds 7.0-7.9 mm-long and 8.9±0.53 calli/petri dish in 8.0-8.9 mm-long buds. However, at the same temperature, the heat shock period lasting 72 hours affected the number of calli in all three flower bud size groups.

Treatment at high temperatures from 32 to 35°C is commonly used to induce the embryogenesis of microspores in different plant species [29]. For the cucurbits, the microspore culture method is less studied but mainly focuses on the anther culture method. Kumar et al. showed that the best response of cucumber microspores in terms of androgenic capability was obtained by incubating anther at 32°C for 1 day [30]. This is in agreement with the observation of H. Song, et al. (2007) [31] who mentioned that heat treatment at 33°C was optimal for embryo induction from microspores in cucumbers. Meanwhile, heat shock at 35°C allowed the formation of haploid plants in squash [32]. However, in watermelon and squash, haploid plants could be obtained without high-temperature treatments [33, 34].

4. Conclusions

From this study, the conditions of isolated microspore culture of melon (*Cucumis melo* L.) were established. Three different groups of bud size, i.e., 6.0-6.9, 7.0-7.9, and 8.0-8.9 mm, which contained the most microspores in the late uninucleate stage of development, were studied. The highest number of calli was observed when 7.0-7.9-mm buds were cultured on MS-13 at pH 5.8. The suitable density for high callus growth is 4×10^4. Heat treatment at 40°C for 48 hours was best suited for callus arising at all flower bud sizes. The cell viability after 7 days reached 75.6%. The development of microspores as well as the formation of calli and embryos were observed and evaluated for cell characteristics and morphology. This study provides the first result of microspores isolated from melon (*Cucumis melo* L.).

CRediT author statement

Minh Ly Nguyen: Conceptualization, Methodology, Investigation, Writing - Reviewing and Editing; Ton Nu Bao Tien Huyen: Data curation, Writing - Original draft preparation.

COMPETING INTERESTS

The authors declare that there is no conflict of interest regarding the publication of this article.

REFERENCES

[1] J.M.S. Simarro (2021), *Doubled Haploid Technology*, Springer, DOI: 10.1007/978-1-0716-1331-3.

[2] A.M.R. Ferrie, K.L. Caswell (2011), "Isolated microspore culture techniques and recent progress for haploid and doubled haploid plant production", *Plant Cell Tissue Organ Cult.*, **104(3)**, pp.301-309, DOI: 10.1007/s11240-010-9800-y.

[3] K. Linde, V. Walbot (2019), "Pre-meiotic anther development", *Current Topics in Developmental Biology*, **131**, pp.239-256, DOI: 10.1016/bs.ctdb.2018.11.001.

[4] J.M.S. Simarro (2010), "Androgenesis revisited", *The Botanical Review*, **76(3)**, pp.377-404, DOI: 10.1007/s12229-010-9056-6.

[5] N.R. Han, S.U. Kim, H.Y. Park, et al. (2014), "Microspore-derived embryo formation and morphological changes during the isolated microspore culture of Radish (*Raphanus sativus* L.)", *Korean J. Hortic. Sci. Technol.*, **32(3)**, pp.382-389, DOI: 10.7235/hort.2014.13170.

[6] P. Sebastian, H. Schaefer, R.H. Telford, et al. (2010), "Cucumber (*Cucumis sativus*) and melon (*C. melo*) have numerous wild relatives in Asia and Australia, and the sister species of melon is from Australia", *Proceedings of the National Academy of Sciences*, **107(32)**, pp.14269-14273, DOI: 10.1073/pnas.1005338107.

[7] J. Gałązka, K.N. Szczytt (2013), "Review of research on haploid production in cucumber and other cucurbits", *Folia Hortic.*, **25(1)**, pp.67-78, DOI: 10.2478/fhort-2013-0008.

[8] M. Lotfi, A.R. Alan, M.J. Henning, et al. (2003), "Production of haploid and doubled haploid plants of melon (*Cucumis melo* L.) for use in breeding for multiple virus resistance", *Plant Cell Rep.*, **21(11)**, pp.1121-1128, DOI: 10.1007/s00299-003-0636-3.

[9] T. Suprunova, N. Shmykova (2008), "*In vitro* induction of haploid plants in unpollinated ovules, anther and microspore culture of *Cucumis sativus*", *Proceedings of the IXth EUCARPIA Meeting on Genetics and Breeding of Cucurbitaceae. Avignon.*, pp.371-374.

[10] J.M. Dunwell (2010), "Haploids in flowering plants: Origins and exploitation", *Plant Biotechnol. J.*, **8(4)**, pp.377-424, DOI: 10.1111/j.1467-7652.2009.00498.x.

[11] Y. Takahata, D.C.W. Brown, W.A. Keller (1991), "Effect of donor plant age and inflorescence age on microspore culture of *Brassica napus* L.", *Euphytica*, **58(1)**, pp.51-55, DOI: 10.1007/BF00035339.

[12] A. Touraev, A. Ilham, O. Vicente, et al. (1996), "Stress-induced microspore embryogenesis in tobacco: An optimized system for molecular studies", *Plant Cell Rep.*, **15(8)**, pp.561-565, DOI: 10.1007/BF00232453.

[13] P. Binarova, G. Hause, V. Cenklová, et al. (1997), "A short severe heat shock is required to induce embryogenesis in late bicellular pollen of *Brassica napus* L.", *Sex. Plant Reprod.*, **10(4)**, pp.200-208, DOI: 10.1007/s004970050088.

[14] S. Weber, F. Ünker, W. Friedt (2005), "Improved doubled haploid production protocol for *Brassica napus* using microspore colchicine treatment *in vitro* and ploidy determination by flow cytometry", *Plant Breed*, **124(5)**, pp.511-513, DOI: 10.1111/j.1439-0523.2005.01114.x.

[15] J.B.M. Custers, J.H.G. Cordewener, Y. Nöllen, et al. (1994), "Temperature controls both gametophytic and sporophytic development in microspore cultures of *Brassica napus*", *Plant Cell Rep.*, **13(5)**, pp.267-271, DOI: 10.1007/BF00233317.

[16] J.G. Humanes, F. Barro (2009), "Production of doubled haploids in *Brassica*", *Adv. Haploid Prod. High. Plants*, Springer, DOI: 10.1007/978-1-4020-8854-4_4.

[17] M.L. Nguyen, T.N.B.T. Huyen, D.M. Trinh, et al. (2022), "Association of bud and anther morphology with developmental stages of the male gametophyte of melon (*Cucumis melo* L.)", *Vavilov Journal of Genetics and Breeding*, **26(2)**, pp.146-152, DOI: 10.18699/VJGB-22-18.

[18] J.B.M. Custers (2003), "Microspore culture in rapeseed (*Brassica napus* L.)", *Doubled Haploid Prod. Crop Plants*, Springer, DOI: 10.1007/978-94-017-1293-4_29.

[19] D. Yi, J. Sun, Y. Su, et al. (2019), "Doubled haploid production in alfalfa (*Medicago sativa* L.) through isolated microspore culture", *Sci. Rep.*, **9(1)**, pp.1-7, DOI: 10.1038/s41598-019-45946-x.

[20] J.M.S. Simarro, F. Nuez (2007), "Embryogenesis induction, callogenesis, and plant regeneration by *in vitro* culture of tomato isolated microspores and whole anthers", *J. Exp. Bot.*, **58(5)**, pp.1119-1132, DOI: 10.1093/jxb/erl271.

[21] M. Soriano, H. Li, K. Boutilier (2013), "Microspore embryogenesis: Establishment of embryo identity and pattern in culture", *Plant Reprod.*, **26(3)**, pp.181-196, DOI: 10.1007/s00497-013-0226-7.

[22] P.C. Martínez, J.M.S. Simarro (2012), "Efficient production of callus-derived doubled haploids through isolated microspore culture in eggplant (*Solanum melongena* L.)", *Euphytica*, **187(1)**, pp.47-61, DOI: 10.1007/s10681-012-0715-z.

[23] E.D. Supena, B. Winarto, T. Riksen, et al. (2008), "Regeneration of zygotic- like microspore-derived embryos suggests an important role for the suspensor in early embryo patterning", *Journal of Experimental Botany*, **59(4)**, pp.803-814, DOI: 10.1093/jxb/erm358.

[24] E.S. Kurtar, N. SarI, K. Abak (2002), "Obtention of haploid embryos and plants through irradiated pollen technique in squash (*Cucurbita pepo* L.)", *Euphytica*, **127(3)**, pp.335-344, DOI: 10.1023/A:1020343900419.

[25] B. Winarto, J.A.T.D. Silva (2011), "Microspore culture protocol for Indonesian *Brassica oleracea*", *Plant Cell, Tissue and Organ Cult.*, **107(2)**, pp.305-315, DOI: 10.1007/s11240-011-9981-z.

[26] L.S. Kott, L. Polsoni, B. Ellis, et al. (1988), "Autotoxicity in isolated microspore cultures of *Brassica napus*", *Can. J. Bot.*, **66(8)**, pp.1665-1670, DOI: 10.1139/b88-227.

[27] B. Huang, S. Bird, R. Kemble, et al. (1990), "Effects of culture density, conditioned medium and feeder cultures on microspore embryogenesis in *Brassica napus* L. cv. Topas", *Plant Cell Rep.*, **8(10)**, pp.594-597, DOI: 10.1007/BF00270061.

[28] E. Abraha, M. Bechyne, M. Klima, et al. (2008), "Analysis of factors affecting embryogenesis in microspore cultures of *Brassica carinata*", *Agricultura Tropica et Subtropica*, **41(2)**, pp.53-59.

[29] N. Shmykova, E. Domblides, T. Vjurtts, et al. (2021), "Haploid embryogenesis in isolated microspore culture of carrots (*Daucus carota* L.)", *Life*, **11(1)**, DOI: 10.3390/life11010020.

[30] H.G.A. Kumar, H.N. Murthy, K.Y. Paek (2003), "Embryogenesis and plant regeneration from anther cultures of *Cucumis sativus* L.", *Scientia Horticulturae*, **98(3)**, pp.213-222, DOI: 10.1016/S0304-4238(03)00003-7.

[31] H. Song, Q.F. Lou, X.D. Luo, et al. (2007), "Regeneration of doubled haploid plants by androgenesis of cucumber (*Cucumis sativus* L.)", *Plant Cell, Tiss. and Organ Cult.*, **90**, pp.245-254, DOI: 10.1007/s11240-007-9263-y.

[33] R. Habiba (2016), "Effect of genotypes, sucrose concentrations and their interaction on anther culture response on summer squash", *Journal of Agricultural Chemistry and Biotechnology*, **7(4)**, pp.113-120, DOI: 10.21608/jacb.2016.40787.

[34] C.M.J. Silva, R.C.S. Dias, N.F. Melo (2021), "The effect of temperature and growth regulators on callus induction in watermelon anthers", *Brazilian Archives of Biology and Technology*, **64**, DOI: 10.1590/1678-4324-2021180505.

DOI: 10.31276/VJSTE.65(2).37-41

Quality assessment of japonica brown rice J02 (*Oryza sativa* L. J02) and its hydrolysis ability for the production of a rice-based drink containing an abundance of dextrin

Thu Trang Vu[1*], Thi Trang Nguyen[1], Hong Quan Duong[1, 2], Van Hung Nguyen[1], Viet Hung Le[3], Viet Hung Nguyen[1, 3], Xuan Lam Nguyen[3], Van Tan Le[3], Giang Hoang[4], Quoc Tuan Hoang[1], Thi Thao Nguyen[1], Tien Cuong Nguyen[1], Ngoc Hung Pham[1], Hong Son Vu[1], Thi Hanh Nguyen[1], Ky Son Chu[1]

[1]*School of Biotechnology and Food Technology, Hanoi University of Science and Technology, 1 Dai Co Viet Street, Bach Khoa Ward, Hai Ba Trung District, Hanoi, Vietnam*
[2]*Ho Chi Minh City University of Food Industry, 140 Le Trong Tan Street, Tay Thanh Ward, Tan Phu District, Ho Chi Minh City, Vietnam*
[3]*Lam Son Sugar Cane Joint Stock Corporation, Lam Son Town, Tho Xuan District, Thanh Hoa Province, Vietnam*
[4]*High Command of Guard Police, Ministry of Public Security, 16 Tran Vu Street, Ba Dinh District, Hanoi, Vietnam*

Received 19 September 2022; revised 17 October 2022; accepted 28 October 2022

Abstract:

Plant-based beverages have become very popular in recent emerging markets. Brown rice milk offers several important health benefits because of its various nutritional ingredients such as proteins, carbohydrates, gamma-aminobutyric acid (GABA), and essential vitamins and minerals. Brown rice milk is also low in fats and cholesterol and free of lactose. In this study, japonica brown rice J02 from Thanh Hoa Province presented high nutrition with high protein (8.6% dm) and lipid (2.2% dm) contents as calculated from dry matter and GABA contents of 32 mg/100 g, which is suitable for the plant-based milk processing. J02 rice is also capable of hydrolysis to obtain high molecular sugar in the liquor with slow digestion ability (dextrose equivalent - DE<40) and high hydrolysis efficiency (up to more than 90%). The results obtained from HPLC analysis indicated that the hydrolysis conditions for the rice drink at 75^{o}C and 150 g/l starch produced Spezyme alpha concentrations at 0.024%w/w and low content in low molecular oligosaccharide (DP<10) in the solution. The results indicated that Japonica rice J02 is a good candidate for the production of a rice-based drink.

Keywords: **degree of polymerization, dextrose equivalent, hydrolysis, Japonica rice, rice-based drink.**

Classification numbers: **3.1, 3.5**

1. Introduction

Rice is the most important foodstuff in Vietnam and many Asian countries. Cultivated Asian rice (*Oryza sativa* L.) makes up about 90% of the world's rice and provides about 20% of the world's dietary energy demand [1]. There are two species of cultivated rice in the world, namely, *Oryza sativa* in Asia and *Oryza glaberrima* in Africa. Among them, *Oryza sativa* is the most cultivated species and represents almost all rice products around the world [2].

Plant-based drinks and beverages have become an emerging beverage market all over the world. The plant-based beverage market was valued at $13.56 billion in 2018 and is estimated to reach $22.45 billion by 2026 while registering a Compound Annual Growth Rate (CAGR) of 6.7% from 2019 to 2026. Because they contain essential minerals and vitamins with low fat content and no cholesterol, plant-based beverages may be used as a substitute for dairy products. Besides, without lactose, plant-based beverages are also suitable for those that are lactose intolerant. Thus, plant-based drinks are considered healthy products [3]. The vegan trend in the food industry is rising with the global vegan food market expanding from $26.16 billion in 2021 to $61.35 billion in 2028 at a CAGR of 12.95% from 2021 to 2028. In recent years, plant-based drinks based on oat, soy, almond, coconut, rice, and cashew have been launched on global markets by various food industries worldwide and rice milk is one of the most popular dairy-free alternatives in Asian countries [4]. Rice milk is considered one of the best plant-based drinks. Naturally, rice milk provides various health benefits and other nutritional ingredients, which further drives the expansion of the global rice milk market. Rice and brown rice containing unsaturated fatty acids help reduce cholesterol in the blood. Vitamin B6 obtained from rice is also well-known to help maintain heart health. Thus, rice milk contains plenty of heart-healthy nutrients with lots

[*] *Corresponding author: Email: trang.vuthu@hust.edu.vn*

of antioxidants such as tocopherol selenium, which aids in the prevention of all types of infections and many other heart diseases. In addition to these factors, the global rice milk market is expected to witness substantial growth at a CAGR of 9% over the forecast period of 2020-2030 [4].

Rice is an essential product of Vietnamese people. The System of Rice Intensification (SRI) is known as a farming methodology that is low water and labour-intensive that uses younger seedlings individually spaced and typically hand weeded with special tools. This method has been applied in Thieu Hoa, Thanh Hoa and was aimed at increasing the yield of rice produced in farming as well as product quality. The production of organic rice according to SRI and SRI2 methods creates a high level of protein products and a low level of carbon emission to produce clean and safe rice guarantees for health and safety. The local company tends to associate with the community and nearby cultivators to develop organic Japonica rice (*Oryza sativa japonica var*. J02) grown in an area that helps decline greenhouse emissions, create an environmentally friendly product, provide a source of clean materials for cultivators, and increase income as well as product price. This method is a point of strength for the company as their rice product is an optimal raw material for producing a domestic rice drink in Vietnam.

Brown rice contains more nutrients than white rice such as digestible fiber and antioxidant compounds like selenium, manganese, tocopherol, and GABA from brown rice germ and endosperm, which are all known to promote beneficial effects on human health [5]. Recent epidemiological studies have shown that the consumption of whole grains can reduce the risk of metabolic disorders, cardiovascular diseases, and some types of cancer [6]. Thus, brown rice is an ideal raw material for rice drink processing. Our previous study was successful at obtaining hydrolysis conditions for rice powder by Spezyme Alpha to apply to rice drink processes [6]. In this study, the organic Japonica rice (*Oryza sativa japonica* var. J02), produced by SRP (Sustainable rice production) farming methodology, was assessed for its quality. The hydrolysis ability was also investigated for the further development of rice milk technology with high benefit and nutrition.

2. Materials and methods

2.1. Materials

Japonica brown rice J02 (*Oryza sativa japonica var*. J02) was obtained from Lam Son JSC, Trieu Hoa, Thanh Hoa. The paddy was farmed by the System of Rice Intensification (SRI) farming methodology, and, after harvest, the paddy was passed through a rice hulling machine system (SH 100, China) according to factory processing standards after many steps such as drying, cleaning, sifting, gravity grading, and magnetic separation. The length of the obtained brown rice grains was not longer than 6 mm; the impurity content was less than 0.2 %; and damaged grain accounted for less than 0.15%. From a sensory aspect, the rice grains had a typical rice scent with no strange odour and were short and slender in shape.

The rice was ground with a superfine, two-stage grinding system (60B, SH CO, China) with the practical size from 20-120 mesh. Spezyme Alpha was kindly supplied from DuPont, Wilmington, Delaware, USA [7].

2.2. Methods

Physiochemical analysis: Protein content was determined according to the method of TCVN 8133-1-09. The fiber, ash, lipid, amylose, moisture, and carbohydrate contents were analysed according to TCVN 4329:2007, TCVN 9939:2013, TCVN 10730:2015, TCVN 5716-1:2008, TCVN 1643:2008, and TCVN 4074:09, respectively. GABA analysis was carried out according to the method described by C.T.T. Quynh, et al. (2013) [8]. The safety of the rice was confirmed by the determination of lead, cadmium, total aflatoxin and aflatoxin B1, carbaryl residue, chlorantraniliprole residue, flutolanil residue, and total mould and yeast according to TCVN 7602:2007; TCVN 7603:2007; TCVN 7569:75962007; TC 86/69 TL; TCCS 10/2010 BVTV; TCVN 7082:2002; TC 96/98-CL; TCVN 8101:2009; and TCVN 8275-1:2009, respectively.

The dextrose equivalent was determined as the percentage (in dry basis) of glucose to the total sugar in the supernatant of the hydrolysed syrup. The hydrolysis yield was expressed as the ratio of obtained reducing sugar to the initial starch content. The glucose and total reducing sugar were determined by the DNS method [9].

Determination of oligosaccharide: Oligosaccharide determination was carried out using HPLC with a refractive index detector (RID). Water (H_2O) (100%) was used as a mobile phase with the flow rate of 0.1 ml/min and sample injection volume of 20 µl [10]. The RID high-pressure liquid chromatography system HPLC 1290 - Agilent was used to analyse the sugar and oligosaccharide contents in the hydrolyzation product. The following instruments: HyperRez XP analysis column, Carbohydrate Na^+, (7.7x300 mm) with guard column HyperRez XP, Carbohydrate Na^+, (7.7x50 mm) (Thermo Fisher Scientific, UK) were used for

this study. Standard linear oligosaccharide standards include glucose, maltose, maltotriose (DP3), maltotetraose (DP4), maltopentaose (DP5), maltohexaose (DP6), maltoheptaose (DP7), maltooctaose (DP8), maltononaose (DP9), maltodecaose (DP10), and linear maltooligosacharide (DP=10-40) [10].

2.3. Hydrolysis of brown rice J02

The hydrolysis of brown rice J02 by Spezyme Alpha (α-amylase) was carried out according to the previous study [6]. Spezyme Alpha is a thermostable starch that hydrolyses α-amylase produced from a strain of genetically modified bacteria *Bacillus licheniformis* that catalyses the hydrolysis of α - 1,4 glucoside bonds inside the polysaccharide chain, thereby converting starch into soluble dextrin, which reduces the viscosity of a starch slurry. The Spezyme alpha enzyme is recommended to be used at a temperature of 83-85°C at an enzyme concentration 0.02-0.025%(w/w) and pH 5.7-5.8 [7].

To apply Japonica rice J02 for plant-based drink processing on an industrial scale, the hydrolysis ability of J02 rice by alpha amylase was carried out at 150 g/l in dry matter with the hydrolysing condition of 75ºC for 60 min with the enzyme concentration of 0.024%w/w without pH adjustment according to a previous study [6]. After partial saccharification, the syrup is heated for enzyme deactivation and to prevent further glucose formation. The obtained rice liquor was identified as reducing sugar content, starch content, hydrolysis yield, and the dextrose equivalent (DE) index. During the hydrolysis duration, the samples were collected at 15 min, 30 min, 45 min, and 60 min and the starch residue, hydrolysis efficiency, and the DE index were analysed.

The oligosaccharide compositions of the obtained rice liquid were also determined by the method described above. All the experiments were carried out in triplicate and the results were present as the average of the experimental results.

3. Results and discussion

3.1. Composition of Japonica brown rice J02

The nutritional value of brown rice J02 was identified by its moisture, starch, total carbohydrate, protein, lipid, cellulose, ash, and GABA contents. The compositions of J02 are presented in Table 1. Brown rice contains 83% grain dry matter whereas proteins account for around 8.6%. The lipid content was 2.2% in brown rice J02 and the cellulose and ash contents were 1.1 and 14%, respectively. Besides these main substances, brown rice J02 also contains GABA with a content of 32 mg/100 g. This brown rice has protein and lipid contents much higher than those in white rice with 6.7 and 0.4% dry matter, respectively [5], because of the remaining rice bran in brown rice. Thus, the rice-based drink obtained from brown rice should provide more nutritional value than normal rice milk.

Table 1. Chemical composition of Japonica rice J02.

Chemical elements	Unit	Content
Moisture	%	14.5±0.2
Starch	% dry matter	83.7±0.7
Carbohydrate	% dry matter	3.3±0.1
Protein	% dry matter	8.6±0.1
Lipid	% dry matter	2.2±0
GABA	mg/100 g	32±1.4
Cellulose	% dry matter	1.1±0.1
Ash	% dry matter	1.4±0

Compared with brown rice nutrients reported in a previous study [5], the protein and lipid obtained from J02 was higher at 15.7 and 14.67%, respectively. The GABA present in the peripheral nervous system is well known as the main inhibitory neurotransmitter in the central nervous system [11]. Brown rice J02 contained 32 mg of GABA per 100 g of rice. Compared with the report obtained by D. Karladeea, et al. (2012) [12], the GABA content in J02 was approximately 10 times higher than Chieng Mai brown rice. Compared with the analysis results of brown rice from Bac Huong (Vietnam) for rice milk production, we find that the nutritional content of the brown rice of the Japanese variety J02 is higher in terms of nutritional content, for example, the protein content was 7.52±0.12 g/100 g while other components were similar [6]. This is the advantage of J02 rice as it can provide products processed from J02 with higher protein content, lipid content, and high concentrations of GABA making it a valuable and suitable raw material for a plant-based drink.

3.2. Food safety of Japonica brown rice J02

Common heavy metal pesticide residues and mycotoxins are presented in Table 2. The results show that all indicators were not detected or at levels much lower than the allowable limit. This confirms the safety of the protein-rich rice J02 when it used to produce a brown rice drink on an industrial scale.

Table 2. Residues of pesticides, heavy metals, and mycotoxins of Japonica rice J02.

Chemical elements	Unit	Content
Lead	mg/kg	0.072
Arsenic	mg/kg	Non detected
Cadmium	mg/kg	Non detected
Total aflatoxin	µg/kg	Non detected
Aflatoxin B1	µg/kg	Non detected
Carbaryl	mg/kg	Non detected
Chlorantraniliprole	mg/kg	Non detected
Chlordane	mg/kg	Non detected
Flutolanil	mg/kg	Non detected
Sulfuryl fluoride	mg/kg	Non detected
Total mould and yeast	CFU/g	Non detected

3.3. The hydrolysis of Japonica rice using enzymes

DE is calculated by the amount of reducing sugars in a total sugar product. Therefore, the dextrose equivalent describes the degree of conversion of starch to dextrose. The purpose of rice hydrolysis is to obtain rice milk with an abundance of long chain oligosaccharides (e.g., starch-derived low digestible oligosaccharides), but not final products of starch hydrolysis such as glucose or fructose, which might increase the glycemic index (GI). The preferred hydrolysis condition gives rice milk with a low DE index (less than 40) and high hydrolysis yield (or high in the ratio of obtained reducing sugar to the initial starch content).

The result obtained in Table 3 indicates that the hydrolysis efficiency and DE values increased with heating time. The DE value was quickly attained at 25 after 15 min of enzymatic reaction. After that, the DE value slowly increased to 32.48 after 30 min of heating and the maximum of DE value was obtained after 60 min of heating with a value of 35.2. The hydrolysis efficiency attained approximately 60% after 15 min of heating. After 60 min of heating, the hydrolysis efficiency was more than 90% in value, higher than the results obtained in a previous study on Bac Huong rice [6]. The results indicate that Japonica brown rice J02 should be considered a prospective raw material for rice drink processing.

Table 3. Effect of hydrolysis time on the composition of oligosaccharides in Japonica rice hydrolysate by Spezyme-α.

Sample	15 min	30 min	45 min	60 min
Starch (g/l)	50±1.4	46.9±0.4	15±0	10±0.7
Degree of polymerization DP <10 (g/l)	43.8±0.2	43.5±0.6	45.5±0.2	42±0.1
Dextrose equivalent (DE)	25	32.48	34	35.2
Hydrolysis efficiency (%)	60.1	62.6	88.05	92.6

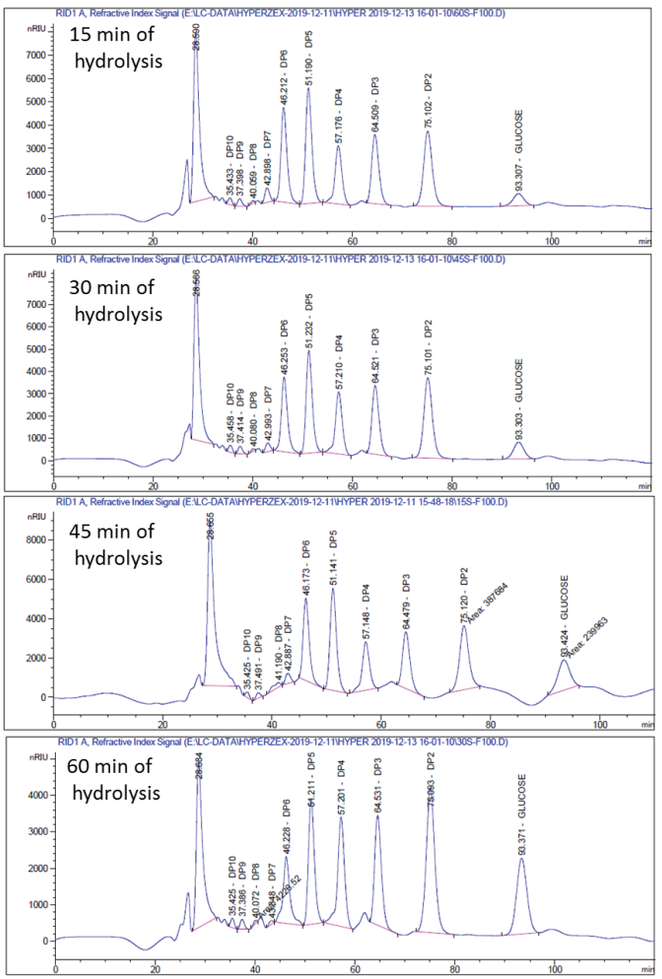

Fig. 1. High-performance liquid chromatography chromatograms of oligosaccharides in Japonica rice hydrolysate by Spezyme-*α*.

Starch is a polysaccharide with 10,000 monosaccharide or dextrose units. By enzyme hydrolysation, the starch molecule is broken up at α1-4 linkage glycosidic bonds to form dextrin with long chains of glucose and oligosaccharides with high or low molecular chain length (DP) of 2-10 shorter molecules and glucose.

In an attempt to indicate the starch hydrolysation, the DE is used. Rice hydrolysis products may contain glucose, maltose, dextrin, oligosaccharides, polysaccharides, etc. Lower DE values and higher in degrees of polymerization DP in the obtained hydrolysis rice products will promote lower digestion energy of rice-based drinks. Thus, this kind of product would be very beneficial for customers with chronic diseases such as diabetes or high blood sugar. The purpose of rice hydrolysis is to obtain rice milk with an abundance of long chain oligosaccharides, which are known as starch-derived low digestible oligosaccharide components. The preferred hydrolysis condition should produce rice milk with a low DE index and high hydrolysis yield. To evaluate the quality of J02 rice gelatinisation and liquefaction by enzyme, the DP amount of obtained hydrolysis products were analysed by HPLC. The results

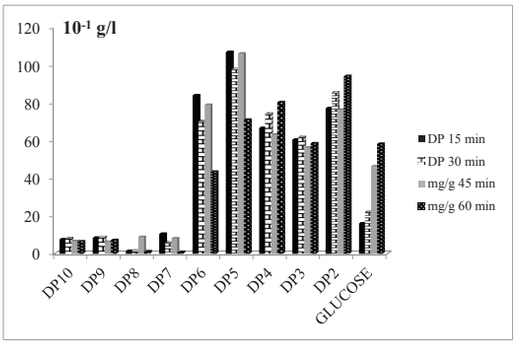

Fig. 2. Effect of hydrolysis time on the composition of oligosaccharides in Japonica rice hydrolysate by Spezyme-*α*.

are presented in Figs. 1, 2, and Table 3. The results indicated that prolonging the heating process did not greatly increase the formation of DP<10 in the solution but did increase the hydrolysis efficiency of rice starch or the formation of DP>10. C.T. Luyen and H.T. Binh (2015) [13]carried out the hydrolysis of several An Giang rice types for rice milk processing. However, the final products contained very high glucose content. This means that the products might quickly increase blood sugar. By using only alpha amylase with the control of hydrolysis conditions in the liquefaction of J02 brown rice, liquid rice products with low DE and low DP components should be achievable for the production of a healthy rice-based drink. It should be concluded that Japonica rice J02 from Lasuco showed the capacity for hydrolysis by enzyme to produce rice liquid containing high molecular sugar, which is very valuable for the production of a rice-based drink.

4. Conclusions

Brown Japonica rice J02 presented high nutritional value with high protein (8.6% dm), lipid (2.2% dm), and GABA contents (32 mg/100 g) and is suitable for plant-based drink processing. The hydrolysis of brown Japonica rice J02 led to the formation of high molecular sugar in the liquor with slow digestion ability (DE<40) and high hydrolysis efficiency (up to more than 90%). The results obtained from HPLC analysis indicated that the hydrolysis condition for a rice drink at 75ºC, 150 g/l starch, and Spezyme alpha concentrations at 0.024% w/w produce low molecular oligosaccharide content (DP<10) in the solution. These results indicate that Japonica rice J02 is a good candidate to produce a rice-based drink.

CRediT author statement

Thu Trang Vu: Concentualization, Methodology, Investigation, Draft preparation; Thi Trang Nguyen, Hong Quan Duong, Van Hung Nguyen: Data curation and Analysis; Viet Hung Le, Viet Hung Nguyen, Xuan Lam Nguyen, Van Tan Le: Editing; Giang Hoang, Quoc Tuan Hoang, Thi Thao Nguyen, Tien Cuong Nguyen, Ngoc Hung Pham, Hong Son Vu, Thi Hanh Nguyen: Data analysis; Ky Son Chu: Validation.

ACKNOWLEDGEMENTS

The research funding from the Ministry of Science and Technology, Vietnam (Project name: "Fulfil the technology and equipment for producing rice milk from protein-rich brown rice in industrial scale"; Grant number: DADL.CN-07/20) is acknowledged.

COMPETING INTERESTS

The authors declare that there is no conflict of interest regarding the publication of this article.

REFERENCES

[1] C. Marina (2021), "Value of wholegrain rice in a healthy human nutrition", *Agriculture*, **11(8)**, DOI: 10.3390/agriculture11080720.

[2] C. Karla (2020), "Temperate japonica rice (*Oryza sativa* L.) breeding: History, present and future challenges", *Chil. J. Agric. Res.*, **80(2)**, pp.303-314, DOI: 10.4067/S0718-58392020000200303.

[3] Persistence Market Research, "Rice milk market", https://persistencemarketresearch.com/market-research/rice-milk-market.asp, accessed 10 July 2022.

[4] K. Aniket, D. Roshan (2020), *Plant-Based Beverage Market by Source (Fruits, Nuts, Rice, Soy, and Others), Type (RTD Tea & Coffee, Plant-Based Milk, and Juices), and Distribution Channel (Hypermarkets & Supermarkets, Convenience Stores, Specialty Stores, and Online): Global Opportunity Analysis and Industry Forecast, 2019-2026*, 260pp, https://www.alliedmarketresearch.com/plant-based-beverage-market, accessed 15 July 2022.

[5] A.S.M. Saled, P. Wang, N. Wang, et al. (2019), "Brown rice versus white rice: Nutritional quality, potential health benefits, development of food products, and preservation technologies", *Compr. Rev. Food Sci. Food Saf.*, **18(4)**, pp.1070-1096, DOI: 10.1111/1541-4337.12449.

[6] D.T. Thanh, D.T. Du, C.K. Son, et al. (2019), "Effect of factors on the hydrolysis of red rice (*Oryza punctate*) by spezyme alpha", *J. Sci. Techno. Univer.*, **137**, pp.106-110 (in Vietnamese).

[7] DuPont (2007), *Spezyme Alpha - Alpha-Amylase for Dry Grind Ethanol Production*.

[8] C.T.T. Quynh, N.H. Dung (2013), "Research for building production process of brown rice (GABA rice) from Vietnam brown rice", *J. Sci. Tech.*, **51**, pp.63-71 (in Vietnamese).

[9] N.T. Cuong, C.K. Son, L.H. Nga, et al. (2020), "Effect of pretreatment methods on enzymatic kinetics of ungelatinized cassava flour hydrolysis", *Catalysts*, **10(7)**, DOI: 10.3390/catal10070760.

[10] H.Q. Duong, M.T. Hoang, T.H.G. Nguyen, et al. (2020), "Control the formation of isomaltooligosaccharide from sweet potato by high performance liquid chromatography with refractive index detector (HPLC-RI)", *Vietnam J. Chem.*, **58(6E12)**, pp.320-325 (in Vietnamese).

[11] M.P.S. Regal, L.B. Cordero, R.P. Ordaz, et al. (2020), "Expression and function of GABA receptors in myelinating cells", *Front. Cell. Neurosci.*, **14**, DOI: 10.3389/fncel.2020.00256.

[12] D. Karladeea, S. Suriyonga (2012), "γ-Aminobutyric acid (GABA) content in different varieties of brown rice during germination", *Science Asia*, **38(1)**, pp.13-17, DOI: 10.2306/scienceasia1513-1874.2012.38.013.

[13] C.T. Luyen, H.T. Binh (2015), "Hydrolysis of starch using alpha -amylaser and glucoamylase during the processing of rice milk from some rice varieties in An Giang province", *AGU Int. J. Sci.*, **3(3)**, pp.1-20 (in Vietnamese).

 DOI: 10.31276/VJSTE.65(2).42-46

The influence of pollutants on plant growth and treatment efficiency of horizontally-constructed wetlands

Nguyen Thanh Binh[1, 2*], Bui Thi Kim Anh[3], Nguyen Van Thanh[3], Dang Dinh Kim[3], Nguyen Minh Phuong[4]

[1]*Faculty of Agriculture, Forestry and Fishery, Hong Duc University, 565 Quang Trung Street, Dong Ve District, Thanh Hoa City, Thanh Hoa Province, Vietnam*
[2]*Graduate University of Science and Technology, Vietnam Academy of Science and Technology, 18 Hoang Quoc Viet Street, Cau Giay District, Hanoi, Vietnam*
[3]*Institute of Environmental Technology, 18 Hoang Quoc Viet, Nghia Do Ward, Cau Giay District, Hanoi, Vietnam*
[4]*Faculty of Environmental Sciences, University of Science, Vietnam National University - Hanoi, 334 Nguyen Trai Street, Thanh Xuan Trung Ward, Thanh Xuan District, Hanoi, Vietnam*

Received 9 August 2022; revised 17 October 2022; accepted 26 October 2022

Abstract:

Constructed wetlands (CWs) have been widely used for wastewater treatment due to advantages such as low cost and easy operation. However, pollutant concentrations directly affect treatment efficiency by inhibiting plant and microbial growth. This study aims to evaluate the relationship between pollutant concentrations, tolerance of plants, and treatment efficiency of horizontal subsurface flow (HSF) CWs receiving synthetic wastewater. The results showed that *Cyperus alternifolius* L. grew well in conditions with concentrations of chemical oxygen demand (COD) and NH_4^+ up to 75 and 125 mg/l, respectively, and pH 5-8. The lowest treatment efficiency was 56.7% at an initial COD concentration of 1000 mg/l. There were several dead plants in the CWs with a NH_4^+ concentration of 200 mg/l. When the initial COD and NH_4^+ concentrations were in the range of 500-750 and 75-125 mg/l, respectively, the treatment efficiencies of organic matter (COD) and NH_4^+ were 82.5-85.1 and 31-69.7%, respectively. The pH value was stable at a neutral level during the treatment process. The concentration ranges of COD (500-750 mg/l) and NH_4^+ (75-125 mg/l) were the optimal thresholds for pollution control while also ensuring normal plant growth. This study serves as a basis for considering wastewater characteristics in the design of HSF CW systems in practice.

Keywords: **constructed wetlands, *Cyperus alternifolius* L., pollutant factors, wastewater treatment.**

Classification numbers: **3.1, 5.1, 5.3**

1. Introduction

Together with fast socio-economic development, the problem of water pollution has raised concerns. Therefore, the efficient removal of nutrients and organic matter in wastewater before disposal is necessary. CWs utilise plants, substrates (e.g., soil, sand, and gravel), and microbial communities in the rhizosphere to transform and remove organic and/or inorganic pollutants [1-3]. With several advantages such as low maintenance cost and lack of chemical treatment, wetland technology has the proven ability to be an eco-friendly and effective wastewater treatment method [4, 5]. There are two main parts of an artificial wetland: substrates (or filter materials) and vegetation. Substrates can improve treatment capacity and stabilise the performance of CWs [5]. Substrates also provide reaction interfaces for various physical, chemical, and biological processes, attachment surfaces for microorganisms, support plant growth, and create favourable hydraulic conditions for sewage flow [6]. Plants play significant roles in wetland treatment processes [2, 3]. With the ability to release oxygen from their roots and root exudates, plants can enhance both aerobic and anaerobic degradation to reduce organic matter, ammonium, and other contaminants in wastewater [1, 7]. Common wetland plants such as reed (*Phragmites australis*), umbrella plant (*Cyperus alternifolius*, *Cyperus papyrus*), and water spinach (*Ipomoea aquatica*) have been widely used in CW-treated wastewater due to their tolerance to pollutants and adaptability [2, 8-10]. Vegetation is an important factor affecting the effectiveness of CWs in eliminating COD, BOD_5, TSS, and NH_4^+ in all kinds of wastewater [1, 2, 8, 11]. However, excessive nutrient concentration could suppress plant growth and transformation processes, thus affecting the wastewater treatment process in CWs. There is a little information about the correlation between pollutant concentration and the treatment time and efficiency of HSF CW. This study aims to evaluate the effects of pollutant factors (varied pollutant concentrations) on plant growth and treatment efficiency of HSF CWs, thus providing the basic for proper application of CWs in wastewater treatment.

*Corresponding author: Email: nguyenthanhbinh@hdu.edu.vn

2. Materials and methods

2.1. Materials

Cyperus alternifolius was collected from the pig farming wastewater treatment system in Chuong My, Hanoi and was grown in HSF CWs filled with sand, limestone, and gravel.

The wastewater samples were synthetic wastewater in which pH values, COD, and NH_4^+ concentrations were varied as presented in Table 1. The basis of the concentration range was to emulate the characteristics of wastewater types and plant tolerance thresholds reported in previous studies [8].

Table 1. Characteristics of the input synthetic wastewater.

pH	COD (mg/l)	NH_4^+ (mg/l)
3	250	25
4	500	50
5	750	75
6	1000	100
7		125
8		150
9		200

2.2. Experiment design

The HSF CWs had a length x width x height of 50x30x30 cm. The HSF CWs were constructed by using limestone (1-2 cm grain size, 10 cm height), gravel (0.5-1 cm grain size, 10 cm height), and sand (5 cm height) as substrates. *Cyperus alternifolius* was grown on filter media with an initial height of 15 cm and density of 18 shoots/CW.

The wetland was constructed and placed outdoors under a glass roof. The temperature ranged from 25 to 32°C, the average humidity was about 82%, and the average period of sunshine was 11.5 hours per day. The experiment was conducted in 7 days with a wastewater volume of 15 l for each system. 50 ml of sample was taken after 24, 48, 72, 96, 120, and 144 hours. The determined factors were pH and pollutant concentrations (COD, NH_4^+). The growth performance of *Cyperus alternifolius* was determined by counting shoots and measuring plant height by the end of the experiment. All the experiments were conducted in triplicate.

2.3. Sample analysis

The removal efficiency, H (%), by the CWs was calculated by using the difference in concentration (mg/l) of the inlet and outlet divided by concentration (mg/l) in the inlet. The hydraulic loading rate was calculated by the inlet flow rate divided by the area of the CW unit. The loading rate ($g/m^2/d$) was calculated by multiplying the hydraulic loading rate by the inlet concentration (mg/l). The removal rate, R ($g/m^2/d$), was defined as the hydraulic loading rate (m/d) multiplied by the difference in concentration (mg/l) between the inlet and outlet.

2.4. Statistical analysis

Statistical analyses of the experimental data were performed using the SPSS 20.0 package for Windows. All data were tested for goodness of fit to a normal distribution, using the Kolmogorov-Smirnov one-sample test.

3. Results and discussion

3.1. Effect of pH on plant growth

pH is an important value in wastewater treatment as it strongly affects the growth of plants and microorganisms. Thereby, it affects the ability to metabolize nutrients, or the pollutant removal capacity of the wastewater treatment method [5].

The changes in pH values during the experiment are presented in Fig. 1. The results showed that the pH value was almost unchanged during the treatment process for wastewater with alkaline pH (pH=8-9), but for wastewater with low pH, it tends to rise to neutral (pH=7.2-7.5).

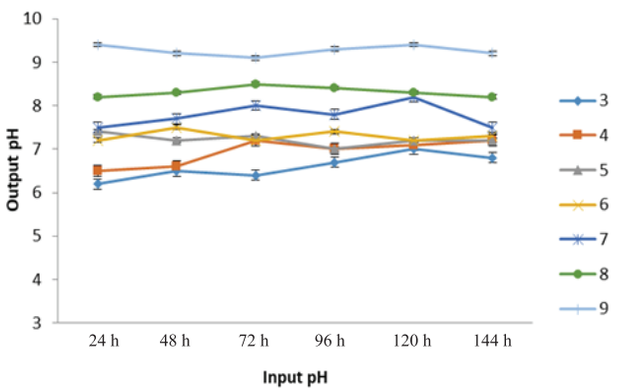

Fig. 1. The change in pH in of the HSF CWs during the experimental period.

Microbial transformation processes and wetland plants could attribute to the neutral pH results. In the range of neutral pH, the aquatic plants grew well in wastewater. After 7 days, the heights of *Cyperus alternifolius* were 16.8-21.5 cm (Fig. 2). The acidic wastewater (pH=3-4) or alkaline wastewater (pH=9) slightly affected plant growth. This result is similar to previous studies' results for some aquatic plants used for wastewater treatment [4, 7]. The height of the plants in those wastewaters only increased by 1.8 cm (pH=3) and 3.8 cm (pH=9), while they increased by 5.5-6.5 cm when grown in wastewater with pH=5-8. The plants also produced new shoots. After 7 days, the numbers of new shoots ranged from 2-11 in which the number of new shoots was highest when the wastewater was at neutral conditions (pH=6-8) (Fig. 3). The growth of *Cyperus alternifolius* increased with the increase of pH, reaching its highest value at pH=7, then the growth slightly decreased from pH 8 to 9.

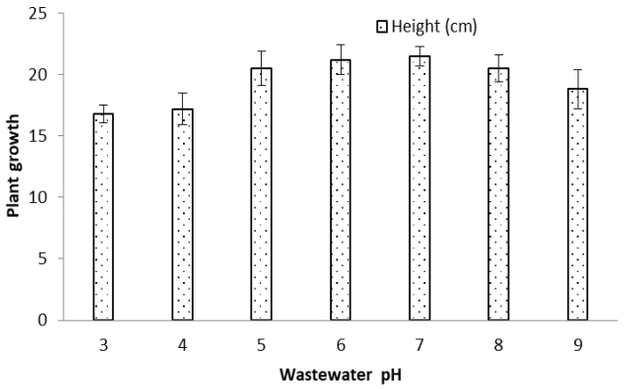

Fig. 2. Effect of pH on the height of *Cyperus alternifolius* in the HSF CWs after 7 days.

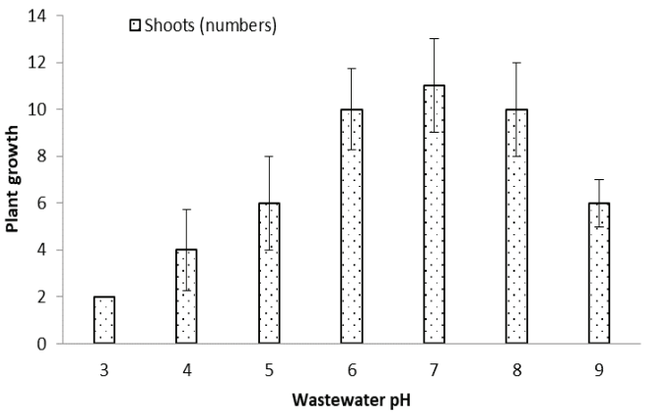

Fig. 3. Effect of pH on the shoot generation of *Cyperus alternifolius* in HSF CWs after 7 days.

3.2. Effect of COD on wastewater treatment removal and efficiency

COD is a significant parameter in wastewater treatment; it is also a value used to evaluate the efficiency of wastewater treatment methods. Previous studies have proven that the presence of vegetation in CWs could remove an average of 57.8% of COD [4, 11]. The potential COD removal of vegetation was different for plant species and wastewater types. As shown in Fig. 4, the COD removal efficiency from synthetic wastewater in the HSF CWs planted with by *Cyperus alternifolius* was highest (H=90%) with an initial COD concentration of 250, and lowest (H=56,7%) with an initial COD concentration of 1000 mg/l. The result (H=90%) was higher than previous studies (H=85%) and even in the study that used same vegetation in treatment (H=69.87%). After 3 days, COD concentrations reduced from 750 mg/l to less than 300 mg/l (meeting the national standard for aquacultural wastewater QCVN 62:2016/BTNMT, column B).

The removal rate of COD by *Cyperus alternifolius* in the HSF CWs increased with the increase of COD concentration from 250 up to 750 mg/l, and the COD removal reduced when the COD concentration was 1000 mg/l. The results shown in Fig. 5 also indicated that HSF CWs planted with *Cyperus alternifolius* could remove 19.16 g/m^2.d after 24 h when COD the concentration was 750 g/m^3. The high potential of COD removal could be due to metabolism activities of microorganisms and the role of vegetation [1, 4].

The effects of COD concentration on the growth of *Cyperus alternifolius* in the HSF CWs during the experimental period are shown in Figs. 6 and 7. The height and the number of shoots of *Cyperus alternifolius* was almost unchanged with COD concentrations of 250-750 mg/l, but they strongly decreased when the COD concentration reached 1000 mg/l. Therefore, *Cyperus alternifolius* could tolerate high COD concentrations up to 1000 mg/l. This result was similar to results of [8] with the plant *Phragmites australis*.

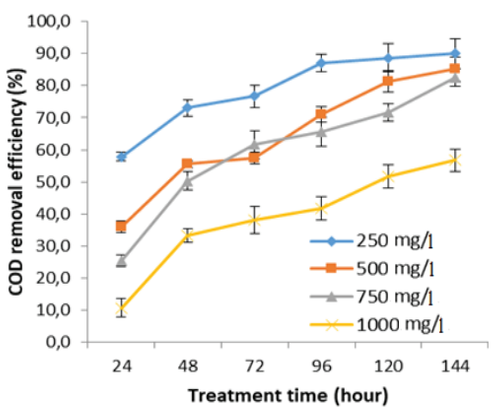

Fig. 4. The treatment efficiency of COD by the HSF CWs planted with *Cyperus alternifolius* during the experiment.

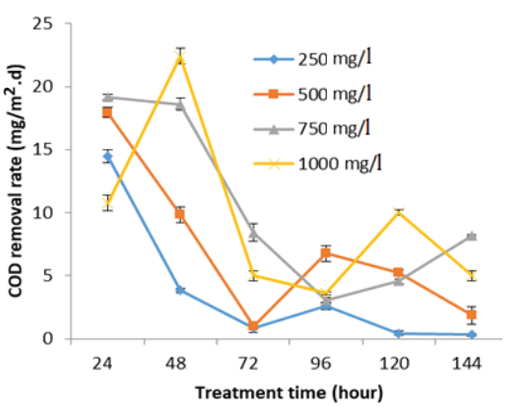

Fig. 5. The removal rate of COD by the HSF CWs planted with *Cyperus alternifolius* during the experiment.

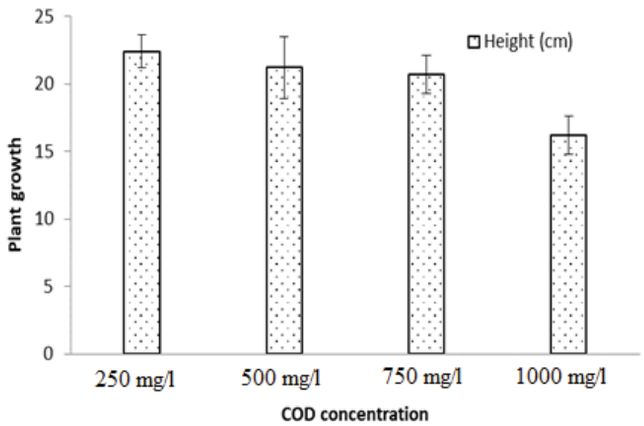

Fig. 6. Effects of COD concentrations on the height of *Cyperus alternifolius* in HSF CW after 7 days.

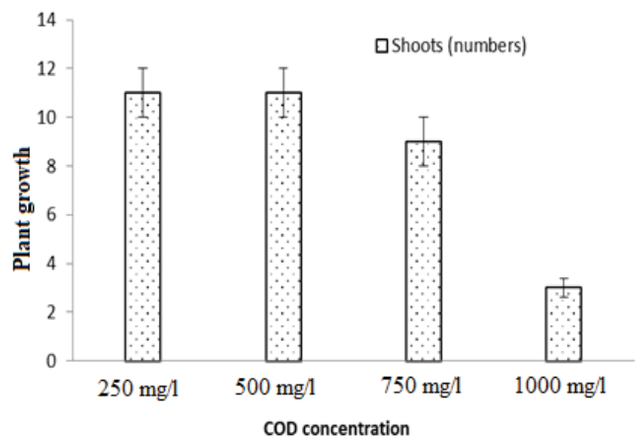

Fig. 7. Effects of COD concentrations on the shoot generation of *Cyperus alternifolius* in HSF CW after 7 days.

3.3. Effect of NH_4^+ on removal rate and wastewater treatment efficiency

In CW-treated wastewaters, vegetation can directly absorb and metabolize nutrients like nitrogen and phosphorus and enhance nutrient transformation processes such as nitrification, denitrification, adsorption, and desorption [3]. The NH_4^+ removal efficiency (%), and NH_4^+ removal rate ($g/m^2.d$) by HSF CWs planted with *Cyperus alternifolius* are shown in Figs. 8 and 9, respectively. In this study, NH_4^+ removal efficiency (%) and NH_4^+ removal rate ($g/m^2.d$) increased with an increase of treatment time. When the NH_4^+ concentrations at the inlet were high, about 75-125 mg/l, and after 7 days of treatment, the NH_4^+ concentrations decreased to only 22.7-86.3 g/l. The NH_4^+ removal efficiencies (%) were 31-69.7%. These results were similar to other studies that reported the removal of NH_4^+-N by CWs planted with *Cyperus papyrus* - about 69.69% [2, 9]. With initial NH_4^+ concentrations of 75-125 mg/l, the NH_4^+ removal rates in this study were 1.22-1.66 g/m^2d after 24 hours and decreased as NH_4^+ concentrations in wastewater decreased over time.

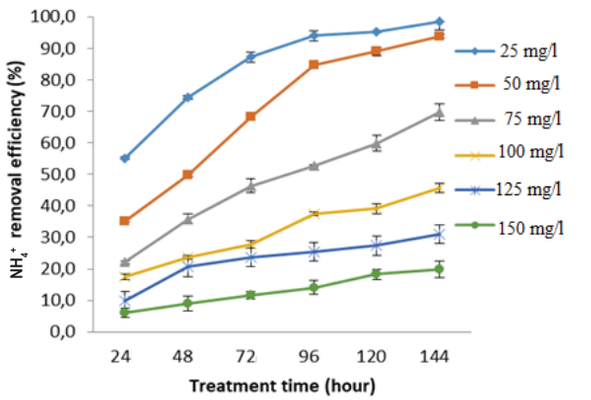

Fig. 8. The NH_4^+ removal efficiency by HSF CWs planted with *Cyperus alternifolius* during the experiment.

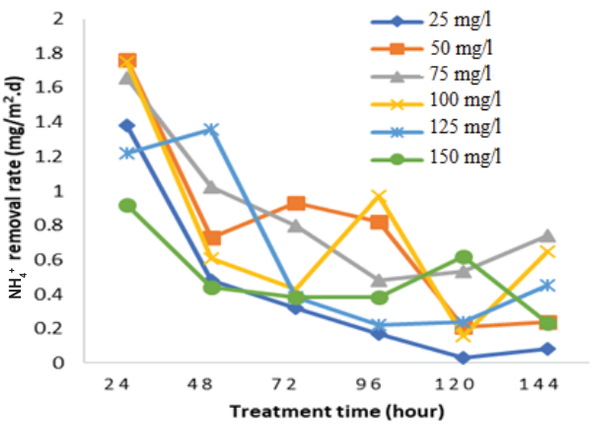

Fig. 9. The NH_4^+ removal rate by HSF CWs planted with *Cyperus alternifolius* during the experiment.

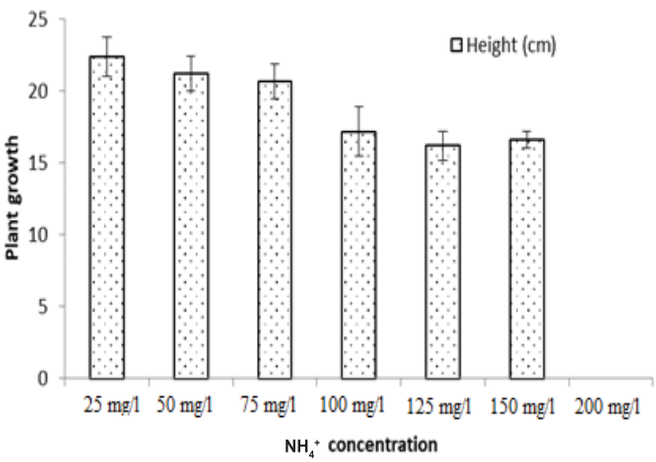

Fig. 10. Effect of NH_4^+ concentration on the height of *Cyperus alternifolius* in HSF CWs after 7 days.

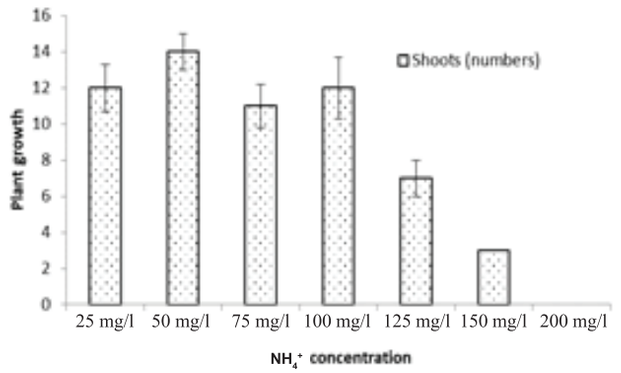

Fig. 11. Effect of NH_4^+ concentration on the shoot generation of *Cyperus alternifolius* in HSF CWs after 7 days.

Plants can directly use ammonium nitrogen (NH_4^+-N) as a nitrogen source in metabolism processes [5]. Nitrogen plays an important role in plant construction and growth. Indeed, nitrogen combines with C, H, and O to make amino acids - blocks of protein - which are elements of protoplasm, enzymes, chlorophyll, and many vitamins [12]. As shown in Figs. 10 and 11, the growth of *Cyperus alternifolius* was affected by NH_4^+ concentration. With an initial NH_4^+ concentration of 25-75 mg/l, plant growth was good with plant heights of 22.4-20.7 cm, and the number of shoots were in the range of 11-14. However, the plant height and capacity of shoot generation decreased with an increase in NH_4^+ concentration. With an initial NH_4^+ concentration of 150 mg/l, several yellow leaves were observed. When NH_4^+ concentration was 200 mg/l, there were some dead plants. High concentrations of NH_4^+ were potentially toxic to *Cyperus alternifolius*'s growth, and therefore could result in their death [13]. The results of this study demonstrated that pH, the concentration of organic matter (COD), and NH_4^+ strongly affected plant growth and the removal efficiency of HSF CW, therefore, considerations for setting up wastewater treatment plants using CWs should carefully take this data into account in practice to ensure treatment performance.

4. Conclusions

This study evaluated the effects of pollutant factors including COD, NH_4^+, and pH on the growth of *Cyperus alternifolius* and the treatment performance of the HSF CW-treated synthetic wastewater. The following concentrations of organic matter (COD: 500-750 mg/l) and NH_4^+ (75-125 mg/l) ensure normal growth of *Cyperus alternifolius* and good treatment performance of the HSF CWs. *Cyperus alternifolius* grew well at pH 6-8, and this plant species could be used as a vegetation element in the HSF CWs due to their ability to endure high concentrations of organic matter (COD: 500-750 mg/l) and NH_4^+ (75-125 mg/l). This study serves as a basis for considering wastewater characteristics in the application of HSF CW systems in practice.

CRediT author statement

Nguyen Thanh Binh: Formal analysis, Data curation, Writing - Original draft; Bui Thi Kim Anh: Conceptualisation, Methodology; Nguyen Van Thanh: Visualisation, Investigation, Software; Dang Dinh Kim: Supervision, Validation; Nguyen Minh Phuong: Writing - Reviewing and Editing.

COMPETING INTERESTS

The authors declare that there is no conflict of interest regarding the publication of this article.

REFERENCES

[1] J.H. Choi, S.P. Seok (2004), "Role of wetland plants as oxygen and water pump into benthic sediments", *Korean J. Limnol.*, **37(4)**, pp.436-447.

[2] F.G. Avila, J.P. Chávez, F.Z. Chimbo, et al. (2019), "Performance of *Phragmites australis* and *Cyperus papyrus* in the treatment of municipal wastewater by vertical flow subsurface constructed wetlands", *International Soil and Water Conservation Research*, **7(3)**, pp.286-296, DOI: 10.1016/j.iswcr.2019.04.001.

[3] K.R. Reddy, W.H. Patrick, C.W. Lindau (1989), "Nitrification-denitrification at the plant root-sediment interface in wetlands", *Limnology and* Oceanography, **34(6)**, pp.1004-1013, DOI: 10.4319/lo.1989.34.6.1004.

[4] N. Pavlineri, N.T. Skoulikidis, V.A. Tsihrintzis (2017), "Constructed floating wetlands: A review of research, design, operation and management aspects, and data meta-analysis", *Chemical Engineering Journal*, **308**, pp.1120-1132, DOI: 10.1016/j.cej.2016.09.140.

[5] H. Wu, J. Zhang, H.H. Ngo, et al. (2015), "A review on the sustainability of constructed wetlands for wastewater treatment: Design and operation", *Bioresource Technology*, **175**, pp.594-601, DOI: 10.1016/j.biortech.2014.10.068.

[6] J. Wu, D. Xu, F. He, et al. (2015), "Comprehensive evaluation of substrates in vertical-flow constructed wetlands for domestic wastewater treatment", *Water Practice Technology*, **10(3)**, pp.625-632, DOI: 10.2166/wpt.2015.077.

[7] O. Shelef, A. Gross, S. Rachmilevitch (2013), "Role of plants in a constructed wetland: Current and new perspectives", *Water*, **5(2)**, pp.405-419, DOI: 10.3390/w5020405.

[8] B.T.K. Anh, N.V. Thanh, P.T. Giang, et al. (2019), "Study on using reed (*Phragmites australis*) and water spinach (*Ipomoea aquatica*) for piggery wastewater treatment after biogas process by constructed wetland", *Journal of Biology*, **41(2se1&2se2)**, pp.327-335, DOI: 10.15625/0866-7160/v41n2se1&2se2.14184.

[9] X. Liu, Y. Zhang, X. Li, et al. (2018), "Effects of influent nitrogen loads on nitrogen and COD removal in horizontal subsurface flow constructed wetlands during different growth periods of *Phragmites australis*", *Sci. Total Environ.*, **635**, pp.1360-1366, DOI: 10.1016/j.scitotenv.2018.03.260.

[10] S.K.M. Sa'at, N.Q. Zaman (2017), "Suitability of *Ipomoea aquatica* for the treatment of effluent from palm oil mill", *Journal of Built Environment Technology and Engineering*, **2**, pp.39-44.

[11] B.T.K. Anh (2016), "Study on the combined system using limestone and constructed wetland to remove manganese, zinc and iron from coal mining drainage", *VNU Journal of Science: Earth and Environmental Sciences*, **32(1S)**, pp.9-14.

[12] J.A. Silva, R.S. Uchida (2000), *Plant Nutrient Management in Hawaii's Soils, Approaches for Tropical and Subtropical Agriculture*, College of Tropical Agriculture and Human Resources, University of Hawaii at Manoa, 158pp.

[13] R.M. Gersberci, B.V. Elkins, S.R. Lyon, et al. (1986), "Role of aquatic plants in wastewater treatment by artificial wetlands", *Wat. Res.*, **20(3)**, pp.363-368, DOI: 10.1016/0043-1354(86)90085-0.

DOI: 10.31276/VJSTE.65(2).47-53

Screening *in silico* the human epidermal growth factor receptor-2 inhibitory effect of isoflavones by molecular docking method for their potential use in breast cancer

Dinh Xuan Ton Tai[1], Le Thi Huong[1], Tran Hoang Mai[1], Vu Manh Hung[2], Nguyen Thi Huyen[1], Bui Thanh Tung[1*]

[1]*Department of Pharmacology, University of Medicine and Pharmacy, Vietnam National University-Hanoi, 144 Xuan Thuy Street, Dich Vong Hau Ward, Cau Giay District, Hanoi, Vietnam*

[2]*Military Medical University, 160 Phung Hung Street, Phuc La Ward, Ha Dong District, Hanoi, Vietnam*

Received 9 August 2022; revised 20 October 2022; accepted 4 November 2022

Abstract:

Isoflavones are secondary phenolic metabolites found in most legumes. These compounds have important pharmacological significance such as anti-osteoporosis, anti-aging, and anti-cancer properties. Breast cancer is one of the most common cancers in women worldwide. Human epidermal growth factor receptor-2 (HER2) is an important target in breast cancer treatment. In this study, we evaluated the ability of sixty isoflavones compounds to inhibit the HER2 enzyme for their potential use in breast cancer treatments by the molecular docking method. Molecular docking was done by Autodock vina software. Lipinski 5 rule is used to compare compounds with drug-like and non-drug-like properties. Pharmacokinetic parameters of potential compounds were evaluated using the pkCSM tool. Our results showed that 35 compounds inhibited HER2 stronger than the positive control. Next, we analysed the drug-likeness according to Lipinski's rule of five and predicted pharmacokinetic-toxicological parameters of these 35 compounds. We obtained two compounds, genistein and biochanin A, which could become promising drugs for breast cancer treatment. However, *in vitro* and *in vivo* studies on the inhibition of the HER2 enzyme need to be conducted.

Keywords: **biochanin A, breast cancer, genistein, HER2, isoflavone, molecular docking.**

Classification number: **3.3**

1. Introduction

Cancer is one of the leading causes of death globally, accounting for nearly 10 million deaths in 2020 of which breast cancer accounted for 2.3 million cases [1]. Breast cancer is considered the leading cause of cancer death in women [2]. In Vietnam, according to statistics from the World Health Organization, there were about 21,555 cases of breast cancer in both sexes and all ages (11.8% of cancer cases) reported in 2020 [1].

Human epithelial growth factor (EGF) receptor type 2 (HER2) is one of the EGF receptor family members. HER2 was first discovered in mice in 1984 by Weinberg's group and was thought to play an important role in the development of breast cancer [3]. HER2 is present at high levels in about 30% of breast cancer cases [4]. HER2 gene overexpression is activated primarily through gene amplification. This leads to the activation of HER2 signalling networks such as MAPK (RAS-RAF-MEK-ERK) and phosphatidylinositol 3-kinase pathways (PI3K) (PI3K-AKT-mTOR) to induce to cell proliferation, angiogenesis, and control of tumour growth [5]. Therefore, HER2 is a specific and promising target for breast cancer treatment.

Isoflavones are a subclass of flavonoids with the diphenylpropane structure (C6-C3-C6). Isoflavones are found in many different plant species such as the *Leguminosae* family, especially *Glycine max* L. and *Trifolium pratense* L. [6]. The tumour inhibitor function of isoflavones has been demonstrated in breast cancer cell lines and animal models [7, 8]. Isoflavones also have other pharmacological effects such as protease inhibition, tyrosine kinase inhibition, and anti-angiogenesis [9]. Studies of soy-based diets revealed soy use significantly decreased total cholesterol, LDL cholesterol, and triglyceride levels [10].

Molecular docking is a modelling technique used to study the binding ability and position of a protein to another structure or small molecule. Molecular docking is one of the most popular methods in structure-based drug design because of its high accuracy in predicting the structure of small molecule ligands in suitable target binding sites [11].

*Corresponding author: Email: tungbt.ump@vnu.edu.vn

2. Materials and methods

2.1. Model docking

Preparation of protein structures: The crystal structure of the enzyme HER2 (ID: 3PP0) was retrieved from the Protein Data Bank RCSB (https://www.rcsb.org/) [12]. The 3PP0 complex contains the co-crystal ligand 2-{2-[4-({5-chloro-6-[3-(trifluoromethyl)phenoxy]pyridin-3-yl}amino)-5Hpyrrolo[3,2-d]pyrimidin-5 yl]ethoxy}ethanol (ID: 03Q).

We removed water molecules and co-crystals ligands from the protein molecule by using Discovery Studio software. Next, we used MGL Autodock Tools 1.5.6 software to add hydrogen atoms, optimise polar hydrogens, and Kollman charges. The active region of the protein was determined in a grid box size of 30x30x30 Å with the grid centre (x,y,z) corresponding to (34, 46, -12) [13]. This protein was saved in PDBQT format to prepare for the docking program.

Preparation of ligands: Based on previous publications, 60 isoflavones have been identified with the ability to inhibit HER2 [14-21]. The structures compounds were downloaded from the PubChem database (https://pubchem.ncbi.nlm.nih.gov/) in SDF format. Then, we converted them to PDB format using Chimera software [22, 23]. Finally, the ligands were optimised by Avogadro software using the conjugate gradients method and converted to PDBQT format using Autodock Tools 1.5.6 [24, 25].

Performance of molecular docking: We began molecular docking enzyme HER2 with isoflavones by using Autodock Tools software. The positive control trastuzumab was downloaded from the PubChem database. Trastuzumab is one of the Food and Drug Administration's (FDA) approved antineoplastic agents for the treatment of HER2-positive breast cancer [26-28]. The docking scores of trastuzumab were used as the positive control for selecting compounds with HER2 inhibitory effects.

Evaluation of docking results: To evaluate the docking results, the co-crystal ligand, after being separated from the protein, was redocked to the active site of the target. The process was performed successfully if the root-mean-square deviation (RMSD) value was less than or equal to 1.5 Å [29]. For substances that need docking, their binding ability is assessed through interaction with amino acids and its interaction energy is calculated by the scoring function of Autodock vina. If the chosen compound had a docking score lower than the positive control trastuzumab, then it was evaluated by Lipinski's rule of five and pharmacokinetic - toxicological (ADMET) parameters.

2.2. Evaluation Lipinski's rule of five

Lipinski's rule of five is used to study drug-like and non-drug-like molecules to evaluate a potential molecular to become a therapeutic drug [30]. We used the online tool (http://www.scfbio-iitd.res.in/software/drugdesign/lipinski.jsp) to evaluate Lipinski's rule of five. After selecting the drug-like compounds, we continued to analyse the pharmacokinetic and toxicological parameters to provide the final results.

2.3. Prediction of ADMET by computational analysis

We use the online tool pkCSM (http://biosig.unimelb.edu.au/pkcsm/prediction) to predict the pharmacokinetic and toxicological properties of the compounds as input data SMILES formulas [31]. Predictive results of ADMET parameters including absorption, distribution, metabolism, elimination, and toxicity of potential compounds were analysed.

3. Results

3.1. Evaluation of the docking model

Before screening the compounds, the co-crystal ligand was re-docked to the active site of the target to determine the root mean square deviation (RMSD), which helps to evaluate the suitability of the docking parameters. To evaluate the similarity structural, we determined the RMSD value by Chimera software. We obtained the structural overlap of the co-crystal ligand before and after docking with the RMSD value of 1.076<1.5 Å, which will demonstrate that the results of molecular docking on the target were reliable (Fig. 1). Fig. 2 shows the 2D interaction between the co-crystal ligand and HER2 protein.

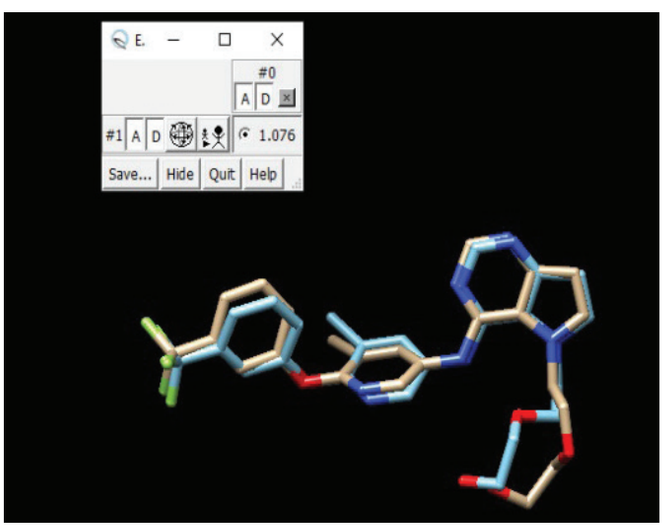

Fig. 1. Co-crystallised ligand re-dock results of HER2.

The results showed that the co-crystallised ligand has a binding bond with many important amino acids such as LYS753, VAL734, ALA751, GLN799, MET801, LEU852, LEU726, PHE1004, GLU770, MET774, LEU785, and LEU796 in its active site.

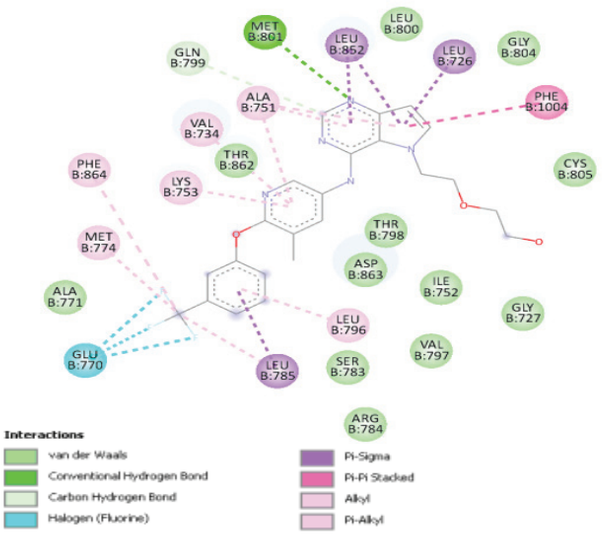

Fig. 2. 2D representation of the interaction of co-crystallised ligand with HER2.

3.2. Molecular docking of compounds to the target protein

After preparing the ligand, we docked sixty isoflavone compounds to screen for HER2 inhibitory activity. Our results obtained 35 compounds that had negative docking scores (ΔG) smaller than the positive control trastuzumab (ΔG=-9.4 kcal/mol), which are shown in Table 1.

Table 1. The docking results of the 35 most potent natural and reference compounds.

No.	Name	Docking score with HER2 (kcal/mol)	No.	Name	Docking score with HER2 (kcal/mol)
1	Genistein	-9.5	19	Daidzein-4,7-diglucoside	-10.4
2	Genistin	-10.4	20	Isoflavone glycoside	-10.3
3	Daidzin	-10.1	21	Alpinum isoflavone	-10.9
4	Malonylgenistin	-10	22	Angustone C	-10.7
5	Biochanin A	-9.7	23	Isolupalbigenin	-10.1
6	Puerarin	-9.5	24	Licoisoflavone A	-9.9
7	Pueraria glycoside	-9.7	25	Licoisoflavone B	-10.2
8	Ononin	-10.4	26	Quercimeritrin	-9.6
9	6”-O-Acetylgenistin	-10.5	27	Angustone A	-10.5
10	6”-O-Acetyldaidzin	-10.2	28	Kraussianone 3	-10.4
11	Sissotrin	-10.5	29	Neobavaisoflavone	-10
12	Prunetin	-9.7	30	Isoderrone	-11.3
13	Sophoricoside	-10.7	31	Chandalone	-11.3
14	Erypoegin K	-10.6	32	Methylgenistein	-9.9
15	Biochanin A 7-O-β-D-glucoside 6”-O-malonate	-9.6	33	6”-O-malonylononin	-10.9
16	Mirificin	-9.8	34	Dihydroisoderrondiol	-11.3
17	3’-Methoxypuerarin	-9.6	35	Ficuisoflavone	-10.9
18	Puerarin 4’-O-glucoside	-10.2		**Trastuzumab**	**-9.4**

The positive control trastuzumab is the first HER2-targeted therapeutic agent to be approved by the FDA for the treatment of breast cancer and metastatic breast cancer [31, 32]. Trastuzumab binds to HER2 and inhibits HER2-mediated malignant transformation (Fig. 3). Trastuzumab has a negative docking score of -9.4 (kcal/mol) and a hydrogen bond with amino acid GLY732; a π - σ bond with LEU852; and a π - alkyl bond with PHE1004, ALA751, and LEU726 to the active site. Currently, trastuzumab is the most common treatment for breast cancer. Many studies have shown that the combination of trastuzumab with substances such as pertuzumab, vinorelbine, capecitabine, and docetaxel in the treatment of HER2-positive advanced breast cancer gives more effective results than when used alone [33].

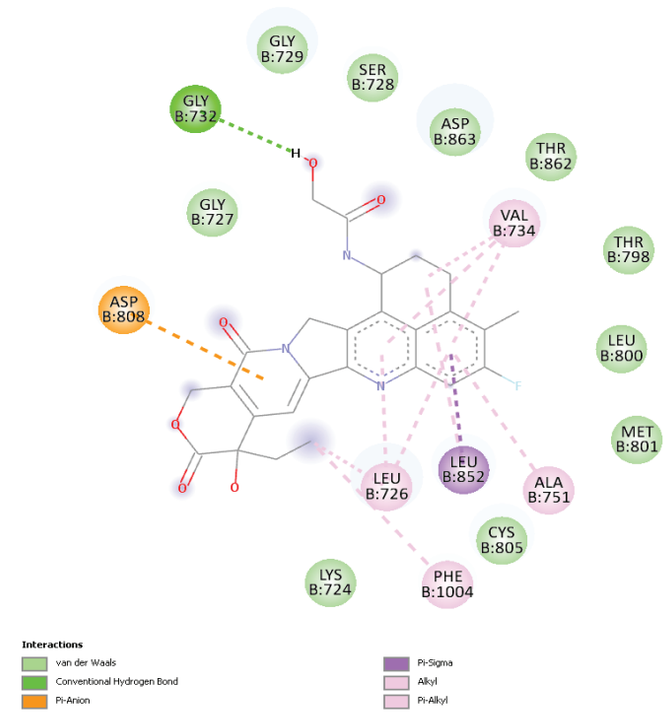

Fig. 3. Interaction between trastuzumab and HER2.

3.3. Lipinski’s rule of five

Compounds are considered to be “drug-like” when they satisfy more than 2 of the 5 criteria of Lipinski’s rule of five: molecular weight (MW) <500 Da; high lipophilicity (logP does not exceed 5); no more than 5 donors of hydrogen bonding (HBD); no more than 10 acceptors of hydrogen bonds (HBA1); and a molar refractivity (MR) between 40-130. Table 2 shows the results of 20 compounds that satisfied more than 2 criteria of Lipinski’s rule of five. Next, these compounds were further predicted as ADMET.

Table 2. The results of 20 compounds that satisfied the evaluation Lipinski's rule of five.

No.	Name	MW	HBD	HBA1	Log P	MR	Drug-likeness
1	Genistein	270.0	3	5	2.42	70.81	Yes
2	Daidzin	416.0	5	9	0.187	101.88	Yes
3	Biochanin A	284.0	2	5	2.723	75.701	Yes
4	Puerarin	416.0	6	9	0.229	101.87	Yes
5	Ononin	430.0	4	9	0.4901	106.77	Yes
6	6"-O-Acetyldaidzin	458.0	4	10	0.758	111.43	Yes
7	Prunetin	284.0	2	5	2.723	75.701	Yes
8	Erypoegin K	354.0	3	6	2.788	93.57	Yes
9	Alpinum isoflavone	336.0	2	5	3.898	92.89	Yes
10	Angustone C	420.0	3	6	5.113	117.69	Yes
11	Isolupalbigenin	406.0	3	5	5.437	117.084	Yes
12	Licoisoflavone A	354.0	4	6	3.634	95.61	Yes
13	Licoisoflavone B	352.0	3	6	3.6038	94.55	Yes
14	Angustone A	422.0	4	6	5.143	118.75	Yes
15	Kraussianone 3	438.0	4	7	4.3073	119.17	Yes
16	Neobavaisoflavone	312.0	5	6	-0.0531	77.146	Yes
17	Isoderrone	336.0	2	5	3.898	92.89	Yes
18	Chandalone	404.0	2	5	5.4069	116.025	Yes
19	Dihydroisoderrondiol	370.0	4	7	2.279	94.82	Yes
20	Ficuisoflavone	354.0	3	6	2.788	93.57	Yes

3.4. Prediction of ADMET profile

The interaction between pharmacokinetics, toxicity, and potency are crucial for effective drugs. The pharmacokinetic profile of a compound defines its ADMET properties. After analysing the twenty above compounds, we obtained two compounds with the best prediction of ADMET and toxicity properties including genistein and biochanin A, which are presented in Table 3.

Table 3. Pharmacokinetic and toxicological prediction results.

Properties		Genistein	Biochanin A
Absorption	Caco2 (logPapp in 10^{-6} cm/s)	0.9	0.897
	Intestinal absorption human (% HIA)	93.387	93.028
Distribution	VDss (log l/kg)	0.094	-0.341
	BBB (logBBB)	-0.71	-0.221
	CNS (logPS)	-2.048	-2.115
Metabolism	CYP2D6 inhibitor	No	No
	CYP3A4 inhibitor	Yes	No
Excretion	Total clearance (log ml/min/kg)	0.151	0.247
	Renal OCT2 substrate	No	No
Toxicity	AMES	No	No
	hERG	No	No
	Oral rat acute toxicity (LD_{50})	2.268	1.851
	Hepatotoxicity	No	No
	Skin sensitisation	No	No

The first property is the absorption process using human intestinal absorption (HIA) and human colon adenocarcinoma-2 cell line (Caco2), which are two important parameters that determine the absorption of a drug. A compound has high Caco2 permeability if it has logPapp >0.9 [34]. Table 3 shows that both compounds have good membrane permeability with genistein at 0.9 and biochanin A at 0.897. All compounds have good intestinal absorption (HIA>80%).

Next is the distribution process. Compounds are considered to be well distributed to tissues if logVDss>0.45 and poorly distributed if logVDss<-0.15 [34]. In Table 3, genistein and biochanin A both have a poor volume of distribution to tissues. In addition, two parameters of permeability across the blood-brain barrier (BBB) and central nervous system (CNS) are also important when evaluating the neurologic safety of the drug. The compound can penetrate the BBB if logBBB>0.3 and the corresponding CNS with values are less than -2 [35, 36]. Calculated results show that both compounds failed to enter the BBB, with little to complete failure to enter the CNS.

Cytochrome P450 enzymes are essential for the metabolism of many compounds in the liver. The two most significant enzymes of cytochrome P450 are CYP3A4 and CYP2D6. Both studied compounds are not inhibitors of CYP2D6. Genistein showed the ability to inhibit CYP3A4. Therefore, the bioavailability of substances metabolized by the CYP3A4 enzyme may be increased if used together with genistein.

Regarding elimination, we predicted total clearance and renal organic cation transporter 2 (OCT2) substrate activity. OCT2 plays an important role in the uptake of organic cations across the basolateral membrane and is considered a major transporter in the active secretion of organic cations in the kidney. Both compounds are not OCT2 substrates. The total clearance values were 0.151 and 0.247 (log ml/min/kg) for genistein and biochanin A, respectively. The toxicity prediction results demonstrated that both compounds are non-mutagenic (AMES), non-hepatotoxic, non-cardiotoxic, and have no skin toxicity.

The interaction between the two compounds with HER2 is shown in 2D by Discovery Studio Visualizer 4.0 in Figs. 4 and 5.

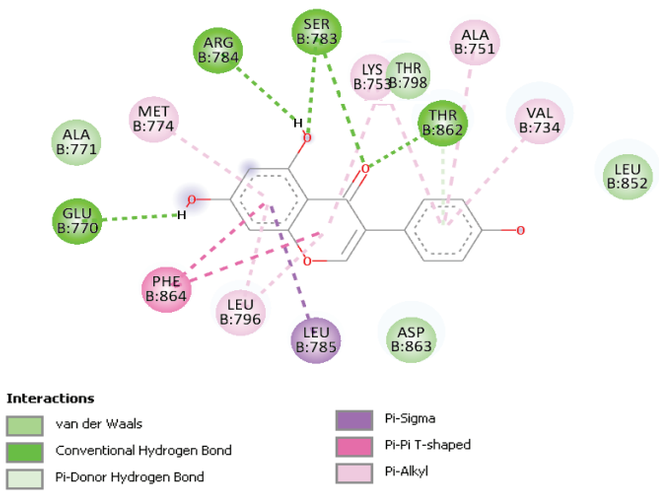

Fig. 4. 2D Interaction between genistein and HER2.

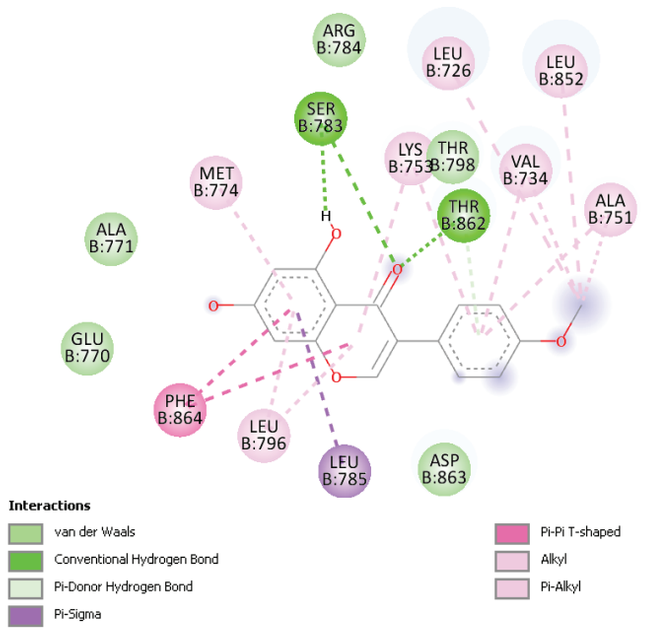

Fig. 5. 2D interaction between biochanin A and HER2.

Figure 4 shows that genistein interacts with essential amino acids by π-alkyl bonds with LYS753, VAL734, ALA751, LEU796, and MET774; by π-σ bond with LEU785; and van der Waals with ASP863 and LEU852. Similarly, biochanin A also has π-alkyl or alkyl bonds with LYS753, VAL734, ALA751, LEU852, LEU726, MET774, and LEU796; π-σ bond with LEU785; and van der Waals with ASP863 and GLU770. Both compounds showed similarity in binding to the co-crystallised ligand of the HER2 enzyme crystal. These are also important amino acids in the active region of the HER2 enzyme. The identification of good binding with amino acids at the active site is an important step and targeting this site can inhibit the activity of 3 PP0.

The results of the docking score values showed that the two compounds have good ΔG energy values: genistein with -9.5 kcal/mol and biochanin A with -9.7 kcal/mol. The energy difference between these two isoflavones is consistent because biochanin A is strongly bound to more important amino acids at the active site. Therefore, it can be confirmed that both of these isoflavones compounds can interact well with the HER2 enzyme.

4. Discussion

In this study, we conducted virtual screening of sixty isoflavones compounds downloaded from the PubChem database. From these results we obtained twenty compounds that satisfy the criteria for an oral drug, and two promising compounds that could be developed into drugs due to their good pharmacokinetic parameters as well as low toxicity: genistein and biochanin A.

Genistein (4',5,7-Trihydroxyisoflavone) is an isoflavone abundantly found in soybeans and other legumes. Other foods that have been shown to contain genistein consist of alfalfa, broccoli, clover sprouts, cauliflower, and sunflower seeds [37]. The compound genistein is believed to be a potent tyrosine kinase inhibitor, cell proliferation inhibition, and differentiates cancer cells [38]. Previous studies have shown that genistein at concentrations ≥1 μM inhibited HER2 protein expression and phosphorylation through an ER-independent mechanism. In the presence of ERa, genistein mimicked E2 and inhibited HER2 protein phosphorylation [39]. Genistein was a potent growth inhibitor in both MCF-7 cells (IC_{50} values of 10.5 ug/ml) and MDA-468 cells (IC_{50} values of 6.5 pig/ml) [40]. According to another study, a high soy diet containing up to 45 mg of genistein per day that could help reduce cancer risk [41].

Biochanin (5,7-Dihydroxy-4'-methoxyisoflavone) is a member of the 7-hydroxyisoflavone group substituted by an additional hydroxyl group at the 5 position and a methoxy group at the 4' position. Biochanin A is a natural isoflavone found in many species of clover (*Trifolium pratense*), especially red clover, and in many herbal supplements. In addition, it is also present in other crops such as soybeans, alfalfa, peanuts, and chickpeas [42, 43]. It was found that biochanin A selectively targets HER-2-positive SK-BR-3 breast cancer cells without affecting normal breast epithelial cells (Michigan Cancer Foundation [MCF]-10A)

[44]. Another reported research has proved that biochanin A displays the best potency towards cancerous breast cells with an IC_{50} of 0.32 µM [45]. In HER2-positive breast cancer, biochanin A was shown to inhibit cell survival, signalling pathways, invasive enzyme expression, and activity in SK-BR-3 cancer cells when they were treated with biochanin A (2-100 µM) and incubated for 72 hours at 37°C [44, 46]. Apart from breast cancer, this compound has also been shown to play a potential role in prostate cancer cells, pancreatic cancer cells, and melanoma cancer cells [44]. Therefore, biochanin A is a good candidate for further research and improvement of the properties of this compound.

5. Conclusions

In conclusion, from sixty isoflavone compounds, we found two highly promising natural HER2 inhibitor compounds that satisfy the criteria of Lipinski's rule of five and ADMET, genistein and biochanin A, with good pharmacokinetic parameters, low toxicity, low hepatotoxicity, and excreted by the kidneys. However, further *in vitro* and *in vivo* studies are needed to evaluate these two potential compounds as breast cancer drugs.

CRediT author statement

Dinh Xuan Ton Tai: Experiment, Writing - Original draft preparation; Le Thi Huong: Experiment, Writing - Original draft preparation; Tran Hoang Mai: Experiment, Writing - Original draft preparation; Vu Manh Hung: Data curation, Validation; Nguyen Thi Huyen: Conceptualisation, Writing - Reviewing and Editing; Bui Thanh Tung: Conceptualization, Methodology, Supervision, Reviewing and Editing.

COMPETING INTERESTS

The authors declare that there is no conflict of interest regarding the publication of this article.

REFERENCES

[1] H. Sung, J. Ferlay, R.L. Siegel, et al. (2021), "Global cancer statistics 2020: GLOBOCAN estimates of incidence and mortality worldwide for 36 cancers in 185 countries", *CA: A Cancer Journal for Clinicians*, **71(3)**, pp.209-249, DOI: 10.3322/caac.21660.

[2] C.E. DeSantis, J. Ma, A.G. Sauer, et al. (2017), "Breast cancer statistics, 2017, racial disparity in mortality by state", *CA: A Cancer Journal for Clinicians*, **67(6)**, pp.439-448, DOI: 10.3322/caac.21412.

[3] A. Schechter, D. Stern, L. Vaidyanathan, et al. (1984), "The *neu* oncogene: An *erb-B*-related gene encoding a 185,000-Mr tumour antigen", *Nature*, **312**, pp.513-516, DOI: 10.1038/312513a0.

[4] D.J. Slamon, G.M. Clark, S.G. Wong, et al. (1987), "Human breast cancer: Correlation of relapse and survival with amplification of the HER-2/*neu* oncogene", *Science*, **235(4785)**, pp.177-182, DOI: 10.1126/science.3798106.

[5] C.N. Prabhakar (2015), "Epidermal growth factor receptor in non-small cell lung cancer", *Translational Lung Cancer Research*, **4(2)**, pp.110-118, DOI: 10.3978/j.issn.2218-6751.2015.01.01.

[6] E. Miadoková (2009), "Isoflavonoids - An overview of their biological activities and potential health benefits", *Interdisciplinary Toxicology*, **2(4)**, pp.211-218, DOI: 10.2478/v10102-009-0021-3.

[7] J. Iqbal, B.A. Abbasi, A.T. Khalil, et al. (2018), "Dietary isoflavones, the modulator of breast carcinogenesis: Current landscape and future perspectives", *Asian Pacific Journal of Tropical Medicine*, **11(3)**, pp.186-193, DOI: 10.4103/1995-7645.228432.

[8] H. Mizunuma, K. Kanazawa, S. Ogura, et al. (2002), "Anticarcinogenic effects of isoflavones may be mediated by genistein in mouse mammary tumour virus-induced breast cancer", *Oncology*, **62(1)**, pp.78-84, DOI: 10.1159/000048250.

[9] O. Ganry (2002), "Phytoestrogen and breast cancer prevention", *European Journal of Cancer Prevention*, **11(6)**, pp.519-522, DOI: 10.1097/00008469-200212000-00002.

[10] A. Vincent, L.A. Fitzpatrick (2000), "Soy isoflavones: Are they useful in menopause?", *Mayo Clinic Proceedings*, **75(11)**, pp.1174-1184, DOI: 10.4065/75.11.1174.

[11] L.G. Ferreira, R.N.D. Santos, G. Oliva, et al. (2015), "Molecular docking and structure-based drug design strategies", *Molecules*, **20(7)**, pp.13384-13421, DOI: 10.3390/molecules200713384.

[12] K. Aertgeerts, R. Skene, J. Yano, et al. (2011), "Structural analysis of the mechanism of inhibition and allosteric activation of the kinase domain of HER2 protein", *Journal of Biological Chemistry*, **286(21)**, pp.18756-18765, DOI: 10.1074/jbc.M110.206193.

[13] N.B. Kim, N.T. Thuy, P.H. Minh, et al. (2021), "Screening bioactive compounds from allium sativum as HER2 inhibitors targeting breast cancer by docking methods", *VNU Journal of Science: Medical and Pharmaceutical Sciences*, **37(1)**, pp.35-47, DOI: 10.25073/2588-1132/vnumps.4295.

[14] T.T. Zhao, F. Jin, J.G. Li, et al. (2019), "Dietary isoflavones or isoflavone-rich food intake and breast cancer risk: A meta-analysis of prospective cohort studies", *Clinical Nutrition*, **38(1)**, pp.136-145, DOI: 10.1016/j.clnu.2017.12.006.

[15] S.E. Kim, K. Kawaguchi, H. Hayashi, et al. (2019), "Remission effects of dietary soybean isoflavones on DSS-induced murine colitis and an LPS-activated macrophage cell line", *Nutrients*, **11(8)**, DOI: 10.3390/nu11081746.

[16] C. Wu, J. Shen, P. He, et al. (2012), "The α-glucosidase inhibiting isoflavones isolated from *Belamcanda chinensis* leaf extract", *Rec. Nat. Prod.*, **6(2)**, pp.110-120.

[17] L.W. Qi, Q.T. Yu, P. Li, et al. (2006), "Quality evaluation of *Radix astragali* through a simultaneous determination of six major active isoflavonoids and four main saponins by high-performance liquid chromatography coupled with diode array and evaporative light scattering detectors", *Journal of Chromatography A*, **1134(1-2)**, pp.162-169, DOI: 10.1016/j.chroma.2006.08.085.

[18] H.B. Xiao, M. Krucker, K. Albert, et al. (2004), "Determination and identification of isoflavonoids in *Radix astragali* by matrix solid-phase dispersion extraction and high-performance liquid chromatography with photodiode array and mass spectrometric detection", *Journal of Chromatography A*, **1032(1-2)**, pp.117-124, DOI: 10.1016/j.chroma.2003.09.032.

[19] T. Blicharski, A. Oniszczuk (2017), "Extraction methods for the isolation of isoflavonoids from plant material", *Open Chemistry*, **15(1)**, pp.34-45, DOI: 10.1515/chem-2017-0005.

[20] J. Bórquez, E.J. Kennelly, M.J. Simirgiotis (2013), "Activity guided isolation of isoflavones and hyphenated HPLC-PDA-ESI- ToF-MS metabolome profiling of *Azorella madreporica* Clos. from northern Chile", *Food Research International*, **52(1)**, pp.288-297, DOI: 10.1016/j.foodres.2013.02.055.

[21] L. Pistelli, I. Giachi, D. Potenza, et al. (2000), "A new isoflavone from *Genista corsica*", *Journal of Natural Products*, **63(4)**, pp.504-506, DOI: 10.1021/np990282k.

[22] S. Kim, J. Chen, T. Cheng, et al. (2021), "PubChem in 2021: New data content and improved web interfaces", *Nucleic Acids Research*, **49(D1)**, pp.D1388-D1395, DOI: 10.1093/nar/gkaa971.

[23] E.F. Pettersen, T.D. Goddard, C.C. Huang, et al. (2004), "UCSF Chimera - A visualization system for exploratory research and analysis", *Journal of Computational Chemistry*, **25(13)**, pp.1605-1612, DOI: 10.1002/jcc.20084.

[24] G.M. Morris, R. Huey, W. Lindstrom, et al. (2009), "AutoDock4 and AutoDockTools4: Automated docking with selective receptor flexibility", *Journal of Computational Chemistry*, **30(16)**, pp.2785-2791, DOI: 10.1002/jcc.21256.

[25] M.D. Hanwell, D.E. Curtis, D.C. Lonie, et al. (2012), "Avogadro: An advanced semantic chemical editor, visualization, and analysis platform", *Journal of Cheminformatics*, **4(1)**, pp.1-17.

[26] L. Moja, L. Tagliabue, S. Balduzzi, et al. (2012), "Trastuzumab containing regimens for early breast cancer", *Cochrane Database of Systematic Reviews*, **12(4)**, DOI: 10.1002/14651858.CD006243.pub2.

[27] M. Shah, M.R. Nunes, V. Stearns (2018), "CDK4/6 inhibitors: Game changers in the management of hormone receptor-positive advanced breast cancer?", *Oncology (Williston Park, NY)*, **32(5)**, pp.216-222.

[25] M.D. Hanwell, D.E. Curtis, D.C. Lonie, et al. (2012), "Avogadro: An advanced semantic chemical editor, visualization, and analysis platform", *Journal of Cheminformatics*, **4(1)**, pp.1-17, DOI: 10.1186/1758-2946-4-17.

[28] A. Lee (2020), "Tucatinib: First approval", *Drugs*, **80(10)**, pp.1033-1038, DOI: 10.1007/s40265-020-01340-w.

[29] H. Gohlke, M. Hendlich, G. Klebe (2000), "Knowledge- based scoring function to predict protein-ligand interactions", *Journal of Molecular Biology*, **295(2)**, pp.337-356, DOI: 10.1006/jmbi.1999.3371.

[30] C.A. Lipinski (2004), "Lead-and drug-like compounds: The rule-of-five revolution", *Drug Discovery Today: Technologies*, **1(4)**, pp.337-341, DOI: 10.1016/j.ddtec.2004.11.007.

[31] R. Nahta (2012), "Molecular mechanisms of trastuzumab-based treatment in HER2-overexpressing breast cancer", *International Scholarly Research Notices*, **2012(4)**, DOI: 10.5402/2012/428062.

[32] A.M. Feldman, B.H. Lorell, S.E. Reis (2000), "Trastuzumab in the treatment of metastatic breast cancer: Anticancer therapy versus cardiotoxicity", *Circulation*, **102(3)**, pp.272-274, DOI: 10.1161/01.cir.102.3.272.

[33] S. Ahmed, A. Sami, J. Xiang (2015), "HER2-directed therapy: Current treatment options for HER2-positive breast cancer", *Breast Cancer*, **22(2)**, pp.101-116, DOI: 10.1007/s12282-015-0587-x.

[34] D.E. Pires, T.L. Blundell, D.B. Ascher (2015), "PkCSM: Predicting small-molecule pharmacokinetic and toxicity properties using graph-based signatures", *Journal of Medicinal Chemistry*, **58(9)**, pp.4066-4072, DOI: 10.1021/acs.jmedchem.5b00104.

[35] N.T. Tien, B.T. Thanh (2018), "Predicting binding modes and affinities for non-nucleoside inhibitors to HIV-1 reverse transcriptase using molecular docking", *VNUHCM Journal of Natural Sciences*, **2(1)**, pp.53-58, DOI: 10.32508/stdjns.v2i1.674.

[36] B.T. Tung, P.H. Minh, N.N. Son, et al. (2020), "Screening virtual ACE2 enzyme inhibitory activity of compounds for COVID-19 treatment based on molecular docking", *VNU Journal of Science: Medical and Pharmaceutical Sciences*, **36(4)**, DOI: 10.25073/2588-1132/vnumps.4281.

[37] N. Jaiswal, J. Akhtar, S.P. Singh, et al. (2019), "An overview on genistein and its various formulations", *Drug Research*, **69(6)**, pp.305-313, DOI: 10.1055/a-0797-3657.

[38] A. Constantinou, E. Huberman (1995), "Genistein as an inducer of tumour cell differentiation: Possible mechanisms of action", *Proceedings of The Society for Experimental Biology and Medicine*, **208(1)**, pp.109-115, DOI: 10.3181/00379727-208-43841.

[39] M.S. Sakla, N.S. Shenouda, P.J. Ansell, et al. (2007), "Genistein affects HER2 protein concentration, activation, and promoter regulation in BT-474 human breast cancer cells", *Endocrine*, **32(1)**, pp.69-78, DOI: 10.1007/s12020-007-9006-1.

[40] G. Peterson, S. Barnes (1991), "Genistein inhibition of the growth of human breast cancer cells: Independence from estrogen receptors and the multi-drug resistance gene", *Biochemical and Biophysical Research Communications*, **179(1)**, pp.661-667, DOI: 10.1016/0006-291x(91)91423-a.

[41] R.A. Dixon, D. Ferreira (2002), "Genistein", *Phytochemistry*, **60(3)**, pp.205-211, DOI: 10.1016/S0031-9422(02)00116-4.

[42] M. Mahmoud, M.R.A. Abdollah, M.E. Elsesy, et al. (2022), "The natural isoflavone Biochanin-A synergizes 5-fluorouracil anticancer activity *in vitro* and *in vivo* in Ehrlich solid-phase carcinoma model", *Phytotherapy Research*, **36(3)**, pp.1310-1325, DOI: 10.1002/ptr.7388.

[43] A. Sundaresan, T. Radhiga, B. Deivasigamani (2018), "Biological activity of biochanin A: A review", *Asian Journal of Pharmacy and Pharmacology*, **4(1)**, pp.1-5, DOI: 10.31024/ajpp.2018.4.1.1.

[44] V. Sehdev, J.C.K. Lai, A. Bhushan (2009), "Biochanin A modulates cell viability, invasion, and growth promoting signaling pathways in HER-2-positive breast cancer cells", *Journal of Oncology*, **2009**, DOI: 10.1155/2009/121458.

[45] A. Sarfraz, M. Javeed, M.A. Shah, et al. (2020), "Biochanin A: A novel bioactive multifunctional compound from nature", *Science of The Total Environment*, **722(9)**, DOI: 10.1016/j.scitotenv.2020.137907.

[46] L. Dickerson, M.D. Salazar, R. Trumbly, et al. (2013), "Differential effects of biochanin A on cell proliferation and ROS- dependent pathways in estrogen receptor positive and HER-2 positive breast cancer cells", *Cancer Research*, **73(8)**, Supplement, DOI: 10.1158/1538-7445.AM2013-4415.

DOI: 10.31276/VJSTE.65(2).54-58

Flavonoid glycoside constituents of the leaves of *Solanum melongena* collected in Thua Thien Hue and their anti-inflammatory activity

Canh Viet Cuong Le[1*], Phuong Ha Tran[1], That Huu Dat Ton[1], Tuan Anh Le[1], Thi Loi Nguyen[2], Thi Kim Thu Vo[2], Thi Quynh Chi Vu[3]

[1]Mientrung Institute for Scientific Research, Vietnam National Museum of Nature, Vietnam Academy of Science and Technology, 321 Huynh Thuc Khang Street, Phu Hoa Ward, Hue City, Thua Thien Hue Province, Vietnam
[2]Institute of Applied Technology, Thu Dau Mot University, 6 Tran Van On Street, Phu Hoa Ward, Thu Dau Mot City, Binh Duong Province, Vietnam
[3]The Centre of Marine Environmental Monitoring and Analysis, Anh Dung Ward, Duong Kinh District, Hai Phong City, Vietnam

Received 16 February 2022; revised 12 April 2022; accepted 20 April 2022

Abstract:

***Solanum melongena* is a member of *Solanum* genus that widely cultivated as fruit vegetable in Vietnam. According to Vietnamese traditional medicine, the fruits and whole plants are used to treat toothache, turgescence, pruritus, and haemorrhoids. As part of our project to study the chemical composition and bioactivity of *Solanum* genus in Vietnam, five flavonoid glycosides including kaempferol-3-O-β-D-glucopyranoside (1), isovitexin (2), kaempferol 3-*O*-*β*-D-glucoside-7-*O*-*α*-L-rhamnoside (3), kaempferol 3-*O*-*β*-D-sophoroside-7-*O*-*α*-L-rhamnoside (4), and kaempferol 3-*O*-*β*-D-sophoroside (5) were isolated from the methanol extract of the leaves of *Solanum melongena* growing in Thua Thien Hue province, by using various chromatography methods. Their chemical structures were determined by detailed analysis of 1D- and 2D-NMR and HR-ESI-MS data as well as comparison with the literature. Compounds (2) and (5) were isolated from *Solanum melongena* for the first time while compounds (3) and (4) were the first isolated from the *Solanum* genus. Besides, compounds 2-4 showed weak anti-inflammatory activities against NO production in RAW 264.7 macrophage line with IC_{50} values ranging from 54.28 to 91.37 µg/ml.**

Keywords: **anti-inflammatory activity, flavonoid, NO production, *Solanum melongena*.**

Classification number: **3.4**

1. Introduction

Solanum melongena is widely distributed in tropical and subtropical regions [1]. As a Vietnamese traditional medicine, the fruits and whole plants are used to treat toothache, turgescence, pruritus, and haemorrhoids in Vietnam [1]. Besides, previous biological studies of isolated compounds and extracts from the plant showed various biological activities such as anti-inflammatory [2-4], cytotoxic [5, 6], anti-oxidant [7-10], anti-diabetic [11], and anti-hypertensive [11, 12] activities. Chemical investigations of *Solanum melongena* displayed the presence of lignans [2, 4], phenolic acids [4, 5], anthocyanins [13, 14], flavanols [14], flavonols [4], sesquiterpenes [5], triterpenes [4], and sterols [3, 4]. Results of our current screening program for anti-inflammatory agents from Vietnamese *Solanum* species revealed that the *Solanum melongena* leaves methanol extract showed anti-inflammatory activity with an IC_{50} value of 65.17 µg/ml. Herein, we described the isolation and chemical structure elucidation of five flavonoids: kaempferol-3-*O*-*β*-D-glucopyranoside (**1**), isovitexin (**2**), kaempferol 3-*O*-*β*-D-glucoside-7-*O*-*α*-L-rhamnoside (**3**), kaempferol 3-*O*-*β*-D-sophoroside-7-*O*-*α*-L-rhamnoside (**4**), and kaempferol 3-*O*-*β*-D-sophoroside (**5**) from methanol extract of the leaves of *Solanum melongena*. In addition, all the compounds were tested for their inhibitory activities on LPS-induced NO in the RAW 264.7 macrophage line.

2. Experimental design

2.1. Plant materials

The leaves of *Solanum melongena* were collected in Huong Tra, Thua Thien Hue, Vietnam in July 2019. The plant sample was identified by Dr. Tran Thi Phuong Anh (Graduated University of Science and Technology, Vietnam Academy of Science and Technology). The voucher specimens (MISR.2019-15) have been deposited at Mientrung Institute for Scientific Research, Vietnam National Museum of Nature, Vietnam Academy of Science and Technology.

2.2. General procedures

HR-ESI-MS spectra were recorded on an Agilent 6550 iFunnel Q-TOF LC/MS system (Agilent Technologies,

[*]Corresponding author: Email: lcvcuong@hueiresd.vast.vn

Santa Clara, CA, USA). All Nuclear magnetic resonance (NMR) spectra were recorded on a Bruker Avance NEO 600 spectrometer (600 MHz for ^{1}H-NMR and 150 MHz for ^{13}C-NMR). Column chromatography (C.C.) was performed using silica gel (Kieselgel 230-400 mesh, Merck) or RP-18 resins (150 µm, Fuji Silysia Chemical Ltd.). The thin-layer chromatography was performed using a pre-coated silica-gel 60 F_{254} (0.25 mm, Merck) and RP-18 F_{254S} plates (0.25 mm, Merck).

2.3. Extraction and isolation

Dried leaves of *Solanum melongena* (3.0 kg) were ultrasound extracted with methanol for 120 min (3 times x 7 l) at 50°C. The methanol solution was concentrating under reduced pressure, then give methanol extract (SM, 200.0 g) was suspended in purified water (2.0 l) and partitioned with *n*-hexane, dichloromethane, and ethyl acetate (3 times, 2 l each) to give corresponding soluble extracts, *n*-hexane (SMH, 66.5 g), dichloromethane (SMD, 14.5 g), ethyl acetate (SME, 17.0 g), and water layer (SMW). The SME fraction was subjected to silica gel C.C. and eluted with dichloromethane/methanol (from 0% to 100% methanol in dichloromethane) to yield 5 fractions so-called SME1-SME5. Four subfractions (SME2A-SME2D) were obtained from the fraction SME2 using an RP-18 column and eluted with methanol/water (1/2, v/v). The SME2D subfraction was continuously separated on a C.C. and eluted with dichloromethane/methanol (10/1, v/v) to yield three smaller fractions, SME2D1-SME2D3. Compound **(1)** (3 mg) was yielded from SME2D1 on a Sephadex LH-20 column eluted with methanol/water (1/1, v/v). The SME2D3 was purified on a Sephadex LH-20 column eluted with methanol/water (1/1, v/v) to yield compound **(2)** (4 mg). The water layer was separated on a Diaion HP-20P column, eluted with water to remove sugars and ionic compounds, and then with an increasing concentration of methanol in water (from 25 to 100%) to obtain four fractions, SMW1-SMW4. Fraction SMW3 was subjected to silica gel C.C. and eluted with mixtures of methanol in dichloromethane (20/1, 10/1, 5/1, 1/1, and 100% methanol) to give five subfractions, namely, SMW3A-SMW3E. Fraction SMW3C was separated on an RP-18 column and eluted with methanol/water (1/2, v/v) to give four fractions, SMW3C1-SMW3C4. Compound **(3)** (6 mg) was yielded from fraction SMW3C1 on a Sephadex LH-20 eluting with methanol/water (1/1, v/v). The SMW2 was subjected to silica gel C.C. and eluted with mixtures of methanol in dichloromethane (20/1, 10/1, 5/1, 1/1, and 100% methanol) to give five subfractions so-called SMW2A-SMW2E. Then, fraction SMW2C was continuously chromatographed on an RP-18 column and eluted with methanol/water (1/3, v/v) to yield four smaller fractions, SMW2C1-SMW2C4. Compound **(4)** (5 mg) was obtained from fraction SMW2C1 on a silica gel column eluting with dichloromethane/methanol (3/1, v/v). Finally, the fraction SWM2C4 was purified on a Sephadex LH-20 column and eluted with methanol/water (1/1, v/v) to give compound **(5)** (4 mg).

Kaempferol-3-*O*-*β*-D-glucopyranoside (**1**): Yellow powder; $C_{21}H_{20}O_{11}$, M=448; HR-ESI-MS: *m/z* 447.0933 $[M-H]^-$ (calcd. for $[C_{21}H_{19}O_{11}]^-$ 447.0927); ^{1}H-NMR (DMSO-d_6, 600 MHz): δ_H (ppm) 6.22 (1H, d, *J*=1.8 Hz, H-6), 6.45 (1H, d, *J*=1.8 Hz, H-8), 8.03 (2H, d, *J*=9.0 Hz, H-2′ and H-6′), 6.89 (2H, d, *J*=9.0 Hz, H-3′ and H-5′), 5.45 (1H, d, 7.8 Hz, H-1″), 3.20 (1H, m, H-2″), 3.22 (1H, m, H-3″), 3.10 (1H, m, H-4″), 3.08 (1H, m, H-5″), 3.34 (1H, dd, *J*=4.8, 11.4 Hz, H_a-6″), 3.55 (1H, brd, *J*=11.4 Hz, H_b-6″). ^{13}C-NMR (DMSO-d_6, 150 MHz): δ_C (ppm) 156.3 (C-2), 133.2 (C-3), 177.5 (C-4), 161.2 (C-5), 98.8 (C-6), 164.4 (C-7), 93.7 (C-8), 156.4 (C-9), 103.9 (C-10), 120.9 (C-1′), 130.9 (C-2′ and C-6′), 115.2 (C-3′ and C-5′), 160.0 (C-4′), 100.9 (C-1″), 74.2 (C-2″), 76.4 (C-3″), 69.9 (C-4″), 77.5 (C-5″), 60.8 (C-6″).

Isovitexin (**2**): Yellow powder; $C_{21}H_{20}O_{10}$, M=432; HR-ESI-MS: *m/z* 433.1129 $[M+H]^+$ (calcd. for $[C_{21}H_{21}O_{10}]^+$ 433.1135); ^{1}H-NMR (DMSO-d_6, 600 MHz): δ_H (ppm) 6.78 (1H, s, H-3), 6.52 (1H, s, H-8), 7.93 (2H, d, *J*=8.4 Hz, H-2′ and H-6′), 6.93 (2H, d, *J*=8.4 Hz, H-3′ and H-5′), 4.58 (1H, d, *J*=10.2 Hz, H-1″), 4.04 (1H, t, *J*=9.0 Hz, H-2″), 3.20 (1H, m, H-3″), 3.13 (1H, m, H-4″), 3.17 (1H, m, H-5″), 3.41 (1H, dd, *J*=6.0, 11.4 Hz, H_a-6″), 3.68 (1H, brd, *J*=10.8 Hz, H_b-6″). ^{13}C-NMR (DMSO-d_6, 150 MHz): δ_C (ppm) 163.5 (C-2), 102.7 (C-3), 181.9 (C-4), 161.1 (C-5), 108.8 (C-6), 163.3 (C-7), 93.6 (C-8), 156.2 (C-9), 103.4 (C-10), 121.1 (C-1′), 128.4 (C-2′ and C-6′), 115.9 (C-3′ and C-5′), 160.5 (C-4′), 73.0 (C-1″), 70.5 (C-2″), 78.9 (C-3″), 70.2 (C-4″), 81.5 (C-5″), 61.4 (C-6″).

Kaempferol 3-*O*-*β*-D-glucoside-7-*O*-*α*-L-rhamnoside **(3)**: Yellow powder; $C_{27}H_{30}O_{15}$, M=594; HR-ESI-MS: *m/z* 595.1657 $[M+H]^+$ (calcd. for $[C_{27}H_{31}O_{15}]^+$ 595.1663); ^{1}H-NMR (DMSO-d_6, 600 MHz): δ_H (ppm) 6.44 (1H, s, H-6), 6.82 (1H, s, H-8), 8.07 (2H, d, *J*=9.0 Hz, H-2′ and H-6′), 6.89 (2H, d, *J*=9.0 Hz, H-3′ and H-5′), 5.48 (1H, d, *J*=7.2 Hz, H-1″), 3.19 (1H, m, H-2″), 3.08 (1H, m, H-3″), 3.84 (1H, *brs*, H-4″), 3.22 (1H, m, H-5″), 3.32 (1H, brd, *J*=10.8 Hz, H_a-6″), 3.56 (1H, brd, *J*=10.8 Hz, H_b-6″), 5.55 (1H, s, H-1‴), 3.63 (1H, dd, *J*=3.0, 9.0 Hz, H-2‴), 3.42 (1H, m, H-3‴), 3.30 (1H, m, H-4‴), 3.09 (1H, m, H-5‴), 1.12 (3H, d, *J*=6.0 Hz, H_3-6‴). ^{13}C-NMR (DMSO-d_6, 150 MHz): δ_C (ppm) 156.7 (C-2), 133.5 (C-3), 177.6 (C-4), 160.9 (C-5), 99.4 (C-6), 161.7 (C-7), 94.5 (C-8), 156.0 (C-9), 105.6 (C-10), 120.7 (C-1′), 131.0 (C-2′ and C-6′), 115.1 (C-3′ and C-5′), 160.1 (C-4′), 100.8 (C-1″), 74.2 (C-2″), 77.5 (C-3″), 69.8 (C-4″), 76.4 (C-5″), 60.8 (C-6″), 98.4 (C-1‴), 70.2 (C-2‴),70.0 (C-3‴), 71.6 (C-4‴), 69.9 (C-5‴), 17.9 (C-6‴).

Kaempferol 3-*O*-*β*-D-sophoroside-7-*O*-*α*-L-rhamnoside **(4)**: Yellow powder; $C_{33}H_{40}O_{20}$, M=756; HR-ESI-MS: *m/z* 791.1807 $[M+Cl]^-$ (calcd. for $[C_{33}H_{40}ClO_{20}]^-$ 791.1801); ^{1}H-NMR (DMSO-d_6, 600 MHz): δ_H (ppm) 6.43 (1H, d, *J*=1.8 Hz, H-6), 6.82 (1H, d, *J*=1.8 Hz, H-8), 8.09 (1H, d, *J*=9.0 Hz, H-2′ and H-6′), 6.92 (1H, d, *J*=9.0 Hz, H-3′ and H-5′), 5.70 (1H, d, *J*=7.2 Hz, H-1″), 3.48 (1H, m, H-2″), 3.49 (1H, m, H-3″), 3.13 (1H, m, H-4″), 3.20 (1H, m, H-5″), 3.27 (1H, dd, *J*=6.0, 10.2 Hz, H_a-6″), 3.51 (1H, overlapped, H_b-6″), 4.42 (1H, d, *J*=7.8 Hz, H-1‴), 3.07 (1H, m, H-2‴), 3.12 (1H, m, H-3‴), 3.45 (1H, m, H-4‴), 3.10 (1H, m, H-5‴), 3.50 (1H, dd, *J*=5.4, 11.4 Hz, H_a-6‴), 3.60 (1H, dd, *J*=3.0, 11.4 Hz, H_b-6‴), 5.55 (1H, d, J=1.2 Hz, H-1⁗), 3.85 (1H, br s, H-2⁗), 3.64 (1H, m, H-3⁗), 3.31 (1H, m, H-4⁗), 3.17 (1H, m, H-5⁗), 1.13 (3H, d, *J*=6.6 Hz, H_3-6⁗). ^{13}C-NMR (DMSO-d_6, 150 MHz): δ_C (ppm) 156.0 (C-2), 133.3 (C-3), 177.7 (C-4), 161.0 (C-5), 99.4 (C-6), 161.6 (C-7), 94.5 (C-8), 156.2 (C-9), 105.7 (C-10), 120.8 (C-1′), 131.1 (C-2′ and C-6′), 115.4 (C-3′ and C-5′), 160.2 (C-4′), 98.0 (C-1″), 82.4 (C-2″), 76.7 (C-3″), 69.7 (C-4″), 76.6 (C-5″), 60.6 (C-6″), 104.1 (C-1‴), 74.4 (C-2‴), 77.03 (C-3‴), 70.1 (C-4‴) ,77.6 (C-5‴), 60.9 (C-6‴), 98.5 (C-1⁗), 69.9 (C-2⁗), 70.3 (C-3⁗), 71.7 (C-4⁗), 69.8 (C-5⁗), 18.0 (C-6⁗).

Kaempferol 3-*O*-*β*-D-sophoroside **(5)**: Yellow powder; $C_{27}H_{30}O_{16}$, M=610; HR-ESI-MS: m/z 611.1595 $[M+H]^+$ (calcd. for $[C_{27}H_{31}O_{16}]^+$ 611.1612); ^{1}H-NMR (DMSO-d_6, 600 MHz): δ_H (ppm) 6.19 (1H, d, *J*=2.4 Hz, H-6), 6.43 (1H, d, *J*=2.4 Hz, H-8), 8.04 (2H, d, *J*=9.0 Hz, H-2′ and H-6′), 6.91 (2H, d, *J*=9.0 Hz, H-3′ and H-5′), 5.69 (1H, d, *J*=7.2 Hz, H-1″), 3.47 (1H, m, H-2″), 3.48 (1H, m, H-3″), 3.12 (1H, m, H-4″), 3.19 (1H, m, H-5″), 3.25 (1H, dd, *J*=6.0, 12.0 Hz, H_a-6″), 3.47 (1H, br d, *J*=12.0 Hz, H_b-6″), 4.61 (1H, d, *J*=7.8 Hz, H-1‴), 3.06 (1H, m, H-2‴), 3.13 (1H, m, H-3‴), 3.45 (1H, m, H-4‴), 3.11 (1H, m, H-5‴), 3.50 (1H, dd, *J*=5.4, 11.4 Hz, H_a-6‴), 3.60 (1H, brd, *J*=11.4 Hz, H_b-6‴). ^{13}C-NMR (DMSO-d_6, 150 MHz): δ_C (ppm) 155.6 (C-2), 132.9 (C-3), 177.5 (C-4), 161.2 (C-5), 98.6 (C-6), 164.1 (C-7), 93.6 (C-8), 156.3 (C-9), 103.9 (C-10), 120.9 (C-1′), 130.9 (C-2′ and C-6′), 115.3 (C-3′ and C-5′), 159.9 (C-4′), 115.3 (C-5′), 130.9 (C-6′), 98.0 (C-1″), 82.4 (C-2″), 77.5 (C-3″), 69.6 (C-4″), 76.6 (C-5″), 60.8 (C-6″), 104.1 (C-1‴), 74.4 (C-2‴), 77.0 (C-3‴), 69.7 (C-4‴), 76.6 (C-5‴), 60.5 (C-6‴).

The chemical structures of five compounds are illustrated in Fig. 1.

2.4. Measurement of NO production and cell viability assay

NO determination and cell viability testing was realized as in the literature [15]. L-NMMA was a positive control for the NO test (IC_{50}=8.01±0.85 μg/ml).

3. Results and discussion

Compound **(1)** was given as a yellow powder. The molecular formula of **(1)** was identified as $C_{21}H_{20}O_{11}$ based on the HR-ESI-MS ion at m/z 447.0933 $[M-H]^-$ (calcd. for $[C_{21}H_{19}O_{11}]^-$ 447.0927). The ^{1}H-NMR spectrum of **(1)** showed signals of four aromatic protons of an AA'BB' system at δ_H 6.89 (2H, d, *J*=9.0 Hz) and 8.03 (2H, d, *J*=9.0 Hz); two aromatic protons at δ_H 6.22 (1H, d, *J*=1.8 Hz) and 6.45 (1H, d, *J*=1.8 Hz); one anomeric proton at 5.45 (1H, d, *J*=7.8 Hz); and two oxymethylene protons at δ_H 3.34 (1H, dd, *J*=4.8, 11.4 Hz) and 3.55 (1H, brd, *J*=11.4 Hz). The ^{13}C-NMR, HSQC spectra of **(1)** displayed 15 carbon signals of a flavonoid aglycone, which corresponded to

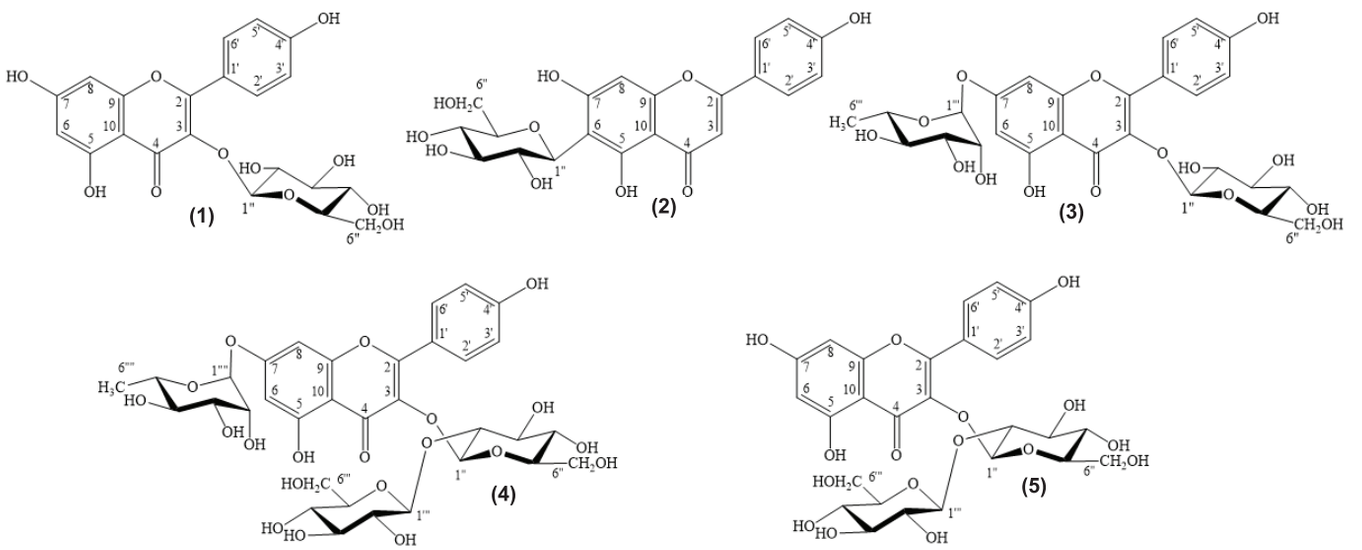

Fig. 1. Chemical structure of compounds (1-5).

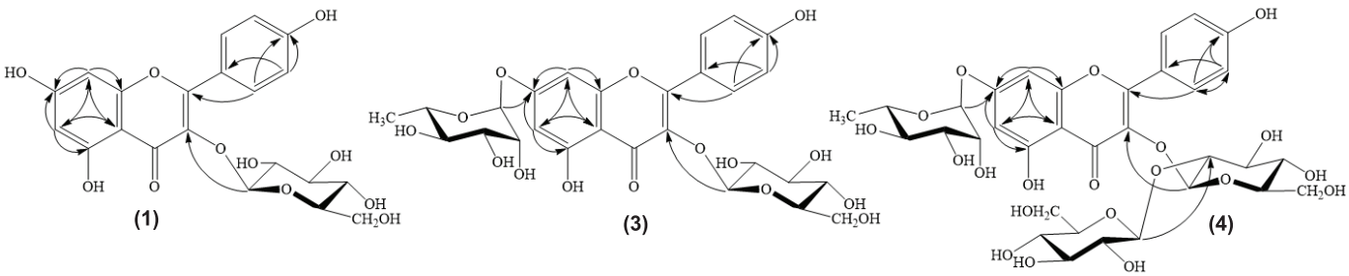

Fig. 2. Key HMBC correlations of compounds (1, 3, and 4).

nine quaternary carbons at δ_C 103.9, 120.9, 133.2, 156.3, 156.4, 160.0, 161.2, 164.4, and 177.5; six methine carbons at δ_C 93.7, 98.8, 130.9 (2xCH), and 115.2 (2xCH); and six carbon signals of a sugar unit, which corresponded to five methine carbons at δ_C 69.9, 74.2, 76.4, 77.5, and 100.9 and one oxymethylene carbon at δ_C 60.8. Analysis of ^{1}H- and ^{13}C-NMR data suggested the chemical structure of **(1)** is a kaempferol glycoside [16]. The anomeric proton ($J_{H\text{-}1''/H\text{-}2''}$=7.8 Hz) and the ^{13}C-NMR data of the sugar unit demonstrated the presence of a *β*-D-glucopyranosyl moiety in **(1)**. Besides, the HMBC correlation from H-1*''* (δ_H 5.45) to C-3 (δ_C 133.2) determines a linkage between the sugar moiety and C-3 of the aglycone (Fig. 2). Based on the spectra evidence and comparison with those of kaempferol-3-*O*-*β*-D-glucopyranoside in the literature [16], compound **(1)** was identified as kaempferol-3-*O*-*β*-D-glucopyranoside. This compound was reported from *Solanum melongena* [17].

Compound **(3)** was obtained as a yellow powder. The molecular formula of **(3)** was elucidated as $C_{27}H_{30}O_{15}$ based on the HR-ESI-MS ion at *m/z* 595.1657 $[M+H]^+$ (calcd. for $C_{27}H_{31}O_{15}^+$ 595.1663). The ^{1}H-NMR of **(3)** showed signals of six aromatic protons of an AX system and an AA*'*BB*'* system at δ_H 6.44 (1H, s, H-6), 6.82 (1H, s, H-8), 8.07 (2H, d, *J*=9.0 Hz, H-2*'*, H-6*'*), and 6.89 (2H, d, *J*=9.0 Hz, H-3*'*, H-5*'*); two anomeric protons at δ_H 5.48 (1H, d, *J*=7.2 Hz, H-1*''*) and 5.55 (1H, s, H-1‴); and a CH_3 group at δ_H 1.12 (3H, d, *J*=6.0 Hz, H-6‴). The ^{13}C-NMR and HSQC spectra of **(3)** displayed the presence of 27 carbon signals including nine quaternary carbons, 16 methine groups, one methylene group, and one methyl group. The comparison of the ^{1}H- and ^{13}C-NMR data of **(3)** with those of **(1)** displayed close similarity except for the additional presence of a rhamnopyranosyl moiety at 98.4 (C-1‴)/5.55 (H-1‴), 70.2 (C-2‴)/3.63 (H-2‴), 70.0 (C-3‴)/3.42 (H-3‴), 71.6 (C-4‴)/3.30 (H-4‴), 69.9 (C-5‴)/3.09 (H-5‴), and 17.9 (C-6‴)/1.12 (H-6‴) in **(3)**. The linkage between C-7 of the aglycone and the glucopyranosyl moiety was confirmed by HMBC correlation from H-1" (δ_H 5.48) to C-3 (δ_C 133.5). Besides, the HMBC correlation from H-1‴ (δ_H 5.55) to C-7 (δ_C 161.7) determines the position of the rhamnopyranosyl moiety at C-7. The structure of **(3)** was confirmed by its good agreement with the ^{13}C-NMR data of those reported in the literature [18]. Therefore, compound **(3)** was determined to be kaempferol 3-*O*-*β*-D-glucoside-7-*O*-*α*-L-rhamnoside. To our best knowledge, this compound was reported from the genus *Solanum* for the first time.

Compound **(4)** was yielded as a yellow powder. The molecular formula of **(4)** was determined to be $C_{33}H_{40}O_{20}$ from HR-ESI-MS ion peak at *m/z* 791.1807 $[M+Cl]^-$ (calcd. for $[C_{33}H_{40}ClO_{20}]^-$ 791.1801). The ^{1}H-NMR of **(4)** showed signals of six aromatic protons at δ_H 6.43 (1H, d, *J*=1.8 Hz), 6.82 (1H, d, *J*=1.8 Hz), 6.92 (2H, d, *J*=9.0 Hz), and 8.09 (2H, d, *J*=9.0 Hz); three anomeric protons at δ_H 4.42 (1H, d, *J*=7.8 Hz), 5.55 (1H, d, *J*=1.2 Hz), and 5.70 (1H, d, *J*=7.2 Hz); and three protons of a methyl group at δ_H 1.13 (3H, d, *J*=6.6 Hz). The ^{13}C-NMR and HSQC spectra of **(4)** displayed the presence of 33 carbon signals including nine quaternary carbons, 21 methine groups, two methylene groups, and one methyl group. The coupling constant of the anomeric protons, including $J_{H\text{-}1''/H\text{-}2''}$= 7.2 Hz, $J_{H\text{-}1'''/H\text{-}2'''}$=7.8 Hz, and $J_{H\text{-}1''''/H\text{-}2''''}$=1.2 Hz, and ^{13}C-NMR data of the sugar units suggest the presence of one rhamnopyranosyl and two glucopyranosyl moieties in **(4)**. The comparison of NMR data of **(3)** and **(4)** revealed that compound **(4)** was also a kaempferol glycoside, but it contained one more glucopyranosyl moiety than **(3)**. The HMBC correlations from H-1" (δ_H 5.70) to C-3 (δ_C 133.3) and H-1‴ (δ_H 4.42) to C-2" (δ_C 82.4) determined the position of a sophorosyl moiety at C-3. Besides, the linkage between C-7 of the aglycone and the rhamnopyranosyl moiety was determined by the HMBC correlation from H-1'''' (δ_H 5.55) to C-7 (δ_C 161.6). Based on the spectra evidence and comparison with those in the literature [19], compound **(4)** was identified as kaempferol 3-*O*-*β*-D-sophoroside-7-*O*-α-L-rhamnoside. This is the first time the compound was isolated from the genus *Solanum*.

The remaining compounds were characterized as isovitexin **(2)** and kaempferol-3-*O*-sophoroside **(5)** by comparison of their NMR data with those previously reported [16, 20].

All isolated compounds were assayed for their inhibitory activities on LPS-induced NO in the RAW 264.7 macrophage line. The results showed that compounds **(2-4)** had a weak anti-inflammatory effect with IC_{50} values of 91.37, 54.28, and 67.45 µg/ml, respectively, relative to the positive control *L-NMMA* with IC_{50} values of 8.01±0.85 µg/ml. Compounds **(1)** and **(5)** were considered to be inactive (IC_{50}>100 µg/ml).

4. Conclusions

A phytochemical study on the methanol extract of the leaves of *Solanum melongena* led to the isolation of five flavonoid glycosides including kaempferol-3-*O*-*β*-D-glucopyranoside **(1)**, isovitexin **(2)**, kaempferol 3-*O*-*β*-D-glucoside-7-*O*-*α*-L-rhamnoside **(3)**, kaempferol 3-*O*-*β*-D-sophoroside-7-*O*-*α*-L-rhamnoside **(4)**, and kaempferol 3-*O*-*β*-D-sophoroside **(5)**. Among them, compounds **(2-4)** showed weak anti-inflammatory activities against NO production in RAW 264.7 macrophage line with IC_{50} values ranging from 54.28 to 91.37 µg/ml. Compounds **(2)** and **(5)** were isolated from this plant for the first time, while compounds **(3)** and **(4)** were first reported from the genus *Solanum*.

CRediT author statement

Phuong Ha Tran, Thi Loi Nguyen, and Thi Kim Thu Vo: Isolated the compounds and elucidated the structures; That Huu Dat Ton and Tuan Anh Le: Evaluated anti-inflammatory activity of isolated compounds; Thi Quynh Chi Vu and Canh Viet Cuong Le: Wrote the manuscript and carried out the data analysis and structure elucidation.

ACKNOWLEDGEMENTS

The research is funded by Vietnam National Foundation for Science and Technology Development (NAFOSTED) under grant number 104.01-2018.321.

COMPETING INTERESTS

The authors declare that there is no conflict of interest regarding the publication of this article.

REFERENCES

[1] V.V. Chi (2012), *Dictionary of Medicinal Plants in Vietnam*, Medical Publishing House, Hanoi, **1**, pp.175-176 (in Vietnamese).

[2] J. Sun, Y.F. Gu, X.Q. Su, et al. (2014), "Anti-inflammatory lignanamides from the roots of *Solanum melongena* L.", *Fitoterapia*, **98**, pp.110-116, DOI: 10.1016/j.fitote.2014.07.012.

[3] B.Y. Yang, X. Yin, Y. Liu, et al. (2018), "New steroidal saponins from the roots of *Solanum melongena* L.", *Fitoterapia*, **128**, pp.12-19, DOI: 10.1016/j.fitote.2018.04.021.

[4] J. Sun, H.X. Huo, Z. Huang, et al. (2015), "A new γ-alkylated-γ-butyrolactone from the roots of *Solanum melongena*", *Chinese Journal of Natural Medicines*, **13(9)**, pp.699-703, DOI: 10.1016/S1875-5364(15)30068-6.

[5] D.Y. Zhao, Y. Liu, Y.P. Sun, et al. (2020), "Sesquiterpenoids with diverse carbon skeletons from the sepals of *Solanum melongena* L.", *Fitoterapia*, **142**, DOI: 10.1016/j.fitote.2020.104517.

[6] S.W. Han, J. Tae, J.A. Kim, et al. (2003), "The aqueous extract of *Solanum melongena* inhibits PAR2 agonist-induced inflammation", *Clinica Chimica Acta*, **328(1)**, pp.39-44, DOI: 10.1016/s0009-8981(02)00377-7.

[7] B.B. Mishra, S. Gautam, A. Sharma (2012), "Purification and characterisation of polyphenol oxidase (PPO) from eggplant (*Solanum melongena*)", *Food Chemistry*, **134(4)**, pp.1855-1861, DOI: 10.1016/j.foodchem.2012.03.098.

[8] P.C. Braga, R.L. Scalzo, M.D. Sassoet, et al. (2016), "Characterization and antioxidant activity of semi-purified extracts and pure delphinidin-glycosides from eggplant peel (*Solanum melongena* L.)", *Journal of Functional Foods*, **20**, pp.411-421, DOI: 10.1016/j.jff.2015.10.032.

[9] P. Nisha, P.A. Nazar, P. Jayamurthy (2009), "A comparative study on antioxidant activities of different varieties of *Solanum melongena*", *Food and Chemical Toxicology*, **47(10)**, pp.2640-2644, DOI: 10.1016/j.fct.2009.07.026.

[10] P.M. Hanson, R.Y. Yang, S.C.S. Tsou, et al. (2006), "Diversity in eggplant (*Solanum melongena*) for superoxide scavenging activity, total phenolics, and ascorbic acid", *Journal of Food Composition and Analysis*, **19(6)**, pp.594-600, DOI: 10.1016/j.jfca.2006.03.001.

[11] Y.I. Kwon, E. Apostolidis, K. Shetty (2008), "*In vitro* studies of eggplant (*Solanum melongena*) phenolics as inhibitors of key enzymes relevant for type 2 diabetes and hypertension", *Bioresour. Technol.*, **99(8)**, pp.2981-2988, DOI: 10.1016/j.biortech.2007.06.035.

[12] S. Yamaguchi, K. Matsumoto, M. Koyama, et al. (2019), "Antihypertensive effects of orally administered eggplant (*Solanum melongena*) rich in acetylcholine on spontaneously hypertensive rats", *Food Chemistry*, **276**, pp.376-382, DOI: 10.1016/j.foodchem.2018.10.017.

[13] S.S. Tanchev, P.J. Ruskov, C.F. Timberlake (1970), "The anthocyanins of Bulgarian aubergine (*Solanum melongena*)", *Phytochemistry*, **9(7)**, pp.1681-1682, DOI: 10.1016/S0031-9422(00)85298-X.

[14] G.N. Medina, V.U. Orona, M.D.M. Rangel, et al. (2017), "Structure and content of phenolics in eggplant (*Solanum melongena*) - A review", *South African Journal of Botany*, **111**, pp.161-169, DOI: 10.1016/j.sajb.2017.03.016.

[15] L.C.V. Cuong, L.T. Anh, T.T.H. Dat, et al. (2021), "Cytotoxic and anti-inflammatory activities of secondary metabolites from *Ophiorrhiza baviensis* growing in Thua Thien Hue, Vietnam", *Natural Product Research*, **35(22)**, pp.4218-4224, DOI: 10.1080/14786419.2019.1693564.

[16] U.L.B. Jayasinghe, B.A.I.S. Balasooriya, A.G.D. Bandara, et al. (2004), "Glycosides from *Grewia damine* and *Filicium decipiens*", *Natural Product Research*, **18(6)**, pp.499-502, DOI: 10.1080/14786410310001620538.

[17] P.S. Ajay, Y. Wang, R.M. Olson, et al. (2017), "LC-MS-MS analysis and the antioxidant activity of flavonoids from Eggplant skins grown in organic and conventional environments", *Food and Nutrition Sciences*, **8(9)**, pp.869-884, DOI: 10.4236/fns.2017.89063.

[18] S. Özden, N. Dürüst, K. Toki, et al. (1998), "Acylated kaempferol glycosides from the flowers of *Delphinium formosum*", *Phytochemistry*, **49(1)**, pp.241-245, DOI: 10.1016/S0031-9422(97)01044-3.

[19] D. Rösch, A. Krumbein, C. Mügge, et al. (2004), "Structural investigations of flavonol glycosides from sea buckthorn (*Hippophaë rhamnoides*) pomace by NMR spectroscopy and HPLC-ESI-MS", *Journal of Agricultural and Food Chemistry*, **52(13)**, pp.4039-4046, DOI: 10.1021/jf0306791.

[20] T. Takemura, Y. Takatsu, M. Kasumi, et al. (2005), "Flavonoids and their distribution patterns in the flowers of *Gladiolus* cultivars", *Acta Horticulturae*, **673(64)**, pp.487-493, DOI: 10.17660/ActaHortic.2005.673.64.

DOI: 10.31276/VJSTE.65(2).59-64

Investigating the diversity of resistant starch in Vietnamese rice collection

Thi Mai Huong To, Thi Linh Nguyen, Thi Ngoc An Do, Lan Phuong Nguyen, Nga T.P. Mai*

University of Science and Technology of Hanoi, Vietnam Academy of Science and Technology, 18 Hoang Quoc Viet Street, Nghia Do Ward, Cau Giay District, Hanoi, Vietnam

Received 20 May 2022; revised 18 July 2022; accepted 8 August 2022

Abstract:

The rapid increase of obesity and type 2 diabetes has recently posed an enormous burden on the healthcare system worldwide. Resistant starch (RS) in rice can escape digestion by enzymes in the small intestine, making its calories unavailable for cells to use. As a result, RS can be used by diabetes patients to prevent diabetes and for obese individuals who do not want extra energy. In our study, 75 Vietnamese rice accessions originating from diverse ecosystems were chosen as plant materials to investigate the diversity of RS content in this collection. The Megazyme kit was used to measure the amount of RS. The release of quinonimine was measured using a spectrophotometer at 510 nm. The results showed that approximately 70% of Vietnamese rice accessions had RS content ranging from 0.015 to 0.2% while only 4% of samples had RS content ranging from 0.6 to 0.8%. The *Indica* subgroups had significantly higher RS content than the *Japonica* subgroup. Higher RS content was found in medium- and short-grain rice rather than in long grain. Finally, rice plants grown in rainfed lowlands (RL) and irrigated ecosystems had higher RS content than those grown under mangrove and upland ecosystems. Our results firstly give information about the diversity of RS in Vietnamese rice and secondly may contribute to the field of nutrition by developing a suitable rice-based diet for patients with diabetes or obesity.

Keywords: **diabetes, diet, obesity, resistant starch, rice, starch.**

Classification numbers: **3.4, 3.5**

1. Introduction

Rice (*Oryza sativa* L.) is the staple food for half of the world's population. Rice is also an excellent source of starch, which is then hydrolysed by enzymes and converted into glucose that cells directly use to produce energy for their activities [1]. However, if the energy supply exceeds the energy requirement, it will be converted into glycogen or fats. Nowadays, thanks to social development and increases in quality of life, overeating and lack of exercise has increased the number of people having obesity and type 2 diabetes. In 2017, approximately 462 million people were affected by type 2 diabetes corresponding to 6.28% of the world's population. The global prevalence of type 2 diabetes will increase to 7,079 individuals per 100,000 by 2030, which will pose a significant burden to the healthcare system [2]. Therefore, solving the problem of diabetes and obesity based on a healthier diet is a priority.

Based on enzymatic hydrolysis, starch is composed of a large digestible starch, which is classified into two types: rapidly digested starch, slowly digested starch, and a small amount of indigestible starch also known as RS [3]. Traditionally, it was assumed that starch was completely digested. It is now known that a portion of starch resistant to digestion by human enzymes in the small intestine will move into the large intestine where it may or may not be fermented by gut bacteria [4]. As a result, RS serves as a dietary fibre, lowers calorie intake, has a low glycaemic index, and gives various advantages to colon health. When consumed, it promotes gut health, reduces glucose and

*Corresponding author: Email: mai-thi-phuong.nga@usth.edu.vn

insulin reactions, and minimises cardiovascular disease risk factors [5]. The RS content of rice ranges from 0.1 to 25.4% [6]. Consuming 18-20% of RS per day is recommended.

RS is classified into five categories based on enzyme resistance [7]. RS1 is starch that is physically protected in cell or tissue structures and is not available for enzymatic hydrolysis in the small intestine. RS2 is present in dehydrated high-amylose starch granules and has a tight form that prevents digestive enzymes from accessing the starch. RS3 is a gelatinised and retrograded starch mainly composed of amylose leached from starch granules after being hydrated. RS4 is a starch that has been chemically modified to prevent enzymatic hydrolysis. Finally, RS5 combines helical amylose and fatty acids that resist amylase digestion [8].

Several studies have assessed the genetic diversity of RS in rice. Natural genetic diversity may be accessed through breeding to improve RS content in high amylose haplotypes with minimal influence on processing quality and cooked rice texture [9]. Q. Li, et al. (2018) [10] identified the *Waxy* gene, which regulated amylose content, whereas eight soluble starch synthases coordinate amylopectin. Other studies indicate that RS was connected with starch synthase *IIa*, *Waxy*, and other starch synthesis-related genes in rice varieties with amylose levels [11, 12]. According to S. Parween, et al. (2020) [12], RS is predominantly linked to the starch synthase *IIa* gene. To find the quantitative trait locus (QTLs) and candidate genes relating to RS, seven QTLs were associated with the RS content among which the SNP 6 m1765761 was located on *Waxy*. Starch branching enzymes IIa (BEIIa), close to QTL *qRS-I4*, were detected and further identified as a specific candidate gene for RS in *Indica* [13]. These studies show that a complicated metabolite network regulates the formation of RS in rice. Even though Vietnam has an extensive collection of rice, there have not been any studies investigating the diversity of RS content within a Vietnamese rice collection.

Therefore, this study aims to determine the content of RS from common rice varieties in Vietnam. The new findings from this study contribute to the global development of the rice field, assist plant breeders and food processors in attempts to develop new rice varieties, and partly solves the diet problem for individuals with obesity and type 2 diabetes.

2. Materials and methods

2.1. Plant materials

The rice population in this study consisted of 75 characterised varieties that were grown in the Vinh Ngoc commune, Hanoi [14].

2.2. Chemicals

Kits: The RS assay kit (Rapid) (Megazyme, Ireland) was composed of amyloglucosidase (AMG) (12 ml, 3,300 U/ml on soluble starch), pancreatic α-amylase (pancreatin, 10 g, 3 ceralpha units/mg), glucose oxidase/peroxidase reagent (GOPOD) reagent buffer, and GOPOD reagent enzymes.

2.3. Other chemicals

Maleic acid (CAS 99 110-16-7), sodium hydroxide (CAS 1310-73-2), calcium chloride (CAS 10043-52-4), sodium azide (CAS 26628-22-8), glacial acetic acid (CAS 64-19-7), KOH (CAS 1310-58-3), and ethanol (CAS 64-17-5) were purchased from Sigma-Aldrich.

2.4. Methods

Extraction of RS: The process of RS extraction is presented in Fig. 1. At the beginning of the process, the rice flour samples were mixed with solution 2 containing pancreatic alpha-amylase and dilute AMG (300 U/ml). Then each mixture was incubated in the IKA Incubator shaker KS 4.000 at a shaking speed of 200 strokes/min at 37°C for 16 hours. During the set time, non-RS had the combined action with two enzymes (pancreatic alpha-amylase and dilute AMG (300 U/ml) to convert into D-glucose. The reaction was completed by presenting an equal volume of ethanol (96% v/v), followed by centrifugation at 3,000 rpm for 10 min, and the RS starch was formed as a pellet. The soluble starch was entirely removed from RS by washing twice with ethanol (50% v/v). The non-RS liquid was removed by decantation.

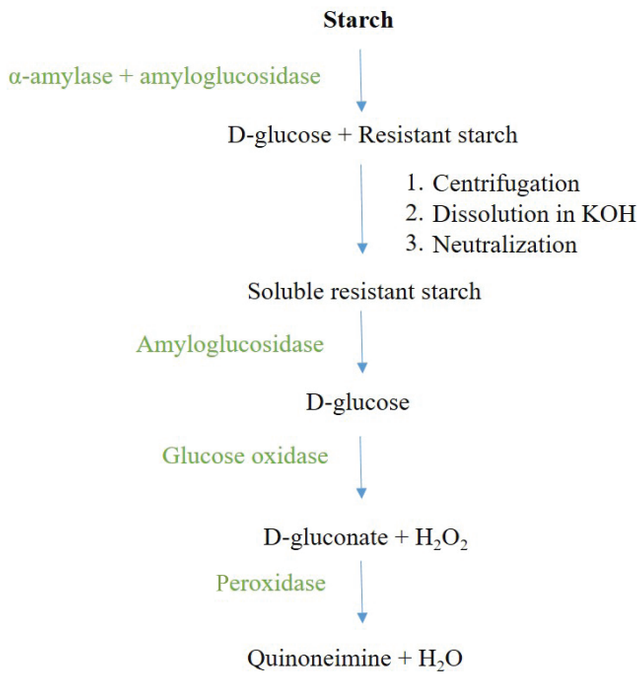

Fig. 1. RS and non-RS hydrolysis reaction (adapted from [15]).

2.5. Measurement of RS

The RS pellet was dissolved using KOH in an ice water bath with a magnetic stirrer within 20 min. After that, the solution was neutralised by adding a 1.2 M sodium acetate buffer (pH 3.8). Soluble RS was solubilised and hydrolysed to D-glucose by presenting AMG (3,300 U/ml), followed by incubating for 30 min in a hot water bath. Finally, the d-glucose was measured with GOPOD. D-glucose was oxidised by glucose oxidase into d-gluconate and hydrogen peroxide. The hydrogen peroxide reacted with peroxidase to create quinonimine. The absorbance was measured at 510 nm against a reagent blank using a UV-1800 UV-VIS spectrophotometer (Shimadzu, Kyoto, Japan).

The content of RS was calculated by using the equation:

% RS = amount of RS in 100 mg sample (mg) = ΔExFx0.00927

where ΔE: absorbance read against the reagent blank and F: conversion from absorbance to micrograms divided by the GOPOD absorbance for this 100 µg of d-glucose.

Statistical analysis: The correlation analysis between RS in different groups was performed using Graph Path v.8.4.3. A t-test was used to calculate the significant difference in RS content among different groups including grain size, *Indica* and *Japonica* groups, and ecosystems (irrigated, upland, RL, and mangrove). The experiment was repeated three times.

3. Results

3.1. Diversity of RS in 75 Vietnamese characterised varieties

The content of RS in 75 rice samples exhibited a continuous distribution ranging from 0.015 mg/100 mg to 0.71 mg/100 mg (Fig. 2). Some rice accessions, including G203, G161, G46, G17, and G160, had the lowest RS content. On the other hand, G98, G95, G70, G133, and G94 were the five rice samples with the highest RS content (Table 1).

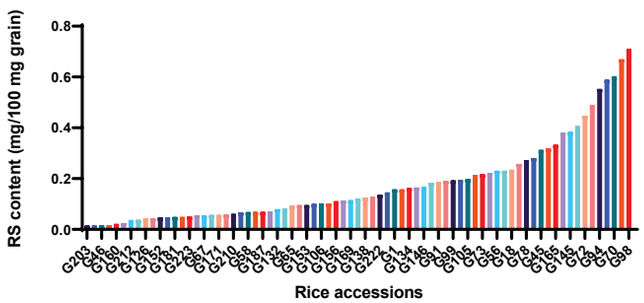

Fig. 2. Diversity of RS content in 75 Vietnamese characterised varieties.

Table 1. Accessions with the highest and lowest RS content.

ID	Name	Mean (mg/100 mg grain)	Origin	DArT P
G203	Plau Ca Banh	0.015	Dien Bien	*Japonica*
G161	Bn1	0.015	An Giang	*Indica*
G46	Nep Ba Lao	0.016	Nam Dinh	*Japonica*
G17	Nep Ga Gay Hai Duong	0.017	Hai Duong	*Indica*
G160	Jasmine	0.022	An Giang	*Indica*
G94	Lua Do	0.553	Thua Thien Hue	*Indica*
G133	A 330	0.589	Khanh Hoa	*Indica*
G70	Coc Moi Dang 2	0.601	Binh Dinh	*Indica*
G95	Lua Cham	0.67	Nam Dinh	*Indica*
G98	Ngoi Tia	0.71	Nam Dinh	*Japonica*

3.2. *Frequency distribution of RS in 75 Vietnamese characterised varieties*

Among the 75 samples, there were 53 samples with RS content between 0.015 and 0.2 mg/100 mg, 14 samples with RS concentration between 0.2 and 0.4 mg/100 mg, 5 samples with RS quantities in the range of 0.4-0.6 mg/100 mg, and 3 samples with RS levels in the range of 0.6-0.8 mg/100 mg (Fig. 3). The results indicate that most rice varieties had an RS level of 0-0.2 mg/100 mg, while some had lower or higher RS content than the common group.

Only three samples showed RS levels between 0.6 and 0.8 mg/100 mg. The samples with the highest RS content were G70, G95, and G98, respectively, with 0.601, 0.67, and 0.71 mg/100 mg. These are the potential candidates for further studies to create commercial high RS rice varieties.

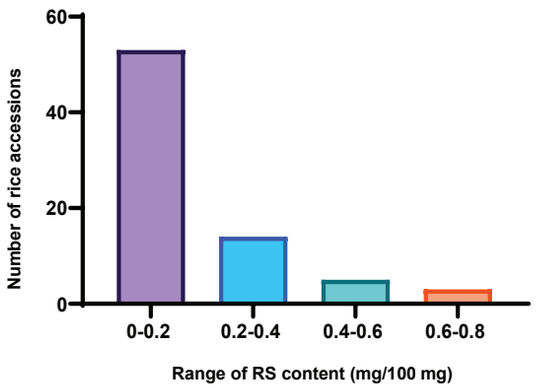

Fig. 3. Frequency distribution of RS content in the 75 characterised Vietnamese varieties.

3.3. Relationship between subgroup population and RS

Based on the structure results using the DArT markers, rice accessions can be classified into two major varieties of Asian cultivated rice: the *Indica* and *Japonica* subspecies. In our collection, there were 45 *Indica* accessions and 30 *Japonica* accessions. Fig. 4A illustrates that the RS content in *Indica* rice was 0.204±0.028 mg/100 mg, whereas it was 0.099±0.005 mg/100 mg in *Japonica* rice. As a result, the *Indica* rice had significantly greater in RS content than *Japonica* rice ($p<0.001$).

Moreover, this study also obtained a significant difference in RS content between grain sizes. RS content was higher in short (0.167±0.01 mg/100 mg) and medium grain (0.217±0.032 mg/100 mg) compared to long grain (0.107±0.004 mg/100 mg) ($p<0.05$) (Fig. 4B).

Figure 4C compared upland (UP), RL, mangrove (MG), and irrigated (IR) ecosystems in terms of the amount of RS. It was noticeable that the rice in RL could be considered to have a tremendous amount of RS (0.251±0.028 mg/100 mg) compared with the RS amount of rice from MG (0.047±0.0008 mg/100 mg) and UP (0.09±0.047 mg/100 mg) ecosystems. There were significant differences in RS content between RL or irrigated (IR) ecosystems and MG and LL ($p<0.001$). However, the RS content was not significantly different between rice is grown in IR and RL ($p>0.05$).

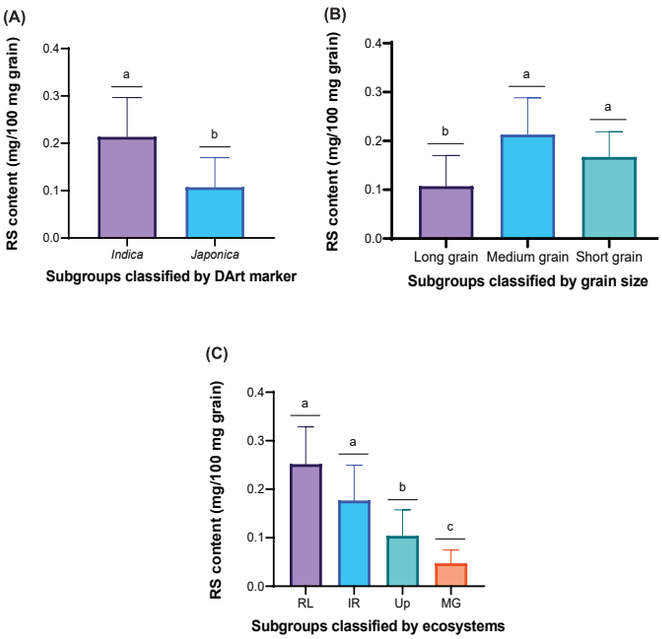

Fig. 4. The association between RS content and (A) rice varieties, (B) grain length, and (C) ecosystem. The letters above the dataset indicate the statistical difference. Abbreviations: RL (rainfed lowland), IR (irrigated), Up (upland), MG (mangrove).

4. Discussion

Our study is the first study investigating the diversity of RS in Vietnamese rice among a large rice collection using the RS assay kit (Rapid) from Megazyme. The results showed a wide range of RS among the 75 investigated rice accessions, ranging from 0.015 to 0.71%. Our study's range of RS content was low compared to the RS content of 10.1 to 18% in others study, which also used the same quantification method [16]. In another study, the RS content of rice ranges from 0.1 to 25.4% [17]. Different methods for RS quantification have been proposed using enzymes [3, 17]. RS values may differ in different studies due to rice varieties, ecosystems, and the quantification methods.

Among the 75 samples analysed, approximately 70.67% of samples had RS content of between 0.015 and 0.2 mg/100 mg, 18.67% of samples had RS concentrations between 0.2 and 0.4 mg/100 mg, 6.67% of samples had RS quantities in the range of 0.4-0.6 mg/100 mg, and only 4% samples had RS levels in the range of 0.6-0.8 mg/100 mg.

Our study also indicated more amylose in *Indica* rice grains than in *Japonica* rice grains. Generally, the amount of amylose in rice grain is positively associated with the amount

of RS [18]. In contrast, amylopectin, which accounts for 80-85% of the starch humans can readily digest, is negatively correlated with the amount of RS [19]. That means more amylose content in the diet will increase the RS level while more amylopectin content in the diet will decrease the RS level. If there is more amylose, rice is digested more slowly and has a lower glycaemic index [1]. This result implies that *Indica* rice is digested slower than *Japonica* rice because it has a higher proportion of RS. Thus, *Indica* rice is a primary source of RS, and it may be used as a therapeutic agent in the diets of people with metabolic problems [20]. The waxy rice, such as *Japonica* and low amylose rice, has faster and more complete starch hydrolysis than intermediate and high amylose rice [18]. The fact is that higher amounts of amylose or RS make it more difficult to cook rice. These types of rice also have a firm texture because RS raises the gelatinization temperature and lowers the peak viscosity values of rice [20]. Moreover, crystallisation also affects RS content. High-amylose starch, which displays a C-type crystalline structure, contains a lower content of A-type crystalline structure than waxy and normal starches in rice [21]. When side chains of clustered amylopectin and amylose form crystalline structures, it is demonstrated that a higher proportion of crystallinity correlates with more rapidly digestible starch [22]. These results indicate that more crystalline structures will decrease the RS content.

Our study found that short and medium grains had higher RS content than long grains in terms of grain size. W. Zhang, et al. (2022) [23] also pointed out that smaller starch granules had higher RS content than bigger ones. X. Shu, et al. (2014) [24] observed that the starch granule diameter is negatively correlated with starch digestibility. The larger surface area in long grains increase enzyme binding rates and consequently ease digestion [25].

Regarding ecosystems affecting RS content, our study showed that the rice from rainfed lowland ecosystems could be considered to have the most significant amount of RS compared to the RS amount of rice from the MG and UP ecosystems. There has not been any study examining the RS content in different rice varieties grown in diverse ecosystems. In some other studies, scientists compared the effects of environmental factors including light, air temperature, water stress, and soil quality in terms of producing amylose and amylopectin, which are also related to RS content [26]. Due to the impact of water supplementation, J.A. Patindol, et al. (2015) [27] reported that during the reproductive stage of growth, rice was sensitive to water deficit and rainy spells. If drought occurs during the ripening stage of rainfed lowland rice, the result is decreased amylose content, which may reduce RS content in grains after that [28]. Therefore, our research results can be considered relevant to other studies.

5. Conclusions

In summary, our research focuses on correlating RS content in rice with different rice types and ecosystems. Regarding the RS amount in different types of rice, the *Indica* rice subgroup had a higher value (0.204±0.028 mg/100 mg) than the *Japonica* rice subgroup (0.099±0.005 mg/100 mg). Short and medium grains had higher RS content than long grains. Regarding ecosystems, the RL showed the greatest amount of RS (0.251±0.028 mg/100 mg), followed by MG (0.047±0.0008 mg/100 mg), and UP (0.09±0.047 mg/100 mg). To have firm conclusions, some other results should be further evaluated in larger amounts of the sample. In the realm of food and nutrition, our results contribute to helping nutritionists and doctors develop a suitable rice-based diet for patients with diabetes or obesity.

6. Recommendations

The results from our study can provide insight into the RS in rice for a future genome-wide association study of RS content to identify the genes or QTLs relating to high RS content in rice.

CRediT author statement

Thi Mai Huong To: Conceptualisation, Methodology and Reviewing; Thi Linh Nguyen: Investigation, Data curation; Thi Ngoc An Do: Investigation; Lan Phuong Nguyen: Investigation; Nga T.P. Mai: Conceptualisation, Methodology, Writing - Reviewing and Editing.

ACKNOWLEDGEMENTS

We thank the Vietnam Academy of Science and Technology for financial support (under grant number USTH.YOUTH.LS.01/22) and for supplying the facilities to perform the project.

COMPETING INTERESTS

The authors declare that there is no conflict of interest regarding the publication of this article.

REFERENCES

[1] R.L. Ordonio, M. Matsuoka (2016), "Increasing resistant starch content in rice for better consumer health", *Proc. Natl. Acad. Sci. USA*, **113(45)**, pp.12616-12618, DOI: 10.1073/pnas.1616053113.

[2] M.A.B. Khan, M.J. Hashim, J.K. King, et al. (2020), "Epidemiology of type 2 diabetes - global burden of disease and forecasted trends", *J. Epidemiol. Glob. Health*, **10(1)**, DOI: 10.2991/jegh.k.191028.001.

[3] H.N. Englyst, S.M. Kingman, J.H. Cummings (1992), "Classification and measurement of nutritionally important starch fractions", *Eur. J. Clin. Nutr.*, **46(2)**, pp.35-50.

[4] D.M. Kasote, S.S. Nilegaonkar, V.V. Agte (2014), "Effect of different processing methods on resistant starch content and *in vitro* starch digestibility of some common Indian pulses", *Journal of Scientific and Industrial Research*, **73(8)**, pp.541-546.

[5] C.Z. Yang, X.L. Shu, D.X. Wu, et al. (2006), "Starch properties of mutant rice high in resistant starch", *J. Agric. Food Chem*., **54(2)**, pp.523-528, DOI: 10.1021/jf0524123.

[6] Y. Zeng, M.K. Ali, J. Du, et al. (2022), "Resistant starch in rice: Its biosynthesis and mechanism of action against diabetes-related diseases", *Food Reviews International*, DOI: 10.1080/87559129.2021.2024221.

[7] D.F. Birt, T. Boylston, S. Hendrich, et al. (2013), "Resistant starch: Promise for improving human health", *Adv. Nutr.*, **4(6)**, pp.587-601, DOI: 10.3945/an.113.004325.

[8] M.H. Chen, C.J. Bergman, A.M. McClung, et al. (2017), "Resistant starch: Variation among high amylose rice varieties and its relationship with apparent amylose content, pasting properties and cooking methods", *Food Chem.*, **234**, pp.180-189, DOI: 10.1016/j.foodchem.2017.04.170.

[9] Q. Chen, J. Zhang, Y. Zhang, et al. (2022), "Protein-amylose/amylopectin molecular interactions during high-moisture extruded texturization toward plant-based meat substitutes applications", *Food Hydrocoll.*, **127**, DOI: 10.1016/j.foodhyd.2022.107559.

[10] Q. Li, X. Liu, C. Zhang, et al. (2018), "Rice soluble starch synthase I: Allelic variation, expression, function, and interaction with waxy", *Front. Plant Sci*., **9**, DOI: 10.3389/fpls.2018.01591.

[11] J. Bao, X. Zhou, F. Xu, et al. (2017), "Genome- wide association study of the resistant starch content in rice grains", *Starch - Stärke*, **69(7-8)**, DOI: 10.1002/star.201600343.

[12] S. Parween, J.J. Anonuevo, V.M. Butardo, et al. (2020), "Balancing the double-edged sword effect of increased resistant starch content and its impact on rice texture: Its genetics and molecular physiological mechanisms", *Plant Biotechnol. J.*, **18(8)**, pp.1763- 1777, DOI: 10.1111/pbi.13339.

[13] N. Zhang, M. Wang, J. Fu, et al. (2020), "Identifying genes for resistant starch, slowly digestible starch, and rapidly digestible starch in rice using genome-wide association studies", *Genes and Genomics*, **42(11)**, pp.1227-1238, DOI: 10.1007/s13258-020-00981-1.

[14] N.T.P. Phung, C.D. Mai, P. Mournet, et al. (2014), "Characterization of a panel of Vietnamese rice varieties using DArT and SNP markers for association mapping purposes", *BMC Plant Biology*, **14(1)**, DOI: 10.1186/s12870-014-0371-7.

[15] Megazyme, Resistant Starch Assay Kit (Rapid), https://www.megazyme.com/resistant-starch-assay-kit-rapid, accessed 30 March 2022.

[16] X. Kong, Y. Chen, P. Zhu, et al. (2015), "Relationships among genetic, structural, and functional properties of rice starch", *J. Agric. Food Chem.*, **63(27)**, pp.6241-6248, DOI: 10.1021/acs.jafc.5b02143.

[17] I. Goñi, L.G. Diz, E. Mañas, et al. (1996), "Analysis of resistant starch: A method for foods and food products", *Food Chem.*, **56(4)**, pp.445-449, DOI: 10.1016/0308-8146(95)00222-7.

[18] P. Hu, H. Zhao, Z. Duan, et al. (2004), "Starch digestibility and the estimated glycemic score of different types of rice differing in amylose contents", *J. Cereal Sci.*, **40(3)**, pp.231-237, DOI: 10.1016/j.jcs.2004.06.001.

[19] X. Shu, L. Jia, J. Gao, et al. (2007), "The influences of chain length of amylopectin on resistant starch in rice (*Oryza sativa* L.)", *Starch*, **59(10)**, pp.504-509, DOI: 10.1002/star.200700640.

[20] S. Mahadevamma, R.N. Tharanathan (2004), "Processing of legumes: Resistant starch and dietary fiber contents", *J. Food Qual.*, **27(4)**, pp.289-303, DOI: 10.1111/j.1745-4557.2004.00620.x.

[21] X. Luo, B. Cheng, W. Zhang, et al. (2021), "Structural and functional characteristics of Japonica rice starches with different amylose contents", *CyTA - Journal of Food,* **19(1)**, pp.532-540, DOI: 10.1080/19476337.2021.1927194.

[22] B.M.J. Martens, W.J.J. Gerrits, E.M.A.M. Bruininx, et al. (2018), "Amylopectin structure and crystallinity explains variation in digestion kinetics of starches across botanic sources in an *in vitro* pig model", *J. Anim. Sci. Biotechnol.*, **9(91)**, DOI: 10.1186/s40104-018-0303-8.

[23] W. Zhang, Y. Liu, X. Luo, et al. (2022), "Pasting, cooking, and digestible properties of *Japonica* rice with different amylose contents", *International J. of Food Properties*, **25(1)**, pp.936-947, DOI: 10.1080/10942912.2022.2069806.

[24] X. Shu, J. Sun, D. Wu (2014), "Effects of grain development on formation of resistant starch in rice", *Food Chem.*, **164**, pp.89-97, DOI: 10.1016/j.foodchem.2014.05.014.

[25] K.S. Sandhu, S.T. Lim (2008), "Digestibility of legume starches as influenced by their physical and structural properties", *Carbohydr. Polym.*, **71(2)**, pp.245-252, DOI: 10.1016/j.carbpol.2007.05.036.

[26] S.A. Zaman, S.R. Sarbini (2016), "The potential of resistant starch as a prebiotic", *Crit. Rev. Biotechnol.*, **36(3)**, pp.578-584, DOI: 10.3109/07388551.2014.993590.

[27] J.A. Patindol, T.J. Siebenmorgen, Y.J. Wang (2015), "Impact of environmental factors on rice starch structure: A review", *Starch*, **67(1-2)**, pp.42-54, DOI: 10.1002/star.201400174.

[28] M. Fofana, M. Cherif, B. Kone, et al. (2010), "Effect of water deficit at grain ripening stage on rice grain quality", *J. Agric. Biotechnol. Sustain. Dev.*, **2(6)**, pp.100-10, DOI: 10.5897/JABSD.9000013.

A study on *in vitro* antioxidant effect of *Cordyceps neovolkiana* DL0004 extracts isolated in Lam Dong, Vietnam

Khac Ky Lam[1, 2, 3], Thi Bao Tran Nguyen[3], Thi Huynh Nhu Nguyen[3], Thi Thanh Lai Le[3], Sao Mai Dam[3], Minh Hiep Dinh[4], Dai Hung Ngo[5*]

[1]*Vietnam National University-Ho Chi Minh City, Linh Trung Ward, Thu Duc District, Ho Chi Minh City, Vietnam*

[2]*University of Science, Vietnam National University-Ho Chi Minh City, 227 Nguyen Van Cu Street, Ward 4, District 5, Ho Chi Minh City, Vietnam*

[3]*Industrial University of Ho Chi Minh City, 12 Nguyen Van Bao Street, Ward 4, Go Vap District, Ho Chi Minh City, Vietnam*

[4]*Ho Chi Minh City Department of Agriculture and Rural Development, 176 Hai Ba Trung Street, Dakao Ward, District 1, Ho Chi Minh City, Vietnam*

[5]*Thu Dau Mot University, 6 Tran Van On Street, Phu Hoa Ward, Thu Dau Mot City, Binh Duong Province, Vietnam*

Received 20 May 2022; revised 8 June 2022; accepted 27 June 2022

Abstract:

***Cordyceps neovolkiana* DL0004 is a group of insect parasitic fungi collected at an altitude of 1650 m above sea level at the top of Langbiang Mountain, Lam Dong province, Vietnam. *C. neovolkiana* DL0004 has been used in traditional medicine and possesses numerous biological effects such as anti-cancer, anti-inflammation, antioxidant properties. In this research, the fungi biomass and fruiting body of *C. neovolkiana* DL0004 were cultured and examined for their antioxidant properties using test methods such as reducing power, scavenging 2,2'-diphenyl-1-picrylhydrazyl (DPPH) free radical, neutralizing 2,2'-azinobis(3-ethylbenzothiazonline-6-sulfonate (ABTS) free radical, and inhibiting xanthine oxidase (XO). The results showed that all 7 extracts of the biomass were more active than the fruiting bodies of *C. neovolkiana* DL0004. Furthermore, the ethyl acetate (EtOAc) extract of *C. neovolkiana* DL0004 biomass showed DPPH, ABTS, and XO free radical scavenging with IC_{50} values (the concentration of the sample required to inhibit 50% of radical) of 107.01 µg/ml, 111.91 µg/ml, and 106.2248 µg/ml, respectively. Moreover, the reducing power of the EtOAc from *C. neovolkiana* DL0004 biomass was 0.184 at 1000 µg/ml. From the obtained results, the biomass EtOAc fraction extract of *C. neovolkiana* DL0004 was demonstrated to contain antioxidant compounds with potential applications in the production of functional foods.**

Keywords: **antioxidant, *Cordyceps neovolkiana*, reducing power, scavenging free radicals, xanthine oxidase inhibitors.**

Classification numbers: **3.4, 3.5**

1. Introduction

Oxidation is a necessary process in the body's metabolism as cells use oxygen to create energy. Free radicals are generated as a result of adenosine triphosphate (ATP) production by mitochondria. However, excessive free radicals will disrupt the redox balance, causing oxidative stress to damage the structures of cells and leading to dangerous diseases such as cancer and heart disease. Therefore, using compounds of natural origin to prevent oxidative stress is of interest [1]. In particular, *C. neovolkiana* DL0004, an insect parasitic fungus isolated and published in Vietnam, has showed some biological activities under laboratory conditions [2]. This species of fungi is attracting research attention worldwide with its anti-cancer, antioxidant, antibacterial, and immune-enhancing properties. The main aim of this study was to identify the antioxidant potential of cultivated biomass and fruiting body extracts of *C. neovolkiana* DL0004 isolated from the top of Langbiang Mountain, Lam Dong province, Vietnam. This study will create an availability of raw materials in the production of functional food products to meet the goal of serving the community.

2. Materials and methods

2.1. Materials

C. neovolkiana DL0004 was collected at an altitude of 1650 m in the top of Langbiang Mountain, Lam Dong province, Vietnam, and the strain was stored at the University of Science, Vietnam National University, Ho Chi Minh City (No. US.F021). This fungal strain was isolated, purified, and identified by molecular pedigree analysis of the region ITS1-5.8S-ITS2.

*Corresponding author: Email: hungnd@tdmu.edu.vn

2.2. Preparation of extracts

Strains were activated to restore fungal-like activity after seed keeping. Transplantation of the strains was conducted from agar to a more nutrient-rich liquid medium to rapidly increase the number of *C. neovolkiana* DL0004 mycelium before inoculating the culture medium. In the next step, the samples were inoculated into Erlenmeyer flasks containing 200 ml of autoclaved potato glucose medium and incubated at 20-25°C for 10-12 days.

The biomass was cultured on liquid-static medium in polypropylene plastic containers. The composition of the medium includes 200 ml of nutrient solution with 20% potato juice, 0.05% sucrose, 0.006% peptone, 0.004% high yeast, 0.0005% KH_2PO_4, and 0.0002% $MgSO_4.7H_2O$. The liquid seed (4%) was cultured statically for 5 days at 23°C. The biomass was collected after 40 days of inoculation and was dried at 60°C to constant weight and stored in a dry place at 20°C.

The mycelium after secondary propagation was inoculated into a semi-solid culture medium consisting of brown rice and millet with a weight of 40 g/box with different ratios and the addition of 70 ml of distilled water (DW)/box. This culture medium box was sterilized at 121°C for 30 min to which 5 ml of mycelium was added (5 ml/box) and then incubated at 22±2°C in the dark for 20 days. After that, the culture medium box was exposed to light to stimulate fruiting. The fruit bodies were collected on the 60th day and then were dried at 60°C to constant weight and stored in a dry place at 20°C.

2.3. Extraction process

The biomass and fruiting bodies of *C. neovolkiana* DL0004 were dried, ground, and extracted by liquid-liquid extraction with the principle of increasing polarity. The biomass was thoroughly extracted in 96% ethanol (EtOH) and evaporated to obtain a total EtOH. The total EtOH extract was fractionated with solvents of increasing polarity such as petroleum ether (PE), EtOAc, n-Butanol (n-BuOH), and DW to obtain the extracts after time in a rotating evaporator. The biomass culture was precipitated with cold EtOH to obtain high exopolysaccharide (EPS). The biomass residue after extraction with EtOH was kept and dried at 50°C to constant weight. Water extraction was carried out by boiling the biomass residue with water at a ratio of 1:10 (w/v). Biomass residues were boiled for 60 min, centrifuged, and evaporated to obtain the polysaccharide extracts (PSs). After that, the PSs were stored in a dry place at 20°C. The biomass extraction moisture content and efficiency were 3.7 and 28.36% EtOH, 1.05 and 5.64% PE, 6.9 and 4.86% EtOAc, 1.96 and 3% n-BuOH, 7.79 and 12% DW, 6.71 and 6.11% PS, and 13.67 g/l EPS.

2.4. Experiment chemicals

2,2'-diphenyl-1-picrylhydrazyl (DPPH) was purchased from Sigma-Aldrich (St. Louis, MO, USA). ABTS, XO and Allopurinol were purchased from Merck. All other reagents were of the highest grade available commercially.

2.5. Reducing power assay

The reducing power assay described by IC. Ferreira, et al. (2007) [3] was followed with slight modification. In detail, 0.5 ml of 0.2 M sodium phosphate buffer of pH 6 was added to 0.2 ml of the *C. neovolkiana* DL0004 biomass solution (1000, 2000, 3000, 4000, and 5000 µg/ml). In the next step, 0.5 ml of 1% $K_3[Fe(CN)_6]$ solution was added to the mixture and incubated at 50°C for 20 min. After that, 0.5 ml of 10% trichloroacetic acid solution was added and mixed. From this mixture, 0.8 ml of supernatant was poured into 2 ml of DW and 0.4 ml $FeCl_3$ 1%, respectively. The optical density (OD) of the liquid was measured at 700 nm.

2.6. 2,2'-diphenyl-1-picrylhydrazyl (DPPH) assay

C. neovolkiana DL0004 extracts were investigated for their radical scavenging activity by using DPPH assay according to method of O.P. Sharma, et al. (2009) [4], which was adapted to the laboratory conditions. Briefly, the 0.5 ml of sample solution was mixed with 0.75 ml of DPPH• solution, vortexed evenly, and incubated for 30 min in the dark at room temperature. The OD of the mixture was measured at 517 nm. Blanks were made by adding 0.5 ml of *C. neovolkiana* DL0004 fruiting body solution (200, 400, 600, 800, and 1000 µg/ml) and *C. neovolkiana* DL0004 biomass solution (1000, 2000, 3000, 4000, and 5000 µg/ml) to 0.75 ml of 80% methanol solution. Blank controls include 80% methanol and 0.75 ml DPPH solution. In the sample, if the IC_{50} value was low, the free radical scavenging activity was high.

The following equation, DPPH inhibition (%) = (1-A/B) x 100, where A is the absorbance difference between sample solution with DPPH• reagent and the sample solution without DPPH• reagent and B is its native solvent, was used to determine the DPPH inhibition. Ascorbic acid was used as a positive control. The experiments were independently performed three times.

2.7. ABTS assay

The $ABTS^+$ radical scavenging activity assay was carried out according to the method of N. Nenadis, et al. (2004) [5]. $ABTS^+$ free radical solution was prepared by adding 7-mM ABTS solution in equal volume to 2.45 mM $K_2S_2O_8$ solution, incubating the solution in the dark for 16 hours, then diluting and adjusting the absorbance of the solution at 734 nm to 0.7±0.02 (solution A). The experiment was carried out by adding 3000 µl of solution

A to 100 µl of the sample solution for analysis. The mixture was incubated in the dark for 30 min and OD was measured at 734 nm.

2.8. XO inhibitory activity

XO is an enzyme capable of generating strong oxidizing reactions and catalysing the oxidation of hypoxanthine to xanthine and from xanthine to uric acid [3]. Uric acid has a maximum absorption wavelength at 290 nm. The initial reaction mixture contained 0.05 XO UI (XO diluted in 50 - mM potassium phosphate buffer pH 7.5) and test samples at different concentrations (stock sample in 5% DMSO solution), which were incubated at room temperature (25°C) for 15 min. Then the reaction was supplemented with xanthine at a concentration of 400 mg/ml and incubated at room temperature for 30 min. Finally, 1 N HCl solution was added to stop the reaction. The absorbance of the reaction mixture was then measured using a spectrophotometer at 290 nm. In parallel with each test sample, a blank was prepared similarly but without the addition of XO enzyme to the well with the enzyme volume replaced by buffer. At the same time, the sample was not incubated, but HCl was added to finish the reaction. The percent inhibition was determined by:

$$\% \text{ Inhibition} = (OD_o - OD_S) \times 100/OD_0$$

where OD_o: optical density of blank (replace XO enzyme with buffer); OD_S: optical density of test sample..

3. Results and discussion

3.1. Reducing power assay

Reducing power is an important property in the expression of antioxidant potential of extracts and is used to screen for experiments showing the presence of reducing agents. W.C. Kan, et al. (2012) [6] also demonstrated that the extracts using alcohol as a solvent are rich in biologically active substances such as nucleosides, polysaccharides, proteins, etc., which have strong antioxidant potential as well as properties of preservation and protection of cell functions. After surveying the reducing potential of the extracts in the concentration range from 0-5000 µg/ml, the results of Fig. 1 show that at the concentration of 1000 µg/ml, all fungi biomass extracts were able to reduce electrons better than the extract from the fruiting body of the fungi. In 2014, when studying the antioxidant capacity of *C. militaris* extract, C.H. Dong, et al. (2014) [7] showed that in the concentration range from 0-10 mg/ml, the reducing power of the extracts exhibited a linear dose-dependent activity and the extracts from the biomass had a stronger reducing power than that of the fruit bodies. In this study, the value of OD of ascorbic acid, 1.23±0.001 at 100 µg/ml, had a stronger reducing power than the value of OD of the extracts at the concentration of 1000 µg/ml in the experiment. For example, from the fungal biomass including aqueous extract 0.075, EtOAc 0.184, EtOH 0.069, and n-BuOH 0.121, respectively, as compared with the results of Huynh Thu's thesis also on *C. neovolkiana* DL0004 including water extracts 0.1, EtOAc 0.19, and n-BuOH 0.13 are roughly equivalent. Therefore, these fractions were used for further experiments.

In the case of PS and EPS from the biomass and fruiting bodies, the values reflected lower reducing potential than those extracted with organic solvents. It is possible that the composition of PS and EPS are very heterogeneous and the molecular functional groups are not arranged to promote maximum chemistry. To overcome these limitations as well as to utilize and increase the activity of the groups of substances in this group of extracts, Z. Tang, et al. (2020) [8] isolated crude polysaccharides from *Amaranthus hybridus* fungus using microwave-assisted extraction. Further purification by chromatography with DEAE-32 cellulose and two fractions with higher reducing power activity were obtained. On the other hand, as announced by L. Xiao, et al. (2020) [9] after adding nanobubble water during *C. militaris* culture to promote mass transfer, chemical reaction, and metabolism, the PS extract had increased reducing activity with achieved OD values of 0.95, 2.13, 2.00, and 1.29 at a concentration of 2 mg/ml.

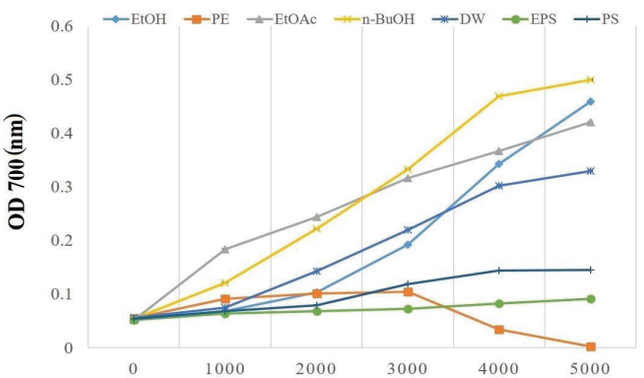

Fig. 1. Reducing power of C. *neovolkiana* DL0004 biomass.

3.2. DPPH assay

To further confirm the antioxidant potential of the extracts, DPPH assays were used in this study. The extracts had the ability to neutralize DPPH free radicals thus contained compounds capable of H^+ donation and electron transfer (Fig. 2).

Figs. 2A, 2B show that at the concentration of 1000 µg/ml, the percentage of DPPH free radical scavenging of the compounds present in the biomass extract was higher than that of the fruiting bodies. The extract from the fruiting bodies with the highest radical scavenging value was only

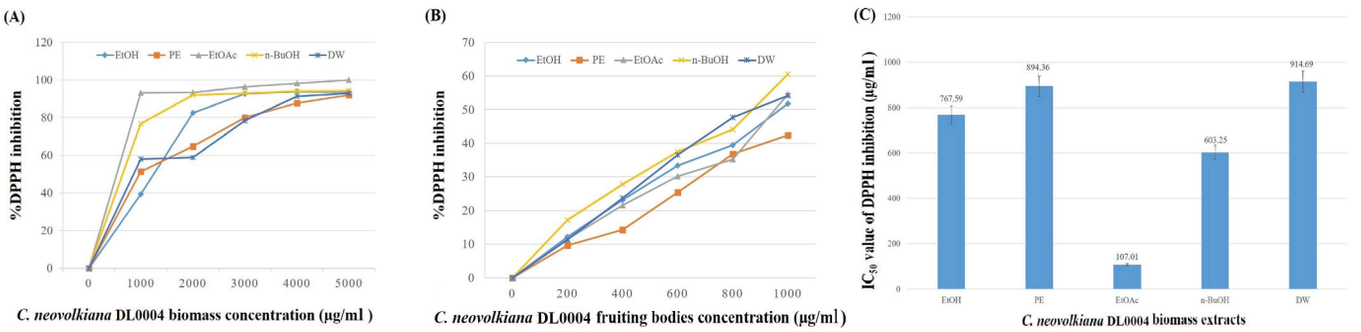

Fig. 2. Percent DPPH inhibition of (A) *C. neovolkiana* DL0004 biomass and (B) *C. neovolkiana* DL0004 fruiting bodies, (C) IC_{50} value of DPPH inhibition of *C. neovolkiana* DL0004 biomass extracts.

60.17% (n-BuOH) at a concentration of 1000 µg/ml. The results showed that the total DPPH radical scavenging capacity of the extracts from the fruiting bodies was smaller than that of the biomass. Moreover, this result is also consistent with the results that we studied and published in 2021 on *C. takaomontana* DL0038A. According to the report of C.H. Dong, et al. (2014) [7] of the comparison between the antioxidant potential of methanol extract from the fruit body and cultured biomass of *C. militaris*, the DPPH radical scavenging efficiency of the fruit body increased with increasing concentration and was higher than those extracted from biomass. According to the results of Fig. 2A, it is seen that EtOAc fungal biomass reached a 93.14% ability to capture DPPH radical at a concentration of 1000 µg/ml compared with ascorbic acid (95.1%) at 10 µg/ml. This result was higher than other extracts and continuously demonstrated high values at the investigated concentrations. Fig. 2C of the IC_{50} values of biomass extracts showed that compounds in biomass EtOAc extract had antioxidant potential.

Figure 2C also shows that the IC_{50} value of DPPH inhibition of EtOAc fungal biomass is 107.01 µg/ml, much lower than that of other fungal biomass extracts, indicating that compounds in fungi EtOAc extract had antioxidant potential. The results were also similar to the EtOAc extract of *C. takaomontana* DL0038A with the lowest IC_{50} value among the previously investigated extracts.

3.3. $ABTS^{\bullet+}$ assay

Because both PS and EPS extracts are insoluble in methanol, which is used as a solvent in DPPH assays the radical scavenging activity against free radical ability was conducted with ABTS assay for comparison to the DPPH results. In the determination of the DPPH radical scavenging ability, the studied sample has the ability to capture $ABTS^{\bullet+}$ radicals. This result showed that there are compounds capable of donating H^+ or transferring electrons to free radicals directly and, as a result, form more stable products (Fig. 3).

Similar to the result of the DPPH assay, the ABTS free radical scavenging ability of most fruiting body extracts was lower than that of biomass extracts (Fig. 3A and 3B). At a concentration of 1000 µg/ml, the n-BuOH extract and the EtOAc biomass extracts achieved radical capture rates of 82.77 and 99.63%, respectively, compared with the 99.81% rate of ascorbic acid at 80 µg/ml.

In the case of PS and EPS groups, the ABTS free radical scavenging ability that we investigated had a low value corresponding to a reducing potential. The reason for this is that the PS and EPS extracts had low ABTS radical scavenging activity. It was pointed out by W. Chen, et al. (2016) [10] in their survey of ABTS radical capture rates of all *C. militaris* polysaccharides that were dehydrated by freeze-drying, spray-drying, and hot air-drying, which were all lower than 50% at a concentration of 6.0 mg/ml. To

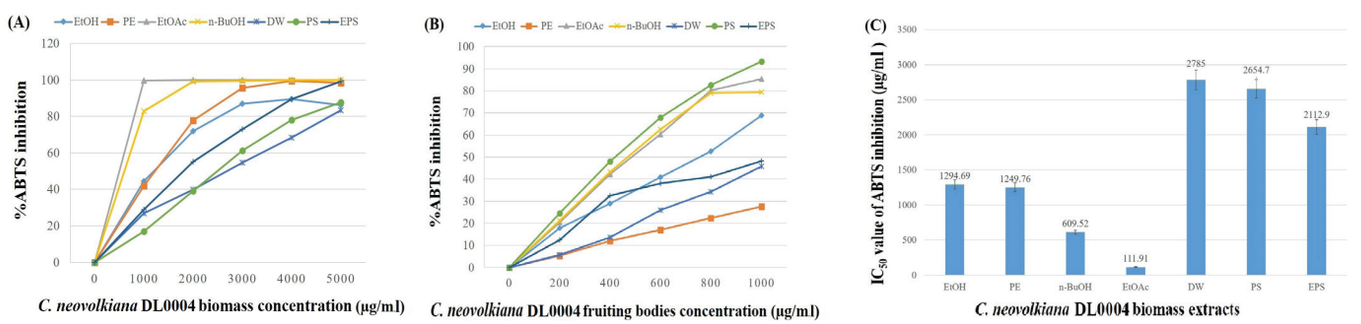

Fig. 3. Percent ABTS inhibition of (A) *C. neovolkiana* DL0004 biomass and (B) *C. neovolkiana* DL0004 fruiting bodies, (C) IC_{50} value of ABTS inhibition of *C. neovolkiana* DL0004 biomass extracts.

improve the activity of this group of extracts, it is necessary to apply many methods of support or to form a mixture with other materials. In 2020, L. Xiao, et al. (2020) [9] published the results of a survey of the ABTS radical scavenging ability of PS extracts from *C. militaris*, which reflected a dependence on the concentration of Nanobubble water (NBW). The NBW-supplemented extracts exhibited higher ABTS radical neutralization at all examined concentrations.

In general, the PS extracts had lower ABTS neutralizing activity in most studies compared with the control combination for the formation of new complexes [11] with the exception of fruit body extracts, which may have routine ABTS values up to 93.25% at concentrations of 1000 mg/ml (<EtOAc biomass value, so we will consider this case in another article). However, it has also been reported that polysaccharide fractions extracted from *C. violaceum*, *F. velutipes*, and *P. ginseng* had a higher ability to neutralize ABTS than vitamin C. This result shows that the application method may be more suitable for hydrophilic antioxidant compounds than other free radicals such as DPPH. Optimizing new reaction conditions can prevent extraction of denatured polysaccharides or weaken structural integrity [12]. Y. Yuan, et al. (2018) [13] found that the high sulphur content in the structure of polysaccharides from *Ulva prolifera* had a clear role in improving ABTS radical scavenging. The presence of ketone or aldehyde groups, high uronic acid content, and abundant monosaccharide components can increase the radical scavenging capacities of ABTS by acidifying polysaccharides.

Figure 3C shows that the ABTS results are similar to the DPPH results as EtOAc biomass has the highest ABTS free radical scavenging ability (IC_{50} value is 111.91 µg/ml). This result is also consistent with the results of the reduction capacity survey, so the highest potential fraction with *in vitro* antioxidant capacity is the biomass EtOAc extract.

3.4. XO inhibition ability

After the results of potential fractionation comprising compounds with antioxidant properties, the ability to inhibit the oxidizing enzyme XO of biomass extracts was investigated. XO is an enzyme capable of oxidizing purines to their final product, uric acid, and increased uric acid is a major cause of arthritis (gout) and metabolic diseases such as diabetes, obesity, high blood pressure, and cardiovascular disease [3]. Antioxidant compounds have the ability to inhibit XO to reduce uric acid levels in the body.

The results of the investigation of XO inhibitory activity of extracts from *C. neovolkiana* DL0004 biomass is shown in Table 1, which demonstrates that most of the extracts were able to inhibit XO activity. EtOAc was able to strongly inhibit XO activity (62.144±0.69% at the concentration of 125 µg/ml) compared with the other extracts. These results were higher than those of Vu Anh Tung at the concentration of 150 µg/ ml with their EtOAc extract from *C. neovolkiana* DL0004 peaking at only 5.37%. Huynh Thu also stated that out of all surveyed fungi, *O. sinensis* showed the highest XO inhibitory activity (at a concentration of 100 µg/ml, high PE and EtOAC inhibited 21.21±0.36% and 16.28±0.20%, respectively) [3]. The fungi *C. neovolkiana* DL0004 and *C. pseudomilitaris* exhibited weak inhibitory activity. The XO inhibitory activity of PS extract from *C. neovolkiana* DL0004 did not increase when increasing concentration.

Table 1. Xo inhibition ability of *C. neovolkiana* DL0004 biomass extracts.

XO inhibition (%)						
Extract	*0*	*62.5*	*125*	*250*	*500*	*1000*
EtOH	0	-	9.144±2.413	54.221±1083	58.047±1.797	99.262±0.125
PE	0	2.55±1.0553	7.55±0.5343	36.98±1.0409	48.9±0.2923	99.58±1.9921
EtOAc	0	31.386±1.018	62.144±0.690	-	-	-
n-BuOH	0	2.663±0.328	3.579±0.404	3.573±0.443	13.742±0.225	43.611±0.153
Water	0	11.794±0.863	20.502±0.744	27.218±0.213	28.769±1.085	31.185±0.740

(-): The OD value was not found at the investigated concentration.

The ability of EtOAc to inhibit XO extract from *C. neovolkiana* DL0004 biomass linearly increased with concentrations from 0 to 125 µg/ml as seen in Table 2 from which the IC_{50} value was 106.2248 µg/ml. Tran Ngoc Quy also published results of XO inhibition from four extracts (hexane, chloroform, ethyl acetate, and water) of *Cordyceps militaris* L. fruit bodies, which indicated that XO inhibitory ability was highest in EtOAc extracts (31.66% at a concentration of 100 µg/ml) [14].

Table 2. Xanthine oxidase inhibition ability of *C. neovolkiana* DL0004 biomass EtOAc extracts.

Concentration (µg/ml)	0	25	50	75	100	125
XO inhibition (%)	0	9.58±0.738	19.269±1.031	34.613±1.175	41.976±0.676	61.976±0.732

4. Conclusions

The results of this study showed that the biomass and fruiting bodies from the *C. neovolkiana* DL0004 fungal strain isolated in Vietnam were successfully cultured and EtOAc-extracted C. *neovolkiana* DL0004 biomass was a high potential antioxidant in scavenging free radicals with IC_{50} 107.01 µg/ml (DPPH), 111.91 µg/ml (ABTS), and 106.2248 µg/ml (XO). From the above results, it was shown that *C. neovolkiana* DL0004 biomass isolated in Vietnam is a potential source of bioactive raw materials. This finding

is the key to future research unlocking the production of functional foods or raw materials for the pharmaceutical industry.

CRediT author statement

Khac Ky Lam: Sample analysis, Data processing, Writing the manuscript; Thi Bao Tran Nguyen: Map drawing, Supporting writing; Thi Huynh Nhu Nguyen: Samples collection, Supporting data analysis; Thi Thanh Lai Le: Samples collection, Supporting data analysis; Sao Mai Dam: Comment on editing the manuscript for completeness; Minh Hiep Dinh: Orientation for research; Dai Hung Ngo: Supervise.

ACKNOWLEDGEMENTS

This study was supported by Department of Biochemistry, Faculty of Biology - Biotechnology, University of Science, Vietnam National University, Ho Chi Minh city; Institute of Biotechnology and Food Technology, Industrial University of Ho Chi Minh city.

COMPETING INTERESTS

The authors declare that there is no conflict of interest regarding the publication of this article.

REFERENCES

[1] U. Attanasioa, F. Pirozzi, R. Poto, et al. (2021), "Oxidative stress in anticancer therapies-related cardiac dysfunction", *Free Radical Biology and Medicine*, **169**, pp.410-415, DOI: 10.1016/j.freeradbiomed.2021.04.021.

[2] V.T. Luyen, D.T. Lao, V.H. Trinh, et al. (2017), "Analysis of nrLSU gene to support identification of fungus belonging to *Cordyceps* genus and clavicipitaceae family", *Journal of Science and Technology*, **55(1A)**, pp.93-98, DOI: 10.15625/2525-2518/55/1A/12385.

[3] I.C.F.R. Ferreira, P. Baptista, M.V. Boas, et al. (2007), "Free-radical scavenging capacity and reducing power of wild edible mushrooms from northeast Portugal: Individual cap and stipe activity", *Food Chemistry*, **100(3)**, pp.1511-1516, DOI: 10.1016/j. foodchem.2005.11.043.

[4] O.P. Sharma, T.K. Bhat (2009), "DPPH antioxidant assay revisited", *Food Chemistry*, **113**, pp.1202-1205, DOI: 10.1016/j.foodchem.2008.08.008.

[5] N. Nenadis, L.F. Wang, M. Tsimidou, et al. (2004), "Estimation of scavenging activity of phenolic compounds using the ABTS^{+} assay", *Journal of Agricultural and Food Chemistry*, **52(15)**, pp.4669-4674, DOI: 10.1021/jf0400056.

[6] W.C. Kan, H.Y. Wang, C. Chiang, et al. (2012), "Effects of extract from solid-state fermented *Cordyceps sinensis* on type 2 diabetes mellitus", *Evidence-Based Complementary and Alternative Medicines*, **2**, pp.1-10, DOI: 10.1155/2012/743107.

[7] C.H. Dong, T. Yang, T. Lian (2014), "A comparative study of the antimicrobial, antioxidant, and cytotoxic activities of methanol extracts from fruit bodies and fermented mycelia of caterpillar medicinal mushroom *Cordyceps militaris* (Ascomycetes)" *International Journal of Medicinal Mushrooms*, **16(5)**, pp.485-495, DOI: 10.1615/intjmedmushrooms.v16.i5.70.

[8] Z. Tang, C. Zhou, Y. Cai, et al. (2020), "Purification, characterization and antioxidant activities in vitro of polysaccharides from *Amaranthus hybridus* L.", *Biochemistry, Biophysics and Molecular Biology*, **8**, DOI: 10.7717/peerj.9077.

[9] L. Xiao, S. Sun, K. Li, et al. (2020), "Effects of nanobubble water supplementation on biomass accumulation during mycelium cultivation of *Cordyceps militaris* and the antioxidant activities of extracted polysaccharides", *Bioresource Technology Report*, **12**, DOI: 10.1016/j.biteb.2020.100600.

[10] W. Chen, G. Liu, H. Yang, et al. (2016). "Effects of processing treatments on the antioxidant properties of polysaccharide from *Cordyceps militaris*", *International Journal of Food Engineering*, **13(1)**, DOI: 10.1515/ijfe-2016-0076.

[11] M. Mirzadeh, M.R. Arianejad, L. Khedmat (2019), "Antioxidant, antiradical, and antimicrobial activities of polysaccharides obtained by microwave-assisted extraction method: A review", *Carbohydrate Polymers*, **229**, DOI: 10.1016/j.carbpol.2019.115421.

[12] S.M.T. Gharibzahedi, B. Smith, Y. Guo (2019), "Ultrasound-microwave assisted extraction of pectin from fig (*Ficus carica* L.) skin: Optimization, characterization and bioactivity", *Carbohydrate polymers*, **222**, DOI: 10.1016/j.carbpol.2019.114992.

[13] Y. Yuan, X. Xu, C. Jing, et al. (2018), "Microwave assisted hydrothermal extraction of polysaccharides from Ulva prolifera: Functional properties and bioactivities", *Carbohydrate Polymers*, **181**, pp.902-910, DOI: 10.1016/j.carbpol.2017.11.061.

[14] T.N. Quy, T.D. Xuan (2019), "Xanthine oxidase inhibitory potential, antioxidant and antibacterial activities of *Cordyceps militaris* L. link fruiting body", *Medicines*, **6(1)**, DOI: 10.3390/medicines6010020.

Isolation and identification of carotenoid-producing *Rhodotorula* sp. from soils collected in the coastal environment of Kien Giang and Tra Vinh provinces

Luong Anh Hue, Nguyen Thanh Trung Nhan, Nguyen Minh Chon*

Biotechnology Research and Development Institute, Can Tho University, 3/2 Street, Xuan Khanh Ward, Ninh Kieu District, Can Tho City, Vietnam

Received 14 September 2022; revised 19 October 2022; accepted 6 December 2022

Abstract:

***Rhodotorula* is a genus of marine yeasts that is considered the most suitable for carotenoid production. In this study, collected soils at Kien Giang and Tra Vinh provinces were cultured on yeast extract peptone dextrose (YEPD) agar for 72 hours at room temperature. Twenty-three isolates exhibiting yellow, orange, and pink pigments were tested for physiological and biochemical characteristics such as carbohydrate fermentation and assimilation, nitrate assimilation, urease production, and growth temperature. Their oval dimensions were 4.24x3.64 µm for isolate 5S1-T and 3.88x3.17 µm for isolate 5S4-T. The two isolates could assimilate carbohydrate and nitrate sources and produce urease. The ITS rDNA sequence of isolates 5S1-T and 5S4-T both had 100% matches to *Rhodotorula sphaerocarpa* CBS:5940 and *Rhodotorula sphaerocarpa* CBS:5939, respectively. The maximum absorbance wavelengths of the solution extractions from the 5S1-T and 5S4-T were 496 and 487 nm, respectively. The total carotenoid content of strain 5S1-T was found to be the highest (1.81 mg/l) followed by strain 5S4-T (1.16 mg/ml). The antioxidant abilities of the 5S1-T and 5S4-T were demonstrated by scavenging the free radical DPPH and ferric reducing capacity. The free radical scavenging activity of the extract from isolate 5S1-T (96.15%) was higher than that of isolate 5S4-T (88.61%) at 0.14 mg/ml. The absorbance at 700 nm of the extracts of both 5S1-T and 5S4-T significantly increased from 0.05 to 0.3 mg/ml. The two strains 5S1-T and 5S4-T of *Rhodotorula sphaerocarpa* discovered in this study could contribute to carotenoid and antioxidant-producing yeasts for industries in the future.**

Keywords: **antioxidant, carotenoid, *Rhodotorula*, yeast.**

Classification numbers: **3.5, 5.3**

1. Introduction

Rhodotorula sp., in the phylum *Basidiomycota* and family *Cryptococcaceae*, is a potential genus for carotenoid production and cultivation on an industrial scale. Carotenoids are natural bioactive compounds that are capable of antioxidant, antibacterial, and antifungal activities. Because of their biological role as vitamin A precursors in humans and their antioxidant properties preventing some forms of cancer, carotenoids have been indicated as a one of the most valuable compounds for applications in food, feed, pharmaceutical, and chemical industries. Carotenoids are also useful as a natural colorant and can be used to avoid artificial colorants in food and beverage industries [1-4].

The marine environment has proven to be a rich source of both bacteria and yeast diversity with bioactive secondary metabolite substances. Marine organisms have recently been concerned with many useful characterizations that can be modified for specific uses. Over 300,000 described species have been discovered in the ocean, which makes up more than 70% of the earth's surface including bacteria and yeast [5].

Rhodotorula sp., which was isolated from soils of the marine zone, has been historically reported in many countries [6-8]. It is commonly known that *Rhodotorula* sp. is being evaluated as a potential natural resource for industrial applications such as the production of carotenoids, bioethanol, enzymes, protein, and silver nanoparticles [8-12]. However, in Vietnam, there is a focus on investigations of potential features of *Rhodotorula* originating from oceanic areas as well as mangrove sediments. As for marine yeasts, *Rhodotorula* sp. will be a novel resource for carotenoid production.

Therefore, this research was conducted to isolate and identify carotenoid-producing *Rhodotorula* sp. from the coastal environments of the Kien Giang and Tra Vinh provinces. The aim is to isolate and characterise novel

*Corresponding author: Email: nmchon@ctu.edu.vn

strains that can produce carotenoids as a group of natural bioactive compounds with potential antioxidant activities and applications for industrial production.

2. Materials and methods

2.1. Sample collection

Soil samples were collected about 50 cm from the face of the waters in the coastal environments of the Kien Giang and Tra Vinh provinces. The soils were kept in a cool box and transported to the laboratory where they were stored at 4°C until further use. This is a suitable temperature to conserve *Rhodotorula* yeast in the samples [13].

2.2. Methods

Isolation of *Rhodotorula:* About 10 g of soil was transferred to 90 ml of sterile distilled water in a 250 ml Erlenmeyer flask and incubated on a rotator shaker (150 rpm) for 30 min at room temperature. The supernatant in the soil was diluted up to 10^{-3} dilutions. Then, 100 µl of each dilution was spread on a YEPD agar plate supplemented with streptomycin sulphate (250 mg/l) and penicillin (250 mg/l). All plates were incubated at room temperature for 7 days. Observing the morphology as well as colours of colonies every 24 hours was conducted to isolate the colonies that contain the pink, red, yellow, and orange colour and properties of yeast including fermentation of carbohydrates (glucose, sucrose, and mannitol), assimilation of carbohydrates and nitrate, urease production, and growth at different temperatures [13-16].

The isolates from *Rhodotorula* sp. were determined and selected for analysis based on N.J.W.K. Van Rij's (1984) [17] description of its micromorphological, physiological, and biochemical characteristics.

2.3. Taxonomy

DNA extraction: Yeast genomic DNA extraction was conducted according to Y.J. Zhang, et al. (2010) [18] with the following modifications. After 3 days of cultivation, 7-10 yeast colonies on solid YEPD medium were placed in a 2-ml eppendorf tube. In the next step, 1 ml of 1X phosphate-buffered saline was added to the yeast and then centrifuged at 10,000 rpm for 4 min (eppendorf centrifuge 5810R, Germany). Afterwards, the supernatant was discarded, the yeast precipitate was retained, and 0.5 ml of TE buffer (50 mM Tris-HCl pH 7.4, 20 mM EDTA) was added followed by the addition of phenol, chloroform, and isoamyl alcohol in a ratio of 25:24:1, respectively, with an equivalent volume to the mixture, which was then placed on ice and centrifuged at 12,000 rpm for 5 min. Moreover, the mixture was incubated at 65°C for 30 min. Furthermore, the mixture was placed in an ice bath to retain heat and centrifuged at 12,000 rpm for 5 min. As a result, the supernatant was transferred to another clean tube, mixed with the corresponding volume of absolute ethanol, and incubated overnight at -20°C. The mixture was centrifuged at 12,000 rpm for 5 min. The supernatant was removed, then 500 µl of 70% ethanol was added to the mixture to wash the pellet (repeated 3 times). Finally, the pellet was air-dried, dissolved in 100 µl 0.1 X TE, and stored at -20°C.

Amplification of ITS gene by PCR: Microscopic and macroscopic features of the isolate were examined by classical microbiological techniques. Then, the isolates were identified by using the molecular biological method [13]. The following universal primers ITS 1 and ITS 4 were used for the amplification of ITS region of the isolates:

Forward primer ITS 1: 5'-TCCGTAGGTGAACCTGCGG-3'

Reverse primer ITS 4: 5'-TCCTCCGCTTATTGATATGC-3'

The PCR consisted of an initial denaturing step of 5 min at 94°C followed by 35 cycles (50 s at 94°C, 50 s at 54°C, and 50 s at 72°C) finished by a final extension step at 72°C for 10 min. A GeneAmp® PCR system ABI 9700, USA was used for the amplification of the ITS region of the samples. After that, the PCR products were detected by electrophoresis (Gel tank MGU-502T, CBS Scientific, and basic power supply, Biorad, USA) through 1.5% agarose gels in Tris-borate EDTA solution and were visualized by staining with SyBr Green. The products were then conducted for sequencing by using Sanger Technique (ABI 3500, Applied Biosystem, USA) at Nam Khoa Biotech Company. The ITS sequence was searched for the closest homology sequence using the BLAST on the GenBank (NCBI).

Extraction and quantification of total carotenoids: The isolates were cultured on YEPD agar a pH 5.6 and incubated for 3 days on the shaker (Thermostable Shaker KS4000, IKA, Germany) (180 rpm/min) at room temperature. After that, the entire broth was centrifuged at 8,000 rpm for 10 min at 25°C. The cell pellets were collected and extracted with 1 ml of dimethyl sulfoxide (DMSO) preheated to 55°C (Waterbath Memmert One, Germany). After centrifugation, the supernatant pigment was pipetted off and the extraction in DMSO was repeated three times. The maximum absorbance wavelength and the total carotenoid content were determined by measuring the absorbance value using a spectrophotometer according to H.M. Kanzy, et al. (2015) [19]. The total carotenoid content was calculated according to the following equation:

$$C = \frac{A \times V \times 10^6}{E_{1cm}^{1\%} \times 100}$$

where C is the total carotenoid concentration (mg/l); A is the maximum absorbance value; V is the total volume (ml); $E_{1cm}^{1\%}$ is the average absorption coefficient of carotenoids in DMSO (2,040).

2.4. Antioxidant assay

Free radical scavenging capacity DPPH assay: The 2,2-diphenyl-1-picrylhydrazyl (DPPH) radical scavenging assay was carried out based on the loss of DPPH colour when a solution of DPPH is in contact with a substance that is capable of antioxidant activity. The evaluation of the antioxidant activity assay was measured according to M.P. De Torre, et al. (2019) [20] with some modifications. A 200-µl sample was added to 200 µl DPPH (0.05 mg/ml) in absolute ethanol. Then, the mixture was incubated for 60 min at room temperature. The extract solution was prepared in DMSO. Stock extracts with various concentrations were made. Finally, the mixture was diluted with 600 µl distilled water and the absorbance was measured at 517 nm. The percentage of DPPH scavenging free radicals was calculated by the following equation:

$$I\ (\%) = \frac{A_{control} - A_{sample}}{A_{control}} \times 100$$

where I is the percentage of inhibition (scavenging free radicals DPPH); $A_{control}$ is absorbance (ABS) of control at 517 nm; A_{sample} is the ABS of the reaction mixture in the presence of extract after the reaction was stopped at 517 nm.

Ferric reducing antioxidant power (FRAP) assay: FRAP analysis was introduced to measure total antioxidant activity and is based on the ability of samples to reduce ferric ion Fe^{3+} to ferrous ion Fe^{2+}, forming a blue complex. The method was conducted according to a modified version of M. Vijayalakshmi, et al. (2016) [21] method. The reaction includes 0.5 ml of various concentrations of samples and 0.5 ml of 1% $K_3Fe(CN)_6$ in 0.5 ml of 0.2 M sodium phosphate buffer (pH 6.6). The reaction mixture was vortexed and then incubated at 50°C for 20 min. At the end of incubation, 0.5 ml of 10% trichloroacetic acid (CCl_3COOH) was added to the mixture and centrifuged at 3,000 rpm for 10 min. A 0.5-ml volume of supernatant of was mixed with 0.5 ml deionised water and 0.1 ml 0.1% $FeCl_3$. The mixture was vortexed well by using a vortex shaker (Mixer Vortex MS2, IKA, Germany). The coloured solution was measured at 700 nm.

2.5. Statistical analysis

Mean values of the data were calculated using Microsoft Excel 2011. Statistical analysis was performed with SPSS version 20. Statistical analyses of the experimental data were handled utilising a one-way analysis of variance (ANOVA). The difference of means of the independent group was tested for significance by using Duncan's multiple range test and the least significant difference test (LSD).

3. Results and discussion

3.1. Isolation of Rhodotorula

The soil samples were collected from coastal areas in the Kien Giang and Tra Vinh provinces. There were 23 pigmented samples isolated from soil samples from Kien Giang and Tra Vinh, which are indicated in Table 1. To be more specific, 19 samples were isolated from soil samples from Kien Giang (82.61%) whereas 4 samples were isolated from soil samples from Tra Vinh (17.39%).

Table 1. Colony morphological characteristics of isolates and the location of the collected soil samples.

No.	Isolates	Province of collected soils	Colony colour	Colony shape	Colony margin	Colony elevation	Colony diameter (mm)
1	2S34-K	Kien Giang	Orange	Irregular	Undulate	Crateriform	0.40
2	2S341-K	Kien Giang	Orange	Irregular	Undulate	Crateriform	0.76
3	2S342-K	Kien Giang	Yellow	Irregular	Undulate	Crateriform	0.83
4	2S31-K	Kien Giang	Bold orange	Circular	Entire	Raised	0.38
5	2S36-K	Kien Giang	Orange	Irregular	Undulate	Raised	0.40
6	2S37-K	Kien Giang	Orange	Circular	Entire	Raised	0.72
7	4S6-T	Tra Vinh	Pink	Circular	Entire	Raised	0.30
8	4S7-T	Tra Vinh	Yellow	Circular	Entire	Umbonate	0.40
9	5S1-T	Tra Vinh	Bold orange	Circular	Entire	Raised	0.83
10	5S4-T	Tra Vinh	Bold orange	Circular	Entire	Raised	0.70
11	23S6-K	Kien Giang	Orange	Irregular	Undulate	Crateriform	0.50
12	23S61-K	Kien Giang	Orange	Circular	Entire	Umbonate	0.50
13	23S63-K	Kien Giang	Orange	Irregular	Undulate	Crateriform	0.30
14	23S69-K	Kien Giang	Orange	Circular	Entire	Raised	0.60
15	24S66-K	Kien Giang	Orange	Circular	Entire	Raised	0.45
16	24S67-K	Kien Giang	Orange	Circular	Entire	Umbonate	0.50
17	39S6-K	Kien Giang	Orange	Circular	Entire	Umbonate	0.73
18	39S61-K	Kien Giang	Orange	Circular	Entire	Raised	0.62
19	39S62-K	Kien Giang	Orange	Circular	Entire	Raised	0.53
20	39S64-K	Kien Giang	Orange	Circular	Entire	Umbonate	0.90
21	39S65-K	Kien Giang	Pale orange	Irregular	Undulate	Crateriform	0.60
22	39S66-K	Kien Giang	Orange	Circular	Entire	Umbonate	0.70
23	39S69-K	Kien Giang	Orange	Circular	Entire	Raised	1.50

Notes: S is soil; K is Kien Giang province; T is Tra Vinh province.

In Table 1, the colonies of 20 isolated samples had colours from yellow to bold orange. Their colony diameters ranged from 0.3 to 1.5 mm. There were three isolates with bold orange colour (13.04%), sixteen isolates with orange colour (69.57%), two samples with yellow colour (8.69%), one sample with pink colour (4.35%), and one sample with pale orange colour (4.35%). Additionally, 16 colony isolates had circular morphology (69.57%), whereas 7 colony isolates had irregular morphology (30.43%). In terms of colony elevation, there were 6 pigmented isolates with crateriform height, which accounted for 30%. Besides this, pigmented isolates with raised height had 11 isolates, which accounted for 47.83%.

After being cultured in YEPD agar medium for 3 days, 23 isolates that had orange, pink and yellow colours were separated and tested for morphological, physiological, and biological characterisation belonging to the yeast.

To identify the preliminary properties belonging to the yeast, the 23 isolates were observed under microscopy to evaluate the cell morphology of the pigmented isolates. As a result, eight pigmented isolates were morphologically similar to yeast, including isolates 2S31-K, 2S36-K, 2S37-K, 5S1-T, 5S4-T, 23S6-K, 24S67-K, and 39S65-K. Based on the results of the physiological and biochemical tests described in Table 2, the two isolates (5S1-T and 5S4-T) had some properties similar to those of the yeast genus *Rhodotorula*. To explain in more detail, 5S1-T and 5S4-T could assimilate carbohydrate sources, namely glucose, sucrose, and mannitol. But the isolates were not capable of fermentation of glucose nor sucrose, which is important to indicate in the classification of the genus *Rhodotorula*. Also, the assimilation of nitrate sources of isolates 5S1-T and 5S4-T was positive. The ability of urease production was recorded by colour changing when isolates 5S1-T and 5S4-T were cultured in a mineral medium containing urea. Regarding physiological characteristics, eight isolates were tested for growth at four temperatures, namely, 20, 25, 30, and 37°C. All isolates experienced good growth at 25 and 30°C. Moreover, the six isolates 2S31-K, 2S36-K, 2S37-K, 23S6-K, 24S67-K, and 39S65-K grew well at 37°C, except for isolates 5S1-T and 5S4-T. According to the taxonomy key in a study, almost all strains of the genus *Rhodotorula* either slowly grow or have no development at 37°C. This result is similar to the growth characterizations of *Rhodotorula mucilaginosa* CRUB 0138 and *Rhodotorula mucilaginosa* PYCC 5166 [1]. Only the two isolates 5S1-T and 5S4-T could grow at 20°C. This is clear evidence that isolates 5S1-T and 5S4-T fall into the group yeast. Nevertheless, isolate 24S67-K was able to produce urease to hydrolyse urea sources and assimilate glucose, sucrose, maltose, and nitrate sources. However good growth of the isolate was observed at 37°C. Therefore, it is unclear which characteristic to use to identify the isolate belonging to the yeast *Rhodotorula*. Therefore, further experiments are needed to accurately identify this isolate.

The isolates 5S1-T and 5S4-T developed a bold orange-coloured colony on YEPD agar medium after 48 hours and grew well after that. The colour of the colony became darker after 5 days. The colony had a circular shape with a mucous and smooth surface (Fig. 1).

Table 2. Physiological and biochemical characteristics of the yeast isolates.

No.	Characteristics \ Isolates	2S31-K	2S36-K	2S37-K	5S1-T	5S4-T	23S6-K	24S67-K	39S65-K
1	Glucose assimilation	+	+	+	+	+	+	+	+
2	Glucose fermentation	-	-	-	-	-	-	-	-
3	Sucrose assimilation	+	+	+	+	+	+	+	+
4	Sucrose fermentation	-	-	-	-	-	-	-	-
5	Mannitol assimilation	+	+	+	+	+	+	+	+
6	Mannitol fermentation	-	-	-	-	-	-	-	-
7	Nitrate assimilation	-	+	-	+	+	-	-	-
8	Urease production	-	+	+	+	+	+	+	-
9	Growth at 20°C	-	-	-	+	+	-	-	-
10	Growth at 25°C	+	+	+	+	+	+	+	+
11	Growth at 30°C	+	+	+	+	+	+	+	+
12	Growth at 37°C	+	+	+	-	-	+	+	+

Notes: +: positive; -: negative.

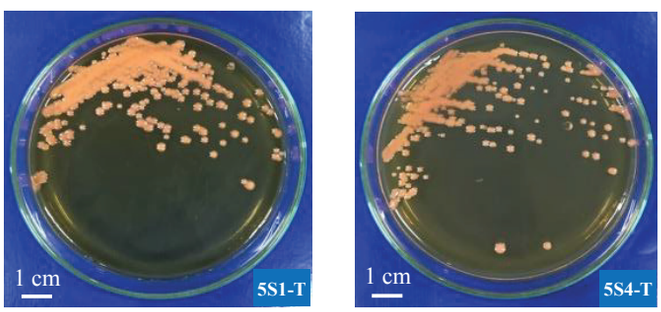

Fig. 1. Colony of isolates 5S1-T and 5S4-T on YEPD agar medium after 5 days.

Scanning electron microscopy (SEM) was applied to capture the cell morphology of yeast isolates. Both the two isolates had an oval shape; moreover, the cell diameter of the isolates were 4.24x3.64 (μm) for isolate 5S1-T and 3.88x3.17 (μm) for isolate 5S4-T, which is indicated in Fig. 2.

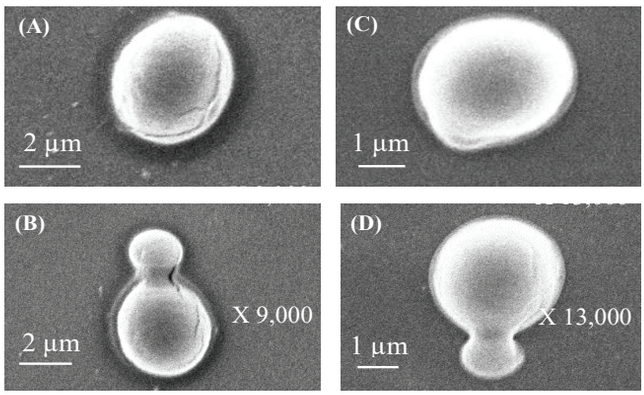

Fig. 2. Cells of isolates 5S1-T and 5S4-T under a scanning electron microscope. (A) The cell of isolate 5S1-T; **(B)** budding cell of isolate 5S1-T; **(C)** cell of isolate 5S4-T; **(D)** budding cell of isolate 5S4-T.

Overall, isolates 5S1-T and 5S4-T could assimilate glucose, sucrose, mannitol, and nitrate sources and hydrolyse urea, but could not ferment carbohydrate sources. Apart from that, their cell morphology was oval, and their type of reproduction was budding, which is a typical feature of yeast. Based on morphological, physiological, and biochemical characteristics, the two isolates 5S1-T and 5S4-T had some properties that were similar to those of the yeast genus *Rhodotorula*. However, the others showed distinct characteristics, so it is crucial to conduct further experiments to identify these.

Molecular biology Identification: Fig. 3 shows that the length of PCR products of the isolates 5S1-T and 5S4-T was approximately 750 bp through amplification of the ITS sequence to identify them accurately.

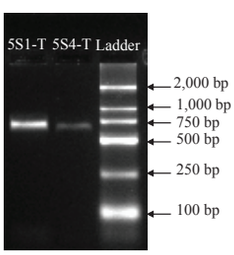

Fig. 3. PCR product of an ITS fragment of isolates 5S1-T and 5S4-T on agarose gel by analysing electrophoresis.

The sequence was compared with ITS sequences deposited in GenBank (NCBI) by using the BLAST tool. The ITS sequence of 5S1-T showed a 100% similarity to *Rhodotorula sphaerocarpa* 5940. The ITS sequence of 5S4-T showed a 100% similarity to *Rhodotorula sphaerocarpa* 5939 (Table 3). Although the two samples, 5S1-T and 5S4-T, also belong to the species *Rhodotorula sphaerocarpa*, the identification of the isolates was different based on the capacity of carotenoid production and growth rate of the colony. Therefore, they could be subspecies of *Rhodotorula sphaerocarpa*.

Table 3. ITS Sequence comparison of isolates on NCBI GenBank.

Isolates	Length	Species	Query cover	Percentage of identification	Accession
5S1-T	610 bp	*Rhodotorula sphaerocarpa* culture CBS:5940. Length: 622 bp.	100%	100%	KY104909.1
5S4-T	559 bp	*Rhodotorula sphaerocarpa* culture CBS:5939. Length: 577 bp.	100%	100%	KY104905.1

3.2. Determination of total carotenoid content

Table 4 provides the pigment extract of *Rhodotorula* sp. 5S1-T, which had a bold orange colour and maximum absorbance wavelength at 496 nm, which was the highest one. The total carotenoid content extracted from isolate 5S1-T was 1.81±0.003 mg/l, corresponding to a maximum absorbance of 0.31±0.001 mg/l, which was a significant difference between the isolates. The predicted carotenoid composition of extract 5S1-T was -carotene, -carotene, lutein, and lycopene. Besides, the 5S4-T extract of *Rhodotorula* sp. had a maximum absorbance wavelength at 487 nm followed by a maximum absorbance of 0.20±0.001, corresponding to a total carotenoid content of 1.16±0.007 mg/l. Based on the maximum absorbance wavelength of the extract, the carotenoid composition of isolate 5S4-T was predicted to be β-carotene and lycopene. These results are similar to studies from several other countries. In Argentina, it was reported by D. Libkind, et al. (2004) [1] that the content of total carotenoid extracted from *Rhodorotula mucilaginosa* CRUB 0138 was 1.04 mg/l. According to the 2016 research by P. Hanachi and F.S. Naghavi (2016) [22] in Iran, the total carotenoid contents of *Rhodorotula slooffiae* and *Rhodorotula mucilaginosa* were 1.216 and 0.604 mg/l, respectively. In another study, the carotenoid produced by *Rhodorotula mucilaginosa* was 8.11 mg/l at 96 hours of cultivation [23].

Table 4. Determination of maximum absorbance wavelength of extracts.

Extract of samples	Extract colour	Maximum absorbance wavelength of extract (nm)	Maximum absorbance (Abs)	Total carotenoid content (mg/l)	Possible carotenoid compounds	Reference
5S1-T	Bold orange	496	0.31±0.001[a]	1.81±0.003[a]	y-carotene, β-carotene, lutein, lycopene	[24] [25]
5S4-T	Bold orange	487	0.20±0.001[b]	1.16±0.007[b]	β-carotene, lycopene	
F			*	*		
CV (%)			0.57	0.57		

Notes: Numbers in a column with distinguished letters are significantly different at p<0.05 by using the LSD test; data were shown by MEAN±SE.

3.3. Antioxidant assay of extract

In this study, two samples of *Rhodotorula* isolated from Tra Vinh province were examined for their antioxidant potential under *in vitro* conditions. All of the samples were able to scavenge the radical DPPH and reduce ferric ions to ferrous ions. The results of antioxidant activity based on DPPH scavenging are given in Table 5. Generally, the inhibition of DPPH of the two extracts shows an upward trend, rising noticeably from 2.86±0.84% at 0.02 mg/ml to 96.15±0.31% at 0.14 mg/ml of extract of strain 5S1-T and from 2.19±0.43% at 0.02 mg/ml to 88.61±0.45% at 0.14 mg/ml of extract of strain 5S4-T. The percentage of observed concentrations of *Rhodotorula* sp. 5S1-T and *Rhodotorula* sp. 5S4-T extracts were a significant difference in statistics ($p<0.05$).

Table 5. Results of antioxidant activity of isolated extracts by using the DPPH.

Isolates / Concentrations (mg/ml)	Percentage of inhibition (%)	
	5S1-T	*5S4-T*
0.00	0.00±0.00^{h}	0.00±0.00^{h}
0.02	2.86±0.84^{g}	2.19±0.43^{g}
0.04	14.32±0.42^{f}	10.07±0.37^{f}
0.06	29.04±0.70^{e}	19.83±1.52^{e}
0.08	38.12±0.39^{d}	34.01±0.66^{d}
0.10	50.63±0.19^{c}	49.77±0.40^{c}
0.12	72.78±0.28^{b}	70.56±0.38^{b}
0.14	96.15±0.31^{a}	88.61±0.45^{a}
F	*	*
CV (%)	2.12	3.22

Notes: Numbers in a column with distinguished letters are significantly different at $p<0.05$ by using Duncan's multiple range test; data were shown by MEAN±SE.

To compare the antioxidant activity of extracts and positive controls, namely, vitamin C and commercial beta-carotene, the value of inhibition concentration at 50% (IC_{50}) was used, which is defined as the concentration of extracts necessary to scavenge the DPPH free radicals by 50%. Given in Fig. 4, the IC_{50} of beta-carotene was the strongest (0.002 mg/ml), followed by vitamin C (0.021 mg/ml), extract of *Rhodotorula sphaerocarpa* 5S1-T (0.093 mg/ml), and extract of *Rhodotorula sphaerocarpa* 5S4-T (0.096 mg/ml). Z. Gerelmaa, et al. (2018) [26] reported that carotenoids extracted from *Rhodotorula glutinis* R12 could scavenge 50% of DPPH at 0.536 mg/ml. A study by F.S. Naghavi (2015) [4] revealed that both strains, *Rhodorotula slooffiae* and *Rhodorotula mucilaginosa*, showed a significant antioxidant effect and had scavenging of 50% DPPH at 0.658 and 0.789 mg/ml, respectively. Using the same method, T.T. Men, et al. (2020) [27] reported that the ethanolic extract of *Kaempferia galanga* showed a scavenging ability of 50% DPPH at 2.404 mg/ml. It is indicated that carotenoids extracted from *Rhodotorula sphaerocarpa* 5S1-T and 5S4-T had high antioxidant activity.

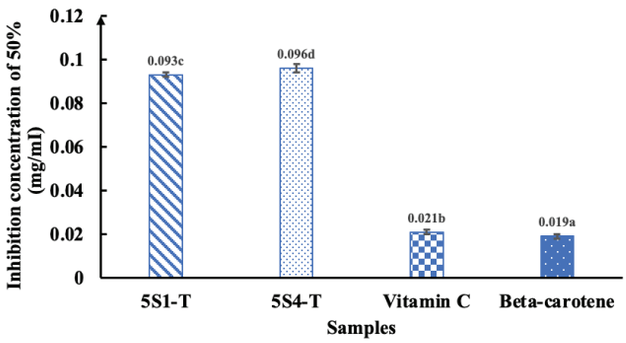

Fig. 4. The inhibition concentration of radical DPPH of 50% of samples (extract 5S1-T, extract 5S4-T, vitamin C, and beta-carotene).

To evaluate the antioxidant activity by using a reducing ferric ion assay, the absorbances of reducing the capacity of the extracts 5S1-T and 5S4-T were recorded and are presented in Table 6. The increased absorbance of the reaction mixture indicates raised reducing capacity [28].

Table 6. Results of antioxidant activity of isolated extracts by using the ferric reducing antioxidant capacity assay.

Isolates / Concentrations (mg/ml)	Absorbance at 700 nm	
	5S1-T	*5S4-T*
0.00	0.03±0.003^{g}	0.03±0.003^{g}
0.05	0.05±0.005^{f}	0.08±0.001^{f}
0.10	0.18±0.004^{e}	0.09±0.003^{e}
0.15	0.32±0.013^{d}	0.14±0.003^{d}
0.20	0.39±0.006^{c}	0.24±0.002^{c}
0.25	0.42±0.008^{b}	0.34±0.001^{b}
0.30	0.47±0.009^{a}	0.42±0.003^{a}
F	*	*
CV (%)	0.01	0.01

Notes: Numbers in a column with distinguished letters are significantly different at $p<0.05$ by using Duncan's multiple range test; data were shown by MEAN±SE.

Overall, the extracts of *Rhodotorula sphaerocarpa* 5S1-T and *Rhodotorula sphaerocarpa* 5S4-T both had a reducing capacity with increasing absorbances from 0.05 to 0.3 mg/ml. They were significantly different in terms of the absorbances of various extractive concentrations. These results demonstrate that the reducing capacity of the total carotenoid extract of *Rhodotorula sphaerocarpa* 5S1-T (0.47±0.009) is higher than that of *Rhodotorula sphaerocarpa* 5S4-T (0.42±0.003). It is proved that *Rhodotorula sphaerocarpa* 5S1-T possesses high antioxidant activity. E.P. Cipolatti, et al. (2019) [29] affirmed that by using the ferric reducing antioxidant capacity, the extracted carotenoid of *Rhodotorula mucilaginosa* presented a potent antioxidant compound. M.R.A. Manimala, et al. (2014) [30] researched the antioxidant activity of carotenoid pigment extracted from *Sporobolomyces* sp. - a genus of yeast as a carotenoid producer - and reported a high efficiency of ferric reducing power for the antioxidant assay with an absorbance of 0.99 at 0.02 mg/ml.

This study discovered two strains of marine yeast falling into the genus *Rhodotorula* as a carotenoid producer. All assays revealed that the total carotenoid extracted from the two strains *Rhodotorula sphaerocarpa* 5S1-T and *Rhodotorula sphaerocarpa* 5S4-T both had good antioxidant activities. Although the two strains belong to the same species *Rhodotorula sphaerocarpa*, the extracts showed different antioxidant abilities. This is evidence to distinguish the subspecies, however, there is a diversity of species in a genus.

Further studies needs to be done to optimise elements such as carbohydrate sources, pH, temperature, and medium to reach the best conditions for producing the carotenoid of *Rhodotorula sphaerocarpa* 5S1-T and *Rhodotorula sphaerocarpa* 5S4-T. It is possible to use carotenoids extracted from these two strains in feed and foods as natural bioactive compounds as well as colorants.

4. Conclusions

Twenty-three samples were isolated from soils collected in the coastal environment of the Kien Giang and Tra Vinh provinces. Based on characteristics of morphology, physiology, biochemistry, and molecular, it is clear that both isolates 5S1-T and 5S4-T belong to the yeast. The ITS rDNA sequence of isolates 5S1-T and 5S4-T evidenced a 100% similarity with *Rhodotorula sphaerocarpa* 5940 and *Rhodotorula sphaerocarpa* 5939. Moreover, the content of total carotenoid extracted from two strains 5S1-T and 5S4-T was determined to be 1.81 and 1.16 mg/l, respectively. Besides, the antioxidant activity of the carotenoid extracts of the two strains was evaluated as a good antioxidant source by testing the DPPH free radical scavenging and ferric reducing antioxidant capacity.

CRediT author statement

Luong Anh Hue: Experimental design, Methodology, Data analysis, and Writing paper; Nguyen Thanh Trung Nhan: Investigation and Data collection; Nguyen Minh Chon: Conceptualization, Review, and Editing.

ACKNOWLEDGEMENTS

The authors would like to thank the staff of the Biotechnology Research and Development Institute, Can Tho University for their support.

COMPETING INTERESTS

The authors declare that there is no conflict of interest regarding the publication of this article.

REFERENCES

[1] D. Libkind, S. Brizzio, M. Broock (2004), "*Rhodotorula mucilaginosa*, a carotenoid producing yeast strain from a Patagonian high-altitude lake", *Folia Microbiologica*, **49(1)**, pp.19-25.

[2] P. Buzzini, A. Martini, M. Gaetani, et al. (2005), "Optimization of carotenoid production by *Rhodotorula graminis* DBVPG 7021 as a function of trace element concentration by means of response surface analysis", *Enzyme and Microbial Technology*, **36(5-6)**, pp.687-692.

[3] P. Buzzini (2000), "An optimization study of carotenoid production by *Rhodotorula glutinis* DBVPG 3853 from substrates containing concentrated rectified grape must as the sole carbohydrate source", *Journal of Industrial Microbiology and Biotechnology*, **24(1)**, pp.41-45.

[4] F.S. Naghavi, H. Parichehr, M.R. Sodi, et al. (2015), "The capability of Rhodotorula slooffiae to produce carotenoid", *Zahedan Journal of Research in Medical Sciences*, **17(2)**, pp.52-56.

[5] W.B. Whitman, D.C. Coleman, W.J. Wiebe (1998), "Prokaryotes: The unseen majority", *Proceedings of The National Academy of Sciences*, **95(12)**, pp.6578-6583, DOI: 10.1073/pnas.95.12.6578.

[6] L. He, J. Liu, S. Qin, et al. (2011), "Identification of an astaxanthin-producing marine yeast strain YS-185 and optimization of its fermentation conditions", *Progress in Fishery Sciences*, **32(4)**, pp.93-101.

[7] K. Kathiresan, K. Saravanakumar, Senthilraja (2011), "Bio-ethanol production by marine yeasts isolated from coastal mangrove sediment", *International Multidisciplinary Research Journal*, **1(1)**, pp.19-24.

[8] M. Li, G.L. Liu, Z. Chi, et al. (2010), "Single cell oil production from hydrolysate of cassava starch by marine-derived yeast *Rhodotorula mucilaginosa* TJY15a", *Biomass and Bioenergy*, **34(1)**, pp.101-107, DOI: 10.1016/j.biombioe.2009.10.005.

[9] G. Katre, C. Joshi, M. Khot, et al. (2012), "Evaluation of single cell oil (SCO) from a tropical marine yeast *Yarrowia lipolytica* NCIM 3589 as a potential feedstock for biodiesel", *AMB Express*, **2(1)**, pp.1-14, DOI: 10.1186/2191-0855-2-36.

[10] L. Cong, Z. Chi, J. Li, et al. (2007), "Enhanced carotenoid production by a mutant of the marine yeast *Rhodotorula* sp. hidai", *Journal of Ocean University of China*, **6(1)**, pp.66-71, DOI: 10.1007/s11802-007-0066-x.

[11] A.W.F. Duarte, I.D. Owoyemi, F.S. Nobre, et al. (2013), "Taxonomic assessment and enzymes production by yeasts isolated from marine and terrestrial Antarctic samples", *Extremophiles*, **17(6)**, pp.1023-1035, DOI: 10.1007/s00792-013-0584-y.

[12] M. Subramanian, N.M. Alikunhi, K. Kandasamy (2010), "*In vitro* synthesis of silver nanoparticles by marine yeasts from coastal mangrove sediment", *Advanced Science Letters*, **3(4)**, pp.428-433, DOI: 10.1166/asl.2010.1168.

[13] S.I. Ghada, G.M. Manal, M.S.A. Mohsen, et al. (2012), "Production and biological evaluation of exopolysaccharide from isolated *Rhodotorula glutininis*", *Aust. J. Basic Appl. Sci.*, **6(3)**, pp.401-408.

[14] D.H. Larone (2002), *Medically Important Fungi: A Guide to Identification*, 4th Edition, ASM Press, 427pp.

[15] Y. Zhao, L. Guo, Y. Xia, et al. (2019), "Isolation, identification of carotenoid-producing *Rhodotorula* sp. from marine environment and optimization for carotenoid production", *Marine Drugs*, **17(3)**, DOI: 10.3390/md17030161.

[16] C.C. Lin, D.Y. Fung (1987), "Conventional and rapid methods for yeast identification", *Critical Reviews in Microbiology*, **14(4)**, pp.273-289, DOI: 10.3109/10408418709104441.

[17] N.J.W.K.V. Rij (1984), *The Yeasts: A Taxonomic Study*, Elsevier Science Publishers, 1082pp, DOI: 10.1016/C2009-0-00558-3.

[18] Y.J. Zhang, S. Zhang, X.Z. Liu, et al. (2010), "A simple method of genomic DNA extraction suitable for analysis of bulk fungal strains", *Letters in Applied Microbiology*, **51(1),** pp.114-118, DOI: 10.1111/j.1472-765X.2010.02867.x.

[19] H.M. Kanzy, N.F. Nasr, H.A.M.E. Shazly, et al. (2015), "Optimization of carotenoids production by yeast strains of *Rhodotorula* using salted cheese whey", *Int. J. Curr. Microbiol. App. Sci.*, **4(1)**, pp.456-469.

[20] M.P.D. Torre, R.Y. Cavero, M.I. Calvo, et al. (2019), "A simple and a reliable method to quantify antioxidant activity *in vivo*", *Antioxidants (Basel)*, **8(5)**, DOI: 10.3390/antiox8050142.

[21] M. Vijayalakshmi, K. Ruckmani (2016), "Ferric reducing anti-oxidant power assay in plant extract", *Bangladesh Journal of Pharmacology*, **11(3)**, pp.570-572, DOI: 10.3329/bjp.v11i3.27663.

[22] P. Hanachi, F.S. Naghavi (2016), "Evaluation of antioxidant activity of *R. slooffiae*, *R. mucilaginosa* extracts", *Electronic Physician*, **8(10)**, pp.3110-3115, DOI: 10.19082/3110.

[23] L.W. Xian, O.C. Zarrabal, M. Kohej, et al. (2018), "Production of pigments by *Rhodotorula mucilaginosa*", *Malaysian Journal of Microbiology*, **14(4)**, pp.344-350, DOI: 10.21161/mjm.144188.

[24] G. Britton, S.L. Jensen, H. Pfander (2004), "Introduction and guidelines on the use of the Handbook", *Carotenoids: Handbook*, Birkhäuser Publisher, 658pp, DOI: 10.1007/978-3-0348-7836-4_1.

[25] M. Butnariu (2016), "Methods of analysis (extraction, separation, identification and quantification) of carotenoids from natural products", *Journal of Ecosystem and Ecography*, **6(2)**, DOI: 10.4172/2157-7625.1000193.

[26] Z. Gerelmaa, C. Zultsetseg, B. Batjargal, et al. (2018), "Selection of culture media for the production of carotenoids with antioxidant activity by *Rhodotorula glutinis*", *Proceedings of The Mongolian Academy of Sciences*, **58(4)**, pp.31-38, DOI: 10.5564/pmas.v58i4.1047.

[27] T.T. Men, N.T.H. Anh, L.T.K. Tu, et al. (2020), "Antioxidant activity of rhizome extracts of medlar (*Kaempferia galanga* L.)", *Can Tho University J. Sci.*, **56(2)**, pp.41-47, DOI: 10.22144/ctu.jsi.2020.110 (in Vietnamese).

[28] M. Rahman, B. Islam, M. Biswas, et al. (2015), "*In vitro* antioxidant and free radical scavenging activity of different parts of *Tabebuia pallida* growing in Bangladesh", *BMC Research Notes*, **8**, DOI: 10.1186/s13104-015-1618-6.

[29] E.P. Cipolatti, R.D. Remedi, C.S. Sá, et al. (2019), "Use of agroindustrial byproducts as substrate for production of carotenoids with antioxidant potential by wild yeasts", *Biocatalysis and Agricultural Biotechnology*, **20(2)**, DOI: 10.1016/j.bcab.2019.101208.

[30] M.R.A. Manimala, R. Murugesan (2014), "*In vitro* antioxidant and antimicrobial activity of carotenoid pigment extracted from Sporobolomyces sp. isolated from natural source", *Journal of Applied and Natural Science*, **6(2)**, pp.649-653, DOI: 10.31018/jans.v6i2.511.

DOI: 10.31276/VJSTE.65(2).79-87

The effect of silver nanoparticle concentration on the antibacterial properties of tri-layer PCL-Ag/PT/PVP wound dressing

Thi Thanh Ngoc Nguyen, Thi Thanh Tam Phan, Thi Hiep Nguyen*

School of Biomedical Engineering, International University, Vietnam National University - Ho Chi Minh City, Quarter 6, Linh Trung Ward, Thu Duc District, Ho Chi Minh City, Vietnam

Received 6 January 2023; revised 10 February 2023; accepted 20 February 2023

Abstract:

To comprehensively manage wound infection, tri-layer fibre membranes have been designed with two antibacterial agents, including silver nanoparticles (AgNPs) and chitosan oligosaccharide (COS), and their antibacterial properties were evaluated using qualitative and quantitative tests. While the first polycaprolactone (PCL) silver layer and the second plasma-treated PCL layer were fabricated by electrospinning, the third COS layer was constructed via coating and heat-vacuum drying. The formation of the membranes and their fibrous and porous structures were examined using scanning electron microscopy (SEM). The antibacterial activities of the membranes against *Pseudomonas aeruginosa*, *Escherichia coli*, and *Staphylococcus aureus* were examined by disk diffusion and percentage reduction assays, which were performed simultaneously as per the certificates from the Ministry of Health Institute of Public Health in Ho Chi Minh city. The tri-layer membranes, named PCLAg50/PT (plasma treatment)/COS and PCLAg500/PT/COS, achieved desirable antibacterial results with extensive inhibition zones and bacterial reduction rates ranging from 99-100%. In addition, while the PCLAg500 membrane exhibited broad inhibition zones and reduction rates ranging from 94.6-97%, the PCLAg50 membrane achieved reduction rates ranging from 67.5-82.1% despite the absence of inhibition zones. As a result, the fabricated tri-layer membranes could reduce local and opportunistic infections. Depending on infectious risks, the concentration of silver utilised as an infection-prevention agent must be adjusted from 50 to 500 ppm to ensure safety.

Keywords: **antibacterial, chitosan oligosaccharide, electrospinning, plasma treatment, polycaprolactone, polyvinylpyrrolidone, silver nanoparticles.**

Classification number: **3.6**

1. Introduction

Traditional dressings have often favoured cotton gauze to dress all types of wounds [1]. Over centuries, advanced dressings have evolved into numerous forms including adherent dressing, semipermeable films, hydrocolloids, hydrogels, alginates, foam dressings, and antimicrobial dressings, effectively supporting treatment for different types of wounds [2, 3]. Among these, antimicrobial dressings play a crucial role in wound infection management or at least in preventing potential risks from external pathogens [4]. In clinical practice, the use of commercial dressings containing antiseptic substances leads to a significant alleviation in wound severity and treatment-related burdens [5]. Besides antibacterial properties, ideal dressings should enable gaseous exchange, exudate absorption, waterproofing, and painless removal [6]. To meet these requirements, ideal dressings should be designed with three layers: an inner-contact layer, a middle absorbent layer, and an outer waterproof layer with suitable characteristics [7]. The inner layer, in direct contact with the wound site, plays a critical role in treating infection and promoting tissue regeneration, necessitating essential features such as antibacterial capability, absorption, and biocompatibility [8]. Meanwhile, the middle layer primarily absorbs the exudate and maintains moisture in the wound bed, while the outer layer, which covers the wound surface and prevents the invasion of pathogens, needs to be waterproof, mechanically robust, and antibacterial [9]. Consequently, dressing characteristics that promote the healing process have attracted significant interest from scientists for further investigation.

Focusing on antibacterial properties, various antiseptic substances used in wound dressings, such as silver,

*Corresponding author: Email: nthiep@hcmiu.edu.vn

chitosan, chlorhexidine, iodine, etc., have proven effective to treat infectious wounds [10]. Among these, silver in the forms of silver ions or silver nanoparticles is known for its outstanding antibacterial efficiency against a wide range of bacteria, including antibiotic-resistant strains [11, 12]. Historically, silver's mechanism of action involves its positive charges entrapping and penetrating the negatively charged bacterial membrane, triggering the disruption of the respiratory process and resulting in bacterial death [13]. Simultaneously, silver nanoparticles convert into silver ions to prolong the antibacterial effect [14, 15]. However, drawbacks related to overdosing or silver's metal ion form have also been documented [16]. Hoping to achieve low toxicity, COS have been proposed as an additional antibacterial indicator.

Although COS dissolves in water or organic solvents, facilitating its use in wound dressings without causing toxicity, it may be rapidly released and degraded in the exuding wounds, shortening the antibacterial treatment duration due to its low molecular weight. To address these limitations, researchers have studied the combination of polyvinylpyrrolidone (PVP) with COS to increase molecular weight. PVP, a non-ionic and water-soluble polymer, is widely used in pharmaceutical applications and approved by Food and Drug Administration. In wound dressings, its advanced properties include hygroscopicity, attributed to the presence of vinylpyrrolidone, which helps to absorb exudate and maintain moisture in the wound bed, significantly promoting wound healing.

Regarding the foundation of wound dressings, numerous polymers have been combined to synthesise multi-functional membranes with advanced characteristics such as high tensile strength, waterproofness, wettability, and biocompatibility. Notably, the electrospinning technique has been widely applied to produce fibre membranes with advanced features for wound dressing, thanks to polymers. Many researchers have taken an interest in a synthetic material known as PCL, which is utilised to fabricate electro-spun membranes with exceptional mechanical, physical, elasticity, and hydrophobic properties. Consequently, it can cover and protect the wound from the external forces while preventing unexpected leakage or absorption. Another advantage of PCL-based membranes is their scaffolding, which can entrap and stabilise silver nanoparticles.

One study reported that silver nanoparticles loaded in PCL electrospun membranes, with a silver content of 500 ppm, exhibited excellent growth inhibition against both gram-negative and gram-positive bacterial strains [17]. In contrast to PCL's features, PT is known as a method to improve polymer wettability. In several studies, a time-stable wetting effect on plasma-treated polymers helped manage weak hydrophobic properties. In fact, PCL surface are hydrophobic, which limits their compatibility with human tissue essential for such applications as dressings. In the dressing application of plasma-treated polycaprolactone, its functional group anchors to the PCL backbone, and these groups tend to etch the polymer surface and attract other hydrophilic components [18]. As a result, the plasma-treated membrane is not only wettable but also a scaffold for hydrophilic solution coatings. In addition, this membrane possesses good mechanical strength and biocompatibility, both of which have been widely utilised in biomedical applications. In another investigation, membranes coated with COS/PVP also demonstrated growth inhibition of both gram-negative and gram-positive bacterial strains [19]. However, this research focuses on the antibacterial properties of silver and COS in polymetric electrospun membranes, encompassing not only growth inhibition but also bactericidal performance.

This work aims to evaluate the antibacterial properties of tri-layer membranes containing two antibacterial agents, COS and AgNPs, against *P. aeruginosa*, *E. coli* and *S. aureus* using qualitative and quantitative testing. The tri-layer membranes consist of: (1) an outer layer with a PCL membrane loaded with silver nanoparticle (50 ppm and 500 ppm), serving as the waterproof cover to maintain an aseptic environment; (2) a middle PCL/PT layer primarily for absorption; and (3) an inner layer featuring COS/PVP coatings, intended to treat wound infections, maintain moisture, ensure non-adherence. Additionally, these membranes were re-examined objectively to confirm their high reliability at the Institute of Hygiene and Public Health.

2. Materials and methods

2.1. Materials

PCL (80,000 Da) and dimethyl sulfoxide (DMSO) were purchased from Sigma-Aldrich Co., St. Louis, MO (USA). PVP K30 (40,000 Da), silver nitrate ($AgNO_3 \geq 99\%$), acetone (AC, CH_3COCH_3, 99.5%), hydrogen peroxide (H_2O_2) 30% (v/v) reagent, EtOH (C_2H_5OH) (100%), and Tween 20 were produced by Xilong Chemical Co., Ltd. (China). Low-viscosity chitosan (CS) (270 kDa) was purchased from Dao Nguyen, Vietnam. Mueller-Hinton broth (MHB)

was supplied by Hi-Media (India). Muller-Hinton agar (MHA) was purchased from Oxoid, UK. CN Agar for *P.* was purchased from Biokar Diagnostics, France. Bacteria *P. aeruginosa* ATCC 9028, *E. coli* ATCC25922, and *S. aureus* ATCC 25913 were supplied from the Marine Laboratory, International University - Vietnam National University, Ho Chi Minh City, Viet Nam. All chemicals were analytical grade and were used directly without further purification.

2.2. Methods

2.2.1. Preparation of PCLAg solutions with silver concentrations of 50 and 500 ppm and PCL solution

$AgNO_3$ solution (100,000 ppm) was prepared by dissolving 1.573 g of $AgNO_3$ in 10 ml DMSO solvent in a dark container, stirring at 200 rpm for 1 hour at room temperature. A PCL solution (12% w/v) was then prepared by dissolving PCL pellets in fresh acetone, stirring at 400 rpm at 70°C for 4 hours. After that, 2.5 ml of freshly prepared liquid $AgNO_3$ was added to 497.5 ml of PCL solution while stirring at 400 rpm for 30 min at room temperature. The solutions of silver nanoparticles stabilised in PCL were successfully prepared by γ-ray (Co-60) irradiation at a dose of 15 kGy and dose rate of 6.5 kGy/h by Gamma GC-5000 (Brit, India), following a previously described procedure [17]. Additionally, the PCLAg50 solution was also obtained by diluting the irradiated PCLAg500 solution ten times with PCL solution (12% w/v).

2.2.2. Preparation of membranes: PCLAg50 and PCLAg500

The electrospun membranes were fabricated with an electrospinning machine designed by the School of Biomedical Engineering, International University, Vietnam National University, Ho Chi Minh City. The following parameters were used: feed rate of 2.5 ml/h, voltage of 15 kV, the rotation speed of 150 rpm, collecting membrane area of 600 m^2, 10 ml syringe, and 18G needle. The bilayer membranes were electrospun with three syringes set up in parallel, and the volumes of PCLAg solution and PCL solution were 45 ml and 15 ml, respectively. PCLAg50/PCL and PCLAg500/PCL (10x10 cm) were placed at the center of the plasma chamber (GaLa Instrumente, Germany) for 2 min of air plasma treatment under the following conditions: 30 W RF power and a frequency of 13.56 MHz.

2.2.3. Preparation of solution: COS-PVP

The coating solution containing COS and PVP was formulated in accordance with previous work [19]. Firstly, chitosan (3%w/v) was immersed in H_2O_2 solution (6% v/v) and stirred at 90°C for 4 hours. The COS-formed solution was filtered before the PVP powder (6% w/v) was added to and stirred for 30 min at room temperature.

2.2.4. Preparation of the tri-layer membranes: PCLAg50/PT/COS and PCLAg500/PT/COS

The bilayer membranes were cut into 6x6 cm pieces and placed in a 5x5 cm exposure area mold. Then, 6 ml of COS-PVP solution was coated onto the surface of the PCL-PT layers in three equal portions. After each coating, they were dried in a vacuum oven at 40°C for one day. Finally, the total collection area of the coated membrane was 5x5 cm. All samples were fabricated with the following parameters shown in Table 1 below.

Table 1. The content of components in the PCLAg/PT/COS membrane.

LAYER	PCL	SILVER		COS
PCLAg	12% w/v	50 ppm	500 ppm	-
PCLAg/PT				-
COS	-	-	-	0.18% w/v

2.2.5. Scanning electron microscopy (SEM)

The surface morphologies of all the membranes were determined by SEM (JSM-IT100 and Smart Coater, JEOL, Japan). After that, the fibre diameter and the porosity of the membrane were measured by ImageJ software (NIH, Maryland, USA).

2.2.6. Antibacterial experiments

Quality antibacterial experiment: The agar diffusion standard method was employed as a quick qualitative evaluation of the antibacterial susceptibility of specimens [20]. The prepared bacterial culture of 10^6 CFU/ml was transferred to sterile agar disks of 90 mm diameter containing 15 ml Miller-Hinton agar. Then, 10x10 mm square samples were gently placed on the surface of the inoculated disks. The disks were incubated for 18-24 hours, and the results were demonstrated by measuring the diameter of inhibition zones around the specimens. The experiments were triplicated.

Quantitative antibacterial experiment: The AATCC100 method was employed as a quantitative evaluation of the antibacterial performance of specimens over 24 hours [21]. An antibacterial membrane and two blank membranes (controls) with diameters of 4.8 cm were placed into separate 250 ml flasks and then 1 ml of diluted suspension with 10^5 CFU/ml was added dropwise. Immediately after, 100 ml of sodium chloride 0.9% was added to the control flasks, and

the bacteria was shaken out from the membrane. Then, 100 µl of this solution was spread on the surface of Miller Hinton agar disks (except for the *P. aeruginosa* sample, which used the CN agar disk) and inoculated at 37°C for 18-24 hours. Finally, the number of bacterial colonies was counted as A. The two remaining flasks were simultaneously inoculated at 37°C for 18-24 hours. As in the preceding procedure, the number of bacterial colonies shaken out of the antibacterial membrane and the blank membrane were denoted as B and C, respectively. The experiments were triplicated. The results are expressed by the formula:

$$R\ (\%) = [(A-B)/A]x100$$

where R (%) is the percentage reduction; A is the number of bacteria recovered from the blank membrane immediately after being treated; B is the number of bacteria recovered from the inoculated antibacterial specimen after 24 hours.

2.2.7. Statistical analysis

Statistical analysis and graphs were done using Origin Pro 8.5.1. Differences between samples were analysed by one-way analysis of variance (ANOVA) followed by the Student's T-test. Data were expressed as mean ±SD.

3. Results and discussion

3.1. Evaluation of surface morphology

The successful fabrication of the tri-layer membranes (including the outer PCLAg layer with two silver concentrations of 50 and 500 ppm, the middle PCLAg/PT layer, and the inner COS-coated layer) and the PCL membrane is demonstrated in Fig. 1. Fig. 1A provides the SEM micrographs, Fig. 1B shows the distributions of the fibre diameters, and Fig. 1C shows the distributions of the pore diameters. All membranes were produced with non-beaded fibres stacked on top of each other to create a bulging and porous structure. There is no significant difference in fibre diameters between groups containing silver concentrations of 50 and 500 ppm. The outer layers of PCLAg50 and PCLAg500 have mean fibre diameters of 1.07 and 1.05 µm, respectively. Compared to those in the outer layers, the fibres in the middle layers, including PCLAg50/PT and PCLAg500/PT, increased slightly to approximately 1.18 and 1.17 µm, respectively. Changes in the surface of all layers were also observed in the mean diameter of porosity. The outer PCLAg layers had mean porosity sizes around 11.51 and 12.89 µm. However, the coated COS layers had significantly reduced mean porosity diameters of 7.76 and 9.45 µm, with only 10% of porosity visible on the surface. The coating method allowed for covering over 90% of the membrane surface. Both diameter and porosity contributed to creating an ideal membrane for wound dressing applications.

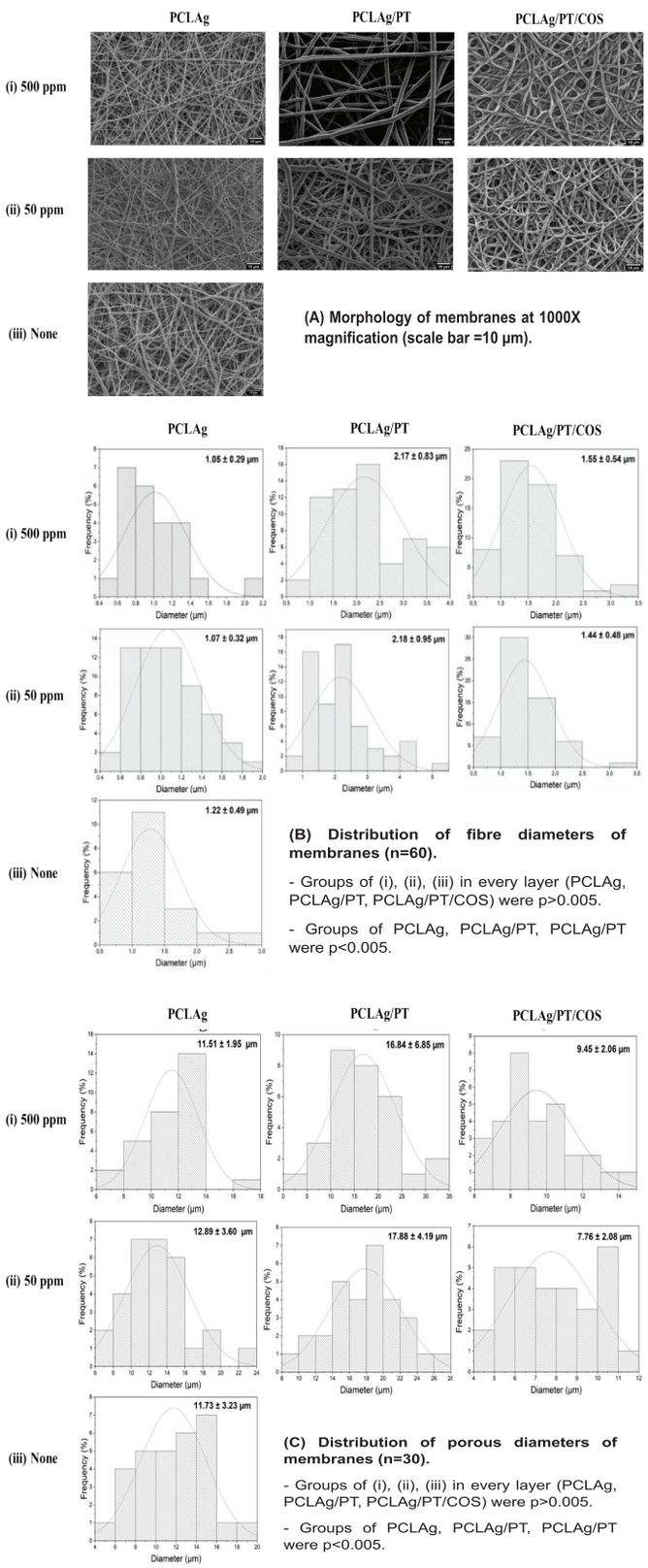

Fig. 1. SEM results of tri-layer membranes including the PCLAg layers, the PCLAg/PT layers, and the COS layers at two concentrations of silver (i) 500 ppm and (ii) 50 ppm.

3.2. Evaluation of antibacterial activities

The antibacterial activities of the PCLAg membranes and the tri-layer PCLAg/PT/COS membranes were examined by qualitative and quantitative tests against *P. aeruginosa*, *E. coli*, and *S. aureus* to comprehensively understand their characteristics over a wide range of applications.

In terms of the antibacterial activity, Fig. 2 and Table 2 demonstrate the results of the PCLAg membranes consisting of silver nanoparticles at 50 and 500 ppm, which show that the inhibition zones of the PCLAg500 membrane against *P. aeruginosa*, *E. coli*, and *S. aureus* were 15.3, 11.4, and 13.6 mm, respectively, whereas those of PCL served as the control. For the quantitative results, the reduction percentages of the membrane with a silver content of 500 ppm against *P. aeruginosa*, *E. coli*, and *S. aureus* achieved expected numbers (over 90%). Regardless of the absence of inhibition zones, the PCLAg50 membrane obtained valuable reduction percentage of over 60%. With this reduction in concentration, there is great potential for using low concentrations of silver nanoparticles in dressings to reduce the accumulation of silver in the skin and blood while still possessing a bactericidal potential of more than 50%.

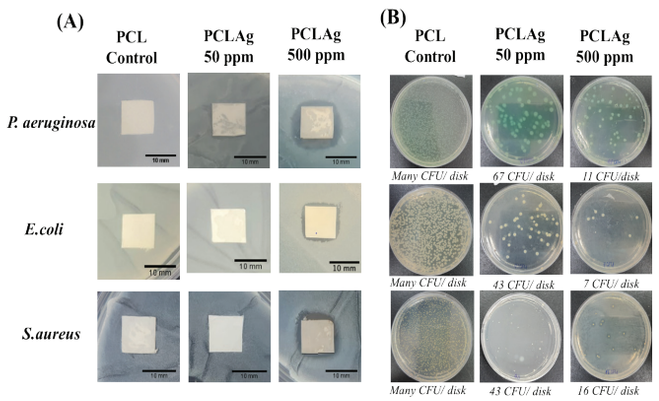

Fig. 2. Images of the antibacterial results of PCLAg50, PCLAg500, and PCL (control) membranes against *P. aeruginosa*, *E. coli*, and *S. aureus*. (A) Inhibition zone with a 10-mm scale bar; **(B)** bacterial colonies 24 hours after injection (n=3).

Table 2. The inhibition diameter and reduction percentage of PCLAg50, PCLAg500, and PCL (control) membranes against *P. aeruginosa*, *E. coli*, and *S. aureus*.

Sample	Inhibition zone diameter (mm)			Reduction percentage (%)		
	P. aeruginosa (-)	*E. coli* (-)	*S. aureus* (+)	*P. aeruginosa* (-)	*E. coli* (-)	*S. aureus* (+)
PCLAg500	15.5±0.05	11.4±0.06	13.6±0.06	94.6	96.8	97
PCLAg50	-	-	-	67.5	86.5	82.1
PCL (Control)	-	-	-	-	-	-

Table 3. The inhibition zone diameter and reduction percentage of PCLAg50/PT/COS, PCLAg500/PT/COS, and PCL (control) membranes against *P. aeruginosa*, *E. coli*, and *S. aureus*.

Sample	Inhibition zone diameter (mm)			Reduction percentage (%)		
	P. aeruginosa (-)	*E. coli* (-)	*S. aureus* (+)	*P. aeruginosa* (-)	*E. coli* (-)	*S. aureus* (+)
PCLAg500/PT/COS	13.7±0.03	13.2±0.01	22.4±0.06	100	99	99.4
PCLAg50/PT/COS	11.9±0.03	12.3±0.02	15.2±0.05	100	99	99.3
PCL (Control)	-	-	-	-	-	-

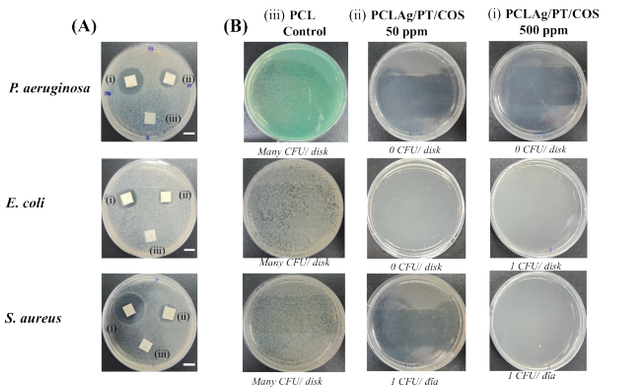

Fig. 3. Images of the antibacterial results of PCLAg50/PT/COS, PCLAg500, and PCL (control) membranes against *P. aeruginosa*, *E. coli*, and *S. aureus*. (A) Inhibition zone with a 10 mm scale bar and **(B)** Bacterial colonies 24 hours after injection (n=3).

All results from the tests on the tri-layer PCLAg/PT/COS membranes containing silver and COS are shown in Fig. 3 and Table 3. From the qualitative results, Fig. 3A and Table 3 show the inhibition zones of the PCLAg500/PT/COS membranes against three strains of bacteria were considerably higher than those of the PCLAg50/PT/COS membrane and the COS-containing surface in direct contact with bacteria. In detail, while the inhibition diameters of the PCLAg500/PT/COS membranes against *P. aeruginosa*, *E. coli*, and *S. aureus* were 13.7, 13.2, and 22.4 mm, those of the PCLAg50/PT/COS membranes were slightly lower at 11.9, 12.3, and 15.2 mm, respectively. In the quantitative results, Fig. 3B and Table 3 show that the aforementioned membranes have comparable reduction percentages against *P. aeruginosa* (100%) and *E. coli* (99%) with the exception of *S. aureus*, which was about 99.4% for PCLAg500/PT/COS and 99.3% for PCLAg50/PT/COS (the difference was not statistically significant). Therefore, the antibacterial efficiency of the tri-layer membrane at the wound site increased when combined with COS, and the silver nanoparticles seem to be a subsequent antibacterial factor to maintain an aseptic environment around to wound, supporting the healing process. In conclusion, the synergistic effect of COS and silver nanoparticles in the PCLAg/PT/COS membranes not only reduces the wound

infection but also disinfects the surrounding environment to promote healing.

3.3. Certification of the antibacterial activities of the tri-layer membranes

PCLAg50/PT/COS and PCLAg500/PT/COS at the Institute of Public Health in Ho Chi Minh city. To objectively guarantee high accuracy of the antibacterial properties of the tri-layer PCLAg/PT/COS membranes, all membranes were examined through a qualitative test (the AATCC147 Standard) and a quantitative test (the AATCC100 Standard) by the Institute of Public Health in Ho Chi Minh city. According to the AATCC145 results, both PCLAg500/PT/COS and PCLAg50/PT/COS samples had relatively similar inhibition zones against *P. aeruginosa* (7.6 and 6.7 mm), *E. coli* (3.0 and 3.1 mm), and *S. aureus* (11.1 and 11.6 mm), respectively (Fig. 4 and Table 4). According to the AATCC100 results, both membranes attained reduction percentages of 100% (Table 4). In conclusion, the investigations conducted by the Institute of Public Health in Ho Chi Minh city demonstrated that PCLAg50/PT/COS and PCLAg500/PT/COS had excellent antibacterial efficacy, agreeing with the aforementioned results.

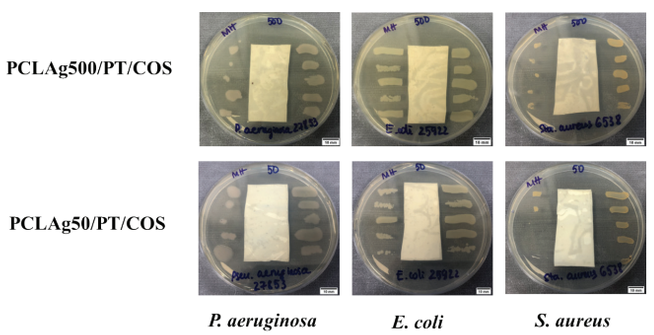

Fig. 4. The inhibition zone images of PCLAg500/PT/COS and PCLAg50/PT/COS membranes against *P. aeruginosa*, *E. coli*, and *S. aureus* implemented by the Institute of Public Health in Ho Chi Minh city.

Table 4. The inhibition diameters and reduction percentages of the PCLAg50/PT/COS and PCLAg500/PT/COS membranes examined at the Institute of Public Health in Ho Chi Minh city against *P. aeruginosa*, *E. coli*, and *S. aureus*.

Sample	Inhibition zone diameter (mm)			Percentage reduction (%)		
	P. aeruginosa (-)	*E. coli* (-)	*S. aureus* (+)	*P. aeruginosa* (-)	*E. coli* (-)	*S. aureus* (+)
PCLAg500/PT/COS	7.6	3.0	11.1	100	100	100
PCLAg50/PT/COS	6.7	3.1	11.6	100	100	100

3.4. Discussion

The aim of this study is to gain a comprehensive understanding of the antibacterial properties of tri-layer membranes to apply the concept of antibacterial dressings for the prevention and treatment of infections. The monolayer PCLAg membranes and the tri-layer PCLAg/PT/COS membranes, consisting of two antibacterial agents of AgNPs in the outer layers and COS in the inner layer, were evaluated for their antibacterial effects using two qualitative and quantitative tests. Simultaneously, the completed tri-layer membranes were objectively reassessed for reliability and transparency at a second prestigious institute prior to conducting pilot-scale production process experiments.

With this aim, all fabrication parameters of the PCLAg/PT/COS membranes incorporating the two antibacterial agents - AgNPs and COS - were determined by consulting and selecting appropriate recent research results [19]. Regarding AgNPs, a silver concentration of 500 ppm in PCL (12% w/v) solution was gamma-irradiated at 15 kGy and analysed by UV-vis spectrometry, displaying an absorption peak of 416 nm indicating the formation of AgNPs [17]. Subsequently, the PCL electrospun membrane was produced to encapsulate AgNPs while preserving their structure from rapid silver ion release. PCL, known for possessing advanced qualities such as biocompatibility, high mechanical and physical strength, and hydrophobicity, was used to fabricate the electrospun membrane as the waterproof covering layer. The shape and size ranged from 15-20 nm, with a distribution of around 0.06%, and notably exhibited a high biological effect (*in vitro*), including bacterial inhibition and biocompatibility. Their antibacterial mechanisms have been reported in numerous studies. However, concerns regarding toxicity due to overdosing and metal ions remain. For this reason, a thorough understanding of their antibacterial characteristics in relation to silver concentration is necessary to minimise potential hazards. In this research, silver nanoparticle concentration in the PCL electro-spun membranes were examined at 500 and 50 ppm to broaden applications. Three bacterial strains - *P. aeruginosa* (gram-negative), *E. coli* (gram-negative), and *S. aureus* (gram-positive) - were selected due to their potential to exacerbate wound infections and the persistent treatment burden posed by their antibiotic resistance. In Fig. 1, SEM results showed the formation of electrospun PCL 12 %w/v,

PCLAg500, and PCLAg50 membranes, which had fibre and porous diameters ranging from 1.05-1.22 µm and 11.51-12.89 µm, respectively. These fibre and porous structures allowed these membranes to effectively distribute and capture AgNPs, enhancing their antibacterial capabilities. In Fig. 2 and Table 2, the PCLAg500 effectively demonstrated its antibacterial properties against *P. aeruginosa*, *E. coli*, and *S. aureus,* with inhibition diameters of 15.5, 11.4, and 13.6 mm, respectively, and reduction percentages of 94.6, 96.8, and 97%, respectively. In contrast, the PCLAg50 membrane, with a silver concentration ten times lower at 50 ppm compared to PCLAg500, showed reduction rates of 67.5, 86.5, and 82.1% against *P. aeruginosa*, *E. coli*, and *S. aureus*, respectively, despite the absence of inhibition zones. Owing to their superior characteristics, the PCLAg layer should be utilised as a covering layer to prevent pathogen spread and offensive odours.

For the construction of the absorption layer as the middle, the PCLAg membrane was treated with air plasma to transform it into a hydrophilic agent [19, 21]. The effectiveness of this air plasma treatment and its mechanism have been investigated in numerous previous studies [22]. In this research, Figs. 1B and 1C demonstrate that the fibre (approximately 2.17 and 2.18 µm) and porous (around 16.84 and 17.68 µm) structures of the PCLAg/PT membrane treated with air plasma were slightly higher than those of PCLAg. In fact, air plasma interacts with the surface of the polymer membrane, changing its surface structures [18]. Simultaneously, it has also been reported that air plasma triggers the formation of new polar groups such as hydroxyl (-OH) and carbonyl (-C=O), attracting water molecules [23]. Therefore, the air plasma treatment of the PCLAg layers produced the middle layers, which underwent structural changes accompanied by the modification of hydrophilic properties. These characteristics facilitate coating of hydrophilic solutions to form the inner layer.

For the fabrication of the third layer, bioactive substances are often incorporated and directly applied to the wound site to promote healing. In the case of an infected wound, several inevitable issues, such as pathogens, excessive exudate, and physical soft tissue injury, impede the healing process. Hence, a membrane coated with COS-PVP solution has proven biological advantages to promote wound healing owing to its excellent antibacterial activity, hemostatic action, and biocompatibility. In detail, COS, a naturally derived bioproduct from shrimp, is known for its antibacterial properties and, especially, its outstanding biocompatibility in tissue engineering applications [24]. Although the exact mechanisms remain unclear, several theories suggest that protonated amine groups in COS interact with the bacterial membrane, leading to leakage of intracellular constituents or disrupted nutrient transportation. However, COS exhibits weak stability due to the low molecular weight, making it difficult to achieve maximum antibacterial performance.

To enhance the benefits of COS, PVP is combined with COS in the coated layer as a delivery agent [19], which supports exudate absorption, moisture retention, and COS delivery to the wound bed. This means that the dressing could absorb exudates and release the maximum amount of COS with the assistance of PVP, increasing its antibacterial performance and healing progress. Additionally, the coating the COS/PVP layer onto the other two layers during use facilitates painless removal. In previous studies, the electrospun membrane coated with 6 ml COS (3% w/v) and PVP (6% w/v) solution was demonstrated to inhibit bacterial growth (*in vitro*) and promote wound healing (*in vivo*). In this work, the formation of a coated layer was evidenced by a significant decrease in porous diameters to 9.45 (PCLAg500/PT/COS) and 7.76 µm (PCLAg50/PT/COS) (Fig. 1). In Fig. 3 and Table 3, although the inhibition zones of PCLAg500/PT/COS membrane against *P. aeruginosa*, *E. coli*, and *S. aureus* were 13.7, 13.2, and 22.4, wider than those of the PCLAg50/PT/COS at 11.9, 12.3, and 15.2 mm, the bacterial reduction results of both membranes were comparable around 100, 99, and 99.4%, respectively.

Finally, the antibacterial tests reassessed at the Ministry of Health Institute of Public Health in Ho Chi Minh city showed that the PCLAg500/PT/COS and PCLAg50/PT/COS membranes achieved broad inhibition zones of approximately 7.6, 6.7, 3.0 and 3.1 11.1, and 11.6 mm, respectively, against *P. aeruginosa*, *E. coli*, and *S. aureus*, respectively, will all exhibit reduction percentages of 100% (Fig. 4 and Table 4). In fact, both tri-layer membranes obtained optimal antibacterial performance despite the silver concentration being 50 or 500 ppm, comparable to the results above. While a silver concentration of 500 ppm captures attention for its high antibacterial performance in sterilising dressing, a silver concentration of 50 ppm still

achieves an acceptable value for infection prevention. In this experiment, silver played a key role in preventing infection by maintaining a sterile environment around the wound by preventing pathogens from entering the wound and helping disinfect the wound fluid. Therefore, a silver concentration of 50 or 500 ppm should be selected by considering the degree of safety and infection.

4. Conclusions

This study reported the antibacterial capabilities of tri-layer membranes containing two antibacterial agents, AgNPs and COS, designated as PCLAg50/PT/COS and PCLAg500/PT/COS, to exploit their synergistic impact for the development of ideal antibacterial wound dressings. The main difference between these two membranes is the concentration of silver nanoparticles in the PCLAg layers of which 50 and 500 ppm were compared to investigate its toxicity due to overdose. The fibre and porous structures of all three layers of the membranes were examined by SEM. The antibacterial performance of both tri-layer membranes reached almost 100%. Meanwhile, the reduction percentages of PCLAg500 were high, approximately 94.6% (*P. aeruginosa*), 96.8% (*E. coli*), and 97% (*S. aureus*). The PCLAg50 membrane values were slightly lower at 67.5, 80.6, and 82.1%, respectively. Although the silver concentration of the outside layer was reduced 10 times to 50 ppm, its reduction percentage was only reduced by 15%. Therefore, applying silver concentrations of 50 or 500 ppm to the outer layer to maintain a sterile wound environment should consider safety and the degree of infection. Finally, applying two antibacterial agents to wound dressings could provide comprehensive antibacterial efficacy to facilitate wound healing.

CRediT author statement

Thi Thanh Ngoc Nguyen: Investigation, Sample analysis, Data processing, Methodology, Writing the manuscript; Thi Thanh Tam Phan: Writing the editing, Methodology. Thi Hiep Nguyen: Supervise and comment on editing the manuscript for completeness.

ACKNOWLEDGEMENTS

This research was funded by the Department of Science and Technology of Ho Chi Minh city under the grant number 01/2020/HD-QPTKHCN.

COMPETING INTERESTS

The authors declare that there is no conflict of interest regarding the publication of this article.

REFERENCES

[1] M.S. Khalaji, I. Lugoloobi (2020), "Biomedical application of cotton and its derivatives", *Cotton Science and Processing Technology: Gene, Ginning, Garment and Green Recycling*, Springer, pp.393-416, DOI: 10.1007/978-981-15-9169-3_16.

[2] S. Dhivya, V.V. Padma, E. Santhini (2015), "Wound dressings - A review", *Biomedicine (Taipei)*, **5(4)**, pp.1-5, DOI: 10.7603/s40681-015-0022-9.

[3] J. Boateng, O. Catanzano (2015), "Advanced therapeutic dressings for effective wound healing - A review", *J. Pharm. Sci.*, **104(11)**, pp.3653-3680, DOI: 10.1002/jps.24610.

[4] L. Rutter (2018), "Identifying and managing wound infection in the community", *Br. J. Community Nurs.*, **23(3)**, pp.S6-S14, DOI: 10.12968/bjcn.2018.23.Sup3.S6.

[5] N. Mayet, Y.E. Choonara, P. Kumar, et al. (2014), "A comprehensive review of advanced biopolymeric wound healing systems", *J. Pharm. Sci.*, **103(8)**, pp.2211-2230, DOI: 10.1002/jps.24068.

[6] Z. Obagi, G. Damiani, A. Grada, et al. (2019), "Principles of wound dressings: A review", *Surg. Technol. Int.*, **35**, pp.50-57.

[7] L. Qi, K. Ou, Y. Hou, et al. (2021), "Unidirectional water-transport antibacterial trilayered nanofiber-based wound dressings induced by hydrophilic-hydrophobic gradient and self-pumping effects", *Mater. Des.*, **201(5)**, DOI: 10.1016/j.matdes.2021.109461.

[8] W. Ji, F. Yang, H. Seyednejad, et al. (2012), "Biocompatibility and degradation characteristics of PLGA-based electrospun nanofibrous scaffolds with nanoapatite incorporation", *Biomaterials*, **33(28)**, pp.6604-6614, DOI: 10.1016/j.biomaterials.2012.06.018.

[9] J.A. Fulton, K.N. Blasiole, T. Cottingham, et al. (2012), "Wound dressing absorption: A comparative study", *Adv. Skin Wound Care*, **25(7)**, pp.315-320, DOI: 10.1097/01.ASW.0000416003.32348.e0.

[10] A.B. Öztürk, B. Özkahraman, Z. Özbaş, et al. (2021), "Advancements and future directions in the antibacterial wound dressings - A review", *J. Biomed. Mater. Res. Part B Appl. Biomater.*, **109(5)**, pp.703-716, DOI: 10.1002/jbm.b.34736.

[11] M. Rai, A. Yadav, A. Gade (2009), "Silver nanoparticles as a new generation of antimicrobials", *Biotechnol. Adv.*, **27(1)**, pp.76-83, DOI: 10.1016/j.biotechadv.2008.09.002.

[12] J. Boateng, O. Catanzano (2020), "Silver and silver nanoparticle-based antimicrobial dressings", *Ther. Dressings Wound Heal. Appl.*, pp.157-184, DOI: 10.1002/9781119433316.ch8.

[13] W.K. Jung, H.C. Koo, K.W. Kim, et al. (2008), "Antibacterial activity and mechanism of action of the silver ion in *Staphylococcus aureus* and *Escherichia coli*", *Appl. Environ. Microbiol.*, **74(7)**, pp.2171-2178, DOI: 10.1128/AEM.02001-07.

[14] J.R. Morones, J.L. Elechiguerra, A. Camacho, et al. (2005), "The bactericidal effect of silver nanoparticles", *Nanotechnology*, **16(10)**, pp.2346-2353, DOI: 10.1088/0957-4484/16/10/059.

[15] M. Raffi, F. Hussain, T.M. Bhatti, et al. (2008), "Antibacterial characterization of silver nanoparticles against *E. coli* ATCC-15224", *J. Mater. Sci. Technol.*, **24(2)**, pp.192-196.

[16] C. Beer, R. Foldbjerg, Y. Hayashi, et al. (2012), "Toxicity of silver nanoparticles-nanoparticle or silver ion?", *Toxicol. Lett.*, **208(3)**, pp.286-292, DOI: 10.1016/j.toxlet.2011.11.002.

[17] C.M. Tran, N.T.T. Nguyen, M.H. Ho, et al. (2023), "One-pot preparation of antibacterial electrospun polycaprolactone membrane embedded with gamma irradiation-induced silver nanoparticles", *Fibers Polym.*, **24**, pp.29-43, DOI: 10.1007/s12221-023-00031-z.

[18] R. Suntornnond, J. An, C.K. Chua (2016), "Effect of gas plasma on polycaprolactone (PCL) membrane wettability and collagen type I immobilised for enhancing cell proliferation", *Materials Letters*, **171**, pp.293-296, DOI: 10.1016/j.matlet.2016.02.059.

[19] V.K. Doan, C.M. Tran, T.T.P. Ho, et al. (2022), "Optimization of oligomer chitosan/polyvinylpyrrolidone coating for enhancing antibacterial, hemostatic effects and biocompatibility of nanofibrous wound dressing", *Polymers*, **14(17)**, DOI: 10.3390/polym14173541.

[20] E. Pinho, L. Magalhães, M. Henriques, et al. (2011), "Antimicrobial activity assessment of textiles: Standard methods comparison", *Ann. Microbiol.*, **61(3)**, pp.493-498, DOI: 10.1007/s13213-010-0163-8.

[21] D. Porrelli, M. Mardirossian, L. Musciacchio, et al. (2021), "Antibacterial electrospun polycaprolactone membranes coated with polysaccharides and silver nanoparticles for guided bone and tissue regeneration", *ACS Appl. Mater. Interfaces*, **13(15)**, pp.17255-17267, DOI: 10.1021/acsami.1c01016.

[22] I. Levchenko, S. Xu, O. Baranov, et al. (2021), "Plasma and polymers: Recent progress and trends", *Molecules*, **26(13)**, DOI: 10.3390/molecules26134091.

[23] N.S. Kasalkova, P. Slepicka, Z. Kolska, et al. (2015), "Wettability and other surface properties of modified polymers", *Wetting and Wettability*, DOI: 10.5772/60824.

[24] T.T.P. Ho, V.K. Doan, N.M.P. Tran, et al. (2021), "Fabrication of chitosan oligomer-coated electrospun polycaprolactone membrane for wound dressing application", *Mater. Sci. Eng. C*, **120**, DOI: 10.1016/j.msec.2020.111724.

 DOI: 10.31276/VJSTE.65(2).88-96

Characteristic and distribution of grain sizes and minerals in sediments from the Vietnamese Gulf of Tonkin

Dang Hoai Nhon[1*], Nguyen Van Thao[1], Tran Duc Thanh[1], Nguyen Dac Ve[1], Bui Van Vuong[1], Lai Thi Bich Thuy[2], Bui Thi Thanh Loan[3], Hoang Thi Chien[1], Duong Thanh Nghi[1]

[1]*Institute of Marine Environment and Resources, Vietnam Academy of Science and Technology, 246 Da Nang Street, Cau Tre Ward, Ngo Quyen District, Hai Phong City, Vietnam*
[2]*Center for Geological Experiment Analysis, Ministry of Natural Resources and Environment, Km9, Nguyen Trai Street, Van Quan Ward, Ha Dong District, Hanoi, Vietnam*
[3]*Institute of Environment, Vietnam Maritime University, 484 Lach Tray Street, Kenh Duong Ward, Le Chan District, Hai Phong City, Vietnam*

Received 23 May 2022; revised 29 July 2022; accepted 16 August 2022

Abstract:

Grain sizes and minerals of sediments from the Gulf of Tonkin were evaluated from 30 surface samples and 50 samples from two cores. The distribution of grain sizes and minerals from these samples were determined to help understand sediment characteristics, origins, and environmental dynamics. There were five sediment types: fine and very fine sands, very coarse, coarse, and medium silts. Minerals in the sediment were identified as decreasing in terms of the content of quartz, illite, kaolinite, chlorite, feldspar, goethite, halite, calcite, gibbsite, aragonite, and montmorillonite. Contents of major minerals such as quartz, illite, kaolinite, and chlorite varied from nearshore to offshore; quartz was higher nearshore than offshore; illite, kaolinite, and chlorite from nearshore were lower than offshore; calcite and aragonite were low nearshore and higher in the offshore; goethite was lower offshore and higher nearshore; and, finally, halite was high offshore and low nearshore. Surface sediments were divided into three groups based on sedimentary environment characteristics: Group 1 was distributed nearshore with strong dynamics, Group 2 in bays and nearshore with weak dynamics, and Group 3 was distributed offshore with quiet dynamics. The origin of the sediments was weathering and erosion from the mainland and islands under the river and sea processes in the Gulf of Tonkin with quartz, illite, kaolinite, feldspar, chlorite, and montmorillonite found present in the sediment. Geochemical processes produced goethite, gibbsite, halite, and pyrite in the sediments while biological substances produced calcite and aragonite.

Keywords: **grain size, Gulf of Tonkin, minerals, Vietnam.**

Classification numbers: **5.1, 5.3**

1. Introduction

The Gulf of Tonkin, shared by Vietnam and China, has contributed significant economic value such as fishing, minerals, and transportation for both countries. Therefore, understanding the environment's characteristics plays a key role in effective natural resource utilisation and supporting sustainable economic development. The distribution and provenance of clay minerals in the Gulf's surface sediments were studied, and four sedimentary sources have been identified, including southern mainland China, Hainan island, the Red river system, and the mouth of the Gulf of Tonkin [1]. The sediments are typically mud, occasionally sand, and poorly to very poorly sorted [2].

Ten sedimentary fields were distributed around the Co To islands (Vietnam), including sandy gravel, gravelly sand, sand, gravelly muddy sand, sand mixed gravel, muddy sand, gravelly mud mixed sand, muddy sand, muddy sandy gravel, and sandy mud. The sediments contained quartz in the form of minerals, detritus, feldspar, mica, and shells. The origins of these surface sediments were mainly continental [3].

On the western coast of the Gulf of Tonkin, rocks, gravel, sand, and mud were present. Rocks and gravel were often found near the rocky coast, while sand and mud were widespread in the intertidal zone, beaches, and estuaries [4]. Sand and silt were also common in the intertidal zone at the mouth of the Red river system [5, 4] and Ha Long bay [6]. The sediment sources of the Red river system and partially eroded and weathered sources of the islands and surrounding geological system have been identified based on smectite in Ha Long bay sediments [7].

Around the Cat Ba islands, eight sediment types were distributed, decreasing coarse silt > very coarse silt > medium sand, very fine sand > very coarse sand, fine > coarse sand, and very fine gravel. The mineral content of sediments decreased with concentration: quartz > illite > aragonite > kaolinite > calcite > chlorite > goethite > halite > feldspar and less montmorillonite and dolomite. Calcite, aragonite, goethite, and halite from marine organisms were formed by chemical processes, while quartz, illite, kaolinite, chlorite, and montmorillonite from terrigenous sources were formed by weathering and erosion [8].

Previous studies on grain size and mineralogy have been conducted in the Gulf of Tonkin, both in Vietnam and China. However, most surveys conducted on the Vietnamese side were

[*]*Corresponding author: Email: nhondh@imer.vast.vn*

about the nearshore and poorly conducted offshore. This study provides further information on offshore grain size and mineral composition to better understand the Gulf of Tonkin's sedimentary environment.

2. Materials and methods

The Gulf of Tonkin covers an area of 126,250 km^2, and its border between Vietnam and China was established in 2000 and took effect in 2004. The Vietnamese side has large river systems such as the Red river, the Ca river, and the Ma river, which meet the Gulf. In addition, several smaller rivers in Quang Ninh province also meet the Gulf. Along the coast, there are ports such as Hai Phong, Nghi Son, and Cua Ong in Vietnam, and Fangcheng in China. The Gulf of Tonkin is influenced by the northeast (NE) monsoon from November to March and by the southwest (SW) monsoon from May to September, which reverses the direction of the current. Near the coast, it flows from NE to SW during NE monsoon and from SW to NE during SW monsoon. In the offshore area, the current is stable from NE and SW during monsoons. Tidal levels in the Gulf of Tonkin vary from north to south, with the highest at Mong Cai (4.7 m) and the lowest at Quang Tri (1.16 m) during spring tides [9].

In July 2018, the Petersen grab collected thirty surface samples to understand the sediment characteristics of the bay, and two sediment cores were hand-cored in the estuary and lagoon to understand changes in the sediment environment in the coastal waterbody (Fig. 1). Surface samples were collected from 0-10 cm from the beach to a depth of 50 m. The C1 core was collected from Tam Giang - Cau Hai lagoon, and the C2 core was collected from Bach Dang estuary. Each 70-cm-long sediment core was cut into sections: 2 cm from 0 to 20 cm, 3 cm from 20 to 50 cm, and 4 cm from 50 cm to the end. The samples were stored at 4^{o}C on the way to the laboratory. At the laboratory, the samples were dried under room conditions for grain size and mineral analysis.

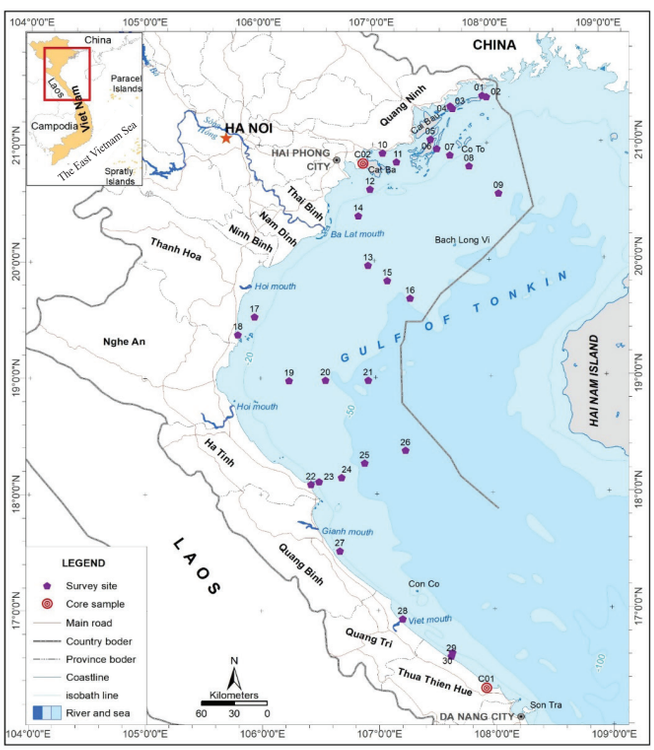

Fig. 1. Sample positions in Gulf of Tonkin.

Grain size analysis: The sediments were salt-washed with distilled water to remove organic matter by H_2O_2, then wet sieved through a 63-µm sieve. The >63 µm fraction left after sieving was evaporated over a warm bath and dried overnight at 105^{o}C, and the particles were sieved between 2000 and 50 µm. For the <63 µm fraction, once all particles had deposited, the water was decanted and filtered through filter paper in a vacuum and dried overnight at 105^{o}C. The <63 µm fraction (5 g) was added to 1 ml 10% NaOH, placed in an ultrasonic bath for 10 min for particles to separate, diluted with distilled water to 1000 ml, then analysed by the pipette method [10]. Sediment parameters were calculated using the GRADISTAT software, and sediment types were classified according to a previous study [11]. This analysis was carried out at the Institute of Marine Environment and Resources, Vietnam Academy of Science and Technology.

Mineral composition analysis: The samples were crushed and sieved with a 0.07 mm sieve. About 2 g of each sample was placed in the sample hole, and the sample was pressed on a 4.5x5 cm glass plate to form a smooth surface. The samples were analysed on a D8 Advance with Cu-$K_{\alpha 1,2}$ radiation, 35 kV voltage, and 35 mA current with 2Θ steps=0.015^o, a 3-sec dwell time and 2Θ range of 5-60^o. This analysis was conducted at the Center for Geological Experimental Analysis of the Ministry of Natural Resources and Environment, Vietnam.

Statistical analysis: Pearson correlation coefficients, clustering, and factor analysis (FA) were used. Correlation coefficients were used to identify the sources of minerals (quartz, illite, kaolinite, chlorite, feldspar, goethite, halite, calcite, aragonite, gibbsite, and montmorillonite) and the conditions of environmental dynamics between grain size parameters (Md, S_0, S_k). Clustering was used to group sedimentary data based on similarity in sediment parameters and to determine the origin, sediment supply, and dynamic conditions of each group. FA was used to estimate which parameters influence sedimentary environments, determine the origin and relationship of minerals, and identify supplies and parameters that strongly control the environment. All these techniques were performed using Origin Pro 2021 software (OriginLab Corporation).

3. Results

3.1. Distribution of sediment types

Five types of sediment were found in the Gulf of Tonkin. The surface sediments included fine sand, very fine sand, very coarse silt, coarse silt, and medium silt. The sediment cores were divided into three types, which were very coarse silt, coarse silt, medium silt. There were no fine or very fine sands.

Fine sand was only found in surface sediments distributed nearshore at depths of up to 30 m from the coast (samples 1, 2, 6, 22, 27), with only one offshore sample (sample 24). Fine sand accounted for 20% of the samples (5/30) (Fig. 2). The mean diameter (Md) was 0.130-0.244 mm, sorting (S_0) was moderately well to poorly sorted (S_0=1.45-3.81), and skewness (S_k) was symmetrical to very coarse skewed (S_k=0.05-0.34).

Very fine sands were only found in surface sediments and were absent in cores. They were distributed from nearshore (samples 4, 11, 17, 28) to offshore (samples 8, 13, 15, 19, 20, 21), accounting for 33.3% of the samples (10/30) (Fig. 2). Md was 0.063-0.112 mm, S_0 was moderately well to very poorly sorted (S_0=1.78-1.53), and S_k was very fine to coarse skewed (S_k=-0.52-0.16).

Very coarse silt was present in both surface and core sediments. Surface sediment was distributed nearshore (samples 7, 10, 12, 14) and offshore (samples 16, 25), accounting for 20% of the samples (6/30 samples) (Fig. 2). The Md varied from 0.032 to 0.061 mm, S_0 was poorly sorted (S_0=2.47-3.92), and S_k was very fine skewed (S_k ranging from -0.61 to -0.38). In C1, very coarse silts were uniformly distributed from 0 to 70 cm, presenting in 100% of the samples (25/25). The Md varied from 0.038 to 0.054 mm, S_0 from 1.79 to 2.41, indicating moderately well to poorly sorted, and S_k ranged from 0.59 to -0.03, showing a very fine to symmetric skew. In C2, very coarse silt was distributed alternately from the top, middle, and bottom of the core, accounting for 60% of the samples (15/25). The Md was 0.031-0.047 mm, S_0 ranged from 2.25 to 2.52, indicating poorly sorted, and S_k ranged between -0.70 to 0.07 indicating very fine to symmetrical skew.

Coarse silt was found in surface and C2 core sediments, distributed nearshore (samples 3, 5, 18) and offshore (samples 9, 26), accounting for 16.6% of samples (5/30) (Fig. 2). The range of Md was 0.021 to 0.029 mm, S_0 was poorly to very poorly sorted (S_0=2.71-4.59), and S_k was very fine to fine skewed (S_k=-0.45 to -0.12). In C2, coarse silt ranging from 4 to 47 cm accounted for 36% of the samples (9/25), Md was from 0.021 to 0.030 mm, S_0 was poorly sorted (S_0=2.59-3.78), and S_k was very fine to symmetrically skewed (S_k=-0.62 to -0.03).

Surface and C2 core sediments contained medium silt. Surface sediments distributed nearshore (samples 13, 29, 30) accounted for 10% of the samples (3/30) (Fig. 2). The Md was 0.013 to 0.015 mm, S_0 was very poorly sorted (S_0=4.00-4.73), and S_k was symmetrical skewed (S_k varied from -0.10 to -0.09). In C2, only 4% of the total samples (1/25) had a length of 38-41 cm, S_0 indicating poorly sorted (S_0=3.06), and S_k showing coarse skewed (S_k=0.30).

3.2. Distribution of minerals in sediments

Various sedimentary minerals were identified including quartz, illite, kaolinite, chlorite, feldspar, goethite, halite, calcite, aragonite, gibbsite, and montmorillonite (Table 1).

Table 1. Contents of minerals in sediment.

Position	Levels	Minerals (%)											
		Mont.	*Illi.*	*Kao.*	*Clo.*	*Qua.*	*Fel.*	*Go.*	*Ha.*	*Py.*	*Gip.*	*Can.*	*Ara.*
Surface sediment (n=30)	Min.	0.0	3.0	3.0	2.0	26.0	3.0	3.0	0.0	0.0	0.0	0.0	0.0
	Max.	3.0	23.0	18.0	7.0	79.0	16.0	7.0	3.0	0.0	0.0	11.0	5.0
	Aver.	0.3	14.3	10.0	5.0	50.5	6.9	4.7	1.8	0.0	0.0	2.7	0.2
	SD.	0.8	5.0	4.7	1.3	13.5	3.7	0.8	0.8	0.0	0.0	3.1	0.9
C1 (n=25)	Min.	0.0	16.0	12.0	5.0	32.0	3.0	2.0	0.0	0.0	1.0	0.0	0.0
	Max.	0.0	25.0	19.0	7.0	48.0	7.0	4.0	2.0	4.0	3.0	3.0	7.0
	Aver.	0.0	19.6	15.0	5.4	41.3	4.8	3.2	0.8	2.6	2.0	0.4	0.4
	SD.	0.0	2.5	1.5	0.6	4.1	1.1	0.8	1.0	1.0	0.5	1.0	1.6
C2 (n=25)	Min.	0.0	17.0	6.0	5.0	35.0	3.0	3.0	0.0	2.0	0.0	0.0	0.0
	Max.	0.0	25.0	16.0	7.0	51.0	13.0	4.0	2.0	4.0	2.0	0.0	0.0
	Aver.	0.0	20.5	12.8	6.0	42.7	6.2	3.6	1.0	2.8	0.4	0.0	0.0
	SD.	0.0	2.1	2.1	0.5	3.7	2.5	0.5	1.0	0.7	0.8	0.0	0.0

Mont.: Montmorillonite; Illi.: Illite; Kao.: Kaolinite; Clo.: Chlorite; Qua.: Quartz; Fel.: Feldspar; Go.: Goethite; Hal.: Halite; Can.: Calcite; Ara.: Aragonite; Gip.: Gibbsite; Py.: Pyrite.

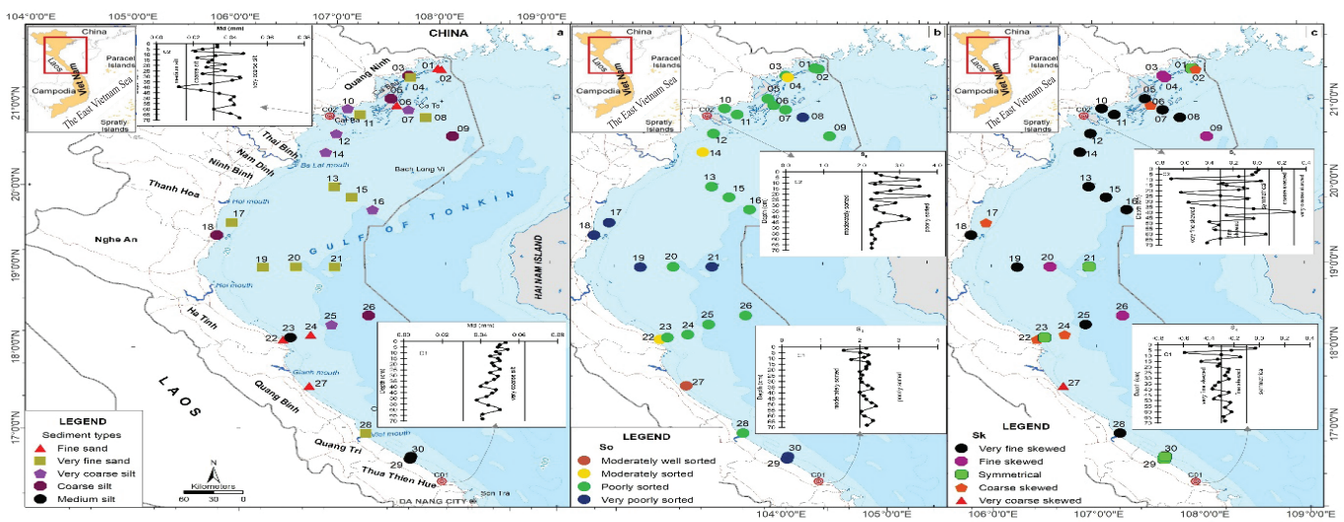

Fig. 2. Distribution of sediment types, sorting, and skewness.

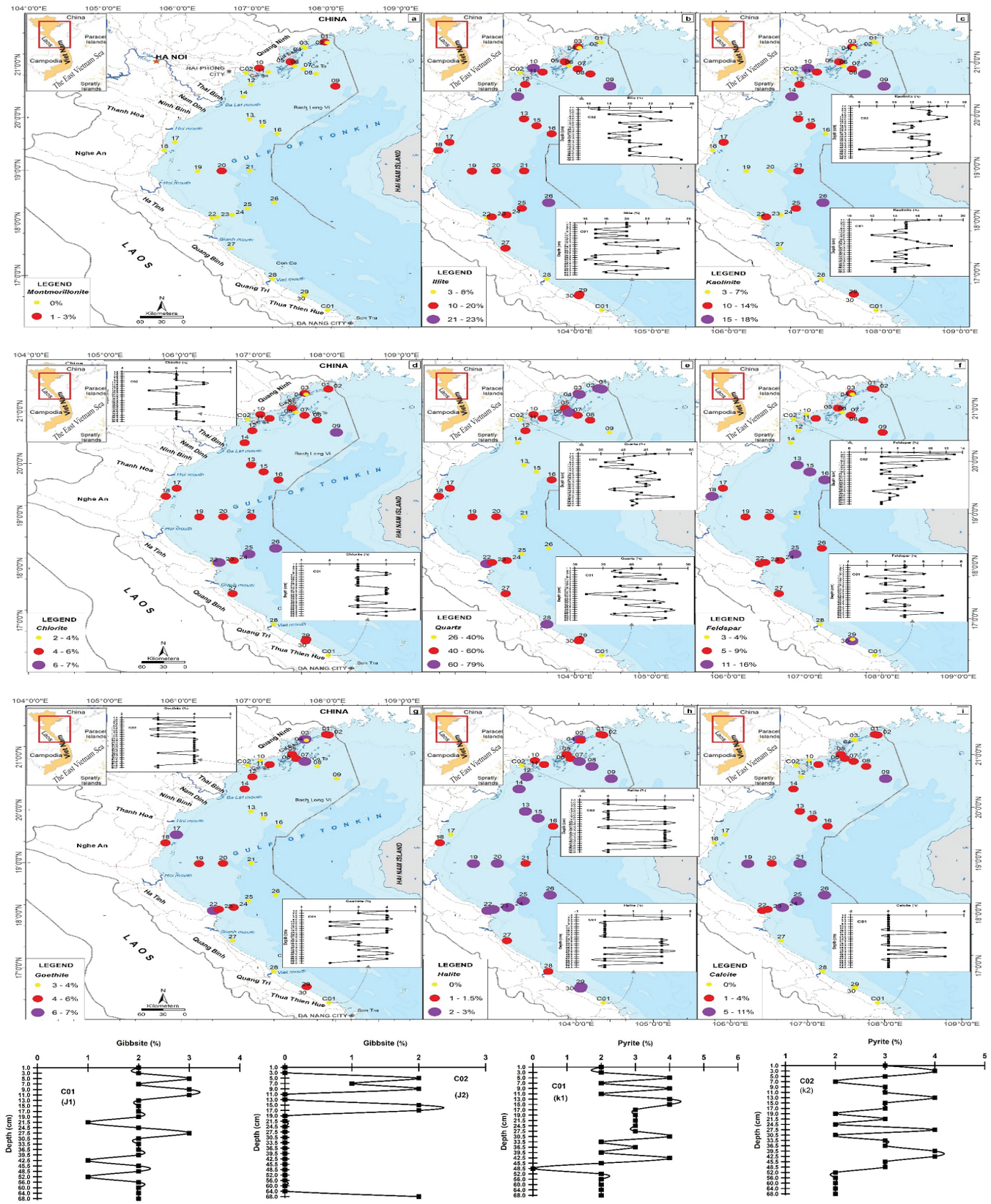

Fig. 3. Distribution of montmorillonite (A), illite (B), kaolinite (C), chlorite (D), quartz (E), feldspar (F), goethite (G), halite (H), calcite (I), gibbsite with (J1, J2) showing depth distribution (J), and pyrite with (K1, K2) showing depth distribution (K).

Montmorillonite was detected in surface sediments at concentrations ranging from 0 to 3%, with highest values of 1-3% found nearshore (samples 1, 5, 10) and offshore (samples 9, 20), but not in other areas. It did not appear in the cores (Fig. 3A).

Illite was found in both surface and core sediments. Surface sediment content ranged from 3 to 23% and averaged 14.3%, with the highest concentrations (21-23%) were found offshore (samples 9, 26) and nearshore (samples 10, 14), 10-20% concentrations were found nearshore (samples 3, 5, 7, 11, 12, 17, 18, 23, 27, 29, 30) and offshore (samples 8, 13, 15, 16, 19, 20, 21, 24, 25), and concentrations of 3-8% were found only nearshore (samples 1, 2, 4, 6, 22, 28). In C1, illite content ranged from 16 to 25% with an average of 19.6%. Illite contents ranging between 21-25% were found from the middle to the bottom core. Contents ranging between 18-20% were found in the top, middle, and bottom, while 16-17% contents were found in the top and middle. In C2, illite contents ranging between 21-25% was distributed in the top, middle, and bottom of the core, with contents of 18-20% distributed in the top, middle, and bottom of the core, and 17% content was found in the top of the core (Fig. 3B).

The kaolinite content in surface sediments ranged from 3 to 18% with an average of 10%. The offshore and nearshore content was 15-18% (samples 9, 8, 26) and (samples 10, 14), respectively. Kaolinite contents ranging between 10-14% were found nearshore (samples 3, 5, 7, 11, 12, 17, 23, 30) and offshore (samples 13, 15, 21, 25), and 3-7% contents were found nearshore (samples 1, 2, 4, 6, 18, 22, 27, 28, 29) and offshore (samples 16, 19, 20, 24). In C1, the content range of 17-19% was found distributed in the top, middle, and bottom of the core. Meanwhile, contents of 15-16% kaolinite were found in the top, middle, and bottom of the core, and contents of 12-14% were distributed in the top, middle, and bottom of the core. In C2, kaolinite content ranged from 6 to 16% and averaged 12.8%, with the higher average content of 15-16% distributed in the top and bottom of the core, the 10-14% content range found most often in the top, middle, and bottom, and the 6-11% content range found in the middle and bottom of the core (Fig. 3C).

The chloride content in surface sediments ranged from 2-7%, with an average of 5.0%. The highest chlorite concentration of 6-7% was found near the coast (samples 12, 23, 30) and in the offshore area (samples 9, 13, 21, 25, 26). A chlorite concentration of 5% was the most abundant and found near the coast (samples 2, 3, 5, 7, 10, 11, 14, 18, 29, 27) and offshore (samples 8, 15, 16, 19, 20, 24). Finally, chlorite contents of 2-4% were found nearshore (samples 1, 4, 6, 22, 28). In C1, chlorite content varied from 5-7%, with an average of 5.4 %. Chlorite content of 6-7% was found in the top, middle, and bottom of the core, while 5-6% content was mostly found from the top to the bottom of the core. In C2, chlorite content varied from 5 to 7% and averaged 6.0%. Contents of 5% and 7% were not as abundant as 6%. Chlorite content in core and surface sediments did not differ significantly among stations and layers (Fig. 3D).

Quartz was the most abundant mineral in surface and core sediments. Surface sediments contained 26-79% quartz and 50.5% on average, with 60-79% contents found mostly nearshore (samples 1, 2, 6, 22, 27, 28), 40-60% contents found nearshore (samples 3, 5, 7, 10, 11, 12, 17, 18, 23, 29, 30) and offshore (samples 8, 16, 19, 20, 24), and finally contents of 26-40% were mostly found offshore (samples 9, 13, 15, 21, 25, 26), with one instance nearshore (sample 14). In C1, content ranged from 32-48% with an average of 41.3%. Quartz contents of 45-48% and 40-44% were found divided into the upper, middle, and lower sections. Meanwhile, contents of 32-39% were found distributed from top to bottom. In C2, the content range of quartz was 35-51%, with 42.7% on average. Quartz contents of 45-51% were found divided into upper, middle, and lower sections, while 40-44% content was found distributed from top to bottom and 35-39% from top to middle (Fig. 3E).

Feldspar was found on the surface and within two sedimentary cores. In surface sediments, feldspar contents ranged from 3 to 16%, averaging 6.9%, with 11-16% distributed nearshore (samples 18, 29) and offshore (samples 13, 15, 16, 25), 5-9% distributed nearshore (samples 1, 2, 3, 5, 7, 11, 17, 22, 23, 27) and offshore (samples 8, 9, 19, 20, 24, 26), and 3-4% content found distributed nearshore (samples 4, 6, 10, 12, 14, 28, 30) and offshore (sample 21). In C1, feldspar contents of 3-7% were found distributed with an average of 4.8%. The highest contents of 6-7% were found distributed at the top, middle, and bottom of the core. Meanwhile, 5% content was found mostly at the top, middle, bottom and 3% content was found in some layers at the top, middle, and bottom of the core. In C2, the feldspar content range was 3-13% with an average of 6.2%. Feldspar contents of 7-13% were found distributed between the top and middle of the core, and 3-6% content was found distributed among the top, middle, and bottom of the core (Fig. 3F).

Goethite contents ranged from 3 to 7%, averaging 4.7%, in surface sediments with contents of 6-7% found distributed nearshore (samples 3, 7, 17, 22). Goethite content of 5% was found both nearshore (samples 1, 2, 5, 6, 11, 12, 14, 18, 23, 30) and offshore (samples 19, 20, 24). Goethite contents of 3-4% were found distributed nearshore (samples 4, 10, 27, 28, 29) and offshore (samples 8, 9, 13, 15, 16, 21, 25, 26). In C1, goethite content ranged from 2-4% with an average of 3.2%. Contents of 3% and 4% were the most common, while 2% content was uncommon. In C2, the range was also 3-4%, with an average of 3.6%, and goethite content of 4% was found distributed mostly from the middle to bottom of the core (Fig. 3G).

Halite content ranged from 0-3% in surface sediments with 1.8% average content. Halite contents of 2-3% were found distributed both nearshore (samples 3, 7, 12, 14, 22, 23, 29, 30) and offshore (samples 8, 9, 13, 15, 19, 20, 24, 25, 26), contents of 1-1.5% were found distributed nearshore (samples 1, 2, 4, 5, 6, 10, 11, 18, 28) and offshore (samples 16, 21), with some nearshore samples (17, 27) found without halite. Halite contents from 0 to 2% for C1 and C2, respectively, were found, averaging 0.8% in

C1 and 1% in C2. Halite content of 2% in both C1 and C2 was mostly found distributed from the middle to the bottom of the core (Fig. 3H).

Calcite and aragonite were carbonate minerals formed from biological materials. In surface sediments, they spread far from the shore and their content was often high, up to 11%, the content of 5-11% distributed mostly offshore (9, 19, 21, 26, 24, 25) and nearshore (14), the content 1-4 % were distributed nearshore (1, 2, 5, 6, 7, 11, 22, 23) and offshore (8, 13, 15, 16, 20), and some nearshore stations did not contain calcite and aragonite (3, 4, 10, 12, 17, 18, 27, 28, 29, 30). C1 had some layers with a content of 3-9% (17.0, 36.5, 42.5, 48.5cm), the remaining layers did not contain calcite and aragonite. In C2, calcite and aragonite were not present (Fig. 3I).

Gibbsite was absent from surface sediments and only found in C1 and C2 and the content was less than 4%. In C1, contents ranged from 1 to 3%, with an average of 2%. Gibbsite content of 2% was more common than 3 and 1% content. For C2, gibbsite content ranged from 0 to 2%, with an average of 0.4%, and contents of 1 and 2% were found distributed only in a few layers, most layers did not appear to contain gibbsite (Fig. 3J).

Pyrite was present only in the C1 and C2 cores and absent in surface sediments. In C1, pyrite content ranged from 0 to 4% with an average of 2.6%. Pyrite content of 2% was most common and spread lower than 3% and 4% contents. In C2, pyrite content averaged 2.8% with a range of 2-4%. Pyrite contents of 2% and 3% were common. Both C1 and C2 contained pyrite of high content below the surface layer (Fig. 3K).

3.3. Correlation between sediment parameters

In surface sediments, the parameters showed both negative and positive correlation (Fig. 4A). There was a strong positive correlation among illite and kaolinite and chlorite (R=0.84); moderate correlation (R=0.50-0.57) was found among halite and illite, kaolinite, chlorite, Md and S_k, and halite and calcite; and there was a weak correlation (R=0.38-0.43) between quartz and Md, S_k, gothite and S_0, and calcite and chlorite. There was a strong negative correlation between quartz and illite, kaolinite and chlorite (R ranging from -0.84 to -0.92); a moderate correlation (R ranging from -0.52 to -0.64) was found between Md and illite, kaolinite, quartz and halite, calcite; and a weak correlation was found between halite and Md, S_0, S_k, and kaolinite and S_k, and Md and chlorite.

In C1, there was no strong positive correlation, however there was a moderate correlation (R=0.57-0.64) between illite and kaolinite, chlorite; there was a weak correlation between kaolinite and chlorite, and between S_0 and quartz (R=0.40). There was no strong negative correlation, however, a moderate correlation (R ranging from -0.66 to -0.73) was found between quartz and illite and kaolinite, and between S_0 and S_k; there was a weak correlation between chlorite and quartz, goethite, and between kaolinite and calcite (Fig. 4B).

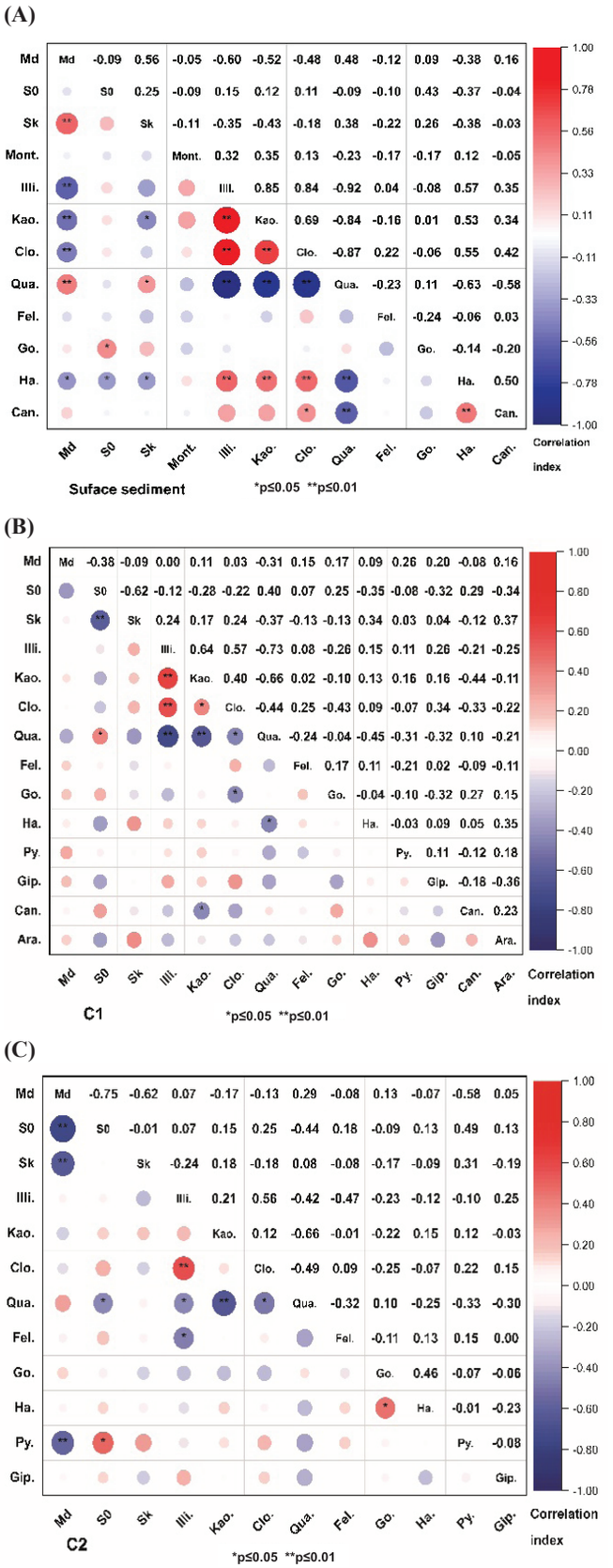

Fig. 4. (A-C) Correlation matrix between sediment parameters.

In C2, there was a moderate positive correlation found between illite and chlorite (R=0.56); a weak correlation (R=0.46-0.49) between halite and gothite, and between pyrite and S_0. A moderate negative correlation (R from -0.58 to -0.75) was found between Md and S_0, S_k and pyrite, and between kaolinite and quartz. There was a weak negative correlation (R ranging from -0.42 to -0.49) between quartz and S_0, illite, chlorite, and between illite and quartz, feldspar (Fig. 4C).

3.4. Characteristic sediment groups

Based on grain sizes and minerals, clustering techniques were used to divide the surface sediments of the Gulf of Tonkin into three groups with different characteristics (Table 2, Fig. 5). Group 1 consists of 7 stations located mainly nearshore (samples 1, 2, 4, 6, 22, 27, 28), which were fine sand, poorly sorted, symmetrically skewed, and containing low contents of illite, kaolinite, chlorite, felspar, calcite, halite, and a high content of quartz. Group 2 had 15 stations, which were divided into nearshore stations (samples 3, 5, 7, 11, 12, 17, 18, 23, 29, 30) and offshore stations (samples 8, 16, 19, 20, 24). This group had very coarse silt, were very poorly sorted, fine skewed, and contained illite, kaolinite, chlorite, halite, feldspar, and calcite. The contents most minerals of Group 2 were higher than those in Group 1, while the quartz content in Group 2 was lower than that of Group 1. Group 3, with 8 stations, was the most abundant of the offshore stations (samples 9, 13, 14, 15, 21, 25, 26) and nearshore (sample 10); they had very coarse silt, were poorly sorted, and very fine skewed. This group consisted of illite, kaolinite, chlorite, feldspar, calcite, and aragonite, were higher in content than those of Groups 1 and 2. However, quartz and goethite contents were lower than Group 1 and 2 (Table 2). Groups of sedimentary parameters were divided into three groups: Group 1 (Md, S_0, S_k, quartz, goethite) represents a strong environment (a zone where land and sea have strong interaction), Group 2 (montmorillonite, illite, kaolinite, chlorite, halite, and calcite), which represents a quiet environment (a zone where land and sea have a weak interaction), and, finally, Group 3 (feldspar) represents a mixed environment (Fig. 5).

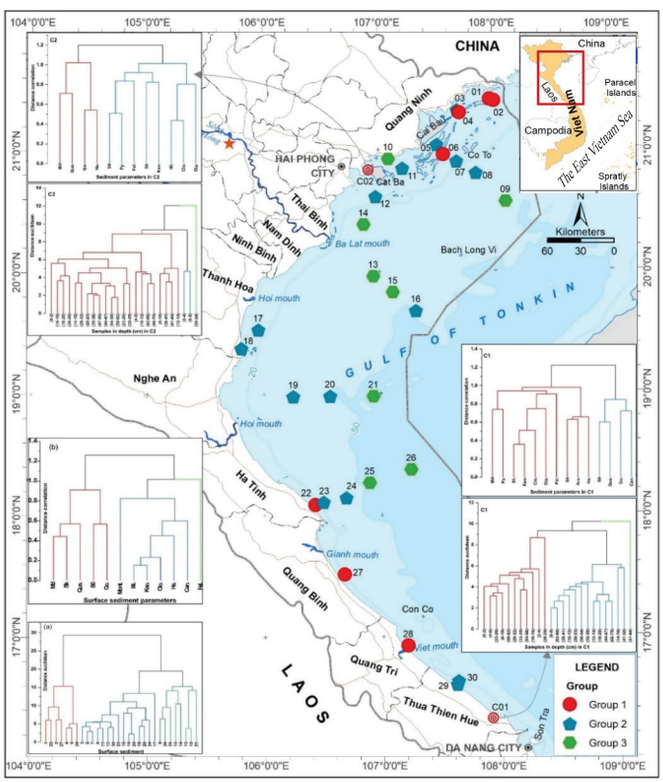

Fig. 5. Distribution of sediment groups.

Table 2. Grain sizes and mineral compositions in groups of sediment.

Position	Group	Number of stations	Sediment parameters			Content (%) of minerals										
			Md (mm)	S_0	S_k	*Mont.*	*Illi.*	*Kao.*	*Clo.*	*Qua.*	*Fel.*	*Go.*	*Ha.*	*Can.*	*Ara.*	*Py.*	*Gip.*
Surface	1	7	0.134	2.57	0.05	0	7	4	3	70	6	5	1	1	0	-	-
	2	15	0.059	4.42	-0.26	0	15	10	5	50	7	5	2	2	0	-	-
	3	8	0.054	3.37	-0.37	1	19	15	6	35	8	4	2	5	1	-	-
C1	1	11	0.049	2.05	-0.26	-	22	16	6	37	5	3	1	0	0	3	2
	2	13	0.045	2.18	-0.33	-	18	14	5	45	5	3	0	0	0	2	2
	3	1	0.048	2.10	-0.24	-	16	14	5	39	4	4	2	2	7	4	1
C2	1	22	0.033	2.66	-0.22	-	21	13	6	42	6	4	1	-	-	3	0
	2	2	0.027	3.01	-0.08	-	18	13	6	41	13	3	1	-	-	3	1
	3	1	0.040	2.25	-0.31	-	20	6	6	51	6	4	0	-	-	2	0

C1 had three groups with different characteristics (Table 2). Group 1 had 11 samples (layers) from the top to the middle of the core, had the highest Md, and were poorly sorted and fine skewed. Contents of illite, kaolinite, and chlorite were higher in Group 1 than in Groups 2 and 3, while quartz was the lowest. Group 2 had 13 samples (layers) mostly found distributed near the bottom of the core, and in some layers near the top and middle. Mineral contents of illite, kaolinite, chlorite, and pyrite were lower in Group 2 than in Group 1, while quartz was the highest. Group 3 had only one sample (layer) distributed in the middle core, containing calcite, aragonite, pyrite, halite, and goethite contents that were higher in this group than in Groups 1 and 2. The contents of other minerals were lower. Sediment parameters were divided into two groups: Group 1 (Md, pyrite, illite, kaolinite, chlorite, gibbsite, feldspar, S_k, aragonite, halite) indicating a quiet environment, and Group 2 (S_0, quartz, goethite, calcite), indicating a more dynamic environment.

There were three sediment groups in C2 (Table 2). Group 1 consisted of 22 samples (layers) that were distributed from the top to the bottom of the core; those sediments had very coarse silt, were poorly sorted, and fine skewed. The contents of illite, kaolinite, and chlorite were high. Group 2, with 2 samples (layers) distributed near the top (2-4 and 6-8 cm), had coarse silt, was poorly sorted, and symmetrically skewed. Mineral contents of feldspar, illite, quartz, and gibbsite were different from those in Groups 1 and 3. Group 3 had only one sample (layer) near the end of the core (50-54 cm) and had a high quartz and low kaolinite content.

4. Discussion

The dynamics of the sedimentary environment are reflected in the distribution of grain size and mineral composition grouped by similarity of grain size and mineral composition. The Gulf of Tonkin is vast, with many conditions affecting the sedimentary environment. The characteristics of surface sediments allow us to understand the bay, while the characteristics of sedimentary cores help understand the local sedimentary environment.

Surface sediments were divided into three groups with different characteristics. The strong dynamic group (Group 1) was distributed nearshore with fine and very fine sand, poorly sorted, and symmetrically skewed. Quartz was the most abundant mineral at 70%, while illite, kaolinite, and chlorite contents were lower. The weak dynamic group (Group 2) was distributed around the nearshore and offshore regions, it had very coarse silt, was very poorly sorted, and fine skewed. Mineral contents of illite, kaolinite, and chlorite increased significantly, and sediments of biological origin increased due to the presence of calcite. The quiet dynamics group (Group 3) was distributed offshore, had very coarse silt, was poorly sorted, and very fine skewed. The contents of montmorillonite, illite, kaolinite, and chlorite were higher than in the previous groups, while the quartz content reduced significantly and marine and biological sediments increased by calcite, aragonite, and halite present. There were four factors (FA) affecting surface sediments, ranging from 10.81 to 40.42% (Table 3). FA1 was 40.42% and indicated Md, S_k, illite, kaolinite, chlorite, quartz, and halite. FA 2 was 14.90% for S_0 and goethite. FA3 was 11.81% for calcite, and FA4 was 10.81% for feldspar and montmorillonite (Table 3). FA1 consisted of sediments supplied by mechanical weathering and erosion of mother rocks from the mainland and islands eroded by the presence of illite, kaolinite, chlorite, and quartz in surface sediments, under the influence of rivers and sea currents distributed in the bay. In addition, FA1 was influenced by environmental and oceanic physico-chemical factors such as waves, currents, tides, and salinity by the presence of Md, S_k, and Halite. FA2 reflects sediment sorting that influences goethite formation through geochemical processes. FA3 reflects that surface sediments had another sediment source from biological material through the presence of calcite. FA4 was affected by montmorillonite and feldspar, indicating sediments from weathering of mother rocks.

The correlation among sedimentary parameters in surface sediments reflect the relationship of sediment supplies, environmental dynamics, and form minerals. The same sediment supplies are shown by the positive correlation between illite, chlorite, and kaolinite. Environmental dynamics are shown between Md and S_k, quartz, illite, chlorite, and kaolinite. The mineral formations are demonstrated by the positive correlation of halite and gothite with S_0, illite, chlorite, kaolinite, and calcite (Fig. 4A).

Table 3. Sediment parameters and factors' effect on sediments.

N_0	Parameters	Surface sediment				C1				C2			
		FA1	*FA2*	*FA3*	*FA4*	*FA1*	*FA2*	*FA3*	*FA4*	*FA1*	*FA2*	*FA3*	*FA4*
1	Md	-0.63	0.00	0.65	-0.07	0.27	0.29	0.41	-0.58	-0.73	0.52	0.21	-0.07
2	S_0	-0.01	0.83	-0.15	0.25	-0.62	-0.45	0.31	0.11	0.75	-0.19	0.12	-0.19
3	S_k	-0.51	0.44	0.48	0.03	0.50	0.47	-0.40	0.33	0.24	-0.60	-0.50	0.32
4	Mon.	0.29	-0.02	-0.07	-0.71	-	-	-	-	-	-	-	-
5	Illi.	0.93	0.20	-0.05	-0.03	0.75	-0.30	0.16	0.16	0.31	0.79	-0.16	0.33
6	Kao.	0.88	0.24	-0.05	-0.22	0.72	-0.16	0.18	-0.04	0.53	0.14	0.10	0.49
7	Clo.	0.86	0.17	0.10	0.23	0.68	-0.39	-0.03	0.25	0.55	0.52	-0.02	-0.13
8	Qua.	-0.96	-0.09	-0.13	-0.15	-0.84	-0.22	-0.39	-0.03	-0.80	-0.32	-0.37	-0.06
9	Fel.	0.12	-0.40	-0.17	0.74	0.13	-0.15	0.65	0.30	0.23	-0.26	0.39	-0.67
10	Go.	-0.18	0.74	-0.08	0.05	-0.36	0.32	0.66	0.02	-0.31	-0.21	0.62	0.22
11	Ha.	0.73	-0.25	0.26	-0.15	0.40	0.49	0.07	0.35	0.08	-0.22	0.79	0.36
12	Py.	-	-	-	-	0.24	0.20	-0.02	-0.70	0.64	-0.40	-0.09	-0.10
13	Gib.	-	-	-	-	0.48	-0.30	-0.11	-0.28	0.16	0.47	-0.04	-0.38
14	Can.	0.48	-0.06	0.77	0.17	-0.45	0.32	0.19	0.21	-	-	-	-
15	Ara.	-	-	-	-	0.01	0.88	-0.06	0.06	-	-	-	-
Eigenvalue		4.85	1.79	1.42	1.30	3.76	2.20	1.55	1.38	3.06	2.23	1.66	1.30
Variance (%)		40.42	14.90	11.81	10.81	26.86	15.75	11.04	9.90	25.51	18.59	13.84	10.80
Cumulative variance (%)		40.42	55.32	67.12	77.93	26.86	42.61	53.65	63.52	25.51	44.09	57.93	68.73

The C1 core was in Tam Giang - Cau Hai Lagoon, which was a quiet environment with four factors affecting the sedimentary environment from 9.90 to 26.86% (Table 3). FA1 was 26.86% by S_0, S_k, illite, kaolinite, chlorite, and quartz. FA2 was 15.75% by aragonite. FA3 was 11.04% by feldspar and goethite. FA4 was 9.90% by Md and pyrite (Table 3). FA1 indicated weak dynamics, showing a combination of S_0, S_k, illite, kaolinite, chlorite, and quartz. The origin of illite, kaolinite, chlorite, and quartz was from the erosion and weathering of rocks around the lagoon. FA2 indicated source sediment supplied from biological materials by the presence of aragonite (Group 3). FA3 indicated physiochemical factors that formed goethite (Group 2). FA4 indicated Md factors affecting pyrite formation.

Correlation in C1 reflects sediment supplies, dynamic conditions, and mineral formation. Sediment supplies are shown by the positive correlation between illite, kaolinite, and chlorite. Environmental dynamics are shown by the negative correlation between quartz, S_0 and illite, kaolinite, chlorite, and S_k. The unfavourable factors for the formations of gothite, halite, and calcite are shown by the negative correlation between them with chlorite, quartz, and kaolinite (Fig. 4B).

In C2, which was taken from the Bach Dang estuary, were four factors affecting the sedimentary environment ranging from 10.8 to 25.51%. FA1 was 25.51% by Md, S_0, kaolinite, chlorite, quartz, and pyrite. FA2 was 18.59% by S_k, and illite. FA3 was

13.84% by halite and goethite. FA4 was 10.8% by feldspar (Table 3). FA1 indicated a weak environment with Md, S_0, kaolinite, chlorite, quartz, and pyrite, with source sediment provided by weathering process of kaolinite, chlorite, and quartz, in addition to the formation of pyrite. FA2 reflected a quiet environment by the deposition of illite and S_k. FA3 indicated the advantage of forming goethite and halite. FA4 indicated the source of feldspar.

The correlation between sediment parameters in C2 shows sediment supplies through the positive correlation between chlorite and illite. Environmental dynamics are shown through Md, S_0, S_k, quartz, and feldspar with illite, kaolinite, and chlorite. Formation of minerals was shown by the positive and negative correlation of pyrite, halite, and gothite with Md and S_0 (Fig. 4C).

5. Conclusions

In the Gulf of Tonkin, surface sediments were found distributed with very fine sand > fine sand = very coarse silt = medium silt > coarse silt. In C1, very coarse silt was distributed across all cores. C2 contained very coarse silt > coarse silt > medium silt. The average mineral content of the sediments was quartz > illite > kaolinite > chlorite > feldspar > goethite > pyrite > halite > calcite > gibbsite > aragonite.

There were three groups of surface sediments with different properties. Group 1 was distributed nearshore and is characterized by a strong environment evidenced by fine sands with high quartz content and low illite, kaolinite, and chlorite content. Group 2 was distributed nearshore and offshore and is in a characteristically weak environment evidenced by very coarse silt, increasing contents of illite, kaolinite, and chlorite, and decreasing quartz content. Group 3 was distributed nearshore and offshore with a characteristic quiet environment as evidenced by the highest content of illite, kaolinite, chlorite, and calcite, and the lowest content of quartz. Both C1 and C2 are characteristically weak environments found in the Tam Giang - Cau Hai lagoon and Bach Dang estuary, respectively, depositing very coarse silt, coastal silt, medium silt, and high contents of illite, kaolinite, and chlorite.

Sediment sources in the Gulf of Tonkin are primarily due to the weathering and erosion of formations from the mainland and islands carried by rivers, waves, currents, and tides through the presence of illite, kaolinite, quartz, chlorite, and feldspar. The presence of goethite, halite, and pyrite in the sediments suggested formation by geochemical processes. The presence of calcite and aragonite in the sediments reflects the origin of the biological material.

CRediT author statement

Dang Hoai Nhon, Nguyen Van Thao, Tran Duc Thanh: Conceptualization, Methodology; Dang Hoai Nhon, Lai Thi Bich Thuy, Nguyen Van Thao: Data curation, Investigation; Dang Hoai Nhon, Nguyen Dac Ve, Bui Van Vuong, Bui Thi Thanh Loan, Hoang Thi Chien, Duong Thanh Nghi: Writing - Original draft preparation; Nguyen Dac Ve, Dang Hoai Nhon: Software, Validation; Dang Hoai Nhon, Tran Duc Thanh: Writing - Reviewing and Editing.

ACKNOWLEDGEMENTS

The authors would like to gratefully acknowledge the Vietnam Ministry of Science and Technology (KC.09.16/16-20, DTDLCN.14/23) and Vietnam Academy of Science and Technology (BSTMV.25/15-18, VAST05.01/20-21) for their support for the projects.

COMPETING INTERESTS

The authors declare that there is no conflict of interest regarding the publication of this article.

REFERENCES

[1] J. Li, J. Gao, Y. Wang, et al. (2012), "Distribution and dispersal pattern of clay minerals in surface sediments, eastern Beibu Gulf, South China Sea", *Acta Oceanologica Sinica*, **31**, pp.78-87, DOI: 10.1007/s13131-012-0194-z.

[2] F. Ma, Y. Wang, Y. Li, et al. (2010), "The application of geostatistics in grain size trend analysis: A case study of eastern Beibu Gulf", *Journal of Geographical Sciences*, **20(1)**, pp.77-90, DOI: 10.1007/s11442-010-0077-1.

[3] C.K.T. Ngo, L.V. Hoang, B.V. Phan, et al. (2020), "The characteristics of the surface sediments in Co To island", *Journal of Mining and Earth Sciences*, **61(2)**, pp.33-40, DOI: 10.46326/JMES.2020.61(2).04.

[4] D.H. Nhon, L.T.B. Thuy, N.H. Hoang, et al. (2019), "Mineral compositions and grain sizes of sediments in intertidal zone in Northern Vietnam", *Vietnam Journal of Marine Science and Technology*, **19(3A)**, pp.63-75, DOI: 10.15625/1859-3097/19/3A/14292.

[5] D.M. Duc, M.T. Nhuan, C.V. Ngoi, et al. (2007), "Sediment distribution and transport at the nearshore zone of the Red river delta, Northern Vietnam", *Journal of Asian Earth Sciences*, **29(4)**, pp.558-565, DOI: 10.1016/j.jseaes.2006.03.007.

[6] D.H. Nhon, L.H. Giao (2017), "Physical features of water and surface sediments in the Ha Long bay, Vietnam", *VNU Journal of Science: Earth and Environmental Sciences*, **33(3)**, pp.33-41, DOI: 10.25073/2588-1094/vnuees.4125.

[7] B.V. Vuong, Z. Liu, T.D. Thanh, et al. (2016), "Initial results of study on sedimentation rate, sediment sources to Ha Long bay: Evidence from the 210Pb and 137Cs radiotracer", *Vietnam Journal of Marine Science and Technology*, **16(1)**, pp.54-63, DOI: 10.15625/1859-3097/16/1/6527 (in Vietnamese).

[8] N.H. Hoang, B.V. Vuong, E. Egidarev, et al. (2020), "Major characteristics of surface sediments within the shallow water of the Cat Ba island, north Vietnam", *VNU Journal of Science: Earth and Environmental Sciences*, **36(4)**, pp.67-89, DOI: 10.25073/2588-1094/vnuees.4631.

[9] N.N. Thuy (1984), *Tide in Vietnam Sea*, Science and Technics Publishing House, 203pp (in Vietnamese).

[10] J.S. Galehouse (1971), "Sedimentation analysis", *Procedures in Sedimentary Petrology*, Wiley-Interscience, New York, pp.69-93.

[11] C.K. Wentworth (1922), "A scale of grade and class terms for clastic sediments", *The Journal of Geology*, **30(5)**, pp.377-392, DOI: 10.1086/622910.

General Instructions on using this template and submitting a manuscript to VJSTE: Thank you for preparing a manuscript for submission to VJSTE. Using this template, or following the guidelines below, will help us in processing your article.

The structure of different types of articles may vary according to the type of study, and the content of the article.

The following are the detailed main components of the original research and review articles submitted to the journal.

From 2023 onwards, you can submit your article at: https://mc04.manuscriptcentral.com/mostvjste

Original research

The original research should have three following parts:

Preliminary section: It includes title, list of all contributing authors with their institutional affiliation, and abstract (160-250 words) with at least 3 keywords.

Title: How to format a science article (replace with your real title)

Author(s): List the author name(s) separated by commas. Use superscript numbers to link affiliations, and symbols *†‡ for author notes. For example, Y. Obsie[1*], S.A. Adem[1, 2]

**Corresponding author(s):* Include the email addresses or telephone numbers of the corresponding author(s). Please use the asterisk (*) symbol for the corresponding author information. This information is at the bottom of the manuscript's first page.

Author's affiliation addresses:

[1]Affiliations should be preceded by superscript numbers corresponding to the author list

[2]For any institutions, please provide the institution name, street, district, city, country

Received ; revised ; accepted

Abstract:
Start your abstract here…
Keywords: **keyword 1, keyword 2, keyword 3…**
Classification number(s): **1.1, 3.4, 5.3, etc.**

Abstract: The abstract should range between 160 and 250 words and be structured in a single paragraph following keywords in a separate line. The abstract should represent the main part of the research manuscript. It should reflect a brief and comprehensive background following the aim of the study (main questions to be addressed), methods used for investigating the problem, a summary of significant findings, main conclusions, and implications of the results.

Keywords: They should come immediately after the abstract and contain 3-7 specific and relevant keywords. They should reflect the research study and the relevant field of research.

Classification numbers: Depend on the Journal's Classification Scheme.

Author(s) are encouraged to write a "Highlights" that summarises the most exciting, interesting points from your manuscript.

Manuscript section: It is the main body of the scientific manuscript including: 1) Introduction; 2) Material(s) and method(s); 3) Results and discussion (separation of these two sections is acceptable); 4) Conclusions; 5) Recommendations/Suggestions/Implications/Study limitations...(if any). These sections may slightly vary depending on the type of research approach and design used in the research. Each section should be numbered.

All of the Figures, Tables, and Equations should be cited in numerical order.

Figures

Fig. #: (Begin each figure caption with a label, "**Fig. 1.**" for example, as a new paragraph).

Fig. 1. The figure caption should begin with an overall descriptive statement of the figure followed by additional text. They should be immediately after each figure. Figure parts are indicated with capital letters **(A)**. If you prefer, you can place both the actual figures and captions logically through the text near where they are cited rather than at the end of the file (but not both). If a paragraph in the main text begins with the name of a figure, write out "Figure" in full (e.g., <para> "Figure 1 shows...").

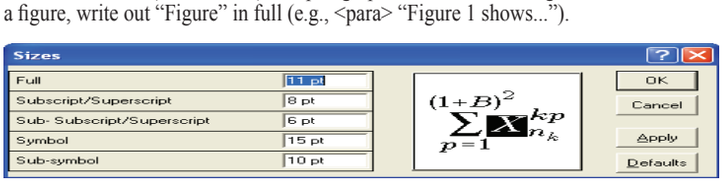

Fig. 1. The figure caption.

Tables

Table #: (Begin each table caption with a label "**Table 1.**", etc. as a new paragraph).

Table 1. Start this caption with a short description of your table. Format tables using the Word Table commands and structures. Do not create tables using spaces or tabs characters.

Table 1. Caption.

a	b	c	d	e
f				
g				
h				

Equations

$$\int_a^b xdx \tag{1}$$

Equations can be included. We do not recommend using the native Word 2007, 2008, 2010 or 2011 equation editor. This can in some cases produce less reliable MathML, the online markup language we use, which may result in display errors. Instead, use the legacy equation editor in Word (Insert menu; select insert object; select word equation) or use MathType (recommended). If you enter equations in simple LaTeX, check that they will convert accurately (Word 2007 and higher can convert simple LaTeX equations).

Closing section: It includes appendices/supplementary materials/data availability statement (if applicable), CRediT author statement (for multiple authors), acknowledgements (if applicable), competing interests, ethics (if any) and a complete list of references corresponding to all the citations given in the text of the manuscript. The appendices/supplementary materials may include data files and other material relevant to the research that should be submitted in separate files if required.

APPENDICES (if any)

The appendices should ideally be under 1000 words (approximately 2 A4 pages) for printing version. With longer appendices, they are only accepted for online publication.

CRediT author statement (for multiple authors)

CRediT offers authors the opportunity to share an accurate and detailed description of their diverse contributions to the published work.

ACKNOWLEDGEMENTS (if applicable)

This section is for the researchers who were funded for the research projects, and it should enclose all sources of financial support.

COMPETING INTERESTS

The author(s) declare(s) that there is no conflict of interest regarding the publication of this article.

REFERENCES

For in-text citation: References should be cited in the bracket with a number [1]. Multiple reference citations are separated by commas [2, 3] or if a series, dashes [4-6]. When citing sources with the author(s) and the year, they should be shortened to the first author's name, followed by et al. (with more than one author) and the year.

For reference list: With less than or equal to three authors, list all the author(s). With more than three authors, the first three should be listed and followed by et al.

References are listed in numerical order, and in the same order in which they are cited in text. The reference list should include all and only those references you have cited in the text. The reference list appears at the end of the article.

The reference consists of: Initial(s) and first/last name of the author(s), author' names separated by commas (Year of publication), "Titles of journal articles or chapter of book", *Title of Journal, Book or Other Publication*, **Volume(Number)** (if any), page numbers (if any), DOI (if any), URL and accessed date (if any) (in its original language if not English).

To cite a website and online/electronic resources, please include the accessed date (day month year).

Example of a reference list:

[1] T. Binzoni, T.S. Leung, D. Boggett, et al. (2003), "Non-invasive laser Doppler perfusion measurements of large tissue volumes and human skeletal muscle blood RMS velocity", *Phys. Med. Biol.*, **48(1)**, pp.2527-2549, DOI: 10.1088/0031-9155-48-15-318.

[2] H.W. Bischoff, H.C. Bold (1963), *Some Soil Algae from Enchanted Rock and Related Algal Species*, University of Texas Publications, 95pp.

[3] R. Busi (2016), "Weedy rice in the Philippines and Vietnam", https://www.aciar.gov.au/publication/technical-publications/weedy-rice-philippines-and-vietnam-final-report, accessed 15 July 2018.

Review articles

They should be different from the original research as they would contain different sections on the literature review. Authors may structure this part as per nature, background, and available literature on the issue argued in the manuscript.

For more detailed instructions, please visit our website: vietnamscience.vn or vietnamscience.vjst.vn

This manuscript template has been used from 2021 onwards.

P-ISSN 2525-2461 • E-ISSN 2615-9937

Vietnam Journal of Science, Technology and Engineering

JUNE 2023 • VOLUME 65 NUMBER 2

EDITORIAL BOARD

EDITORIAL OFFICE

113 Tran Duy Hung Str., Cau Giay Dist., Hanoi, Vietnam

Tel: (84.24) 39436793; Fax: (84.24) 39436794

Email: vjste@most.gov.vn

Website: vietnamscience.vn or vietnamscience.vjst.vn

PUBLICATION LICENCE

No. 459/GP-BTTTT 20th July 2021

No. 50/GP-BTTTT 1st February 2023